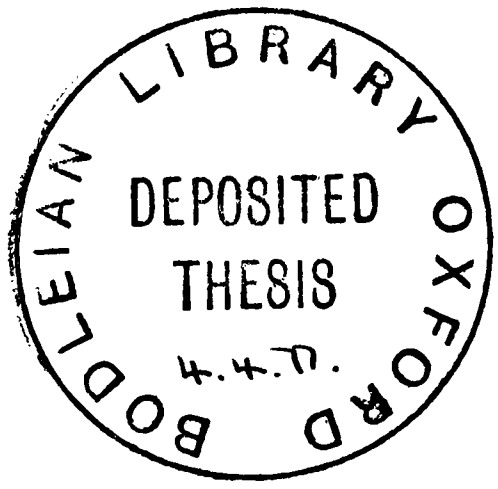
DENDRITIC SOLIDIFICATION

D.J.Allen, M.A.

St. John's College

A thesis submitted in supplication for the degree of Doctor of Philosophy in the University of Oxford.



Department of Metallurgy
and Science of Materials

Michaelmas Term 1976.

CONTENTS

Abstract

Acknowledgements

Chapter I, "Introduction" 1

(a) Thermodynamics of Solidification, p.1 : (b) Interface Kinetics, p.3 : (c) Heat and Mass Transport, p.7 : (d) Interface Shape Evolution, p.11.

Chapter II, "Literature Survey" 15

(a) Dendritic Morphology and Microsegregation ((1) Dendritic Growth, (2) Dendrite Spacing, (3) Dendritic Morphology, (4) Microsegregation), p.15 : (b) Temperature Gradient Zone Melting and Related Phenomena ((1) Heat Flow; (2 - 6) TGZM in Solid-Liquid Systems: (2) Diffusion, (3) Convection, (4) Interface Stability, (5) Interface Kinetics, (6) Interactions with Crystal Defects; (7) Other Migration Phenomena), p.25 : (c) Transparent Organic "Metal Analogues", p.51 : (d) Previous Work by the Author, p.53.

Chapter III, "The Apparatus" 61

(a) Optics, p.61 : (b) The Specimen Cell, p.62 : (c) Fixed-Plates Stage, p.63 : (d) Moving-Plates Stage: Original Design, p.64 : (e) Apparatus Modifications, p.66 : (f) Temperature Measurements in Cells, p.70 : (g) Contrast, p.81.

Chapter IV, "Dendritic Growth" 85

(a) Literature Survey, p.85 : (b) Dendritic Morphology in Thin Cells ((1) Succinonitrile Alloys, (2) CBr_4 Alloys), p. 89 : (c) Dendrite Spacings, p.96 : (d) Dendrite Growth Temperatures, p.99 : (e) Solidification in a Temperature Gradient, p.101 : (f) Discussion, p.104.

Chapter V. "A Model of Interdendritic Solidification" 113

(a) Background, p.113 : (b) Basic Equations, p.114 : (c) Liquid-State Diffusion, p.117 : (d) Application to Dendritic Growth, p.120 : (e) Solid-State Diffusion, p.123 : (f) Microsegregation in Aluminium-Copper Alloys, p.128.

Chapter VI, "Temperature Gradient Zone Melting-Analysis". 136

(a) Solute Distribution Within Migrating Zones: Exact Solutions, p.136 : (b) Solute Distribution Within Migrating Zones: Approximate Solutions, p.147 : (c) Solute Distributions Outside Migrating Zones, p.151 : (d) TGZM of Droplets and Inclusions, p.153 : (b) TGZM With Varying Temperature, p.168.

Chapter VII, "Temperature Gradient Zone Melting-Experimental" 172

(a) Measurements of Diffusion Coefficients, p.172 : (b) Bi-Phase Droplets, p.174 : (c) Liquid Film Instability, p.175 : (d) TGZM During

Solidification, p.176 ; (e) TGZM Velocity and Droplet Size, p.183 : (f) Solidification at Gas Bubbles in Liquids, p.193 : (g) Grain Boundary TGZM, p.194.

Chapter VIII, "Temperature Gradient Zone Melting-Theoretical Applications" 195

(a) Diffusion Versus Heat-Flow "Control", p.195 : (b) Interface Kinetics, p.199 : (c) Fibre Coarsening - Theory of McLean, p.204 : (d) TGZM During Crystal Growth, p.212 : (e) TGZM During Dendritic Solidification, p.221.

Summary and Conclusions 224

References 228

Plates

Appendix A A-1

Appendix B A-2

Appendix C A-8

Abstract

Chapter I contains a summary of solidification theory, including theories of the interface processes in pure materials and alloys and applications of analytical diffusion treatments to complex solidification problems. Chapter II contains more detailed literature surveys related to the present work. Section (a) gives a summary of work on dendritic growth, spacing and segregation, including a collation of spacing data, to complement an earlier, more discursive review.(1) Section (b) gives an extensive discussion of theoretical and experimental studies of temperature gradient zone melting and similar migration phenomena. Section (c) is a summary of experimental studies using transparent organic analogues for metallic solidification as in the present work, while section (d) covers previous work(1) by the author. Literature surveys also appear in chapter IV(a) (dendrite tip shapes, effects of convection and the container surface), Chapter V(a) (interdendritic solidification models), chapter VIII(c) (theory of fibre coarsening) and chapter VIII(d) (temperature gradient zone melting during crystal growth.)

Chapter III describes the temperature gradient stages for the optical microscope used in the experimental work of chapters IV and VII. A new type of stage was designed for fixed-area studies during solidification, in which the hot and cold plates were together driven across the stage

while the specimen cell was held stationary in the microscope viewfield. Horizontal and vertical thermal gradients in specimen cells, with and without the plates moving, were measured with thermocouples and by observing temperature gradient zone melting. As a result, the apparatus was modified to reduce local convective heat losses, to control the heating plate temperatures and reduce heat transfer problems in order to make the thermal field reproducible, and to minimize vertical thermal gradients in cells. Some observations on optical perfection and image contrast are also presented.

Chapter IV describes experimental studies on dendritic growth of succinonitrile and CBr_4 alloys in thin specimen cells using the above apparatus. The effects of constraint by the cell walls on growth direction were studied, partly to test the effectiveness of the technique in reproducing bulk dendritic growth features but also to investigate the crystallography of preferred dendritic growth direction. For a given material, dendritic growth form depended largely on grain orientation, and some orientations produced growth forms reasonably similar to bulk growth. There were, however, distinct differences between different alloys although all were cubic, non-faceting, with preferred growth direction [100]. Dendrite spacings and tip temperatures were also measured. There was clear evidence of the influence of convection on primary spacing. Growth temperature measurements were in reasonable agreement with theory.(51)

Chapter V covers theoretical developments of established models of interdendritic solidification. Liquid-state diffusion is discussed in order to correct errors in earlier work and integrate the diffusion analysis with the more intuitive "complete mixing"[49] treatment of dendritic solidification. An analytical treatment[49] of solid-state diffusion is marginally improved and included in the analysis but found to remain quite inaccurate. Previous calculations on microsegregation in aluminium-copper alloys[103] are re-assessed, using self-consistency of the results to obtain a reliable estimate of the solid-state diffusion coefficient, and it is concluded that only one-quarter of the observed[104] homogenization during solidification can be explained by the solid-state diffusion model.

Chapter VI describes theoretical work on temperature gradient zone melting. In previous work, the concentration gradient across a migrating region has generally been assumed, e.g. as linear. Such an assumption is not adequate to discuss TGZM during solidification. In this chapter, exact TGZM diffusion solutions are presented for special cases. These are then used to derive approximate solutions of wider validity. Besides describing TGZM during solidification, these solutions show serious faults in previous treatments of fibre coarsening by differential migration[124] (see also chap. VIII(c)), droplet shape distorsions,[144] and interface stability during TGZM.[129] Solid-state diffusion outside migrating zones and droplets is also analyzed: "forces" on migrating droplets and droplet shape distorsions and

retardations during TGZM are discussed. An expression is given for the distance migrated during solidification by an interdendritic liquid pool.

Chapter VII covers experimental studies of TGZM in organics. Migration of interdendritic liquid pools during solidification was shown experimentally to be similar to droplet migration in a static thermal gradient. Detailed observations of migration velocities as a function of droplet size in succinonitrile showed considerable variations at low temperatures. Possible explanations in terms of interface kinetics affected by adsorption, or dislocation dragging by migrating drops, are presented and discussed. Much smaller size dependences of migration velocity were obtained at higher temperature and these were satisfactorily explained in terms of the curvature effect alone. Grain boundaries in succinonitrile were sometimes observed to migrate up the temperature gradient like liquid drops, suggesting that they (and perhaps also dislocations) can behave as microscopic liquid zones. Some observations on gas bubbles and diffusion coefficient measurements in TGZM are also presented.

Chapter VIII includes various applications of TGZM theory. The simplicity of the theory is used to advantage in calculating the purity required of a "pure" material in which phase transformations can be said to be "controlled" by heat flow rather than solute diffusion: a purity $\gtrsim$ 99.99% is obtained. It is shown that despite their very different thermal properties, organic materials

remain good analogues for metals in this respect. The theory of chapter VI is shown not to invalidate theories[18] of interface kinetics in TGZM, but some special features of the melting kinetics are discussed. The theory[124] of fibre coarsening by differential migration is extensively amended but shown not to account for experimental observations satisfactorily. Using insights gained from the introduction of a dimensionless parameter unifying the theories of various solidification phenomena in a thermal gradient (chap. IV(e)), it is shown that droplets inside a crystal growing with a planar interface often migrate as fast as the crystal grows. Implications for high-quality crystal growth are discussed. Finally, some amendments and extensions to earlier work[1] on homogenization and coarsening by TGZM during dendritic solidification are presented.

Acknowledgements

It is a pleasure to acknowledge all those who helped in this work. In particular, I wish to thank the following:

Professor Sir Peter Hirsch, F.R.S., for provision of laboratory facilities;

Dr J.D.Hunt, for his invaluable help and encouragement throughout my seven years as undergraduate and graduate at Oxford;

Drs W.Bardsley, D.Hurle, C.Goodman and P.Tufton, for helpful discussions on crystal growth. Dr M.McLean, for an extensive discussion of solid-state migration.

Dr D.R.H.Jones, for useful discussions on apparatus and experiments with organic materials. Dr R.D.Doherty, for a pre-print of reference 176;

The staff of the Main Workshop and Student Workshop, especially Mr D.Pinfold, for apparatus construction, and Mr J.Short, for patience;

Mr A.McKnight and Mr J.Norton, for photographic assistance;

Mr D.Hawes, Miss G.Edgecock, Mrs B.Hall, Mrs H.Suggett, and the rest of the departmental administrative and maintenance staff;

Mrs G.B.Dean, for typing this thesis;

Miss H.R.Davies, for a little help and much encouragement;

Mr K.Fisher, for not breaking my apparatus;

Mr R.Series, for not stealing my apparatus;

and all my colleagues, past and present, who have helped to create a stimulating and congenial atmosphere in which to work.

D.J. Allen

Chapter I: "Introduction"

The purpose of this work was to study dendritic solidification, using transparent organic materials as analogues for metals. A central aim was to follow up ideas from the preceding Part II project[1] on the significance of temperature gradient zone melting (TGZM) in interdendritic liquid pools. Several related theoretical and experimental studies were also carried out.

This chapter contains a summary of basic solidification theory, while the general background to the work is covered in Chapter II and some later chapters also contain specialised literature surveys.

(a) Thermodynamics of Solidification

Thermodynamics places rather broad restrictions on possible solidification processes.[2] On a free energy-composition graph (Fig. I. 1), solid of composition c_S (eq.) is in equilibrium with liquid of composition c_L (eq.). Diffusionless solidification (i.e. no composition change) is possible when the bulk liquid composition $c_L < c(T_o)$. Diffusional solidification is possible when $c_L < c_L(\text{eq.})$: for $c_L = c_{L_1}$, the bulk solid composition forming is restricted to $c_{s_1} \ll c_s \ll c_{s_2}$ and the molar free energy of solidification is ΔG.

Phase diagrams depend on the shapes of the G - c curves and their variation with temperature, as discussed in chapter VIII, (d). In this thesis, an idealized binary

diagram (Fig. I. 2) is assumed except where it is stated otherwise, with constant liquidus slope m (= $+dT/dc_L$, a negative quantity) and distribution coefficient k (= (c_S/c_L), < 1). The equilibrium conditions are altered by pressure, and by the pressure difference across a curved solid-liquid interface. To separate these effects, we will conventionally take "pressure", p, as the pressure in the liquid, p_L: then the "curvature effect" (or Gibbs-Thompson effect) is the subsequent alteration of pressure in the solid due to interfacial curvature, $(p_s - p_L)$. In a one-component system:

$$\frac{dT}{dp} = \frac{\Delta V_f}{\Delta S_f} \qquad (1)$$

$$= \frac{V^L - V^S}{S^L - S^S}$$ where V, S are molar volume, molar entropy, and superscripts L and S refer to liquid and solid.(3a)

$$\Delta T_c = \Theta_c \left(\frac{1}{r_1} + \frac{1}{r_2}\right), \quad \Theta_c = \frac{\sigma V^S}{\Delta S_f} \qquad (2)$$

where r_1 and r_2 are principal radii of curvature of the solid, σ is solid-liquid surface energy, here assumed constant, ΔT_c is the "curvature undercooling" or depression of the melting-point due to curvature: extra "torque" terms are introduced when σ is orientation-dependent.(4) (See also appendix C.)

Departures from equilibrium may be allowed for by including a "kinetic undercooling" term, ΔT_k, so that the total interfacial undercooling in a pure material is:

$$\Delta T = \Delta T_c + \Delta T_k \qquad (3)$$

In binary systems, (I.3) is replaced by two equations containing the extra variables c_S and c_L. It is conventional to eliminate c_S between these two equations to obtain an equation of the form:

$$\Delta T = -mc_L + \Delta T_c + \Delta T_k \qquad (4)$$

containing only T and c_L. (See section (b) and chapter VIII,(b).) In (I.4), ΔT is measured from the pure material melting-point and $(-mc_L) = \Delta T_s$, "solute undercooling". An alternative convention (used e.g. in dendritic growth theories) is to measure ΔT from the alloy liquidus temperature. Then the $(-mc_L)$ term in (I.4) is replaced by $(-m(c_L - c_0)) = \Delta T_d$, "diffusion undercooling" where c_0 is the alloy composition.

(b) Interface Kinetics

The kinetics of processes occurring at the solid-liquid interface may be described formally by "response functions"[2], relating interface behaviour (e.g. velocity, v) to conditions at the interface (T, c_S^*, c_L^*, where c^* denotes interfacial composition.) Rigorous thermodynamics has little to say about the response functions. So it is commonly assumed that bulk thermodynamics can be applied locally to the interface processes, in isolation from other concurrent processes. Then, in Fig. I.1, c^* replaces c: the driving force for interface motion, ΔG_k, replaces G, and $\Delta\mu_A$, $\Delta\mu_B$ become chemical potential differences across the interface. The defects of this assumption should be noted. The interface processes may be thermodynamically coupled with other concurrent

processes, and might involve long-range interactions.[2] Although reaction rates may be discussed in thermodynamic terms, there are problems (see e.g. Christian [5]). Finally the application of bulk thermodynamics to surfaces is not strictly valid and is unable to treat phenomena such as adsorption.

Nevertheless, useful results have been obtained for several mechanistic models of interface processes in one-component systems, where only a single response equation relating v to ΔG_k (or ΔT_k) is required. The simplest assumption is that atoms can cross the solid-liquid interface at any point. In this case, called "normal growth", theories[6] predict:

$$v = \mu_1 \Delta T_k \qquad (5)$$

where μ_1 is a constant and ΔT_k is generally expected to be negligible by comparison to other undercooling terms.[7] Rounded growth forms, as observed e.g. in metallic growth from the melt, are consistent with this mechanism. However, many crystals exhibit flat crystallographic facets on growth or dissolution, depending on geometry: facets form when the interface is convex as seen from outside the growing phase, but not when the interface is concave[8] (e.g. Fig. II.5). A plausible explanation for such observations is that atoms can only cross the interface easily at the edges of atomic layers ("lateral growth"), so that facets appear when new crystal layers or holes in layers are required. Assuming the nucleation of new layers to be rate-controlling,

Volmer and Marder[9] found:

$$v = \mu_3 \exp(-A/\Delta T_k) \qquad (6)$$

where μ_3 and A are constants. This equation often fails to fit experimental data. Frank[10] suggested that screw dislocations intersecting the surface would provide self-perpetuating sources of layers, whose lateral growth would be rate-controlling. This mechanism gives[11]

$$v = \mu_2 \Delta T_k^{\,2} \qquad (7)$$

in the simplest case. Other factors which are thought to modify these simple kinetic equations include dislocation configurations, surface diffusion, and adsorption, as discussed in a famous original paper[12] and recent reviews.[13,14]

Burton, Cabrera and Frank[12] and Jackson[15] discussed the occurrence of normal or lateral growth in terms of atomically "rough" or "smooth" interfaces. They argued that normal growth requires a rough interface, in which the microscopic equilibrium configuration of the interface includes one or more layers containing a mixture of "solid" and "liquid" atoms: atoms could easily cross such an interface without significantly altering its structure or energy. Jackson's bond model produced a simple, fairly successful rule: if

$$\alpha = \frac{n_s}{n} \frac{\Delta S_f}{R} \qquad (8)$$

where n_S and n are coordination numbers in surface and bulk respectively and R is the gas constant, then:

$\alpha < 2$ - rough interface - no faceting (9)

$\alpha > 2$ - smooth interface - facets can form.

However, Cahn,[16] using a "diffuse interface" model where interfacial atoms are not definitely assigned to either phase, suggested that normal growth can only occur when the driving force is sufficient to surmount periodic maxima in interfacial energy occurring as the mean interface position alters with respect to the crystal lattice planes. Hence, Cahn predicted that all materials should undergo transitions from lateral to normal growth with increasing driving force. Experimental evidence for this has been submitted by Cahn et al,[17] but criticised by Jackson et al.[7] The latter authors pointed out that periodic variations in macroscopic interfacial energy may be irrelevant if the deciding factor is how single atoms behave.

The above considerations remain qualitatively valid for binary alloys, but since two resonse equations are required, equations such as (I. 5-7) are then insufficient. A second response equation has often been specified implicitly in the arbitrary assumption that the interface distribution coefficient, (c_S^*/c_L^*), remains equal to the equilibrium distribution coefficent $k = (c_S(eq.)/c_L(eq.))$, despite departures from equilibrium (see e.g. Tiller[18]). Baker and Cahn[2] reviewed theories of binary interface kinetics, most of which were based on the phenomenological approach of irreversible thermodynamics. This technique requires a choice of "fluxes" and "conjugate driving forces" of two processes (coupled or otherwise) which together describe the overall process correctly. Baker and Cahn concluded

that these theories were unsuccessful, since two different pairs of processes appeared to be equally valid choices, but gave contradictory results. They stressed that an experimental observation of diffusionless solidification[19] shows that it is possible for one component to increase its chemical potential on solidification ("solute trapping"). Langer and Sekerka,[20] however, assuming a diffuse interface in which free energy and composition vary continuously, were able to discuss interface processes and bulk diffusion in terms of a single irreversible-thermodynamic formalism. They concluded that a uniquely valid choice of fluxes and conjugate driving forces does exist. Their results included the diffusive flux across the interface, as well as the velocity, in the response equations. Thus, departures from equilibrium could occur at a stationary interface with a diffusive flux across it. These topics are discussed again in chapter VIII.

Despite our lack of understanding of alloy interface kinetics, an important simplifying assumption is often used. When ΔG_k is thought to be negligibly small, Fig. I.1 shows that c_S^* and especially c_L^* must be very close to the equilibrium values. Consequently, "local equilibrium" at the solid-liquid interface is generally assumed when normal growth is expected to occur.[2]

(c) Heat and Mass Transport

Heat flow and solute diffusion during solidification are interlinked via the interface conditions. The response equations, together with equations of continuity of temperature and conservation of heat and matter at the

interface, provide the interfacial boundary conditions required for a description of heat and mass transport in the bulk phases.[2] The interfacial conservation equations are (see Fig. I.3):

$$v\Delta H_f = -K_L G_L + K_S G_S \tag{10}$$

for heat, where K is thermal conductivity, G thermal gradient (= dT/dz), ΔH_f the latent heat of fusion. For the ith solute component:

$$v(c_{L_i}^* - c_{S_i}^*) = -D_{L_i}\left(\frac{\partial c_{L_i}}{\partial z}\right)_{\text{interface}} + D_{S_i}\left(\frac{\partial c_{S_i}}{\partial z}\right)_{\text{interface}} \tag{11}$$

where D is diffusion coefficient and v, G, $(\partial c/\partial z)$ are measured normal to the interface.

Heat and mass transport occur by conduction and diffusion in both phases, and by convection in the liquid. Convection is driven by density differences arising from temperature or composition differences.[22] Since heat conduction and diffusion are weakly coupled, a temperature gradient acts as a driving force for diffusion. This thermotransport[23] effect may be incorporated into Fick's first law:

$$J = -D\,\text{grad}\, c - D'c\,\text{grad}\, T \tag{12}$$

or $J = -D(\text{grad}\, c + S_T c\,\text{grad}\, T)$

hence modifying (I.11), where J is diffusive flux and S_T is called the Soret coefficient. An alternative possibility is:

$$J = -D(\text{grad}\, c + S_T c(1 - c)\,\text{grad}\, T) \tag{13}$$

In principle, solidification analyses should proceed by simultaneous solution of the above interface equations and

the equations of heat and mass transport, with the complication that the interface motion and shape evolution cannot strictly be specified a priori (a "free-boundary" problem[21]). In practice, various simplifications are used. The divergence of the temperature field, and the latent heat term in (I.10), are often small enough to justify the assumption of an approximately linear temperature gradient. It may be reasonable to neglect solid-state diffusion, thermotransport and convection by comparison with liquid-state diffusion. In many cases, problems can be solved by making assumptions about the interface motion and shape stability, and justifying the assumptions subsequently.

Simple, useful results have been obtained for unidirectional heat flow, on the assumption of a planar interface. When no convective mixing occurs, steady-state growth can be achieved. After an initial transient while solute piles up ahead of the advancing interface, the concentration at any fixed distance z_i from the interface becomes constant. Transformation of Fick's second law into coordinates z_i moving with the interface together with the condition $(\partial c_L/\partial t)_{z_i} = 0$), yields the steady-state diffusion equation (Tiller, Jackson, Rutter and Chalmers[24]):

$$\frac{d^2 c_L}{dz^2} + \frac{R}{D_L}\frac{dc_L}{dz} = 0 \qquad (14)$$

where R is the isotherm velocity, which in this case equals the velocity of the growth front. This is solved for the boundary conditions $c_L = c_\infty$ at $z_i = \infty$ and $c_L = c_L^* = (c_\infty/k)$ at $z_i = 0$, giving (Fig. I.4):

$$c_L = c_\infty + c_\infty(\frac{1}{k} - 1)\exp(\frac{-Rz_i}{D_L}) \qquad (15)$$

and $c_S = c_\infty$. Hence the distance (D_L/R) is a measure of the length of the diffusion profile in the liquid. Similar equations apply to steady-state melting, with diffusion profile length (D_S/R) in the solid.[25] Transient phenomena have also been described analytically, but only for the physically unrealistic assumptions of constant, or discontinuously changing, interface velocity.[26]

When the liquid is maintained completely homogeneous (e.g. by vigorous convective mixing), and solid-state diffusion is neglected, a simple materials balance gives the solute distribution. Let the volume of material be V, of which the fraction solid f_s increases by df_s: then the solute rejected from the solid, $c_L(1 - k)V\,df_s$, equals that mixed into the liquid, $(1 - fs)V\,dc_L$. So:

$$\frac{df_s}{dc_L} = \frac{1 - f_s}{c_L(1-k)} \qquad (16)$$

This is integrated, using the initial condition $c_L = c_0$ when $f_s = 0$, to give the Scheil equation[27] (Fig. I.5):

$$c_S^* = kc_0(1 - f_s)^{(k-1)} \qquad (17)$$

which also describes segregation in the final solid, and has been used to predict interdendritic microsegregation (Chapter II.)

The assumption of complete liquid mixing is unrealistic,

since convective flow velocity must tend to zero at the solid-liquid interface. Burton, Prim and Slichter[28] modelled partial liquid mixing by assuming a diffusion-dominated layer close to the interface with complete mixing elsewhere in the liquid. They thus derived a modified form of the Scheil equation, with k being replaced by the "effective distribution coefficient" $k_{eff} = (c_S^*/c_\infty)$.

(d) Interface Shape Evolution

Unidirectional heat flow does not necessarily result in solidification with a planar interface. Experimental observations on nonfaceted materials have been roughly related to a parameter (Rc_∞/G) (e.g. Audero and Biloni.[29]) As this parameter increases, an initially planar interface breaks down to an array of unbranched cells growing up the temperature gradient: with further increases in (Rc_∞/G), these become side-branched dendrites growing in preferred crystallographic directions (Fig. I.5). These observations illustrate one aspect of the free-boundary nature of solidification problems: that although equation (I.13) is a valid diffusion solution for any R, it becomes an unstable solution under certain conditions which diffusion theory alone does not specify.

The earliest treatment of this subject was the "constitutional supercooling" theory of Chalmers et al.[30,24] These authors suggested that when the liquid adjacent to the interface is supercooled, a small solid protrusion can grow rapidly away from the interface and thus initiate breakdown

to cells. By using equation (I.15) to obtain the liquidus temperature gradient at the interface, and comparing this to the actual temperature gradient, Chalmers et al predicted stability when:

$$\frac{G}{R} \gg \frac{-mc_\infty(1 - k)}{kD_L} \qquad (18)$$

A more general derivation is given in Chapter VIII. (d). Mullins and Sekerka[31] rigorously analyzed the stability of interfaces to infinitesimal shape perturbations. They showed that any such perturbation could be discussed by Fourier analysis as a combination of sinusoidal perturbations of various wavelengths. The diffusion equations for heat and solute were solved for planar and perturbed interfaces, on the assumption that the steady-state equation (I.14) was applicable. Mullins and Sekerka showed that this assumption was valid for the case of a perturbation which neither grows nor decays in amplitude, and gave arguments to show that the borderline between stability and instability was thus correctly determined. This analysis, besides avoiding arbitrary assumptions, included factors which the constitutional supercooling theory ignored. However, if these factors (curvature, latent heat evolution, and a correction for $G_S \neq G_L$) are assumed negligible, Mullins and Sekerka's stability criterion reduces to equation (I.13). Later, Sekerka[32] presented a "time-dependent" analysis, dropping the steady-state assumption but retaining a restriction to small perturbations for which the linear analysis is valid.

The earlier "time-independent" stability analysis has also been applied to unidirectional melting[33,34] and TGZM.[35,36]

While perturbation analysis has successfully predicted stability criteria for simple growth shapes, it has left other questions largely unanswered. Steady-state or oscillatory growth shapes such as cell and dendrite tips cannot be simply determined. Since linear time-dependent perturbation analysis is restricted to the initial development of instability, it cannot deal with general non-steady state shape changes such as the coarsening of dendritic structures. Alternative techniques, of varying validity, have been used in these cases.

Dendritic growth presents an important free-boundary problem (see Chap. II, (a) (1) and Chapter IV). A paraboloidal dendrite tip shape is an exact steady-state solution for an isothermal interface,[37] but can only be approximately correct in the real, non-isothermal case. Furthermore, current analytical treatments obtain a range of possible tip sizes and associated growth rates, but an extra criterion is required to specify which possibility actually occurs. The common assumption that shape adjusts to maximize the growth rate (or equivalently[38] to minimize the undercooling) is plausible but arbitrary: an analogous assumption for eutectic growth has however received support from an analysis of the mechanism of change of spacing.[39] Jin and Purdy[40] have applied the irreversible-thermodynamic principle that the rate of entropy production

is minimized at steady state. Burden[38] has used perturbation analysis to predict the primary tip radius, a questionable approach in view of the known instability which leads to secondary arm formation. Oldfield[41] suggested that the apparent indeterminacy arises from the artificial constraint involved in the assumption of an isolated paraboloidal tip shape. Nash and Glicksman[21] recently obtained exact dendritic growth solutions by a potential-theoretic free-boundary analysis for an isolated non-isothermal tip, but without removing the indeterminacy. They suggested that the indeterminacy results from the steady-state analysis, which discards information on how the system adjusted to attain the steady state. Bartholomew[42] obtained cell growth solutions by a numerical analysis without introducing an explicit external criterion, but noted that his iterative procedures had some characteristics in common with a stability criterion.

Only a few non-steady state shape changes have been described by exact analytical treatments (see e.g. Nichols[43]). Models of coarsening and microsegregation commonly use experimental dendritic growth data in order to predict how the initially grown structure developes (the "hindsight" approach.) Simplifying assumptions are generally required to describe the initial structure, to specify arbitrary restrictions on the way the shape changes, and to analyze the diffusion problem thus specified (e.g. Kattamis et al[44]).

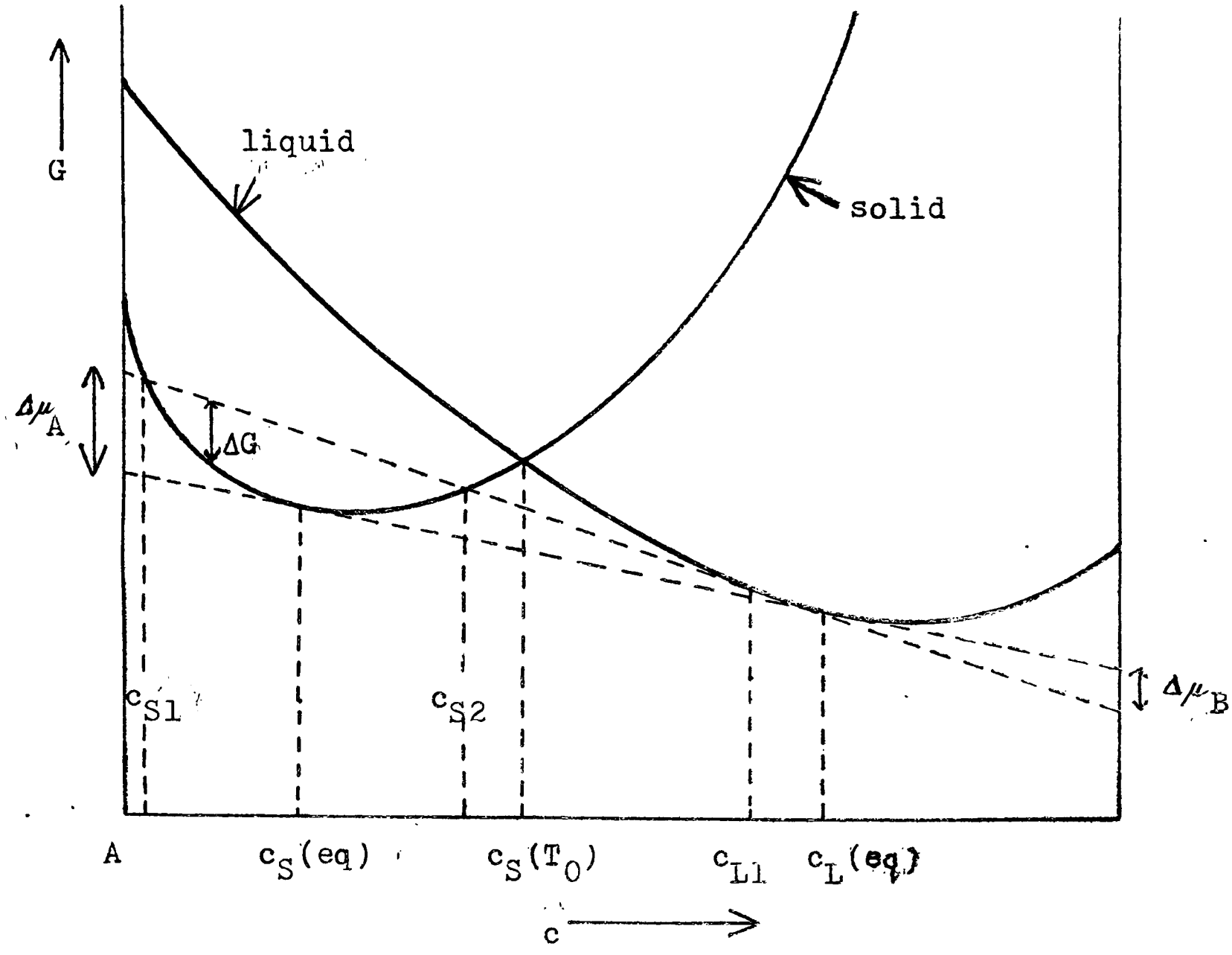


FIG. I.1. Free energy - composition curve.

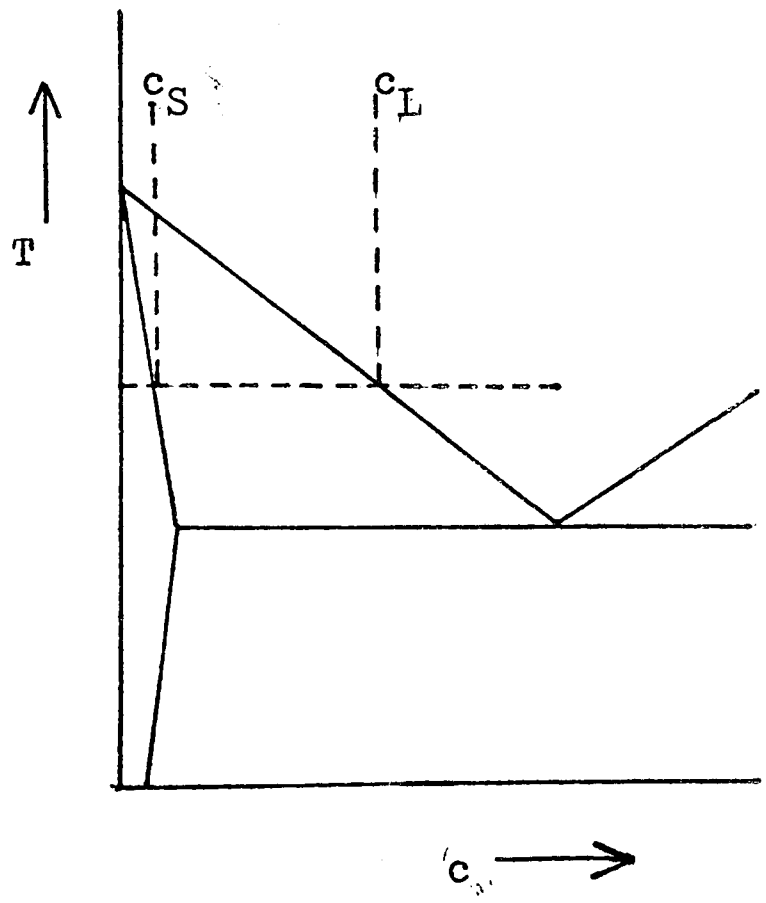


FIG. I.2. Idealized binary diagram.

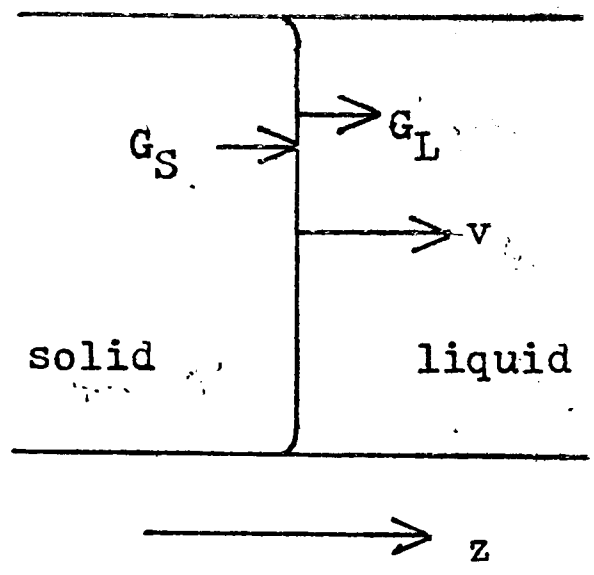


FIG. I.3. Definition of terms, (I.10) and (I.11).

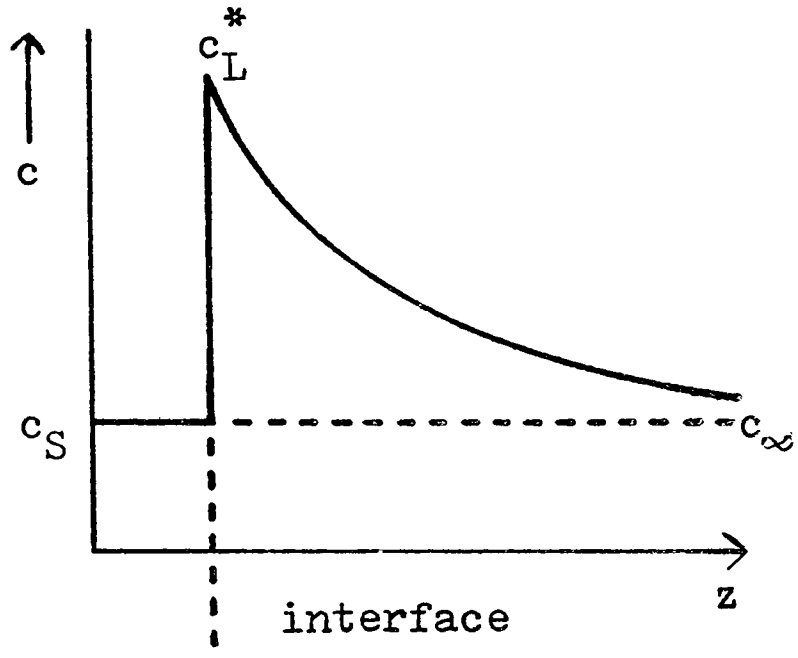


FIG. I.4. Steady - state solidification (no mixing)

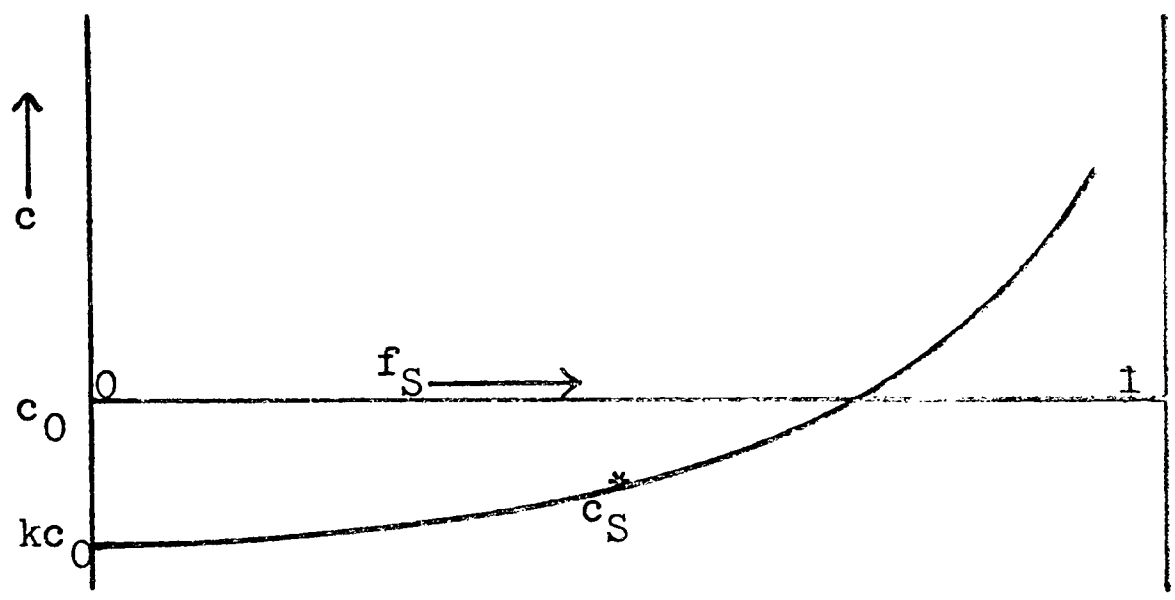


FIG. I. 5. The Scheil equation (complete mixing)

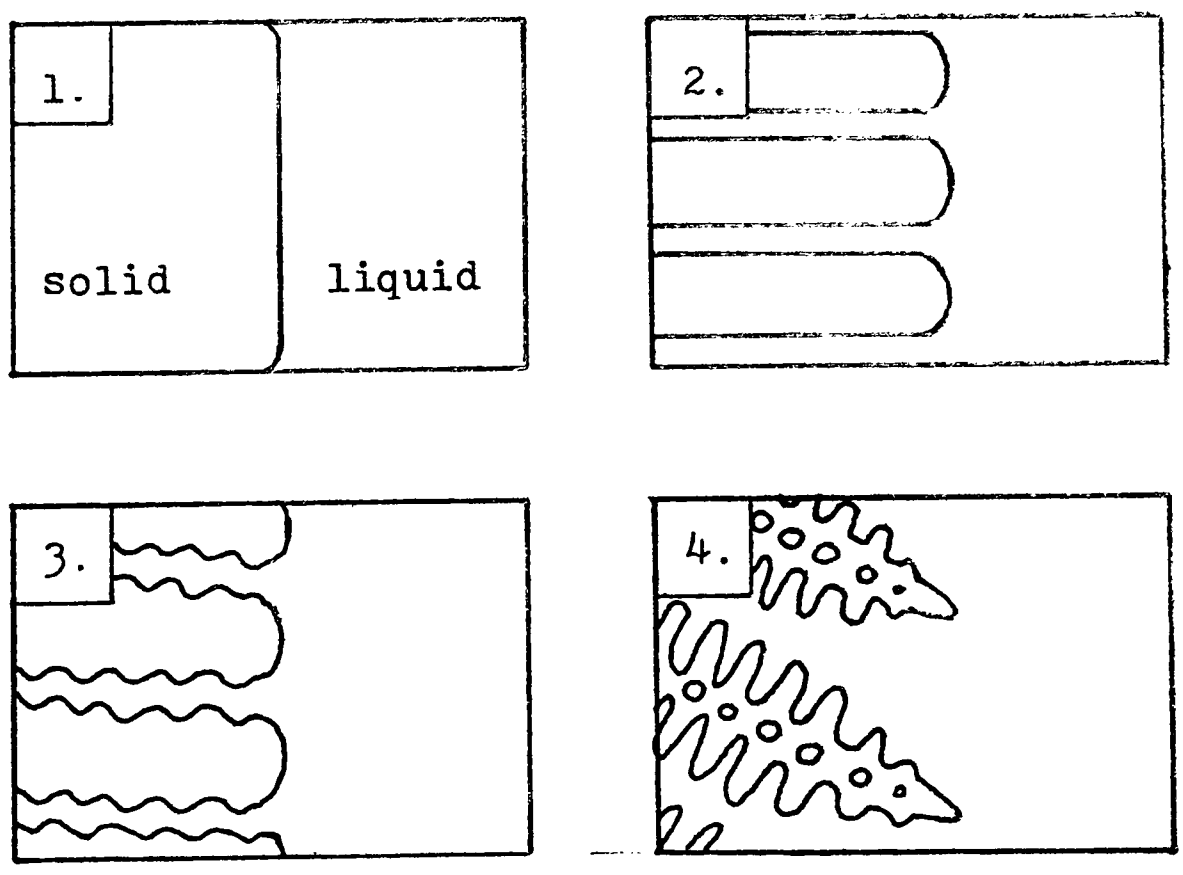


FIG. I. 6. Solidification structures (schematic) With increasing Rc_∞/G , (1.)planar (2.)cells (3.)branched cells (4.)dendrites.

Chapter II; "Literature Survey"

(a) Dendritic Morphology and Microsegragation

(1.) Dendritic Growth

The earliest model, by Zener,[45] applied a spherical growth analysis to dendrite - like growth, showing that the diffusion distance is of the order of the tip radius. This suggested that small tips should grow fastest. However, the reduction in driving force due to the curvature effect becomes dominant for very small radii, and so a maximum occurs in the growth rate - tip radius graph. If the radius r is that which maximizes growth rate R:

$$Rr^2 = \text{constant} \qquad (1)$$

and $$\Delta T_d \propto R^{\frac{1}{2}} \qquad (2)$$

Ivantsov,[46] and Horvay and Cahn,[37] found exact diffusion solutions for an isolated steady-state paraboloidal dendrite growing with an isothermal interface. Later treatments incorporated the curvature effect and interface kinetics, which must make the interface non-isothermal, by assuming a paraboloidal tip shape as an approximation. Nash and Glicksman[21] recently incorporated the curvature effect in an exact isolated-tip solution, involving calculated growth shapes which deviated from paraboloidal, having sharper tips. All these analyses agree within

a factor of two or three. However, the experimental validity of the maximum velocity assumption is uncertain (chap. IV). A rough analysis of the effect of interactions with neighbouring dendrites suggested significant reductions in the predicted growth velocity.[47] By contrast, it has been suggested that fluid flow reduces the undercooling.[48] Perhaps most importantly, theory and experiment have shown a marked effect of temperature gradient on undercooling.[49-51] This is discussed in chapter IV.

(2.) Dendrite Spacings

Dendrite arm nomenclature has been described previously.[49,1] Primary dendrite arms grow close to the heat flow direction and are comparable in length to the grain. Secondary arms grow from the sides of primaries, tertiaries grow from secondaries, etc. A considerable amount of dendrite spacing data exists, but there are problems in its interpretation. Many earlier papers fail to distinguish primary and secondary arms, although the description may show which type of spacing was measured. Another problem is that coarsening in the semi-solid region may greatly alter the initial growth morphology. The importance of coarsening has only been realized within the last ten years, but it has been suggested that coarsening makes final secondary spacings largely independent of initial spacings[44] and makes primary cell spacing measurements from solidified or decanted specimens an unreliable guide to growth spacings.[52] Finally, secondary spacings measured from quenched semi-solid specimens should be distinguished

from those observed in fully solidified specimens.

Several authors have collated primary spacing data.[52-56] There is general agreement that primary spacing decreases as G and R increase and solute content c_0 decreases. Results generally fit a formula:

$$\lambda_1 \propto G^{-m} R^{-n} c_0^{+p} \qquad (3)$$

where λ_1 is primary spacing, and the exponents m, n and p all most commonly lie around 0.25 - 0.5. There are conflicting reports on the influence of convection, as discussed in chapter IV. Jacobi and Schwerdtfeger[56] showed that λ_1 depends somewhat on the type of spacing measured in dendrite arrays (e.g. neighbouring arms in the same row or in different rows of a distorted hexagonal array.) The occurrence and form of the cell-dendrite transition is disputed. Many workers have suggested that it occurs at a critical value of $(G/R^{1/2})$, but Davies[57] made a statistical analysis of the data and found no consistent criterion. Sharp and Hellawell[52] found a discontinuous increase in λ_1 when side-branching begins, but other workers have observed a continuous cell-dendrite transition.

Present theories of primary spacing are not fully convincing. Rohatgi and Adams[58] suggested that primary spacing adjusts to keep the interdendritic supercooling constant: Flemings[59] suggested that this constant value might be related to local curvature undercoolings. Okamoto et al[54] suggested that the primary spacing should be related to the length of the diffusion field ahead of the

growing secondary arms. These calculations are discussed in chapter V. Bolling and Fainstein-Pedraza [53] presented a semi-empirical formula, in which thermal conductivity and latent heat of fusion were rather arbitrarily introduced as scaling factors used to convert the term in G into the dimensions of R. For cellular growth, Bolling and Tiller[60] suggested that cell shapes should adjust to keep the variation of c_L^* with distance in the growth direction constant, the higher temperature at the centre being partly counteracted by higher curvature at the sides, and thus gave a crude diffusion treatment. Donaghey and Tiller[61] treated the cellular growth front as planar in a more sophisticated diffusion treatment. Bartholomew[42] reviewed these theories and carried out a numerical treatment of cell growth.

Recently, Hunt[55] gave an order-of-magnitude analysis in which spacings were calculated, essentially, by using the minimum undercooling assumption to find the sizes of single primary arms and hence obtaining the primary spacing from a calculation of fraction solid at a given temperature. He used a modified form of an earlier dendritic growth analysis[50] together with the analysis of fraction solid by Bower, Brody and Flemings.[49] The latter analysis breaks down near the growth front and was therefore matched to a simple assumed tip shape: Hunt argued that this severe approximation was acceptable because the final result was not sensitively dependent on the shape assumed. Hunt obtained:

$$\lambda_1 \propto G^{-\frac{1}{2}} R^{-\frac{1}{4}} c_0^{+\frac{1}{4}} \quad \text{approximately} \qquad (4)$$

Secondary arm spacings, λ_2, also decrease as cooling rate, F, increases, but appear to decrease as c_0 increases. Table II.1 summarizes results on fully solidified castings, many of which are expressed in terms of an empirical formula:

$$\lambda_2 = (\text{constant}) F^{-n} \quad \text{or} \quad \lambda_2 = (\text{constant}) \theta_f^{\,n} \qquad (5)$$

θ_f is "local solidification time",[49] calculated by dividing estimated actual freezing range by cooling rate. In general, n ~ 0.3 - 0.5.

(3.) Morphological Development (See ref. 1 for a fuller review)

There is now ample evidence of extensive coarsening, by re-melting and by coalescence, during dendritic solidification. Kattamis et al[44] measured λ_2 in A1 - 4½ wt% Cu in a series of castings whose solidification was interrupted by quenching after various times, and in a series of specimens held isothermally in the semi-solid range for different times. All these results, when plotted against time in the semi-solid region, fitted the Bardes and Flemings[62] graph for fully solidified castings. The quench-interrupted solidification experiments demonstrated directly that λ_2 trebles in the later stages of solidification. The authors concluded that the final secondary spacing was primarily determined by coarsening kinetics. Several later

quench-interrupted solidification experiments (Table II.2) have confirmed that λ_2 generally increased by around x3 - x10 during solidification. Feest and Doherty[63] showed by quenching and microanalysis that substantial increases in sidearm spacing occurred before coalescence, while the spacing between remaining liquid pools went on increasing after sidearm arrays had coalesced into solid plates. The most extensive studies have been made by quenching during steady-state growth in a temperature gradient. Young and Kirkwood,[64,65] using Al-Cu alloys, fitted data on many specimens to a single graph of λ_2 against time in the semi-solid region, with n = 0.31, lying somewhat above the Bardes-Flemings plot. However, for a given time in the semi-solid region, there were indications that λ_2 increased with G and decreased with R.

Coarsening has been described as a surface energy-driven process, in which diffusion is driven by concentration differences due to differences of interfacial curvature. Greenwood[66] discussed isothermal coarsening of spherical precipitates in solids. Writing c_r as the matrix concentration at the surface of a precipitate of radius r, and $\bar{c}$ as average matrix concentration, Greenwood assumed:

$$\bar{c} = c_{\bar{r}} \tag{6}$$

and hence derived a simple growth rate expression:

$$\frac{dr}{dt} = \frac{-D(c_r - \bar{c})}{r} \tag{7}$$

which is plotted in Fig. II.1. Particles of $r < \bar{r}$ shrink, while those of $r > \bar{r}$ grow: taking $r = 2\bar{r}$, Greenwood found:

$$\bar{r}^3 = \bar{r}_0^3 + kt \qquad (8)$$

where r_0 is initial radius and k is constant, for diffusion-controlled coarsening. This result was confirmed by the statistical particle-size distribution theories of Lifshitz and Slyozov[67] and Wagner,[68] as reviewed by Greenwood[69] and Kahlweit[70] and recently generalized by Tien et al.[71] These theories are based on the above, rather crude diffusion treatment. A modification by Ardell[72] predicted faster coarsening in systems of high precipitate volume fraction, resulting from reduced diffusion distances. Dendrite coarsening is more complex. Analytical estimates of the time required for a sidearm to remelt have been based on "thinning" at constant length,[44] "shrinking" at constant diameter,[73] and detachment from the primary by root remelting.[74,44] The models compare quite well with observations on transparent materials,[75,73,1] which also show that root remelting occurs after a decrease in R.[76] Simple remelting time predictions can only be compared qualitatively to observations obtainable from metallic systems, such as $\lambda_2 - \theta_f$ plots.[44] Kattamis et al[77-79] circumvented the problem by using the "shrinking" type of model to calculate the rate of change of solid-liquid interface area, for comparison with observations on Al-Cu and Mg-Zn-Zr.

Sidearm coalescence can be detected by microanalysis, since the in-filling solid composition differs from that of the sidearms.[80,63] Hence the common "plate-like" morphology,[49] once attributed to "cellular dendritic" growth,[81] can generally be shown to result from sidearm coalescence,

as observed in cubic,[80,82,63] tetragonal[83] and hexagonal[29] materials (though cruciform unbranched primary arms can be a growth form.[84]). Direct observations have shown coalescence by infilling from the roots outward[1] and by the joining of the sidearm heads.[85] Coalescence (but not remelting) has also been observed in primary arms, altering their apparent spacing.[52]

(4.) Microsegregation

The general features of dendritic microsegregation have been studied by microanalysis.[49,52,59,65,80,86-97] Solute concentration profiles across dendrite arms are commonly U-shaped (or the reverse when k > 1): The minima for primary arms may be deeper than or equal to the minima for secondary arms, and there may or may not be a concentration increase along the lengths of secondary arms. Doherty and Melford[88] found an extensive uniform-composition base of the U, thought to have been deposited in the initial dendritic growth. Kattamis[92] observed a subsidiary concentration hill at the base of the U, resulting from recalescence (see also ref. (98).) Subramanian et al[86] found uniform composition across quaternary arms, which they suggested was due to complete homogenization by solid-state diffusion during solidification. Weinberg and Teghtsoonian[95] found anisotropic "saw-tooth" segregation across secondary arms in Cu - Ni, where k > 1: the higher concentration occurred near that side of the arm which was colder during solidification. Similar, less pronounced

anisotropy occurred in k < 1 systems. Several workers (e.g. [87-89]) have reported more severe microsegregation in equiaxed zones than in columnar zones of castings: Doherty and Melford[88] observed a discontinuous increase in severity of microsegregation at the columnar-equiaxed boundary. Åström et al[97] recently studied microsegregation in 1 μm-thick δ-ferrite plates by using high-resolution scanning transmission electron microscopy. Practical interests in microsegregation include interactions between solutes,[88,93] secondary inclusion formation,[99,100] deoxidation[99] and solidification cracking.[97]

Bower, Brody and Flemings[101,49] discussed the assumptions underlying the common use of the Scheil equation (I.15) to predict microsegregation in castings. They argued that the interdendritic liquid is "completely mixed" by diffusion when $(4D_L\theta_f/\lambda_1^2) \gg 1$, as is usually true, and concluded that the only serious omission was the neglect of solid-state diffusion. Brody and Flemings[101] modified the Scheil equation to incorporate solid-state diffusion by numerical and approximate analytical techniques, finding that homogenization during solidification depends on a parameter $\alpha = D_S\eta = 4D_s\theta_f/\lambda^2$. These and similar calculations suggested that homogenization during subsequent cooling to room temperature is negligible for Al-Cu,[49] significant for Fe-Ni,[93] and substantial for Ti alloys.[94] Some comparisons of these theories with experiments have found good agreement[49,94,102] but there is evidence that the theoretical predictions are often overestimates. Kirkwood and Evans[103]

suggested that discrepancies between theory and experiment on Al-Cu[49] could be removed by a better choice of diffusion data, but these conclusions are re-assessed in chapter V (f.). Ahearn and Flemings, quoted by Young[65] found consistently less microsegregation in Sn-Bi than the Scheil equation predicts, although solid-state diffusion should have been negligible since $D_S \sim 10^{-10}$ cm^2/sec in this system. Detailed analyses of the proportions of material at different compositions in cast titanium alloys[94] showed less composition variation than predicted, especially in the central composition range. The greatest discrepancies were observed by Flemings et al[93] in Fe-Ni alloys, where calculated $\propto$ values (for $\lambda = \lambda_1$) were roughly sixty times too low to fit the data. The authors accepted that better geometrical models could not entirely remedy the discrepancy, and suggested that coarsening homogenizes dendrites by dissolving fairly pure solid and re-depositing less pure material. Subramanian et al[82] noted that coarsening also modifies the geometry of solid-state diffusion, so that $\propto$ is underestimated when calculated from λ measurements on fully solidified specimens. Kirkwood and Evans,[103] however, argued that such errors should be small because most of the solid-state diffusion was predicted to occur in the final stages of solidification. Feest and Doherty[63] and Dauncey[96] showed that dendritic growth temperature depression below the liquidus temperature significantly reduced microsegregation in Cu-Ni and Cu-Sn. Flemings,[59] following earlier work,[49] gave an approximate analytical

treatment of microsegregation in cells, modifying the Scheil equation to allow for the (considerable) growth temperature depression, and also allowing for diffusion parallel to the temperature gradient in inter-cellular liquid pools.

(b) Temperature Gradient Zone Melting and Related Phenomena

The principles of temperature gradient zone melting (TGZM) are illustrated in Fig. II.2, which shows a liquid zone inside a solid in a temperature gradient. The composition of the liquid at the hotter interface differs from that at the colder interface, and so solute diffuses from cold to hot, causing freezing at the cold end and melting at the hot end. Similar migration processes occur for solid inclusions, gas bubbles and pores, for a variety of driving forces and by various transport mechanisms. Whitman[117] was the first to describe TGZM, as a natural purification mechanism for Arctic floe-ice. Later, the phenomenon was "re-discovered" by Pfann[118] and Chernov.[119] Since then, research has been stimulated by technological applications to crystal growth,[120] semiconductor device manufacture,[172] the swelling of nuclear fuel elements,[121] and the degradation of microelectronic circuits[122] and fibre-composite materials.[123,124] Academic interest has been concerned with the investigation of interface kinetics,[18] the use of "inert markers" in diffusion studies,[125,126] and the effects of inclusion migration on deformation and recrystallization.[126] Several reviews have been published.[120,121,126-130]

Tiller[18] showed that slow interface kinetics retards

droplet migration through its effect on the interfacial concentrations, and demonstrated that migration velocities may be calculated by combining separate treatments of heat flow, mass transport, and interface kinetics (see Fig. II.4).

(1.) Heat Flow

Tiller,[18] using an electrostatic analogy, determined the temperature distributions in slab (planar-sided), cylindrical and spherical zones embedded in a matrix in a temperature gradient. Defining v as migration velocity, G_∞ as the temperature gradient in the solid far from the zone, and G_L as the temperature gradient (found to be constant) within the zone:

$$G_L = \frac{K_S}{K_L} G_\infty - \frac{v\Delta H_f}{K_L} \qquad \text{(planar zones)} \qquad (9)$$

$$G_L = \left(\frac{2K_S}{K_S + K_L}\right)G_\infty - \frac{v\Delta H_f}{K_S + K_L} \qquad \text{(cylindrical zones)} \qquad (10)$$

$$G_L = \left(\frac{3K_S}{2K_S + K_L}\right)G_\infty - \frac{v\Delta H_f}{(2K_S + K_L)} \qquad \text{(spherical zones)} \qquad (11)$$

The latent heat term is generally negligible. Cline and Anthony[161] obtained a similar expression for elliptical zones, and further details are given by Carslaw and Jaeger[131] and Geguzin and Krivoglaz.[126] Geguzin et al[132] obtained experimental confirmation of these equations by relating measured TGZM velocities in cylindrical and spherical inclusions.

(2.) TGZM in Solid-Liquid Systems - Diffusion

Previous analyses of TGZM of liquid zones through solids

have been based on liquid-state diffusion. Pfann[118] assumed a linear concentration gradient in the liquid. Tiller[18] used the Laplace equation $\nabla^2 c_L = 0$, leading to a linear concentration gradient, stating that this was a good approximation because $(vl/D_L) \ll 1$ where l is zone length. Hurle, Mullin and Pike,[133,129] by contrast, assumed the steady-state equation (I.14) which implies $\nabla^2 c_L \neq 0$. They showed, however, that this predicts an approximately linear concentration gradient when $(vl/D_L) \ll 1$. These somewhat conflicting approaches therefore produced similar results for the diffusion-controlled migration velocity provided that $(vl/D_L) \ll 1$. The interfacial liquid concentrations follow the liquidus, which is (Fig. II.2):

$$\frac{dc_L^*}{dz} = + \frac{G}{m} \tag{12}$$

and so, assuming a linear concentration gradient within the zone,

$$\frac{dc_L}{dz} = + \frac{G}{m} \quad \text{everywhere} \tag{13}$$

Combining (II.13) with the solute conservation equation, (I.11):

$$v = \frac{-D_L G}{m c_L^* (1 - k)} \tag{14}$$

This result is equivalent to Tiller's equation 9 for freezing interface velocity, but Tiller's equation 10 for melting interface velocity effectively replaces $c_L^*(1 - k)$ by $(c_L^* - c_{S\infty})$ where $c_{S\infty}$ is the bulk composition of dissolving solid.[18]

Tiller did not explain this step, but we shall show (chapter VI.) that it implicitly makes reasonable allowance for solid-state diffusion. Several authors have shown that thermotransport affects TGZM, introducing a multiplying factor on the right-hand side of (II.14) which was found to be $(1 + mS_T c_L)$ from (I.12),[134,161] or $(1 + mS_T c_L(1 - c_L))$ if (I.13) is used.[135] Calculations from experimental thermotransport data showed the correction factor to be negligibly different from unity for brine in ice,[134] but ~ 1.16 for brine in solid potassium chloride[161] and $\sim 0.73 - 0.75$ for aluminium-copper.[135]

Early work by Wernick[136,137] showed up variations in TGZM velocity with zone size and migration direction relative to gravity, indicative of interface-kinetic and convection effects, which prevented an accurate test of the diffusion-controlled TGZM theory. Later studies on aqueous salt solution droplets in ice,[134,138,139] and aluminium-copper,[135] have proved more successful. Hoekstra et al[134] found that their ice data did not fit equation (II.14) well, and Tiller[140] explained this in terms of adsorption-limited interface kinetics: however, Seidensticker[141] and Jones[142,139] improved the agreement using more accurate diffusion data. Actual velocities then fell below those predicted by (ii.14) by about ten per cent in many cases, perhaps[141,142] more for sodium chloride solution. (Seidensticker and Jones used similar, but not identical, published data, some of which included thermodynamic calculations from conductivity data which may not be valid for concentrated solutions.

Seidensticker also applied thermal conductivity and density corrections.) The remaining ten per cent discrepancy may be due to interface kinetics (section (b.)(5)). Watson[135] studied upward TGZM of droplets in aluminium-copper, thus eliminating convection. Measurements using implanted copper wire zones were susceptible to errors arising from oxide contamination and the initial dissolution of the copper: the results, corrected for thermal conductivity differences, thermotransport, and solid-state diffusion[1] yielded $D_L = 4.3 \times 10^{-5}$ cm^2/sec. Two runs were carried out using intrinsic liquid zones, formed by melting eutectic micro-segregates when the specimen was displaced up the temperature gradient at the start of a run. Migration distances were measured on quenched specimens. These more accurate results yielded $D_L = 3.30 \times 10^{-5}$ cm^2/sec in good agreement with Jordan's result, $D_L = 3.26 \times 10^{-5}$ cm^2/sec, from solidification experiments.[143]

While equation (II.14) has generally been accepted as a good approximation, some calculations would appear to require a very accurate diffusion solution. Jones,[144,145] who assumed the steady-state equation, argued that droplet elongation during TGZM may be related to the departure from linearity of the concentration gradient within the drop. McLean[124] calculated the difference between the velocities of the hot and cold ends of a migrating zone resulting from a temperature-dependent diffusion coefficient, implicitly assuming a linear concentration gradient across the zone. Hurle, Mullin and Pike[129] calculated the constitutional

supercooling in migrating zones from the steady-state equation, and gave a qualitative discussion of interface stability. More exact stability calculations[35,36] also assumed the steady-state equation. These treatments are criticized in chapters VI and VIII . Lozovskii,[146] assuming linear concentration gradients, discussed diffusion in TGZM for binary and ternary alloys in terms of intrinsic diffusion coefficients. He showed that hydrodynamic flow occurs in the liquid due to inequalities in the numbers of atoms per unit volume in solid and liquid (N_S and N_L), and to inequalities in the intrinsic diffusion coefficients and liquidus slopes of different components. The first factor introduced a term (N_L/N_S) on the right-hand side of (II.14), with c_L^* and k referring to concentrations in atoms per unit volume. The second factor merely determined the inter-diffusion coefficient D_L as used in (II.14) for binary alloys, but the effective diffusion coefficient derived for ternary alloys was more complex. Cline and Anthony[173] carried out similar calculations, while ignoring differences between N_S and N_L, and concluded that "a physical flow of liquid across the droplet"significantly increases TGZM velocity at high temperatures. Their calculations are valid, but this physical interpretation is not: the factor emerging from their treatment which results in faster migration at high temperature is equivalent to $c_L^*(1 - k)$ in (II.14). Their calculated "liquid flow velocity" (U_1), being measured in a coordinate system which moves with the droplet, becomes equal to (-v) when the intrinsic diffusion coefficients are equal, and therefore does not represent flow across the droplet.

(3.) TGZM in Solid-Liquid Systems - Convection

Pfann[127] and Tiller[18] demonstrated that convection increases TGZM velocity, since the effect of homogenizing the centre of the zone is to increase concentration gradients at the edges (Fig. II.3). Osinovskii[147,126] analyzed TGZM with convection (neglecting the variation of density with composition) for a horizontal temperature gradient. He showed that convection introduces a vertical component of migration velocity. For the case of negligible interface kinetics, Osinovskii's result (slightly simplified) introduces a multiplying factor

$$\frac{2}{25}\frac{g\alpha_L r^4 G}{\gamma_L D_L} \qquad (15)$$

on the right-hand side of (II.14), where g is acceleration due to gravity, α_L is liquid expansion coefficient, r droplet radius and γ_L kinematic viscosity. Osinovskii also discussed convection in a vertical temperature gradient and found that droplets of the sizes commonly observed in experiments were below a critical size, below which convection should not occur in either upward or downward TGZM.

Wernick[137] found that planar aluminium zones of thickness 125 μms migrated 70% faster downwards than upwards for similar temperature gradients. Hoekstra et al[134] found upward and downward TGZM velocities in brine droplets up to 70μms in diameter to be equal within ~ 5%, as predicted by

Osinovskii. Wald and Bell[148] investigated the "travelling heater" method of crystal growth, in which a temperature difference appears across the molten zone ($\sim$1cm width) because of the motion of the heater. They found convection rather than diffusion to be the main transport mechanism and estimated the diffusion-dominated layer thickness to be $\sim$ 800 μms.

(4) TGZM in Solid-Liquid Systems - Interface Stability

Seidensticker,[35] Delves[36] and Woodruff[33] used the Mullins and Sekerka approach (chapter I) to discuss TGZM. They found that planar zones were generally unstable and that the relative magnitudes of K_S and K_L were important in determining which interface becomes non-planar. However, Cline and Anthony[171] found that thin brine zones in potassium chloride were stable and showed theoretically that slow isotropic interface kinetics was stabilizing. Cline and Anthony[170] also discussed droplet stability in this system, attributing the deposition of small droplets from the back corners of migrating flattened cubic drops to the reduced thermal gradients at drop sides in this system.

Wernick,[137] Lozovskii and Popov[149] and Cline and Anthony[174] made observations on the stability of wire[137,149,174] and planar[149] zones migrating on the surface[137,149] and through the bulk[174] of germanium[137] and silicon.[149,174] The results tended to support Tiller's rule,[18] which predicted stability when migration occurs normal to the facet plane in systems exhibiting anisotropic interface kinetics (the facet plane being {111} here.) Stability was improved

for low thermal gradients,[149] thin zones,[149,174] and bulk as opposed to surface migration.[174] Droplets, apart from those containing gas bubbles,[167] those in the brine-KCl system discussed above, and some large drops in faceting systems,[168] migrated without breaking up (e.g. refs. 134, 150, 161).

(5) TGZM in Solid-Liquid Systems - Interface Kinetics

Tiller[18] analyzed TGZM when both interface kinetics, as described by equations (I.5 - I.7), and diffusion are important. In this summary, we will alter the notation, writing suffices m, f to refer to melting and freezing interfaces respectively, defining velocities v_m, v_f along the migration direction, and using $c_{S\infty}$ for the bulk composition of the dissolving solid. The equilibrium interfacial compositions will be denoted c_{LO}^*, c_{SO}^*; parameters c, k refer to solute concentrations as usual.

The principles of the analysis are shown in Fig. II.4. Slow interface kinetics reduces c_{Lf}^* below c_{LfO}^*, while increasing c_{Lm}^* above c_{LmO}^*, so that the concentration gradient in the zone and the migration velocity are reduced. From the solute conservation equations, Tiller obtained his equations 9 and 10 (as discussed in section (b)(2)):

$$v_f c_{Lf}^*(1 - k) = -D_L\left(\frac{dc_L}{dz}\right) = \frac{-D_L}{l}\left(c_{Lf}^* - c_{Lm}^*\right) \qquad (16)$$

$$v_m(c_{Lm}^* - c_{S\infty}) = +D_L\left(\frac{dc_L}{dz}\right) = \frac{+D_L}{l}\left(c_{Lf}^* - c_{Lm}^*\right) \qquad (17)$$

where l = zone length. These equations were solved simultaneously with interface-kinetic equations based on (I.5 - I.7), expressed in terms of the difference between c_L^* and c_{LO}^* rather than ΔT_k (with μ_2, μ_3, and A becoming negative for melting.) The results, amended to correct sign errors in the μ_0' terms of Tiller's equations 12 - 14, were:

$$v_f = \left(\frac{-D_L G}{mc_{Lf}^*(1-k)}\right) / \; 1 + \left(\frac{D_L \Gamma_1}{mc_{Lf}^*(1-k).l}\right) \qquad (18)$$

where $\Gamma_1 = \left(\frac{1}{\mu_{1f}} + \frac{v_m}{v_f \mu_{1m}}\right)$, for normal growth: (19)

$$v_f = \left(\frac{-D_L G}{mc_{Lf}^*(1-k)}\right) / \; 1 + \left(\frac{D_L v_f^{-\frac{1}{2}} \Gamma_2}{mc_{Lf}^*(1-k).l}\right) \qquad (20)$$

where $\Gamma_2 = \left(\frac{1}{\mu_{2f}}\right)^{\frac{1}{2}} - \left(\frac{v_m}{v_f \mu_{2m}}\right)^{\frac{1}{2}}$), for the screw dislocation mechanism: (21)

$$v_f = \left(\frac{-D_L G}{mc_{Lf}^*(1-k)}\right) / \; 1 + \left(\frac{D_L v_f^{-1} \Gamma_3}{mc_{Lf}^*(1-k).l}\right) \qquad (22)$$

where $\Gamma_3 = \left(\frac{A_f}{\ln(\mu_{3f}/v_f)} + \frac{A_m}{\ln(\mu_{3m}/v_m)}\right)$ (23)

for two-dimensional layer nucleation. Tiller suggested that variations of v with l should be observed for l within the range 10^{-6} - 10^{-5} cms for normal growth, 10^{-3} - 10^{-2} cms

for screw dislocation kinetics, 10^{-2} - 10^{-1} cms for layer nucleation kinetics.

Later, Tiller[140] integrated the above equations to obtain distance-time relations, and found that migration at constant velocity indicates screw dislocation kinetics. This prediction is a mathematical artefact resulting from the use of a limiting case (Tiller's equation 10c) which amounts to neglecting the diffusion term and hence removing explicit temperature and time-dependence from the analysis. Tiller also described interface kinetics controlled by layer spreading after two-dimensional nucleation, as affected by adsorption to layer kinks. He obtained a modified equation (II.18) with Γ proportional to 1: Jones and Chadwick,[150] however, used a modified equation (II.22) to discuss a similar problem. Jones and Chadwick,[150] and Lozovskii and Konstantinova[151] described simple re-arrangements of the Tiller formulae for graphical analyses of experimental results.

Shewmon,[152] Seidensticker,[153] and Jones[154] showed that much simpler formulae were applicable when the diffusion term could be neglected (i.e. $(c_{Lf}^{*} - c_{Lm}^{*}) \ll (c_{LfO}^{*} - c_{LmO}^{*})$, Fig. II.4.) For an interface-kinetic equation $v = \mu \Delta T_K^{n}$, the TGZM equation is:

$$v = \mu (Gl)^{n} \qquad (24)$$

Experimental studies on interface kinetics in solid-liquid systems based on measurements of the size dependence of

TGZM velocity are summarized in Table II.3. Several workers found no evidence of a size effect for droplets migrating parallel to the temperature gradient in brine-ice systems: Jones[139] calculated that a kinetic effect within the range $\mu_2 \gg 1$ cm.s^{-1} °K^{-2} could have been concealed by experimental errors of approximately ±10% in measured velocities. Jones also calculated a kinetic term of the order $\mu_2 \sim 1$ cm.s^{-1} °K^{-2} from the ~10% discrepancy between measured velocities and diffusion-control calculations, but this conclusion must be regarded as tentative in view of the experimental error and uncertainties in diffusion data. However, droplets in certain grains migrated "diagonally" at angles to the thermal gradient[138,139] with reduced velocities, deviating towards directions along which the drops were elongated.[139] Some drops oscillated between rounded and faceted shapes:[139] some elongated in the migration direction just before merging with the bulk liquid:[138] a few were virtually stationary.[139] Jones found that velocities in diagonal migration fitted a formula which allowed for reduced thermal gradients along the migration direction, but (despite the appearance of facets on the diagonally migrating drops) made no allowance for interface-kinetic retardation. Later, Jones[145] attributed droplet elongations in the migration direction to ΔT_{Kf} exceeding ΔT_{Km} (see below) and calculated $\mu_{1f} \ll 4.1 \times 10^{-3}$ cm.s^{-1} °K^{-1}, or $\mu_{2f} \ll 9.3 \times 10^{-1}$ cm.s^{-1} °K^{-2}, the equality applying if $\Delta T_{Km} \sim 0$. In summary, several phenomena seem to indicate interface-kinetic effects despite the absence of a size effect. Tiller[140] postulated that with adsorption varying as l^3

and surface area varying as l^2, Γ might be proportional to l, so that interface kinetics could cause size-independent droplet retardations. This idea seems rather speculative.

Size effect experiments also suggested negligible interface kinetics in metallic Al-Si alloys, Ga in GaAs, Li in LiF, and perhaps Cr in SiC, although results in this last case were contradictory. (Table II.3). Surface wetting problems[149,155,156] and oxidation[135,149,169] may have affected some of the measurements. Kumagawa et al[156] suggested that dissolution of surface contaminants in thin zones restricted the dissolution of feed crystal (SiC), hence causing a size effect.

Many results were discussed in terms of screw dislocation kinetics, with μ_2 in the range 10^{-3} - 10^{-5} $cm.s^{-1}\ {}^{o}K^{-2}$ in general agreement with solidification data (e.g. table 3.23 of Brice[130]). Russian data[151] showed that μ_2 may vary considerably with temperature and alloy composition within a given system. Jones and Chadwick[150,154] studied compositional effects in salol-azobenzene. An analysis assuming equation (II.20)[150] obtained μ_2 independent of azobenzene content, but a re-analysis[154] using equation (II.24) found n values increasing with azobenzene content from 2.9 to 4.4 as compared to n = 2.7 for nominally pure salol. (Unfortunately μ was also stated to increase with azobenzene content in the later analysis, an increase which "merely reflects the increase in n": such a statement seems erroneous since, for consistency with the earlier analysis, μ would have to decrease as azobenzene content increased.)

These authors observed erratic, diagonal droplet migration, with some stationary droplets, and concluded that such phenomena indicated dislocation kinetics with the stationary drops having no intersecting dislocations. Seidensticker[153] observed facet formation on the melting interface only, as did later authors,[150,161,172] which he explained in terms of the necessity to form a new layer as in Woodruff's rule[8] (Fig. II.5). Jones[154] argued that the freezing interface had a different curvature undercooling from the faceted melting interface. This may be ruled out because there cannot be a net force on the droplet (in the absence of body forces[126]) and so, with constant pressure inside the droplet and $(p_S - p_L)$ being determined by curvature, it follows that the average curvatures of opposite halves of the drop must be equal. (Chapter VI (d)(1)).

One experiment[157,158] was explained in terms of layer nucleation kinetics. Hamaker and White grew single crystals of indium antimonide from polycrystalline feed material by TGZM of 200 - 1200 μms thick indium-rich and lead-rich zones. In indium zones, TGZM velocity with crystal growth on {111} "A" planes was independent of size and may be called v_{max}: velocities for growth on {111} "B" planes varied with size between ~ 0.7 - 1.0 v_{max}, while velocities for growth along <110> varied between ~ 0.2 - 0.8 v_{max}. Lead zones behaved similarly. Microstructural studies of {111} growth surfaces revealed growth steps with "no evidence of screw character", while the surfaces of <110> crystals appeared to consist largely of parallel ridges, formed from intersecting {111} planes, with spacing ~40μms. The layer nucleation equation

was found capable of fitting the data with discrepancies $\lesssim$ 6% (assuming $\mu_m = \mu_f$), as compared to discrepancies $\lesssim$ 20% for the screw dislocation kinetics equation. Hamaker and White's conclusions seem slightly uncertain. The {111} "A" results show negligible kinetics, and therefore melting kinetics should always be negligible here (a plausible conclusion since the melting polycrystals should not facet.[8]) Calculated best-fit Γ_2 values for {111} "B" indicate $\mu_{2f} = 3.9 \times 10^{-5}$ cm.s^{-1} $^oK^{-2}$ (In zones), $\mu_{2f} = 4.4 \times 10^{-7}$ cm.s^{-1} $^oK^{-2}$ (Pb zones), and thus the In result at least seems comparable with other μ_2 data. Most strikingly, however the <110> data indicate much slower kinetics than for {111} "B" even though {111} planes still formed the growth interface: this may perhaps be due to the narrow facets formed on <110> crystals.

Jones and Chadwick[150] observed small velocity variations with droplet size in camphene: the variations and the experimental scatter in velocity measurements were both about 10%. These effects were too small to give a clear indication of the interface-kinetic mechanism. Assuming normal growth, low-temperature runs yielded $\mu_1 \sim 2 \times 10^{-3}$ cm.s^{-1} $^oK^{-1}$, a higher temperature run gave $\mu_1 \sim 2 \times 10^{-2}$ cm.s^{-1} $^oK^{-1}$, and the highest-temperature run (~ 5 C^o below the melting-point of pure camphene) gave $\mu_1 \gtrsim 4 \times 10^{-2}$ cm.s^{-1} $^oK^{-1}$, which presumably represented a limiting range consistent with the absence of an observable size effect. The assumption of screw dislocation kinetics gave μ_2 values between 3×10^{-2} and 6.4 cm.s^{-1} $^oK^{-2}$ which were thought to be unacceptably high. However, a theoretical estimate

using Cahn's theory[16] gave $\mu_1 \sim 10 cm.s^{-1}\ {}^oK^{-1}$ and the results were only reconciled to this value by means of an extrapolation to the pure material melting point. Since any actual measurement of $\mu_1 = 10\ cm.s^{-1}\ {}^oK^{-1}$ would have required an improvement in experimental accuracy by a factor of about 250, this extrapolation seems very speculative. The much lower μ_1 values actually obtained were explained in terms of adsorption.

Cline and Anthony studied TGZM in brine-solid KCl,[161,162,164,165,167,170,171] Au-Si,[168] and Al-Si[169,172-174] (and also studied shape relaxation,[160] isothermal heating,[166] and accelerational field migration[159,163] in brine-KCl). Their results were expressed in terms of "kinetic potential" $K\ (= RT|\Delta T_k|/mc_L)$, the chemical potential discontinuity at the interface due to kinetics. Droplet velocity measurements were combined with published diffusion data to calculate $(K_m + K_f)$ values directly: the results may be written:

$$(K_m + K_f) = K_o + Av^n \qquad (25)$$

In brine-KCl,[164] n decreased from unity to about one-quarter as v increased (for A held constant): most[159-161,163-165] though not all[162] of the data confirmed the existence of a significant positive K_o term, although there was considerable scatter.[159,161] In Al-Si,[173] n was somewhat greater than one and there was no K_o term. These results clearly do not fit any simple kinetic equation (e.g. (I.5 - I.7)).

Droplets in brine-KCl formed facets on 100 melting interfaces. Whem migrating along <100> , droplets became flattened in the plane perpendicular to the migration direction, with dimensions w by w by l (l being thickness parallel to G), where w > l. This shape distorsion was discussed in terms of interface kinetics, which acts to reduce v_m, being counteracted by curvature differences which act to increase v_m and reduce v_f. Hence a "steady-state" shape was predicted:

$$\frac{w}{l} = 1 + \frac{(K_m - K_f)}{4\sigma V^s} w \qquad (26)$$

For one droplet, Cline and Anthony[161] calculated $(K_m + K_f) = 1.4 \times 10^7$ ergs/mole from (II.25), and $(K_m - K_f) = 1.3 \times 10^6$ ergs/mole from (II.26). They did not comment on this comparison, but the implication that K_m only slightly exceeds K_f is surprising because the melting interface was faceted while the freezing interface was rounded. Shape distorsions increased the temperature gradients within droplets, thus increasing their velocities. This factor largely explains observed size effects.[161] Migration velocities were nevertheless two to ten times below predictions assuming diffusion control.[164] Drops migrating along <110> behaved differently:[164] larger drops became chevron-shaped with faceted freezing interfaces (Fig. II.6), but smaller drops remained nearly cubic with rounded freezing interfaces. A small drop migrated about 15% faster along <110> than along <100>.[164] One anomalous droplet, thought to have migrated along a low-angle boundary, travelled along <100>

without flattening at several times the velocity which would have been expected from comparison with other drops.[161] The Al-Si results are discussed in section (b)(6).

Jones[144] gave a shape distorsion analysis similar to the above but including predicted distorsions due to diffusion (section (b)(2).) He obtained:

$$\frac{|\Delta T_c|_0 - |\Delta T_c|_{1/2}}{mc^*_{Lf0}} \sim \frac{v_f l^2}{8D_L^2} + \frac{|\Delta T_{Kf}| - |\Delta T_{Km}|}{2mc^*_{Lf0}} \qquad (27)$$

in our notation, where $|\Delta T_c|_0$, $|\Delta T_c|_{1/2}$ refer to curvatures at the back and side of the drop respectively. Elongations of the order of $(l/w) \sim 1.8$ for $l \sim 50\ \mu$ms were observed in camphene and discussed in terms of diffusion (i.e. the kinetic term in (II.27) was found to be negligible.)[144] Elongations of the order $(l/w) \sim 1.25$ for $l \sim 50\ \mu$ms in brine-ice were discussed in terms of interface kinetics.[145] (See chapters VII and VIII).

(6.) <u>TGZM in Solid-Liquid Systems - Interactions with Crystal Defects</u>.

Cline and Anthony measured grain-boundary energies by studying migration across low-angle boundaries in brine-KCl.[162,163] Small droplets with low driving forces were trapped on boundaries, since the total surface and interface energy is thus minimized, but other droplets escaped by extending the boundary or by detaching from it after distorting in shape. Ashby and Centamore[175] studied the more complex situation when boundaries as well as inclusions are mobile.

Nichols[121] discussed the possibility of inclusion trapping by dislocations, and calculated that gas bubbles of the order of 10^{-2} μms diameter might be trapped by a single dislocation. Geguzin et al[126] analyzed creep controlled by the migration of inclusions attached to dislocations. Recently, Doherty and Strutt[176] discussed the results of McLean and Loveday[177] and Cline and Anthony[160,161] in terms of dislocation trapping during TGZM, as described in chapter VII.

Cline and Anthony[172,173] studied droplets of aluminium migrating in silicon along <100> (in which case four {111} facets formed the melting interface) and "at a few degrees" off <100> (when two of the melting interface planes became rounded.) Arrays of droplets (of typical diameter ~100 μms), as used in diode manufacture, were studied by infrared transmission microscopy.[169] After migrating one centimetre, <100> droplets had suffered typical r.m.s. sideways displacements of ~ 100 μms, but off- <100> droplets were displaced much less (~ 40 μms). These net displacements typically resulted from about twenty separate, apparently random, displacement events (i.e. one per ~ 500 μms migrated). Further work showed that such displacements were largely eliminated in crystals of low ($\lesssim 5 \times 10^{-4}$ cm^{-2}) or high ($\gtrsim 5 \times 10^{-7}$ cm^{-2}) dislocation density. "Few if any" dislocations were observed in the doped trails behind migrating droplets (low dislocation density is a general feature of crystals grown by TGZM.[120]) The authors suggested that displacements were due to preferential dissolution occurring when only one of the facets

on the melting interface was intersected by a dislocation. (Scatter in observations on brine-KCl was explained similarly.[159,161]) However, taking the average number of dislocations intersecting a drop to be (dislocation density x diameter squared), we obtain 5 - 5000 dislocations per drop for the range of dislocation densities where serious displacements were found. These figures seem too large to fit the authors' model: clearly, much remains to be explained.

(7.) Other Migration Phenomena

Knight observed that droplet TGZM in ice was associated with sub-boundary formation[178,179] and propagation of liquid-filled cracks from migrating droplets.[180] He suggested that local pressure could affect droplet TGZM velocity. Cline and Anthony[169] observed cracking and revealed the stress fields associated with aluminium drops in silicon by polarized infrared microscopy. They discussed internal stresses generated by differential thermal expansion when a crystal containing inclusions is heated[166] or when droplet temperature increases because of TGZM,[169] showing that temperature changes of a few degrees could cause plastic flow or cracking. However, Geguzin and Krivoglaz[126] showed analytically that diffusional relaxation of inclusion stress fields could occur rapidly.

Wilcox[128,181,182] and Cline and Anthony[167] found that liquid droplets which themselves contained gas bubbles migrated down temperature gradients (i.e. towards cold) in

several systems, including camphor-anthracene.[182] The gas bubbles were observed at the cold ends of droplets.[167] The phenomenon was explained[181,167] in terms of vapour transport across the bubble with countervailing fluid flow in the liquid driven by temperature-dependent variations in gas-liquid surface energy. Hoekstra et al[134] studied TGZM of aqueous KCl droplets in ice, and found that at the temperature at which the KCl should have become solid, migration velocity merely fell discontinuously by about one-third. They suggested that the slower-moving inclusions were solid KCl surrounded by a thin aqueous layer. Tiller[183] discussed the effects of evaporation during TGZM of planar zones.

Pfann[118] noted that solute trails of changed composition would be deposited in TGZM. Such trails have been observed in growing crystals by Bardsley et al,[184] as described in chapter VIII (d.). Doped solute trails have been used to produce p-n junctions:[172] in this context, solid-state diffusion behind migrating zones has been discussed by Lozovskii et al.[185] TGZM may be used to grow purified crystals[120,186] or to remove inclusions from crystals.[128] Goodman[187] observed TGZM of droplets formed by surface contamination on silicon: recently, Seidensticker et al[188] found that droplets thus generated migrated into growing crystals. Wagner[189] used surface TGZM to remove contaminants from droplets in nucleation studies. Geguzin et al[132] noted that "spheroidization" and TGZM proceeded simultaneously in dendritic structures in a static thermal gradient.

Many other driving forces besides thermal gradients can cause migration. Electric fields cause ionic migration, and electric currents also set up local thermal gradients via the Peltier, Joule and Thomson effects.[190,133] Migration occurs in accelerational fields due to pressure differences across inclusions (because c_L^* varies with pressure) and sedimentation fluxes within inclusions (diffusion biased by psuedo-gravitational forces), as observed by Wilcox and Shlicta[191,192] and Cline and Anthony.[159,163] Migration may also occur in inhomogeneous stress fields, and therefore inclusions undergo diffusion-elastic interactions with each other and with nearby crystal defects.[126] Brownian motion (random diffusional migration with no driving force) is important for small bubbles.[121] Hurle et al[129] gave a unified treatment of migration in terms of chemical potential gradients across migrating zones, noting that the feed material may be a different phase from the growing material and that this in itself could provide the driving force for migration.

Surface diffusion and volume diffusion in the matrix may be important for non-liquid inclusions. Shewmon[152] showed that $v \propto r^{-1}$ (r being inclusion radius) for surface diffusion control, which is likely to occur in submicron-size inclusions,[121] while $v \not\propto r$ for matrix diffusion. Geguzin and Krivoglaz[126] discussed the vacancy concentration in the matrix near a migrating inclusion. The equilibrium (temperature-dependent) concentration is maintained provided that:

$$v' \ll D_v/r \qquad \text{when } r > l_v \tag{28}$$

$$v' \ll D_v r/l^2 \qquad \text{when } r < l_v$$

where v' is migration velocity relative to the crystal lattice, D_v vacancy diffusion coefficient and l_v the spacing of sources and sinks for vacancies in the matrix. Inclusions may then migrate in a temperature gradient, because of vacancy fluxes due to thermotransport and vacancy concentration gradient in the matrix. If the matrix-inclusion interface is not a vacancy source and sink (as e.g. in coherent precipitates) v' is zero but v (relative to the specimen end-face) is non-zero and the inclusion migrates with the lattice. If the matrix-inclusion interface is a good source and sink for vacancies, the inclusion migrates by matrix diffusion only when it distorts the temperature field (because of unequal thermal conductivities in inclusion and matrix) and v may be of either sign.[125,126] Diffusion within solid inclusions (which is qualitatively similar to diffusion in liquid inclusions) and vapour transport in gas bubbles and pores may also be important. For vapour transport (assuming negligible interface kinetics), TGZM velocity is inversely proportional to pressure within the bubble when the mean free path $l_g < r$ so that gaseous diffusion occurs. Thus $v \not\propto r$ except for small bubbles, where the Laplace pressure ($=2\sigma/r$, excess pressure due to curvature) dominates and so $v \propto r$. When $l_g > r$, as may occur in empty pores, the

(faster) migration rate is assumed to be controlled by evaporation and condensation, when $v \propto r$.[126]

There have been many experiments on TGZM and Brownian motion in gas bubbles, as reviewed by Nichols[121] and Geguzin and Krivoglaz.[126] Barnes and Mazey[193] first studied TGZM of gas bubbles by electron microscopy, obtaining thermal gradients by increasing the beam current. They found $v \propto r^{-1}$ for helium bubbles of $< 10^{-1}$ μms diameter produced by α-particle bombardment of copper foils, consistent with a surface diffusion mechanism. Similar results were obtained by Cornell and Williamson[194] on krypton bubbles in uranium dioxide. More quantitative studies on small bubbles, using Brownian motion to avoid the problem of estimating the temperature gradients, have in most cases found migration velocities several orders of magnitude smaller than those predicted on a surface diffusion model.[195-197] Willertz and Shewmon[196] interpreted the discrepancy in terms of faceting and layer nucleation kinetics. Biersack and Diez[198] observed velocities increasing with size for larger gas bubbles in NaCl and discussed the results in terms of slow evaporation-condensation interface kinetics. Addition of zirconium oxychloride was shown to poison out the evaporation-condensation process, since bubbles then became immobile. Bubble shape changes were discussed in terms of thermal field distorsion effects as well as the curvature effect. Interface-kinetic effects were also observed for bubbles in adamantane[199] and camphor[200] and in extensive Russian work on alkali halides:[126] as in liquid-inclusion

studies (e.g.[150,161]) the smallest bubbles were immobile in some experiments.[198,200]

Recent work (e.g. Jones and May[201]) has shown that melt-grown lamellar and fibrous composites coarsened unusually rapidly when exposed to temperature gradients. Jones[123] showed that fibres could migrate distances comparable to the scale of the structure in reasonably short times by solid-state TGZM. He suggested that differential migration, occurring when fibre motion is affected by dislocation or adsorption interface kinetics, could cause fibres to collide and coalesce. Jones also showed that spheroidization might be accelerated because fibre ends would migrate more rapidly than the rest of the fibre by a surface-diffusion mechanism. He also discussed solid-state migration in accelerational fields.[202] McLean[124] modelled coarsening in lamellar structures in terms of differential migration due to a temperature-dependent bulk diffusion coefficient (i.e. hot lamellae migrate faster and move away from colder lamellae). The analysis gave reasonable values for activation energies of diffusion when compared to experimental results, whereas an analysis of coarsening due to curvature did not. (See chap. VIII (c).)

Special factors arise in ionic materials[191,192,126] and solid solutions. Anions and cations must migrate together in ionics, since departures from stoichiometry introduce strong electric fields, as does segregation to interfaces. One result is that (in ionics only) pore migration in electric fields requires both surface and volume diffusion.[126]

Inclusion shape distorsions have been analyzed by Nichols[43,121] and Geguzin and Krivoglaz.[126] The latter used expansions in spherical harmonics and showed that inclusions can migrate without distorsion. They gave a linear analysis for small distorsions, and a non-linear analysis for the large distorsions occurring when $v' > D_s/r$ in solid solutions, where $\partial c/\partial t$ is large and the crystal lattice near the migrating pore is distorted. Geguzin and Krivoglaz discussed the curvature effect in terms of work done against the internal stress normal to the interface when an atom is brought from the bulk to the surface, as in Herring's treatment[4] on which conventional curvature equations (e.g. I.2) are based. However, they also suggested that surface equilibration may occur by diffusion in the surface, rather than by bulk-surface interchange as described above. For this case a different curvature equation was derived, in terms of $(\frac{1}{3}\sigma_{ii})$ rather than (σ_{nn}). This would seem relevant only to surface diffusion analyses (chapter VI (d)(1).).

Nichols[121] described a general approach to migration calculations, in which velocity was calculated as the product of driving force and inclusion mobility. Force terms were determined from the rate of change of free energy with position, or by summing forces on separate atoms obtained from diffusion theory. Mobility terms were calculated for specific transport mechanisms from random-walk diffusion theory. The results agreed with atomic mobility treatments provided that inclusions could be assumed to stay spherical

while migrating.

(c) Transparent Organic "Metal Analogues"

Jackson and Hunt,[207] with the aid of the Jackson[15] model of solid-liquid interface structure, identified a few organic substances which solidify, as metals do, without faceting. Sufficiently low entropies of melting were found in systems with a high-temperature "plastic crystal" phase, in which a simple crystal structure is stabilized by molecular rotation and the entropy is therefore high. Jackson and Hunt used these materials as transparent analogues for metallic solidification, using optical transmission microscopy to observe growth in thin specimen cells on a temperature gradient microscope stage.[208] This technique is often preferred to alternative methods for the direct observation of solidification,[209] such as surface studies,[210] radiography,[211] ultraviolet[212] and infrared[169] microscopy, electron microscopy[213,177] and holography,[214] due to greater convenience, better control of the thermal field, and good resolution even during rapid solidification. Specimen cell thicknesses are commonly restricted to about one primary dendrite spacing, to minimize overlapping images, and so growth is to some extent two-dimensional. Ionic analogues for metals have generally been preferred for larger-scale direct observations.[76,215-217]

In the original apparatus design,[208] a thin specimen cell rests across the gap between fixed plates maintained at different temperatures. The alloy may be solidified by the

motor-driven motion of the cell across the plates, the growth interface thus remaining approximately stationary in the microscope viewfield. An electrically heated hot plate is used with a water-cooled cold plate, or a low temperature plate designed to avoid condensation problems. Specimen cells are made by fusing glass cover slides together on three sides and filling the gap (25-75 μms) between them with liquid alloy by surface tension.

Subsequently, Ross[218] found that play in the drive system caused a "wobble" in growth rate, which he eliminated by introducing a point bearing drive system. He found that fused cells were sufficiently warped to impair heat transfer from the plates, and therefore use epoxy resin-glued cells: later designs[219] used twinstick for greater convenience. Green[219] used recirculating hot water and recirculating ice-water systems in controlled temperature heating plates, claiming to achieve a stability of better than 0.05°C, after an attempt to control an electrically heated hot plate with an Ether controller had proved unsuccessful. Burnell[220] constructed a motor-driven cell rotation device. Jones[221] designed a "thermally symmetrical" stage, with robust cells sandwiched between two pairs of heating plates (the upper plates being spring-fitted to the lower plates) with the aim of eliminating the vertical temperature gradient which otherwise appears across the cell. The cells were made from thick glass slides glued together with epoxy resin. With an insulated microscope objective lens, vertical gradients were reduced to about 1 - 2°C/cm.[222] Okamoto et al[116]

pumped liquid alloy, at the liquidus temperature, along the growth front in thin cells. Jennison[223] also studied convection in thin cells, by observation of small (6 - 14 μms) floating latex spheres.

Timmermans[224] reviewed plastic crystals, including compounds not studied by Jackson and Hunt. Wulff and Westrun,[225] who measured the latent heat of fusion of succinonitrile by calorimetry, suggested that an earlier, anomalously high result obtained by freezing-point depression measurement was due to suppression of the plastic crystal phase by solute. As the current "Handbook of Physics and Chemistry" quotes the earliest data of all (from 1905) for the latent heat of fusion of succinonitrile, it seems likely that undiscovered "metal analogues" exist. Data on the physical properties, phase diagrams etc. of organics is available from references cited by Jackson and Hunt,[207] and from standard handbooks.[226-228] Experimental studies have recently produced useful data on phase diagrams (succinotrile-CBr_4, camphene-CBr_4, and CBr_4-meta-dinitrobenzene,[218] CBr_4-C_2Cl_6[34]), purification techniques for succinonitrile[229] and camphene,[230] thermal conductivities,[231,229] miscibility and thermal stability.[232,218,1] Table II,4 summarizes experimental studies of organic metal analogues.

(d) <u>Previous Work by the Author</u>

A Part II Thesis[1] describes studies of coarsening, TGZM and solidification using organic analogue materials as discussed above. Qualitative studies of TGZM during

solidification showed that migration distances could exceed secondary arm spacing. A simple model of TGZM confirmed this possibility: the model was used to predict migration distances for comparison with observed secondary spacings[62] in alloys. Solid-state diffusion ahead of the melting interface, and coarsening by differential TGZM of sidearms, were also analysed. Published work on microsegregation, notably the observations of "saw-tooth" segregation[95] and of greater microsegregation in the equiaxed rather than columnar regions of castings,[88] were discussed with reference to TGZM. Special features of $k > 1$ alloys were noted. Qualitative observations were made on dendritic growth morphologies and the growth, coarsening and coalescence of secondary arms. These observation bore out the contention that final secondary spacing is largely determined by coarsening. As discussed in later chapters, these early studies of dendrite growth shapes and of the size-dependence of droplet TGZM velocity were incomplete and misleading, while an inappropriate approximation led to wrong conclusions on differential TGZM and the cell-dendrite transition. The previous work also used an assumed linear concentration gradient in the liquid during TGZM, a first approximation which is questioned in the present work.

Table II.1 Final Secondary Dendrite Spacings

Authors	Material	n	notes
Michael and Bever[104]	Al-Cu	-	see (a)
Horwath and Mondolfo[105]	Al-Cu	0.25	see (b)
Spear and Gardner[106]	Al alloys	0.337	see (c),(g)
Bardes and Flemings[62]	Al-4½ wt%Cu	0.39	see (d)
Kattamis and Flemings[107]	Fe,Ni alloys	0.48	undercooled
Flemings et al[93]	Fe,Ni alloys	0.28	normal castings
Kattamis, Holmberg and Flemings[108]	Mg-Zn	0.4	see (e)
Matyja, Giessen and Grant[109]	Al alloys	-	see (f)
Weinberg and Teghtsoonian[95]	Cu alloys	-	see (a)
Kotler, Casey and Cole[110]	Pb-Sb	-	see (a)
Backerud and Liljenvall[111]	Al-Cu	-	see (g)
Northwood and Homewood[112]	superalloys	-	see (a)
Suzuki et al[113]	steels	0.39	see (j)
Brody and Nurminen[94]	Ti alloys	0.3-0.5	see (g)
Okamoto and Kishitake[56]	Al alloys	¼-⅓	see (h)
Jacobi and Schwerdtfeger[56]	steels	~0.5	see (i)
Edvardsson et al[114]	steels	0.173	

Notes:

(a) λ_2 decreases with increasing cooling rate.

(b) λ_2 decreases linearly with c_0 up to the eutectic, then increases again

(c) this paper defines dendrite cell size and its relation to λ_2.

(d) collated data covering a range of 10^7 in θ_f, hence accurate. Includes both columnar and equiaxed castings. Some primary spacing data erroneously included[1,64]: excluding this, n = ⅓ is a plausible fit.[1]

(e) λ_2 in dendritic structures ~ diameter of spherical grains in grain-refined Mg-Zn-Zr for equal Θ_f

(f) Splat-cooled materials: results fit the extrapolated graph of Spear and Gardner.[106]

(g) λ_2 decreases with increasing c_0, the most rapid variation being at low c_0.

(h) Same graph applies for various solutes.

(i) Marginally faster variation with G than R.

(j) Tertiary spacing $\lambda_3 \sim 1/5\ \lambda_2$.

Table II.2. Secondary Arm Coarsening During Solidification

Authors	Material	M	notes
Kattamis, Coughlin and Flemings[44]	Al-Cu	~3	
Kattamis, Holmberg and Flemings[108]	Mg-Zn-Zr	$\gtrsim$ 2	grains
Kattamis[115]	Mg-Zn-Zr	$\gtrsim$ 5	grains
Kattamis et al[77,78,79]	Al-Cu, Mg-Zn-Zr	-	see (a)
Feest and Doherty[63]	Cu-Ni	~3	"arms"
	" "	~5	"plates"
Dauncey[96]	Cu-Ni, Cu-Sn	~4	
Sharp and Hellawell[52]	Al-Cu	3	
Young and Kirkwood[64]	Al-Cu	~ 5-10	typical result
Okamoto, Kishitake and Bessho[116]	cyclohexanol	-	see (b)
Allen[1]	succinonitrile	2-3	

Notes:

M is the factor by which λ_2 (or spherical grain diameter in the case of grain-refined Mg-Zr-Zn alloy) increases during solidification (as compared to the initial value).

(a) Measurements of surface area per unit volume as a function of time, showing a decrease due to coarsening.

(b) Initial spacing $\lambda_2' \propto G^{-0.40} R^{-0.49}$. M ~ 1¼-2 for the early stages of solidification.

Table III.3. Interface Kinetics in TGZM

Authors	Material	Results
Kingery and Goodnow[203]	brine in ice	no size effects
Hoekstra et al[134]	aqueous KCl,NaCl in ice	" " " "
Jones[139]	aqueous and HCl in ice	" " " "
Jones and Chadwick[150]	Nominally pure camphene	see text
Steen[204]	metallic Al-Si alloy	no size effects
Mlavsky and Weinstein[205]	Ga in Ga As	see (a)
Wright[155]	Cr-Ta in SiC	see (b)
Kumagawa et al[156]	Cr in SiC	see (b)
Geguzin et al[132]	Li in LiF	see (c)
Geguzin et al[206]	Li in LiF	see (d)
Tiller[18] (from data of Wernick[137])	Al in Ge	$\mu_2 = 5 \times 10^{-4}$
Seidensticker[153]	Au in Ge	$\mu_{2m} = 2 \times 10^{-5}$ (see (e))
Jones and Chadwick[150]	salol-azobenzene alloy	$\mu_2 = 1.7 \times 10^{-4}$
Jones[154]	salol-azobenzene alloy and nominally pure salol	see text
McLean and Loveday[177]	Pb in Al	$\mu_2 = 9 \times 10^{-5}$ (see Doherty[176])
Lozovskii and Konstantinova[151] (summary of Russian work)	Cr in SiC	$\mu_2=6.9\times10^{-5}$, see (b)
	Sn in Si	$\mu_2=3\times10^{-5}$ (950°C)
	Sn in Si	$\mu_2=2\times10^{-4}$ (1200°C)
	(80%Sn 20%Al)in Si	$\mu_2=3\times10^{-5}$ (800°C)
	(80%Al 20%Sn)in Si	$\mu_2=3.23\times10^{-4}$(800°C)
	Al in Si	$\mu_2=1.37\times10^{-4}$(1100°C)
Hamaker and White[157,158]	Pb and In in InSb	A=4-50, $\mu_3=10^4$ (or $\mu_2 \sim 3\times10^{-5}$-$10^{-7}$)
Cline and Anthony[164]	Brine in solid KCl	see text
Cline and Anthony[173]	Al in Si	see text
Cline and Anthony[168]	Au in Si	a size effect

Notes:
μ_2 is in units of cm sec^{-1} $°C^{-2}$. Under materials column "x in y" means liquid x, solid y.

(a) thick zones migrated more slowly, because of greater As evaporation.[183]

(b) contradictory results. Wright[155] found no size effects, but velocity reduced ~ x 2 when initial surfaces not cleaned. Kumagawa[156] found no size effects when initial surfaces cleaned, but rapid fall-off in v below 30 μms diameter when surfaces not cleaned.

(c) no size effects, diameter 30 - 70 μms, thermal gradient migration.

(d) no size effects, diameter 3 - 30 μms, migration in electric field.

(e) from Γ_2 = 220 $cm^{\frac{1}{2}}$ $sec^{-\frac{1}{2}}$ ^oC, assuming $\mu_{2m} \ll \mu_{2f}$. If $\mu_{2m} = \mu_{2f}$, author stated μ_2 becomes 4 x 10^{-5}. This is an error, correct result would be 8 x 10^{-5}.

Table II.4. Experiments with Organic Analogues.

Authors	Experiments
Jackson and Hunt[76]	dendrite remelting, equiaxed zone
" " " " [232]	eutectic classification
" " " " [233]	eutectic growth shapes
Jackson, Uhlmann and Hunt[7]	crystal growth mechanisms
Ross[218]	dendrite tip curvature
Green[219]	dendrite growth temperature
Burnell[220]	" " " and direction
Allen[1]	dendrite coarsening.TGZM
Potter[234]	hot tearing
Jones and Chadwick[150]	TGZM
" " " " [231,235]	solid-liquid surface energies
Jones[144]	TGZM, drop shapes
Glicksman and Schaeffer[236]	planar-cell breakdown
Blodgett, Schaeffer and Glicksman[214]	holography, growth shapes
Glicksman, Schaeffer and Ayers[229]	accurate surface energies
Morris and Winegard[84,237]	dendrite tip shapes
Wilcox[182,238]	TGZM, etc.
Davis[239]	TGZM
Chen and Jackson[34]	melting interface stability
Chien and Kattamis[85]	sidearm coalescence
Ovsienko, Alfintsev and Maslov[240]	dendritic growth
Sigsbee and Anthony[200]	gas-solid TGZM
Okamoto, Kishitake and Bessho[116]	dendritic growth, convection
Kisakurek (private communication)	equiaxed zone, segregation
Simpson, Beingessner and Winegard[241]	grain growth (solid state)
Shih and Li[230]	" " " " "
Rudman[242]	X-ray crystallography

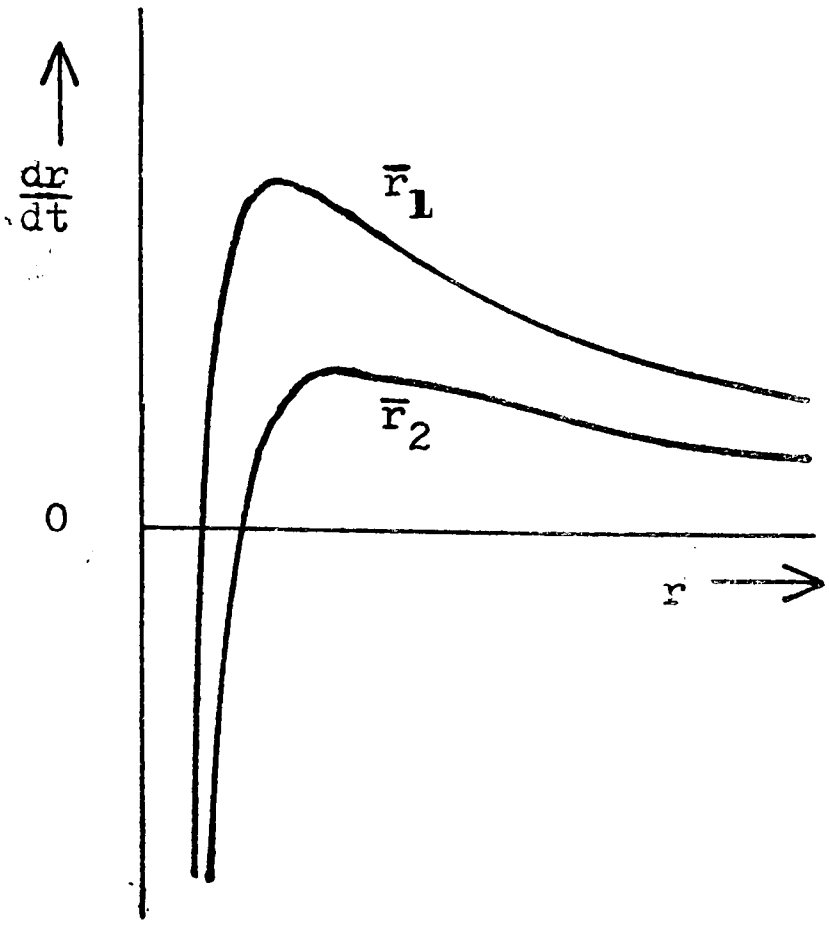


FIG. II. 1. Coarsening (after Greenwood). $\bar{r}_2 = 3/2\ \bar{r}_1$.

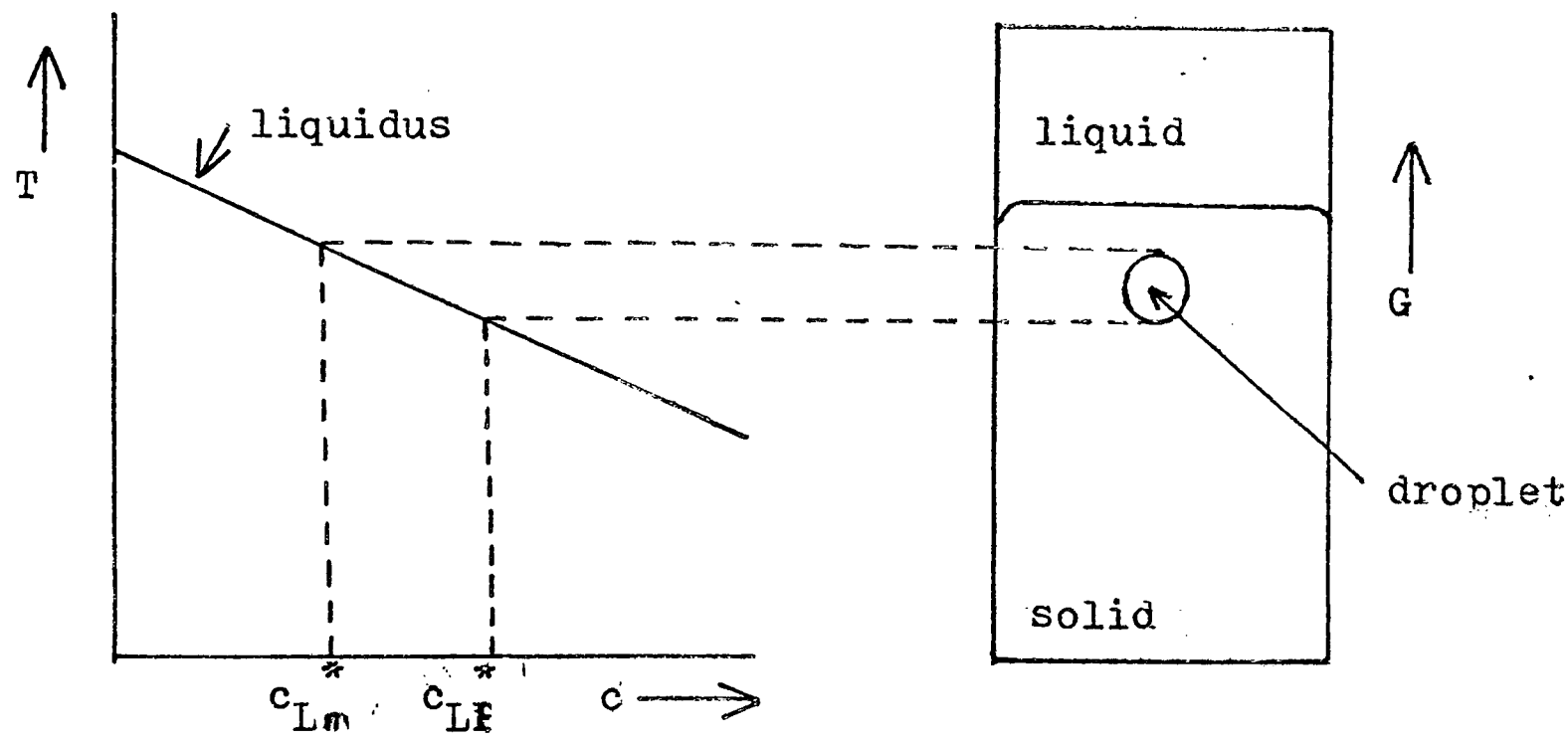


FIG. II. 2. Showing why TGZM occurs.

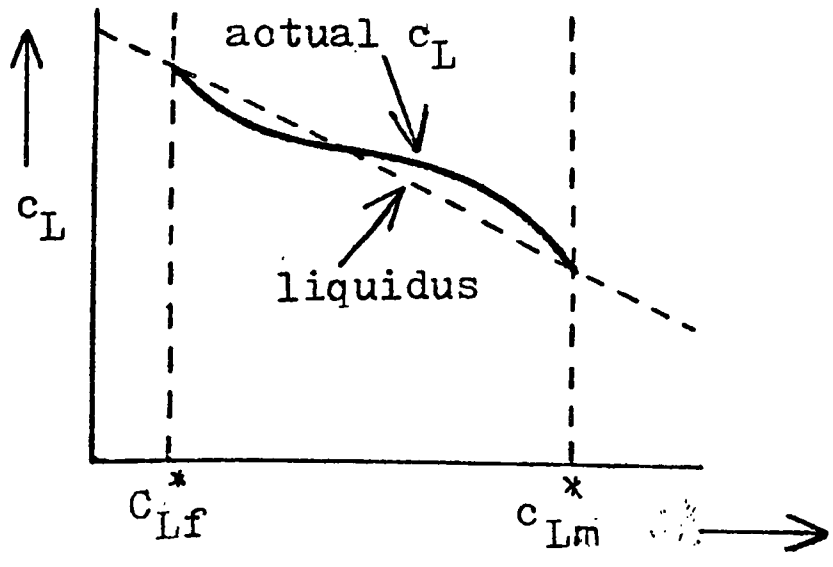


FIG. II. 3. Convection in TGZM.

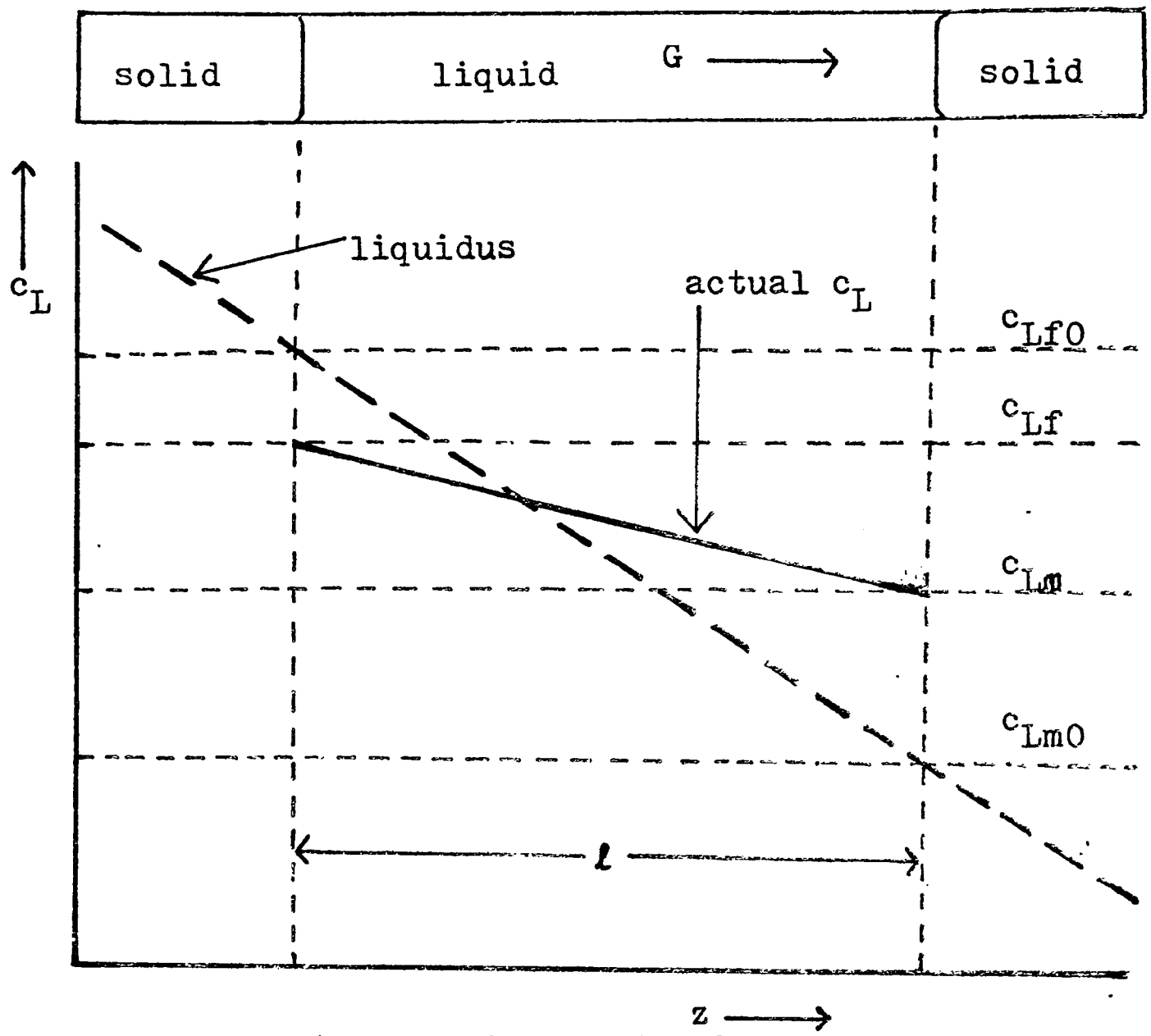


FIG. II. 4. Principles of TGZM.

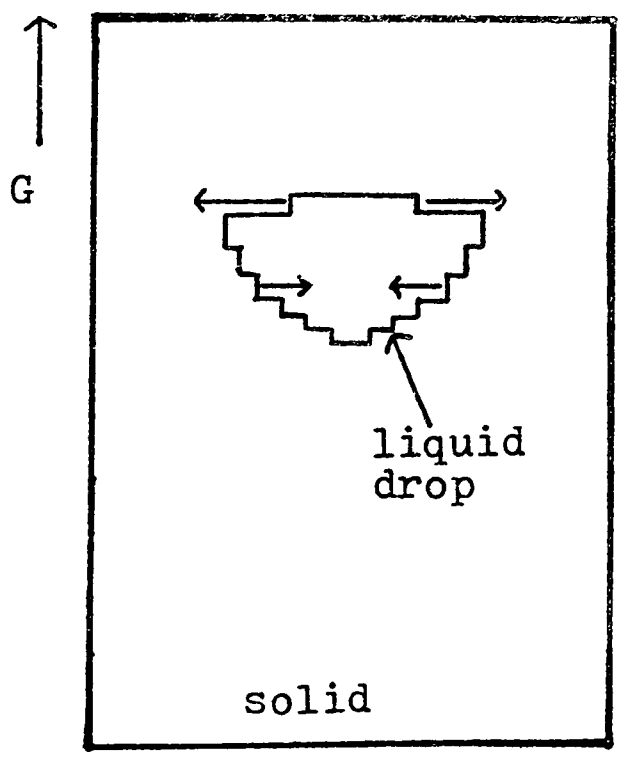


FIG. II.5. Faceting in TGZM.

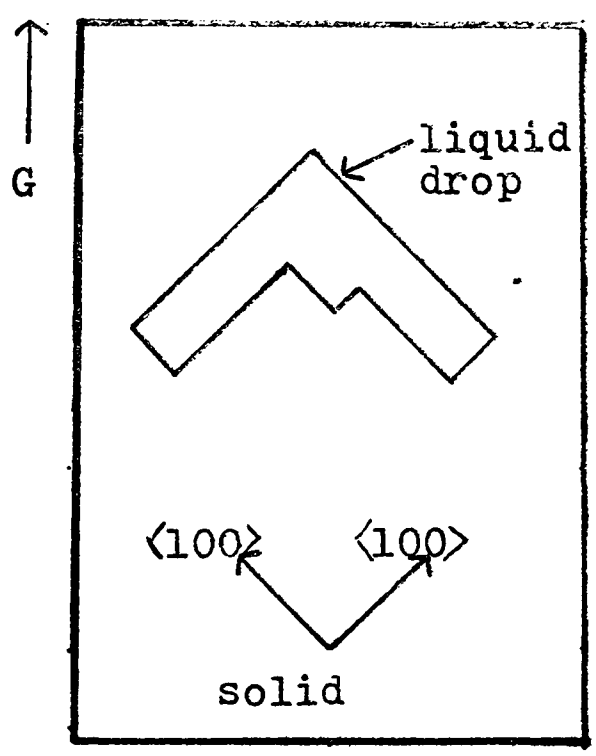


FIG. II.6. "Chevron" shaped droplet.

Chapter III. The Apparatus

Some of the work presented here was carried out using the microscope stage with fixed heating plates described in reference 1. The cell motion in this apparatus made interdendritic solidification studies difficult: reference marks were required to identify a selected area of the specimen, and continual re-adjustments of the stage position were needed to keep the area in view.(1) A new stage, in which the heating plates moved while the cell remained stationary, was designed to overcome these problems. Experimental work proceeded in parallel with various modifications to this apparatus, resulting from an improved understanding of the thermal conditions. To show the state of the apparatus for each experiment, the modifications are described in chronological order (section (e)), and interruptions of the form: (Experiments of Chapter A) are inserted at the correct points. Reasons for the alterations are discussed in section (f).

(a) Optics

A Wild M.20 microscope was used for bright-field transmission optical microscopy. Objectives of magnification x 4 and x 10 and a long-working distance objective labelled "x 32" but magnifying ~x 21 in this system, were available. Direct observations were made with x 10 eyepieces fitted with a graticule scale. The eyepieces could be replaced by a photographic attachment tube with an EXA-1a 35 mms camera

and a beam splitter to allow monocular observation of the viewfield. Photographic magnification was determined by photographing a stage micrometer (earlier work[1] being re-assessed and repeated following discovery of an error in the "x 32" objective calibration.) Results may be expressed in terms of the distance along the specimen represented by the long axis of the photographed viewfield. The graticule scale was also recalibrated by comparison of direct-observation and photographic distance measurements, mainly using the x 10 objective and obtaining objective magnification ratios from the photographic calibrations. Results (Table III.1) for the graticule scale applied only to the centre of the viewfield, i.e. between 30 - 70 on the scale. Distance per scale division was ~½% lower at the sides and there was considerable curvature of field (Table III.2). No such differences between centre and sides were found in photographs. The vertical fine focus control was calibrated as 1 division = 1.04 μms $\pm$0.02 μms. Thus, for vertical distance measurements in a medium of refractive index μ, 1 division corresponded to 1.04 μ μms. For instance, in solid succinonitrile (μ = 1.432[214]), 1 division = 1.49 μms.

(b) <u>The Specimen Cell</u>

24 x 24 x ~0.13 mm glass cover slides were stuck together with twinstick round three sides (Fig. III.1), leaving a space ~ 16 x 20 x 0.125 mms between the slides which was filled with liquid organic alloy under the action of surface tension. Cells were filled while resting on a clean glass

plate on an electric heater. Organic alloys were weighed out and melted together in stoppered bottles on the heater, stirred by shaking, and then poured onto the plate on which the cells lay. Cells filled rapidly through the open end and were then removed to cool. The heater temperature was held just above the alloy melting-point to minimize evaporation and chemical degradation and thus control composition. Air bubbles were carefully removed to avoid distorsion of the temperature field during experiments.

40 S.W.G. (122 μms diameter) copper-constantan thermocouples were Araldited into some cells during construction (Fig. III.1). Thermocouples were made by butt-welding inside thin Degussit alumina tubes (to minimize bead size) with a fine oxygen-gas torch flame, and carefully straightened with tweezers.

(c) Fixed-Plates Stage

This section summarizes a previous full description[1] (see also Chap. II (c) and Fig. III.2). The baseplate and heating plates were essentially similar to those described in section (d): optics and cells were common to the two stages. A synchronous a.c. motor with variable gear train drove a rotating spindle coupled flexibly to a threaded drive rod, which screwed into a PTFE block attached to a horizontal brass slider which was thereby driven across the stage. The slider ran within upper grooves in a pair of PTFE blocks fixed to the baseplate, while the hot and cold plates were held within lower grooves by set-screws. The cell rested across the gap between the

plates, held within a cage which itself fitted inside a rotatable cog wheel mounted on the slider. Perspex draught shields rested on the cell and below the microscope table. (Experiments of chap. IV.(b) (1) and (c) (1), and chap. VII, (e) (1)).

(d) Moving-Plates Stage: Original Design

The baseplate, made of 1/16 in. brass sheet, was screwed to the lateral traverse of the microscope and also moved forwards and backwards with the microscope table on which it rested. A pair of single-grooved PTFE blocks and their brass supports were bolted to run laterally across the baseplate. A variable-speed d.c. motor (General Time) was bolted to a raised vertical section at one side. Two hollow brass tubes for water-cooling were brazed to the baseplate. (Fig. III.3) An illumination hole, below the cell position, was covered by a Perspex draught shield. Three motors, nominally rated at 12 volts and 0.1, 1 and 10 r.p.m., were available. They were driven from the mains via a transformer, rectifier and Variac. The experimental calibration formulae (TableIII.3) were accurate to $\pm$ 1% within the range V = 3-25 volts applied. For a given Variac setting, the measured voltage applied fell by 1-2% when the motor was connected up to drive the plates on the stage. However, measured motor speeds on and off load were identical to an accuracy ~$\pm\frac{1}{4}$% for given applied voltage. Therefore, calibration and constant-speed running were not significantly affected by fluctuating loads. Small over-runs occurred after power to the motor was switched off, as recorded in

Table III.4. The drive rod was driven from the motor spindle via 1:1 gears (alternative gear ratios 2:1 and 1:2 were also available.) One end of the brass drive rod was 6BA-threaded, and screwed into a brass block mounted on the cold plate. The opposite end was pointed, and held against the end of a conical hole by a compression spring between the gear wheel and a brass support fixed to the baseplate (Fig. III.4). This point-bearing system (Chap. II.(c)) successfully achieved a steady drive.

The heating plates were 1/16 in. copper sheets: copper was used for its high thermal conductivity, to minimize temperature variations within the plates. They were linked rigidly together by a thin, slotted stainless steel connector bolted between their bases, setting a variable gap of 0.1 to 1.2 cms between the plate edges (Fig. III.5). The hot plate was heated by a 25-watt, 250-volt Solon soldering iron element, secured against the underside by a thin brass strip and fed from a Variac. The cold-plate was water-cooled via a brass tube of outer diameter 0.4 cms. brazed to its base. Initially, mains water was fed directly to the cold plate and baseplate, flexible tubes being used to allow the plates to move. The heating plates were held at their sides within narrow grooves in the PTFE guide-blocks and thus constrained to move laterally across the stage. To prevent the PTFE warping under thermal expansion stresses and hindering plate movement, the guide-blocks were screwed to the baseplate and to the vertical sides of brass supports of L-shaped cross-section which

were also fixed to the baseplate. The brass cell holder ran above the heating plates and was fixed to the L-shaped brass pieces. A PTFE ring, with a square hole to hold the cell, rested on the plates and fitted snugly into a hole in the brass cell holder. This ring could be rotated to select a desired cell orientation before a solidification run. (Experiments of chap. VII. (b)).

(e) Apparatus Modifications

The first alterations were designed to improve thermal insulation and overcome cell-plate heat transfer problems. To reduce draughts by "double glazing", an empty cell was rested on the specimen cell, and glass cover slips were taped over the top of the PTFE ring and across the gap at the base of the heating plates. A Perspex "box" was built to cover most of the baseplate (Fig. III.6.), leaving small holes for electrical and water-cooling connections and using a moveable top cover with a hole for the microscope objective. Most importantly, the cell and its PTFE ring were rested on a glass slide of 1.3 mms thickness which was fixed across the tops of the heating plates. This thick glass slide (cut from a photographic plate) was held in place by pressure (Fig. III.7) and thus moved with the heating plates. This alteration changed the heat transfer considerations fundamentally. (Experiments of chap. IV (d) and chap. VII (a) (1)).

The second series of modifications were introduced to control the thermal field and eliminate long-term

instabilities. A Eurotherm 040 controller with 031 thyristor was first used to control the hot plate temperature . The control thermocouple was soldered to the hot plate base, originally positioned at the side (near the PTFE), and satisfactory control was obtained with integral time constant 20 sec, derivative 2 sec. While the indicated deviation from the set temperature stabilized at zero ($\pm 0.2^{o}C$) within about five minutes, this apparent accuracy was deceptive. The temperature measured within a cell above the hot plate centre (where the heating element was) rose initially to ~ 5 C^{o} above the set point and took ~ 30 mins to relax to the set temperature. This indicated transient heat flow into the PTFE, and the control thermocouple was repositioned near the plate centre to minimize such transients. Nevertheless, measured temperature in a later, similar test again took ~ 30 mins to stabilize (though without overshooting). This was attributed (from similar experience[243] with furnaces) to stabilization of the controller electronics.

Finally, manufacturer's data for the control system specified a set-point accuracy $< 1.5\ \mu V$ or $0.1^{o}C$, with $< 10\ \mu V$/year drift, $< 3\ \mu V$ per ^{o}C sensitivity to ambient temperature and $0.2\ \mu V$ per volt sensitivity to mains voltage variations. For our copper-constantan control thermocouples, this implied errors of $\pm 0.1^{o}C$, $\pm 0.25^{o}C$/year, $\pm 0.06^{o}C$ per ^{o}C ambient temperature variation, $\pm 0.004^{o}C$ per volt supply variation, suggesting overall accuracy $\pm \sim 0.5^{o}C$ after full stabilization.

A similar system was then applied to the cold plate, using a control thermocouple on the cold plate base to control the power supply to a heater in the cooling water circuit. A 350-watt electric "cup heater", and plastic inlet and outlet tubes for water, were cemented into a 150-ml glass beaker which was made watertight by the cap of cold-setting cement. Mains water was fed via this heating system to the cold plate and baseplate. Long time constants (integral 110 sec, derivative 12 sec) were required because of the thermal lag introduced by the separation of heater and thermocouple, and stabilization could take over an hour. (Stability was then generally reliable, but was occasionally upset by large fluctuations in mains pressure).

It was found that the thermocouple in a cell could be about $1^{\circ}C$ hotter under maximum illumination than when unlit, though (from interface position studies) a cell with no thermocouple was heated only $\sim 0.05^{\circ}C$. ($G \sim 60^{\circ}C/cm$, plate spacing $\sim$ 8 mms, thermocouple near centre of gap between plates.) A Wild KG 1 heat filter reduced the heating effect to about one-seventh of this. (Experiments of chap. IV. (b) (2.), and chap. VII. (c), (d), (f) and (g)).

The hot plate of the fixed-plates apparatus, with a 0.16 mms diameter observation hole drilled near its centre, was used as an isothermal stage (experiments of chap. IV,(d)).

The third design modification was aimed at eliminating vertical temperature gradients in cells. Tin oxide-coated

glass slides (Corning Glass Co.) were tried out as transparent hot plates, but discarded because of excessive resistivity variations. The final design (Fig. III.10) was first tested with a crude mock-up, using hammer-bent brass sheets for the upper plates. This showed that greatly reduced vertical gradients were obtainable, particularly when draught shields were fitted along the sides of the glass slides. For the actual apparatus, L-shaped upper plates were made from horizontal 1/16 in. brass sheets brazed into slots in brass blocks, bolted to the far ends of the lower plates through slotted bolt-holes. The upper plate edges could thus be postioned vertically above the lower plate edges, or independently adjusted up to 1 mm to either side of this position. The upper plates ran 3.3 mms above the lower plates: into the gap were tightly packed two glass slides of 1.225 mms thickness, separated by a layer of compressible material (asbestos paper) at each end. The cell (of total thickness $\sim$ 0.4 mms) fitted within a new cell holder on the lower glass slide, leaving an air-gap of $\sim$ 0.5 mms between the cell and the upper glass slide. The cell holder was rectangular with a square hole for the cell, made by Aralditing together two acetate sheets, $\sim$ 0.6 mms thick and held stationary in new grooves $\sim$ 1.0 mms deep across the tops of the PTFE guide-blocks. (Tests showed that this cell holder was sufficiently rigid to prevent observable cell motion when the plates moved.) Cell rotation was thus not possible, but new cell holders with differently oriented holes for cells could be made easily. Perspex draught

shields fitted snugly between the glass slides and PTFE blocks, and were glued to acetate sheet glued to the brass covers of the PTFE blocks: the cell holder fitted tightly through holes in the draught shields. (Experiments of chap. IV (c) (2) and chap. VII (a) (2) and (e) (2)).

(f) Temperature Measurements Within Cells.

Thermocouple beads were positioned centrally within cells, with the leads running along isotherms in order to minimize temperature distorsions. The two thermocouple wires ran to separate junctions with copper wires within the cold junction bath (a paraffin-filled tube inside a thermos flask containing an ice-water mixture) and the copper wires were connected to the terminals of a Cambridge potentiometer, reading to accuracy $\pm$0.002 mV or $\pm$0.04^{o}C. Unless otherwise stated, temperature measurements were made under minimum lighting, with the thermocouple bead in focus in the viewfield centre. A single thermocouple was always used, temperature being measured as a function of bead position with respect to the plate edges (i.e. the z_p coordinate (chap. VII.(d))). As discussed below, the variation of temperature with position in such experiments should closely parallel the variation of temperature with position in a stationary cell provided certain conditions are fulfilled. In most runs, the plates were moved a known distance (measured either from a motor run of fixed duration and speed, or from manual rotation of the drive rod while observing the plate edge through the microscope) and then at least four minutes

were allowed for thermal re-equilibration before the temperature was measured and the plates moved again. In some runs (especially those of chapter IV (d), used in dendrite tip temperature measurements) temperatures were measured during continuous plate motion, to investigate whether T (z_p) was altered by the plate motion. The differences observed were not very significant and the instantaneous displacement experiments noted below gave more useful information on the subject. Succinonitrile-filled cells were always used.

Fig. III.11 shows a typical run with the original moving-plates apparatus. The nonlinear thermal gradient across the plate gap indicated large heat losses from the cell upper and lower surfaces. Brass-backed cells (with small holes for viewing) were tried in an attempt to increase heat flow along cells relative to heat losses, but it then became apparent that cell temperature depended mainly on the area of cell in contact with the two plates, with $T(z_p)$ being higher when a greater area of cell lay on the hot plate rather than the cold plate. Thus, there was clearly a greater "thermal resistance" to heat transfer between cell and plates than to heat flow along the cell, and a temperature-position measurement run as described above would not determine accurately the thermal field in a stationary cell. The graph of Fig. III.11 indicated that heat transfer problems were still significant in normal cells, since the "tail" of varying temperature to a depth of $\sim$ 5 mms on each plate represented a temperature difference across the cell-plate interface which gradually fell to zero.

So, unless the cell covered each plate to a depth of at least ~ 5 mms, $T(z_p)$ would again be expected to vary with coverage. As the "tails" represented temperature variations of several degrees in the cell above the plates, $T(z_p)$ in the plate gap would probably vary considerably with varying heat transfer coefficients of different cells. When the plates were moved under the cell, thermal re-equilibration would require altered heat inputs from the plates. So $T(z_p)$ would be expected to rise considerably during a solidification run because of the need to extract more heat at the cold plate,(1) especially near the centre of the gap between the plates where excess heat could not be extracted readily. For all these reasons, a re-design was required to improve heat transfer characteristics.

The solution adopted was to fix a thick glass slide across both plates and rest the cell on this (section (e)). The resulting T versus z_p plot (Fig. III.11) was not markedly altered, except for the improved linearity due to greater longitudinal heat flow. Nevertheless, we may show that the heat transfer characteristics were substantially improved. The thick glass slide, having five times the thickness of glass of the cell without the insulating succinonitrile, carried most of the heat flowing between the plates. The steady-state temperature distribution in the slide (albeit including "tails" of varying temperature above the plates due to slide-plate interface resistance) should therefore have been largely unaffected by the cell position on top of the slide. (Nevertheless, quantitative

experiments were carried out with at least 4 mms of cell coverage over each plate. This was achieved for a T - z_p measurement run, given 24 x 24 mms. cells with centrally positioned thermocouple beads, when the plate gap was 8 mms or less). Furthermore, as the cell rested on glass at all points of the plate gap, its temperature at a given z_p was held close to that of the slide by intimate thermal contact. Thus $T(z_p)$ in the cell was unable to differ greatly from $T(z_p)$ in the slide, even during a solidification run, and variable cell-slide heat transfer coefficients were not very important. The other modifications of the first series were stimulated by the experiments of chapter IV.(c), demonstrating the importance of thermal fluctuations in cell and dendrite growth. The "box" and "double glazing" prevented such short-term fluctuations but did not remove long-term effects of varying room temperature, as discussed later.

The thermal equilibrium conditions of the full system were studied by calculation, and also by direct measurement of input and output temperatures of the water used to cool the cold plate and baseplate, together with measurements of flow rate. The hot plate heater, rated at 25W 250V, maintained the hot plate some 50°C above room temperature with an applied voltage of ~ 100V. Thus its output, equalling heat losses to the surroundings was roughly 1 - 2 calories/second. Calculations (assuming temperature gradient ~ 50°C/cm) suggested that the heat loss via the glass slide was ~ 0.1 cals/sec and the heat loss via the steel connector between the plates was ~ 0.5 cals/sec. Measurements of heat gain by the cooling

water gave ~ 20 cals/sec. when the cold plate and baseplate were ~ 10°C below room temperature: presumably the main heat gain was from the baseplate. It seems likely that the heat gain from the PTFE was ~ -1.0 cals/sec for the hot plate, ~+0.2 cals/sec for the cold plate. Assuming heat flow to one PTFE guide ~ 0.5 cals/sec, the temperature gradient in the copper plate ~1°C/cm giving a temperature difference of ~ 2°C between centre and edge of the plate.

The two T - z_p plots of Fig. III.11 show markedly different cold plate temperatures at different times of year, due to varying mains water temperature. Experiments also showed a fall of ~ 3°C in hot plate temperature resulting from a fall of 10°C in room temperature, despite constant applied voltage: they also showed that mains voltage could fluctuate by ~ 5 - 10%. For experiments such as those of chapter VII (d) a reproducible temperature field was required and the controllers described in section (e) were therefore installed. The plate temperatures then became independent of room temperature (except for the temperature sensitivity of the controllers, section (e)) but the cell temperature was still influenced by external temperatures, the sensitivity reaching a maximum of ~ 0.1°C change per °C change in room temperature for a thermocouple at the centre of an 8 mms plate gap. Room temperature varied by ±2°C (average was ~19°C) in quantitative experiments, introducing an error ±0.2°C. Larger errors would have been obtained had not the baseboard been held at roughly the same temperature as the controlled cold plate by the water-cooling system, as the air temperature inside the Perspex "box" was found to be closer to the baseboard temperature than the room

temperature. Further experiments showed the important cooling effect of the objective lens. When this lens was removed from the focused position above the thermocouple bead, the measured temperature in cases similar to Fig. III.11 rose by as much as 1°C, even when asbestos paper insulation had been stuck over the metal sides of the lens. (Because of the lens cooling effect, the dendritic growth velocity in the experiments of chapter VII (d) altered from ~10% below the plate velocity as the tips moved from one side of the viewfield to the other.) Adding these sources of error to the specified accuracy of the Eurotherms discussed in section (e), an accuracy of $\sim \pm 1^{\circ}C$ in temperature measurements is suggested. From comparison of actual temperature measurement runs, lower errors of $\sim \pm 0.5^{\circ}C$ at worst were found indicating perhaps that the Eurotherm specifications were over-pessimistic or that some errors cancelled out.

The effect of the thermocouple itself on the thermal field in the cell was studied by comparing TGZM velocities in cells with and without thermocouples. As shown by (VII.2), a graph of v^{-1} versus z_p should be linear when D_L and the phase diagram parameters m, k are constants, and G is roughly linear. Linear $v^{-1} - z_p$ graphs were indeed found for nominally pure succinonitrile in the absence of a thermocouple (Fig. VII.1). Typical results in a thermocouple cell are shown in Fig. III.12. These may be understood by reference to Fig. III.13. This shows the expected thermal field in the glass slide with no cell, the expected field in a

cell containing a thermocouple resting between the plates and unsupported by glass, and finally the expected thermal field in the cell and glass when the cell rests on the glass. The thermocouple, having much higher thermal conductivity than the glass or the organic, is almost isothermal: as its K $\sim 10^2$ x that of glass while its width is $\sim 10^{-1}$ that of the glass slide, its effect is important. As shown in Fig. III.13 (c), G is increased near the thermocouple on either side, and so v^{-1} (TGZM) should be reduced. Results such as Fig. III.12 show that the greatest thermal field distorsion occurs within $\sim \pm 100$ μms of the thermocouple but some distorsion persists at longer range. In a 50°C/cm thermal gradient, the thermocouple thickness of 122 μms represents ~ 0.6°C and so the error in dendrite tip temperature (chap. IV.(d)) introduced by this thermal field distorsion effect should not be greater than ± 0.3°C.

Alterations to the thermal field when the plates moved were studied by making (virtually) instantaneous displacements to the plates and measuring temperatures within cells as these relaxed to a new equilibrium value. Results (Fig. III.14) show ΔT as the difference between thermocouple temperature at time t and the final equilibrium temperature at $t \to \infty$ after an initial plate displacement at t = 0: ΔT_0 represents the difference in equilibrium temperatures before and after the displacement. Two types of re-equilibration might be expected. Firstly, the cell must be heated or cooled to a new temperature corresponding to a

hotter or colder part of the glass slide. Secondly, as the hot plate moves within the grooves to a new and colder part of the PTFE guides, transients in its temperature might be expected, as noted in section (e). If, as with the original control thermocouple position of section (e), the hot plate temperature rose above the equilibrium value, this would make ΔT approach zero more rapidly when the hot plate was displaced toward the cell but would make ΔT approach zero more slowly when the hot plate moved away from the cell. No such differences in equilibration on heating and cooling were actually observed, indicating that transients in plate temperature were unimportant with the repositioned control thermocouple. The ΔT - t curves of Fig. III.14 were used to calculate the alteration of the thermal field during a solidification run as described in chapter VII (d).
Also shown in Fig III.14 are the results of instantaneous displacement experiments with the final apparatus (after the third series of modifications, section (e)). Equilibration is then much faster, due to the extra glass slide and the reduced influence of the microscope objective.
One objection to this series of results might be the influence of the thermocouple itself on equilibration: its high specific heat would retard equilibration, while its high conductivity would accelerate it. This objection cannot be entirely discounted, but experiments showed no change in bead temperature when the thermocouple wire outside the cell, two centimetres from the bead, was strongly heated by a soldering iron and it therefore appears that heat gains

and losses via the thermocouple wire were not important.

The third and final series of modifications followed studies of the vertical temperature gradients in cells, using the assumption that TGZM in succinonitrile follow the direction of maximum temperature gradient. Chapter VII.(e) shows that this assumption should be accurate at G $\sim 50^{\circ}$C/cm as in most of these experiments, and that deviations from the maximum G direction at lower G would not introduce systematic errors. Changes in droplet heights were studied from the vertical fine focus control, using the calibration of section (a): for each drop, a particular level of focus (e.g. outer bright ring just on the point of disappearing) was maintained by fine focusing during TGZM. From the ratio of horizontal to vertical distances travelled and a measurement of horizontal G from thermocouple runs, the vertical gradient could be calculated. Individual focus height measurements showed a scatter of ± 1 - 2 microns. For a typical measurement, based on height change during horizontal migration through 28 microns, the error in G_{vert} was therefore about 8% of G_{hor} and, averaging over about ten readings, this was reduced to around $2\frac{1}{2}\%$ G_{hor} or, typically, $\pm 1^{\circ}$C/cm. A series of measurements (Table III.5a) showed how the vertical gradient varied with position across the gap: we adopt the convention that G_{vert} is positive when the base of the cell is hotter. The results of Table III.5 show that cooling from above, e.g. by the lens, is important but the tendency for heat flow to be upward from hot plate to cell but downward from cell to cold plate is also clear:

external cooling dominates where the cell is hottest. The above experiments were performed with a thick Perspex shield resting on the cell, with the "x 32" lens. Other experiments confirmed that this was about the most effective form of all insulation, typically giving $G_{vert} \sim +10^{o}C/cm$ at around $50^{o}C$ while uninsulated cells gave $G_{vert} \sim +20^{o}C/cm$. The objective lens was not shielded with asbestos paper in these studies: adding this insulation only slightly reduced the vertical gradient.

The modified apparatus (Fig. III.10), by contrast, gave greatly reduced vertical gradients. Results are given (Table III.5b) for a variety of experiments with comparatively low temperature gradients as shown in Fig. III.15. To obtain these low gradients, water was fed to the cold plate via the cup heater from a hot-water boiler, since the cup heater could not heat water by more than about $10^{o}C$. In these experiments the upper plate edges were directly above the lower plate edges ($\pm \sim 50\ \mu ms$) and it is seen that vertical gradients below $1^{o}C/cm$ were easily obtained, at least on the hotter side of the plate gap. In practice, vertical gradients were further reduced by altering the insulation on the upper plates. As these were not in direct contact with the PTFE guides, they could be slightly hotter than the respective lower heating plates if well insulated. Thus, our apparatus obtained lower vertical gradients than that of Jones[221](chap. II(c)) with the plates stationary, because of greater flexibility and the reduced influence of the objective lens resulting from the existence of an air-gap

between the upper glass slide and the cell. The relative merits of the two stages were less clear-cut for experiments on solidification. In our apparatus, only a thin cell moved relative to the plates, while in Jones's apparatus thick cells moved. So, much less distorsion of the thermal field was caused in our apparatus, permitting experiments such as chap. VII.(d) comparing observations with and without the plates moving. However, heat extraction during solidification was asymmetrical in our apparatus, because the cell was in contact with the lower glass slide but not the upper slide. Consequently, a vertical thermal gradient was set up when the plates moved. This was not easy to measure, as small vertical displacements could be expected when the plates moved if the glass slide varied in thickness. Attempts were made to get round this problem by simply re-setting the Eurotherms to cool the cell, but this introduced a new effect: the lower hot plate cooled more slowly, being in contact with hot PTFE and less open to the air, introducing a high positive vertical gradient. (This type of behaviour is a drawback to be considered in any future stage design based on programmed plate temperature reduction to achieve solidification). So, experiments were performed to measure the heights of dust particles in cells as a function of plate position in order to correct for vertical displacements of the cell, and then droplet TGZM was studied as previously while the plates moved. Results showed $G_{vert} \sim -2^{o}C/cm$ for cooling with plate velocity 3 μms/sec. (corresponding to solidification runs), $G_{vert} \sim +2\frac{1}{2}^{o}C/cm$ for warming with

plate velocity 3 μms/sec (i.e. plates moving to the left, Fig.III.3) Thus a vertical gradient of about 2°C/cm. was attributable to plate motion at 3 μm/sec: higher gradients would be expected for higher speeds but such speeds did not allow long enough for accurate studies of vertical TGZM. The Jones[221] apparatus might produce lower vertical gradients during solidification because of its greater symmetry of heat input and extraction.

(g) Contrast

The phase interface in organic alloys is visible mainly because of the refractive index difference between the phases.[244,245] A convex object of higher refractive index than its surroundings behaves as a lens, bringing the parallel light from the microscope condenser to a focus above the object. So, when the microscope plane of focus is raised above the object, a bright "Becke line"[245] is seen inside the object, with a compensating dark ring outside it. The reverse occurs with the plane of focus below the object. Since the refractive index of the solid phase is higher in succinonitrile and camphene,[214] this analysis suggests that dendrite tips should act as convex lenses but that liquid droplets should behave in the opposite way (i.e. focus above drop, Becke line outside drop, etc.). These effects were observed experimentally. It was found that the sizes of out-of-focus droplets were slightly overestimated (i.e. not more than 20%) when their edges were taken as the boundary between the bright

and dark rings. As suggested by the theory, any piece of curved solid-liquid interface could give refractive index contrast, but a sharp focus could only be obtained for curved interfaces passing through the vertical. Sometimes, a faint black line of unknown origin was observed to delineate non-vertical sections of the interface in focus.

Table III.1 Microscope Calibrations

Objective lens	Camera viewfield long axis (μms)	Graticule full scale (100 divisions)(μms)
x 4	1824 ± 8	3003 ± 50
x 10	732 ± 3	1205 ± 8
"x 32"	339½ ± 3	558.9 ± 10

Table III.2 Microscope Curvature of Field

(Average of five runs using vertical fine focus to measure apparent height of dust particles as a function of position on the graticule scale, with x 10 eyepieces: arbitrary zero set for apparent height at scale centre.)

Graticule scale position	0	10	20	30	40	50	60	70	80	90	100
Apparent height (μms)	8.3	5.3	1.8	0.8	0.1	0	-1.5	0.5	2.9	6.4	9.3

(Accuracy per height measurement ~ ±1-2 μms).

Table III.3. Motor Speed Calibrations

For: V = applied voltage, measured on Avometer 25 volts d.c. range,

R = plate velocity (cm/sec) when driven via 1:1 gears by a 6 BA threaded drive rod:

$R = 1.237 \times 10^{-3} V - 1.423 \times 10^{-3}$ (10 r.p.m. motor)

$R = 8.523 \times 10^{-5} V - 6.688 \times 10^{-5}$ (1 r.p.m. motor)

$R = 8.184 \times 10^{-6} V - 4.005 \times 10^{-6}$ (1/10 r.p.m. motor, anticlockwise)

$R = 8.052 \times 10^{-6} V - 4.164 \times 10^{-6}$ (1/10 r.p.m. motor, clockwise)

Table III.4 Motor Over-runs.

Over-run = distance moved by plates (observed) after motor power switched off. 1 r.p.m. motor: 1:1 gears, 6 BA threaded drive rod.

V	3	5	7.8	10	15	20	
Over-run (μms)	2	4	9	12	22	32	(pushing plates)
"	2	4	9	13	25	35	(pulling plates)

Table III.5. Vertical Gradients

(a) prior to final modifications, Fig. III.7.

Eurotherm settings: hot plate, 2.850 mV (69.3°C)

cold plate, 0.780 mV (20.0°C)

Room temperature = 17.8°C

Plate spacing = 7.84 mms. Estimated $G_{hor} \sim 40^{\circ}C/cm \pm 25\%$

z_p	284	1209	2414	3619	6029	7234	μms
(G_{vert}/G_{hor})	-.17	-.01	+.17	+.31	+.52	+0.63	
G_{vert}	-6.8	-0.4	+6.8	+12.4	+20.9	+25.1	°C/cm

(b) after final modifications, Fig. III.10

Eurotherm settings: 0.300 mV apart, mainly hot plate 2.300 mV (56.6°C), cold plate 2.000 mV (49.5°C): other settings close to this.

Room temperature 20°C ± 1°C

Plate spacing = 7.27 mms. G_{hor} from Fig. III.15.

z_p	1958	3075	4266	4473	5311	5870	μms
G_{vert}	+2.8	+2.5	+1.4	0.0	0.0	+0.8	°C/cm

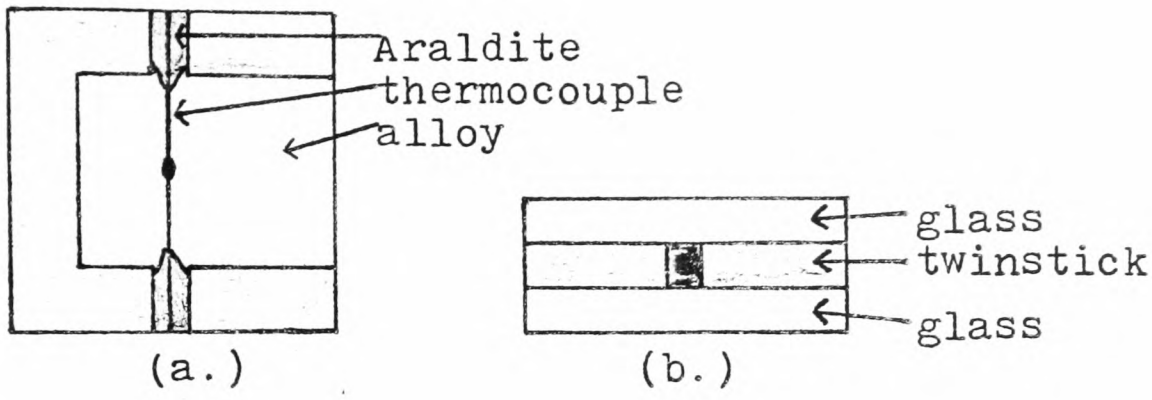


FIG. III. 1. Specimen cell (a.)plan (b.) elevation (expanded scale.)

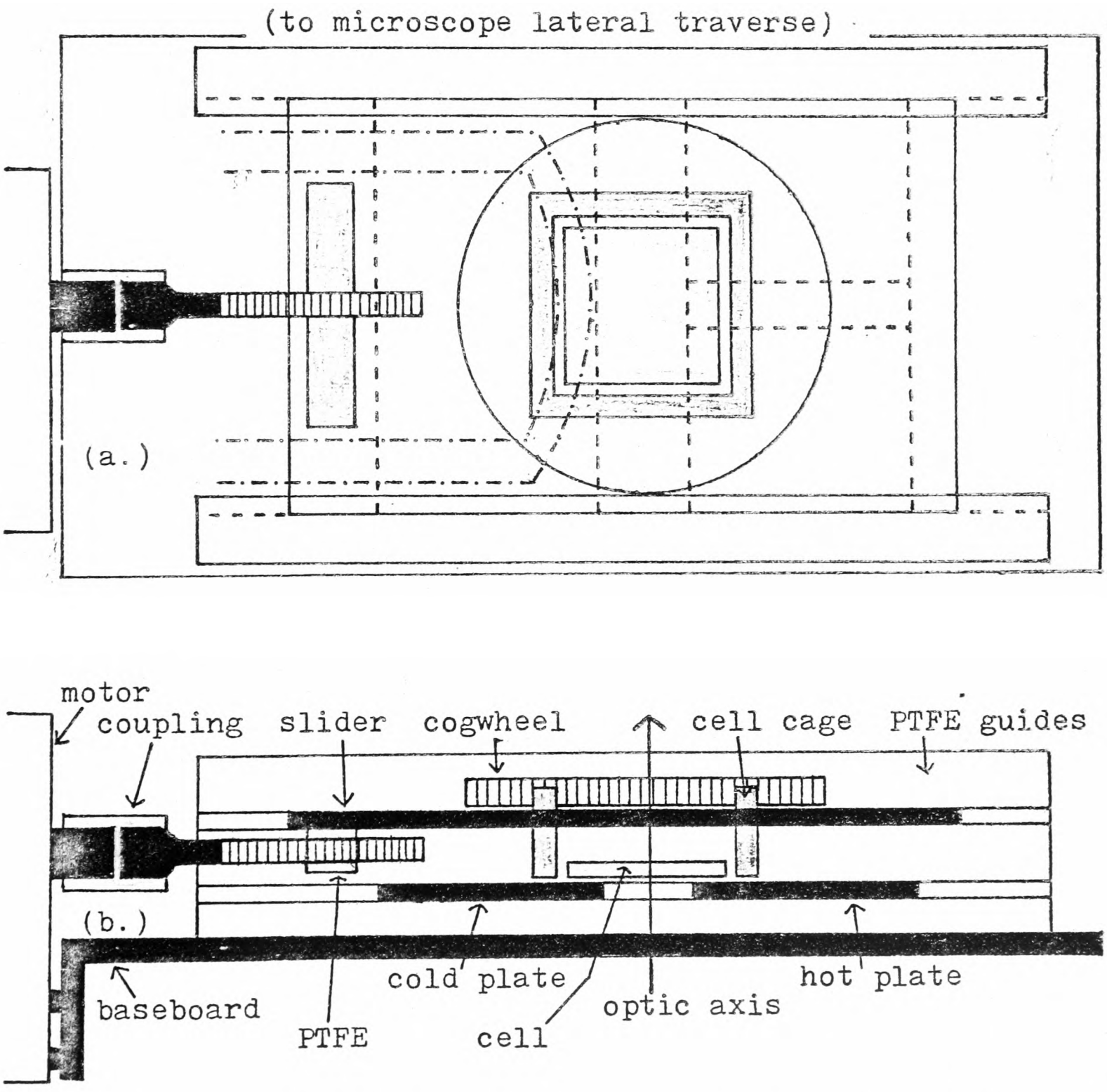


FIG. III. 2. Fixed - plates stage (a.) plan (b.) elevation.

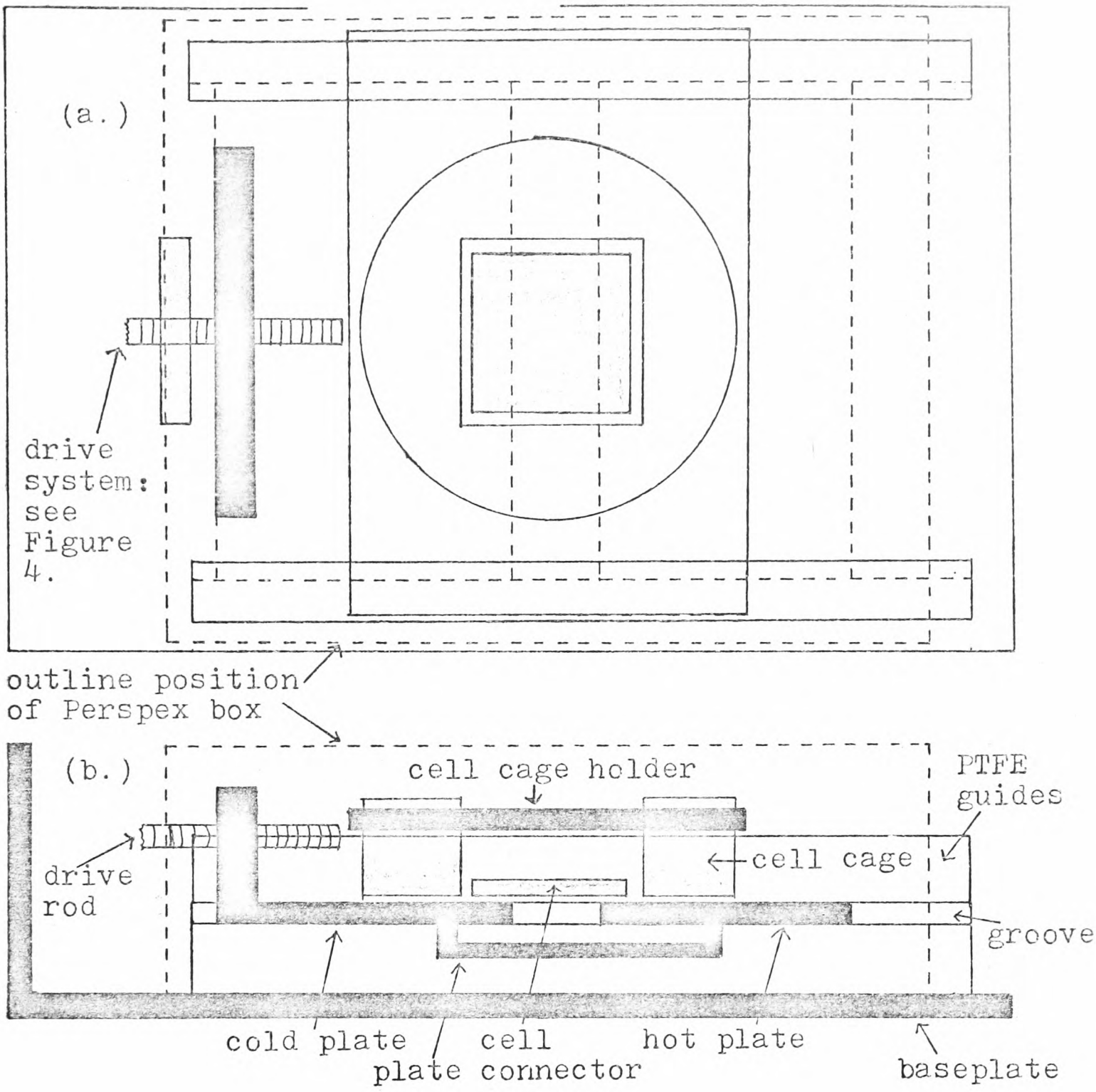


FIG III. 3. Moving - plates stage : (a.) plan, (b.) elevation (expanded scale). Part of drive system omitted.

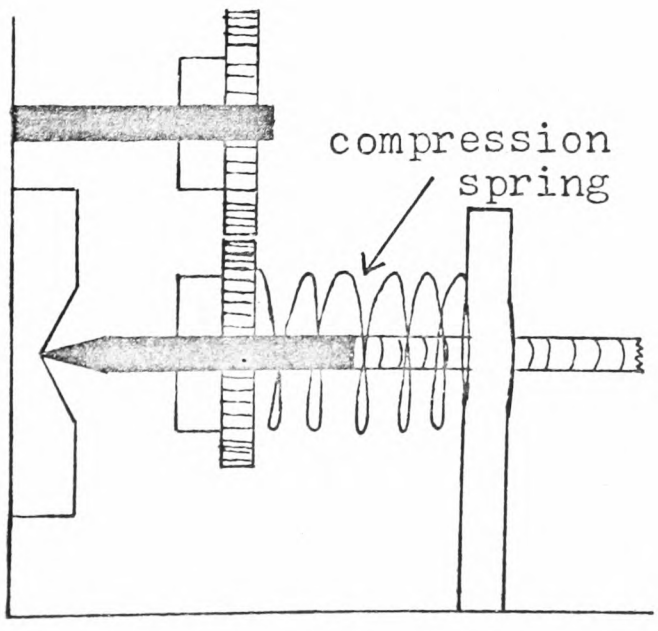


FIG. III. 4.
Drive system with point bearing.

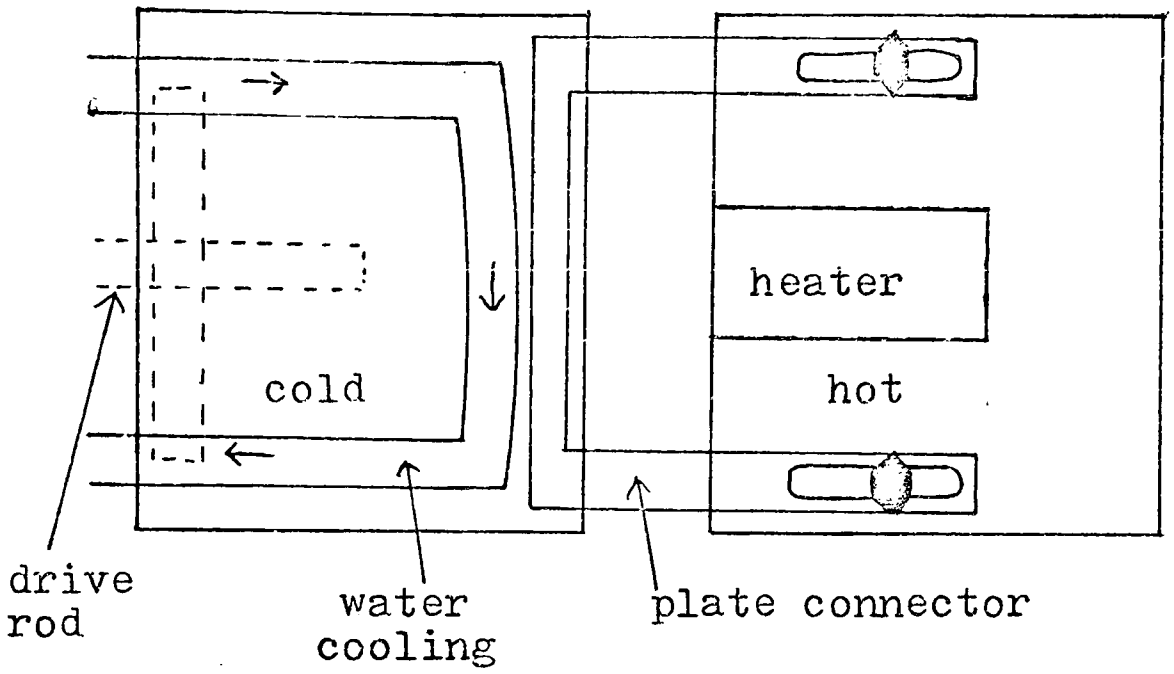


FIG. III. 5. The heating plates
(plan, viewed from base)

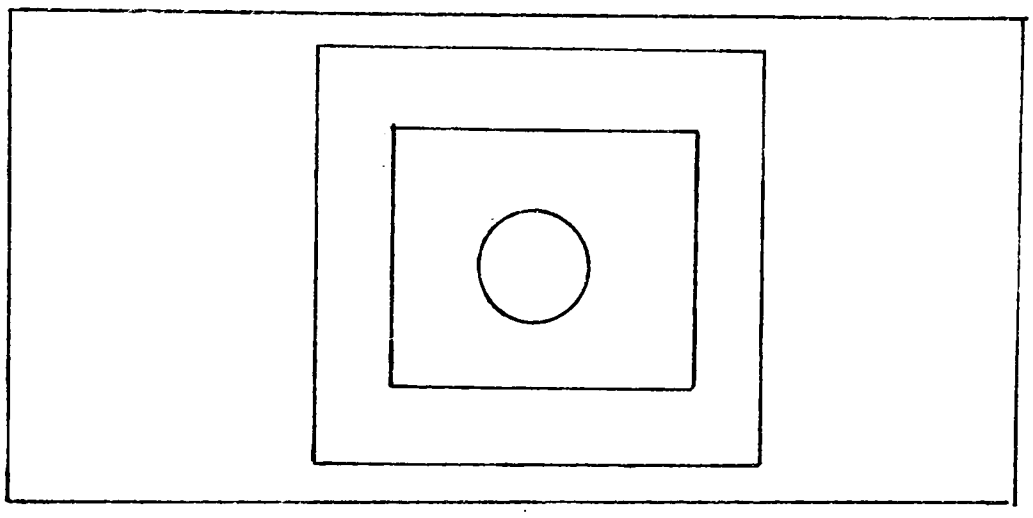


FIG. III. 6. Perspex insulating box. (top view)
A moveable cover, with a hole for the objective lens, fits over a hole in the top.

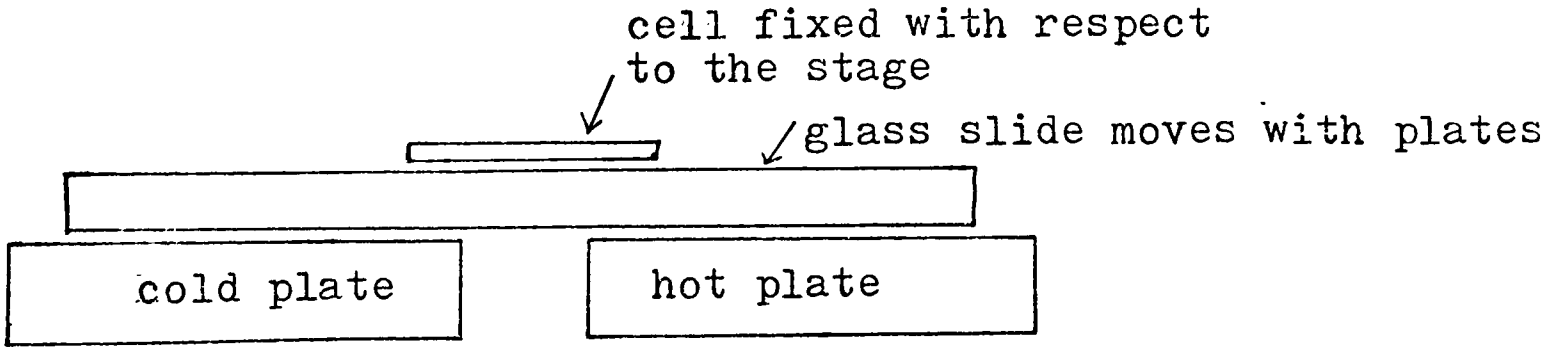


FIG. III. 7. Glass slide on heating plates

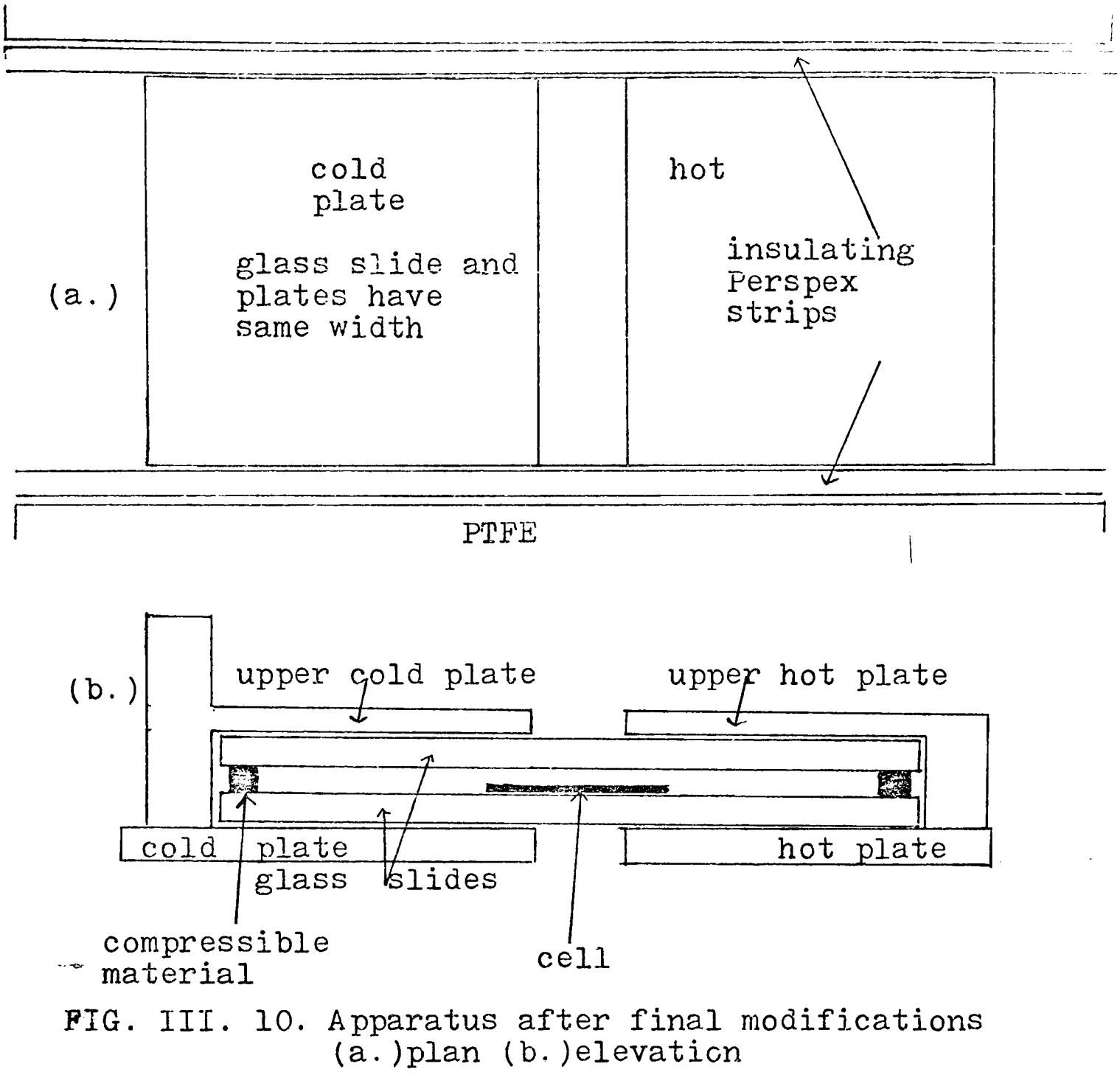


FIG. III. 10. Apparatus after final modifications
(a.)plan (b.)elevation

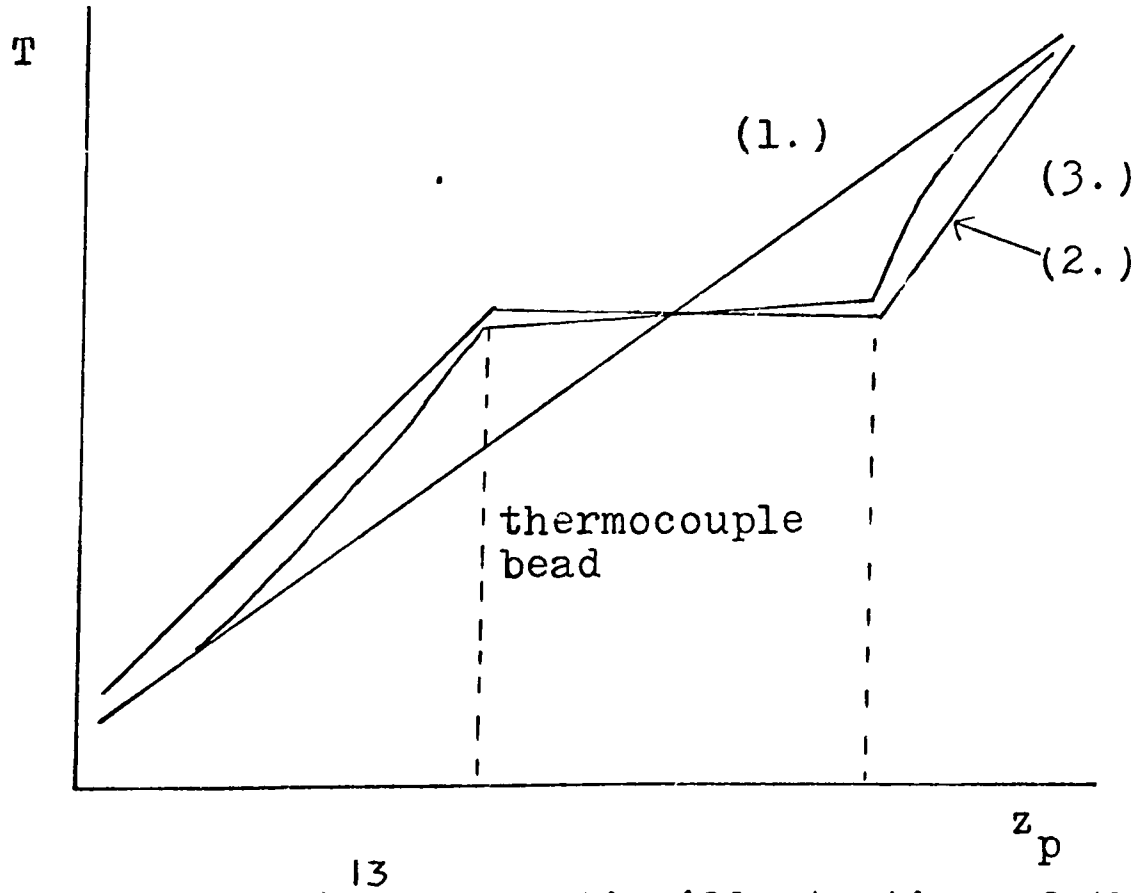
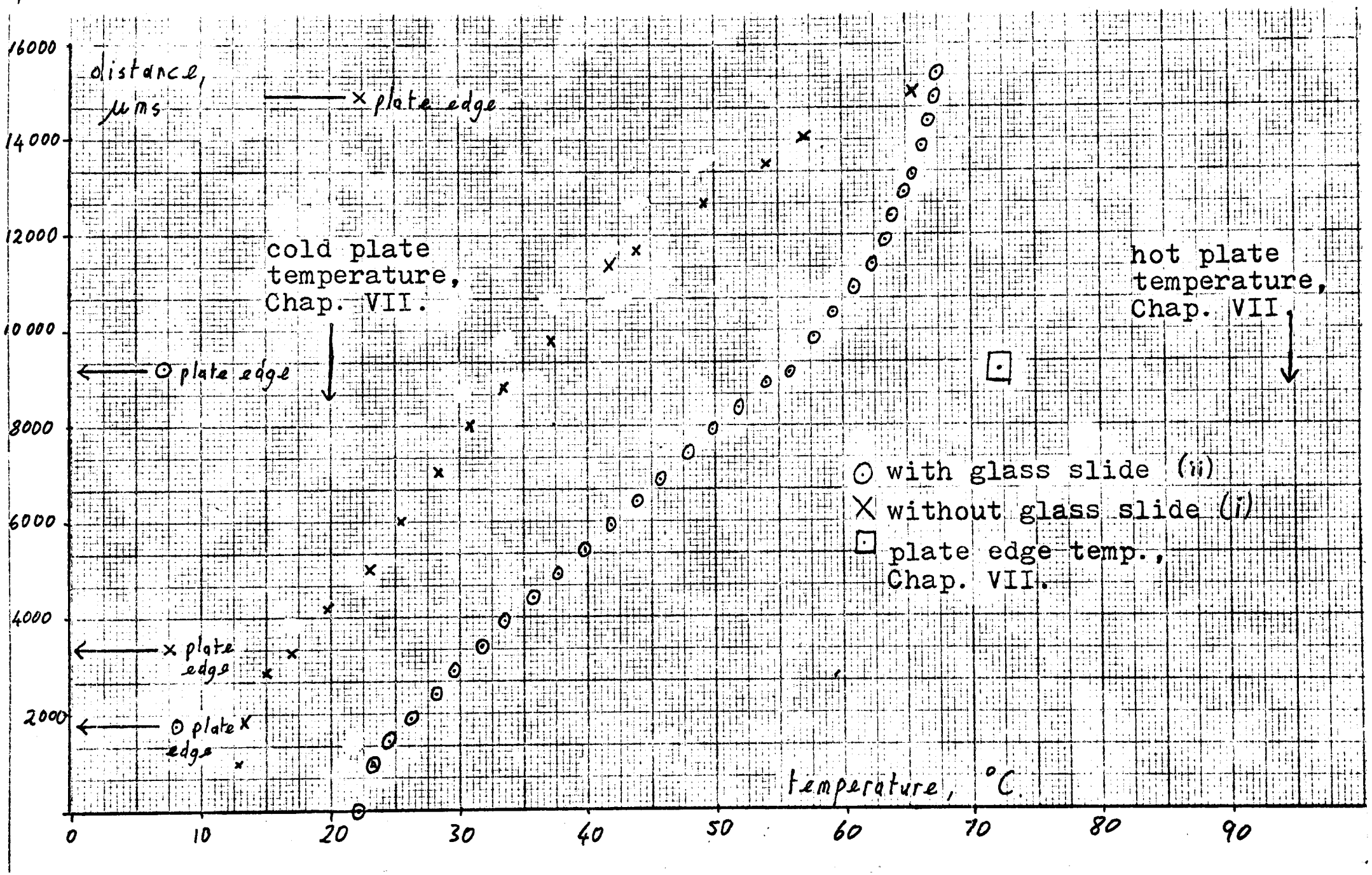


FIG. III. 13. Schematic illustration of thermal field (1.)in glass slide alone (2.) in cell with thermocouple alone (3.)in apparatus with the cell resting on the slide, temperature then being measured in the cell.

FIG. III. 11. Temperature field measurements in cells.



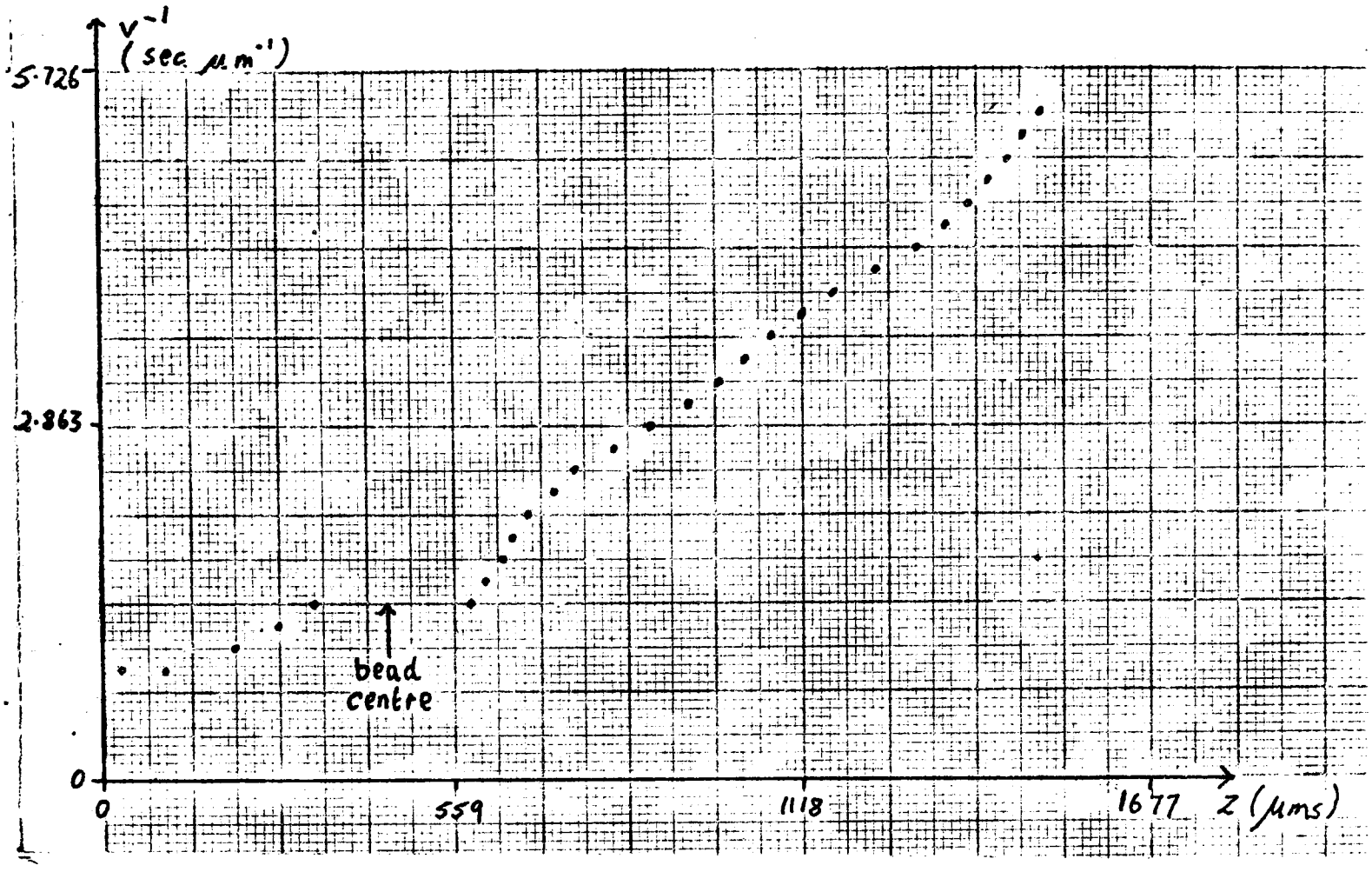


FIG. III. 12. TGZM in a cell containing a thermocouple.

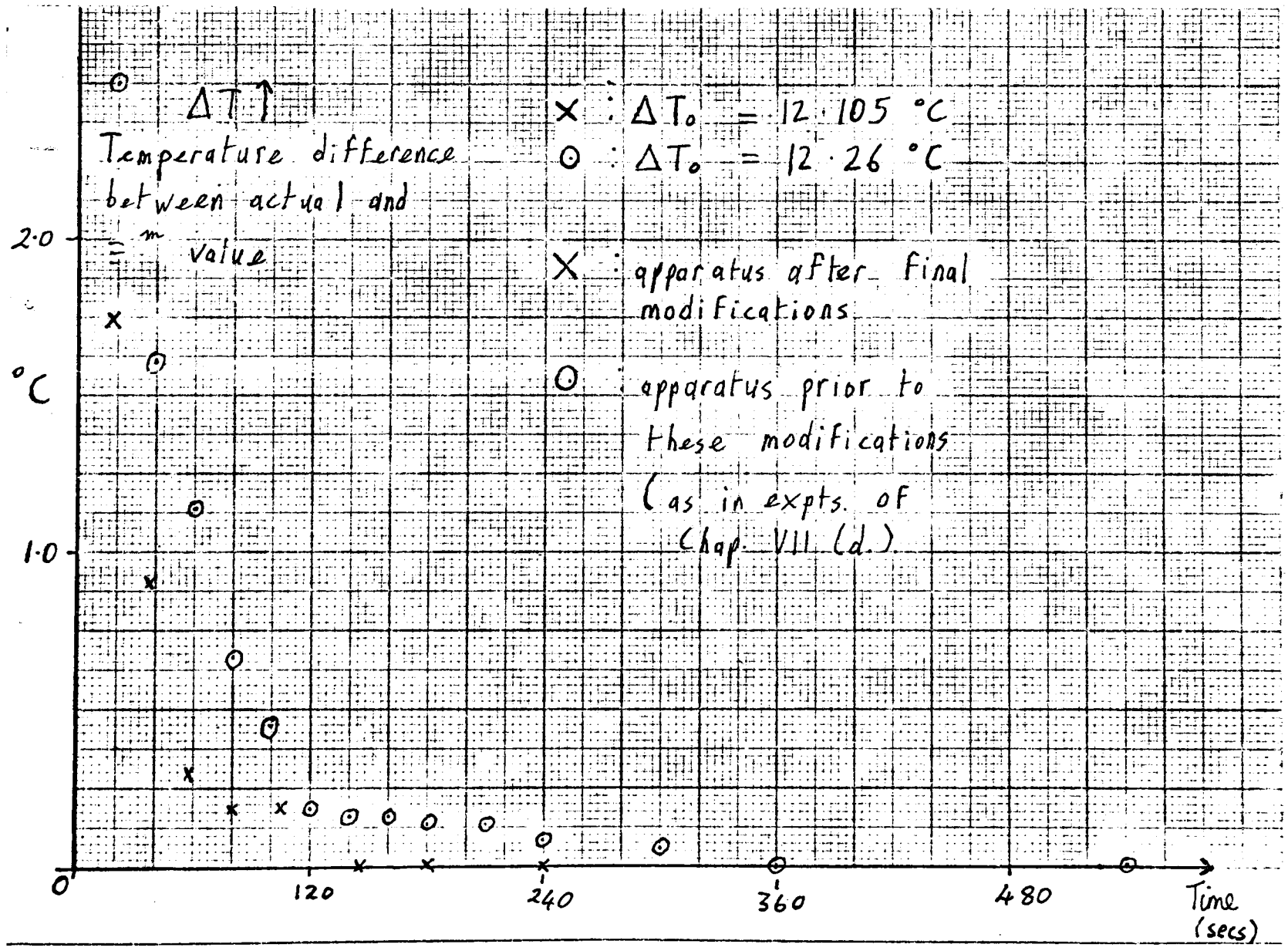


FIG. III. 14. Thermal re - equilibration results.

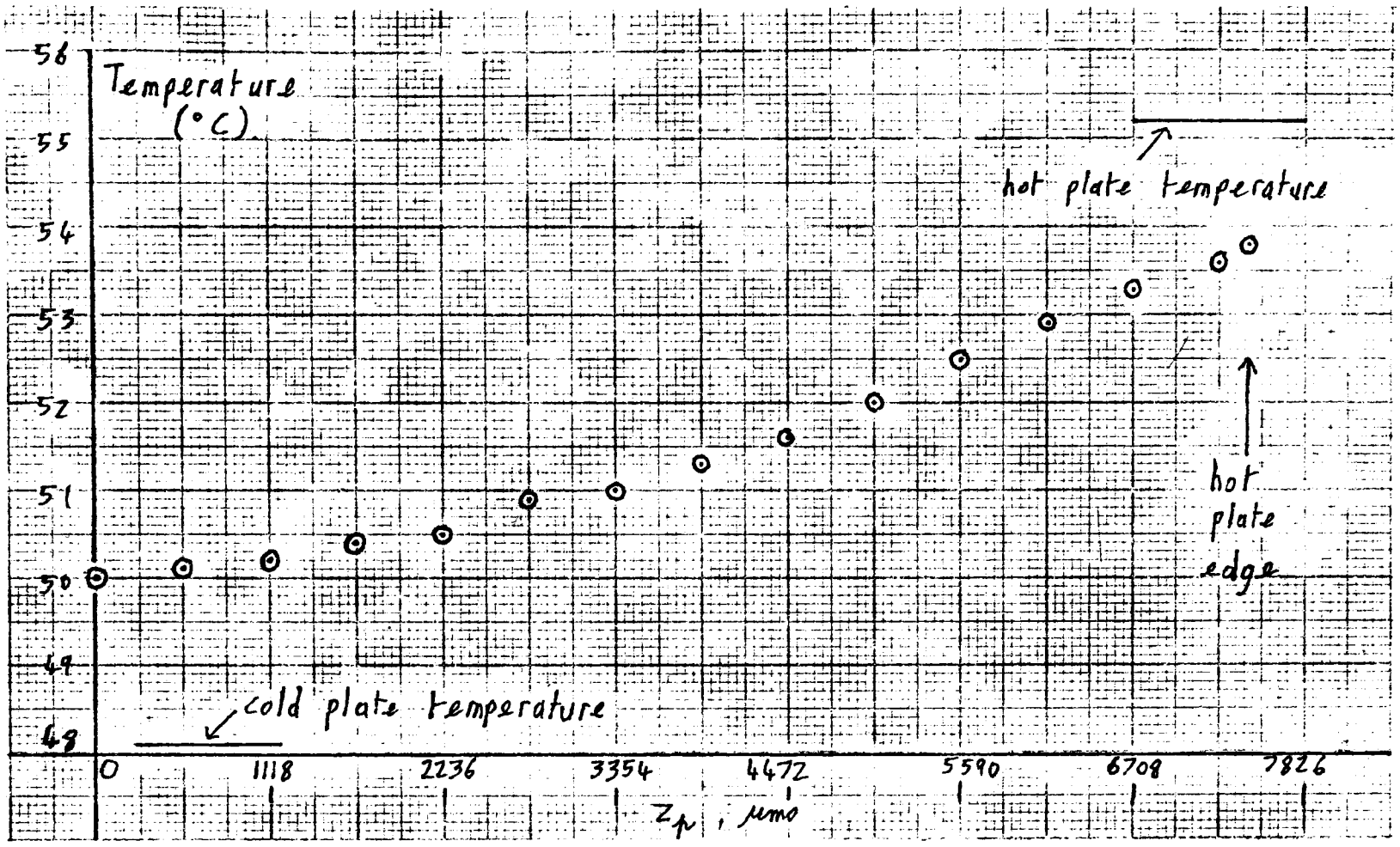


FIG. III. 15. Thermal field results on final apparatus.

Chapter IV. Dendritic Growth

This chapter covers experimental work on dendritic growth shapes, tip temperatures and spacings in thin specimen cells, with a theoretical interpretation and discussion of a simplifying notation for solidification in a temperature gradient. The following literature survey relates to the effects of convection and the container surface on dendritic growth, and the "minimum undercooling" assumption.

(a) Literature Survey

In cubic crystals, <100> is the preferred dendritic growth direction,[81,207] although cells deviate towards the heat flow direction (e.g. Sharp and Hellawell[246]) and dendrites deviate upstream when fluid flow occurs (e.g. Okamoto et al.[116]). Ross[218] showed that deviations from <100> also occur in thin cells. He observed "misoriented" dendrites in which secondary arms formed very near the primary tip and grew at about 45° to the primary growth direction. While "normal" dendrites also produced secondary arms at less than 90° to the primary growth direction during slow growth, secondary arms from such grains always became orthogonal during rapid growth. One of Ross's photographs of rapid dendritic growth in CBr_4 - 9 wt.% borneol (his plate (17)) is noteworthy:

four separate primary growth directions existed in the same grain as sketched in Fig. IV.1. Ross concluded that "misoriented" dendrites occurred in grains without a <100> direction in the plane of the cell, so that constrained off-<100> growth occurred. Morris and Winegard[237] observed similar "misoriented" dendrites in succinonitrile-camphor, and argued that since the primary tip radius oscillated in magnitude during secondary arm formation, "steady-state" dendritic growth theories were not valid. However, Blodgett et al[214](who studied camphene-cyclohexanol) confirmed Ross's findings that not all primary arms behaved in this way. The author[1] noted that secondary arms in "normal" dendrites formed well back from the primary tip, causing little or no oscillation in its shape. The author also identified secondary arms in misoriented dendrites as 100 directions on the basis of their prominence and growth at $\sim 90^{o}$ to each other, but this conclusion is shown to be incorrect in the present work. Kahlweit,[247] studying NH_4Cl-water in which non-faceted dendritic growth occurs,[216] observed a variety of growth forms in thin cells which he identified with varying undercoolings. "<100>" dendrites, similar to "normal" dendrites, appeared at the lowest undercoolings: then came "<110>" dendrites, similar to "misoriented" dendrites. Kahlweit did not state how these orientations were determined, and it seems probable that guesses based on symmetry arguments were used as in the author's earlier work. At greater undercoolings, repeated primary

tip splitting was observed and finally "<111>" dendrites appeared, with threefold symmetry and discontinuously higher growth rates. Kahlweit used semi-quantitative interface stability arguments to explain the variations of morphology with undercooling on the basis of anisotropic surface energy and interface kinetics with the latter becoming more important at high growth rates. He did not discuss the possibilities of oriented nucleation or of development of preferred orientation during growth. Hunt[248] noted that surface-nucleated grains in cyclohexanol did have a fixed orientation with respect to the surface, and that the types of grains nucleated depended on surface cleanness and growth conditions. Bower and Flemings[249] studied primary arm orientations at a chill surface in an aluminium casting, using the Laue X-ray back reflection technique to determine crystallographic orientations. They concluded that off-<100> growth occurred, with primary arms either representing projected <100> directions onto the plane of the chill surface, or intersections of {100} planes with the chill surface. This implies that when dendrites are forced to grow off-<100> , they either deviate through the minimum possible angle from <100> ("projections"), or else are restricted to a greater angle of deviation by being required to grow on a direction in a {100} plane ("intersections"). The apparent uncertainty in preferred growth direction on a surface seems surprising. It may be that, in the case of "intersections", what appeared to be primary arms were actually solid plates on {100} planes formed by

coalescence during the later stages of solidification.

Experiments on the influence of fluid flow on primary dendrite spacing have produced conflicting results. Bardsley et al[184] observed a "spiral arm" pattern of cells on the interface of a Czochralski-grown germanium crystal, caused by crystal rotation. Sharp and Hellawell[250] found that Al-Cu specimens grown downwards had similar primary spacings to those grown upwards under similar conditions and suggested that convection only affects the spacing when the diffusion-dominated layer[28] is reduced below the cell spacing. Verhoeven [251] found that mechanical stirring ahead of the primary tips left spacings unchanged for high G ($\sim 50^{\circ}C/cm$), but caused dendrite clustering with primary spacing reduced by a factor of two or three for low G (~ 3-$15^{\circ}C/cm$). He suggested that fluid flow penetrated the dendrite tip region only in the latter case, where the primary spacing was initially greater. Okamoto et al,[116] however, found that forced fluid flow along the growth front in thin specimen cells of cyclohexanol removed the normal dependence of λ_1 on G and R, and increased λ_1 from 50-150 μms without flow to ~400μms with fluid flow. Hämäläinen[252] suggested that arrays of growing cells (in the usual sense) were associated with convection cells in the bulk liquid. Tassa and Hunt[48] argued that fluid flow played a part in determining the transition between dendritic and lamellar eutectic growth.

Very recently, Burden and Hunt[217] observed λ_1 an order of magnitude higher in downward than in upward dendritic growth of ammonium chloride in water under otherwise similar growth conditions. They argued that, as primary arm spacing adjusted to the extent of neighbouring

radial diffusion fields, and convection carried the light, pure water rejected by the NH_4Cl dendrites upwards, the radial field width and λ_1 were reduced in upward growth but increased during downward growth by convection.

Several workers have carried out experimental tests of the minimum undercooling criterion for dendritic growth. Undercooling theories have been shown to agree quite well with measured dendrite tip temperatures when growth at the minimum undercooling is assumed in some[51,48] but not all[253] cases. However, the more direct approach of comparing observed and predicted tip radii has proved less successful. Burden[38](his table 2), Jin and Purdy,[40,253] and Edvardsson et al[114] all found measured tip radii from quenched speciments exceeding those predicted for minimum undercooling, by factors of about ten and one hundred respectively in the first two experiments listed. Ross,[218] who used in situ observations on organics, found that primary tip radii obeyed the relationships ($r \propto R^{-\frac{1}{2}} c_o^{-\frac{1}{2}} G^o$) predicted by the minimum undercooling principle and Zener's[45] theory. Thus, measured radii equalled the predicted radii or some constant multiple of these: in the absence of surface energy or diffusion data, Ross was unable to apply a more quantitative test.

(b) Dendritic Morphology in Thin Cells

(1) succinonitrile alloys

The first point to be established was the contact angle between solid organic, liquid organic, and the glass cell walls. Experiments using fine-bore glass tubes inserted into cells showed that liquid succinonitrile

wetted the glass surface. Dendrites grew close to one side of a glass tube, as shown in Plate 3, but without touching the glass. On emergence from the tube end, dendrites changed their growth direction, showing that the glass surface had constrained the dendrites to grow away from their most favoured direction.

As the specimen cell thickness was very small by comparison with dendritic growth distances, only a grain with a <100> exactly parallel to the cell sides could provide primary arms growing along the centre of the cell thickness. In practice, primary arms invariably grew towards one or other of the cell walls and then along the wall (Fig. IV.2), as shown by fine-focusing (chapter III (f)), on the chosen dendrite and on dust particles on the inside cell walls. Base-growing primary arms, when photographed, generally have upward-growing secondary arms above the plane of focus and therefore (chapter III (g)) with outer bright rings (e.g. Plate 17). The reverse applies to top-growing primaries whose secondary arms have outer dark outlines (e.g. Plate 16). Studies on succinonitrile-0-20 wt.% CBr_4 alloys showed that basic growth morphologies depended largely on grain orientation relative to the cell walls, and that four different classes of behaviour could be distinguished. Our coordinate system is defined in Fig. IV.3: the cell plane is x-z, with horizontal temperature gradient along the z axis. ↙ *Insert paragraph opposite.*

Type 2 grains also produced one "normal" primary arm, but with four sidearms visible, probably at angles of 90^{o} to each other but none exactly in the x or y directions (e.g. Plate 4). All four sidearms thus appeared because

none was growing directly into the nearest wall. If the sidearms here and in type 1 are ⟨100⟩ directions, this implies that there is now no ⟨100⟩ direction orthogonal to the "normal" arm which lies in or near to the x-z plane, unlike the previous case. When the cell was rotated and re-solidified, the original "normal" growth direction persisted to more than 45° away from the z direction, growing ahead of a bunch of roughly orthogonal sidearms (Plate 5). Suddenly and unpredictably, a "misoriented" primary arm would appear from this bunch of sidearms, at roughly 90° to the original "normal" primary. This "misoriented" growth form, as discussed in section (a), was a constant and definite growth direction characterized by non-orthogonal sidearms forming at the primary tip. It grew at a slightly lower temperature (perhaps 0.1 - 0.2°C) than a "normal" arm, and so the "normal" arm persisted as the primary growth direction at more than 45° away from the z direction. Type 3 grains were similar to type 2 but with two distinct "misoriented" directions, one top-growth and one base-growth, each between about 70°-110° from the "normal" direction and at about 15-30° to each other in the view plane, Plate 6. The structure of a "misoriented" primary arm, shown in Plate 7, is of one vertical and two horizontal sidearms, the former leaning along the z direction. We may thus identify "misoriented" dendrites as the projections of ⟨100⟩ directions into the x-z plane when the ⟨100⟩ is not close to the x-z plane. Their vertical sidearms are presumably also ⟨100⟩ types, at 90° to that ⟨100⟩ which generated the "misoriented" primary. The horizontal sidearms, however, cannot be ⟨100⟩ as suggested in ref. 1. It is

not obvious why these sidearms grow at about 45° to the "misoriented" primary, when a ⟨100⟩ direction (that of the "normal" primary) is present at ~ 90° to the "misoriented" primary: work on CBr_4 described below illuminates the question. The sidearms may be ⟨110⟩ or ⟨111⟩. If the ⟨100⟩ providing the "normal" primary is close to the x-z plane, the other two ⟨100⟩ directions would yield virtually identical "misoriented" growth directions when projected into the x-z plane (Fig. IV.5 (a)). So, presumably, that which is closer to the x-z plane forms the "misoriented" primary in a type 2 grain. If the ⟨100⟩ providing the "normal" primary is somewhat further out of the x-z plane, the other two ⟨100⟩ directions can both provide "misoriented" primaries, at a sufficiently large angle to each other to allow independent existence, in a type 3 grain (Fig. IV.5 (b)).

Type 4 grains produced no primary arms of either type in any orientation. One such grain was solidified (not at steady state) and photographed for a variety of cell orientations, with a reference marker tape stuck to the top surface (e.g. Plate 8). From these photographs, prominent "secondary arm" directions were identified at angles 55°, 60° and 65° to each other (±5°) on photographs. Thus it appears that these grains were those with ⟨111⟩ close to the y direction so that no ⟨100⟩ was close enough to the x-z plane to form a primary arm. During steady-state solidification, although no "normal" or "misoriented" primary formed, a type of "split" primary could form (Fig. IV.6) in one of the strong growth directions provided that this

direction was not close to the z direction. This behaviour is not understood.

The above classification may not be exhaustive and some surprising transient effects must be noted. Particularly on initiation of solidification, transient "misoriented" forms could appear as shown in Plates 9 and 10. Similar structures appeared in secondary arms (Plate 11). Unlike the previous "misoriented" forms, these did not have a fixed growth direction (see Plate 9) and the sidearms appeared to be ⟨100⟩ (see Plate 10). For base-growing dendrites only, a confusing "double primary" structure sometimes appeared (Plate 12 and Fig. IV.7) where a tertiary arm grew strongly in the colder, upper part of the cell and supplanted the original primary, a consequence of the vertical temperature gradient. Sometimes, primary tips split in similar circumstances (Plates 13 and 14): it was not clear whether overgrowth caused splitting or vice versa. Plate 14 strongly resembles a feature in Fig. 13 of Young and Kirkwood,[64] who studied bulk Al-Cu, suggesting that tip splitting does not only occur in thin cells.

(2) CBr_4 alloys

Studies of CBr_4 and of CBr_4-8½ wt.% borneol revealed qualitatively different behaviour to the succinonitrile alloys, despite the fact that all the alloys were cubic, non-faceting, and with ⟨100⟩ as principal growth direction. In CBr_4, tip shapes were much less like the paraboloidal shape suggested by theory[46] than tip shapes in succinonitrile (Fig. IV.8 and fig. 4 of Morris and Winegard[84]). The strong curvature at the tip itself suggests

anisotropic surface energy, with a minimum on 100 , and this was confirmed by observations of non-spherical liquid droplets with fourfold symmetry, the strongest curvature being on the same plane as the dendrite tip. "Misoriented" dendrites were observed only on one exceptional occasion, near a large air bubble and thus probably involving unusual vertical thermal gradients. When a "normal" primary had four sidearms which did not grow in the x-z plane as in the previous type 2 grains, the primary arm at 90° to this was also "normal", i.e. sidearms did not appear until some distance back from the primary tip. In the exceptional case, one such primary became "misoriented" on approaching the air bubble: its vertical sidearms grew strongly, appeared closer to the primary tip, and caused horizontal sidearms to appear close to the tip as well and become non-orthogonal.

This behaviour gives a guide to why "misoriented" dendrites have the shape they do. As the <100> from which the primary growth derives is at a considerable angle to the x-z plane, the vertical sidearm leans strongly forward along the z direction. (Fig. IV.9). Consequently, its solute field interferes with that of the primary tip, ensuring that the most rapid growth occurs to either side of the tip rather than at the tip itself. Consequently two horizontal secondary arms form. As these to some extent replace the primary tip, they do not initially grow orthogonally along the <100> directions. In some cases (Plate 15) their directions later alter to the <100>, though in other cases they do not (Plate 7). Presumably, the anisotropic surface energy

of CBr_4 in some way stabilizes against secondary arm formation near the primary tips and thus prevents "misoriented" forms, except when a high vertical gradient causes unusually strong vertical growth.

CBr_4-8½ wt.% borneol was found to behave quite differently. The alloy was studied because Ross's plate 17 (Fig. IV.1) indicated that some non-<100>, possibly <110> primary arms were formed. We were not able to reproduce this behaviour, but did find non-<100> primaries as shown in Fig. IV.10. These were somewhat similar to the transient structures of Plate 9, in that the sidearms corresponded to "normal" primary growth directions and thus appeared to be <100>. Unlike the transient structures, however, these were long-lasting primary arms, with a fixed growth direction, and able to grow millimetre-scale distances in competition with "normal" primaries from the same grain. (They grew at indistinguishably different tip temperatures from the "normal" arms but did tend to become overgrown after, say, 2 mms.) Their growth directions were not exactly intermediate between the "normal" growth directions, suggesting that they were not exact <110> directions.
The contrast with the behaviour of pure CBr_4 is remarkable. Clearly, co-operative growth of several "secondary" type arms near the primary tip is a common phenomenon. We may note that all Kahlweit's[247] structures except "<111>" dendrites have been observed here and satisfactorily ascribed to grain orientation effects, althouth the differences between different materials do indicate different anisotropies of surface energy and/or interface kinetics (and, perhaps,

dislocation behaviour - chapter VII (e)). Direct confirmation of grain orientation was sought using the X-ray transmission Laue technique, but only a few low-angle spots were obtained and so the films could not be indexed. Attempts to increase the thickness of diffracting material and reduce absorption, by using glancing incidence on the specimen cell and removing one of the glass walls, did not improve results. It is probable that the high temperature factor in these alloys due to molecular rotation[224] prevented strong reflections.[242]

(c) Dendrite Spacing

(1) fixed-plates stage

Primary dendrite spacings were measured as a function of growth velocity ($G \sim 50^{\circ}C/cm$, to $\pm 30\%$, remaining constant) in two sets of experiments. Results are shown in Table IV.1.(i).

Experiments on succinonitrile-9% CBr_4 were carried out by nucleating and studying two different grains within the same cell. The first was type 2 with primary arms of the "normal" type growing at the cell top: the second was type 1 with its primary arms growing at the cell base. All results refer to spacings within a single row of dendrites except the $R = 118.5\ \mu m/sec$ results where two rows of dendrites, one above the other with the lower row fitting between gaps in the upper row, were obtained. λ_1 then refers to spacings within either row. The rotation facility was always used to bring the growth direction parallel to G before a run.

In experiments on succinonitrile-12% CBr_4, only one type 1 grain was used and the cell was turned over in order to bring the dendrite growth position to the top and bottom

of the cell alternately. The order of successive runs showed that any systematic variation e.g. due to macrosegregation was slight, and was designed to minimize the effect of such a systematic variation on the comparison of top and base runs.

Taking $D_L \sim 3 \times 10^{-6}$ cm^2/sec (chap. VII.(a)), the parameter(D_L/R) was at most 0.2 mms so that initial transient effects should have been completed after a distance $(D_L/kR) \sim 2$ mms *approximately*.[26] Nevertheless, there was a general tendency of λ_1 to continue increasing throughout longer periods of growth, especially in cellular structures. In run (13) of the 12% CBr_4 series, λ_1 was $\sim 55\,\mu$ms initially (planar interface breakdown), $\sim 83\,\mu$ms after 15 mins growth, $\sim 144\,\mu$ms after 60 mins and finally $\sim 202\,\mu$ms after 120 minutes. Thus, although measurements for corresponding top and base runs were taken after the same period of growth (at least in the 12% CBr_4 runs), the variation of λ_1 with growth time must be considered carefully when these results are interpreted.

Of the two sets of runs at 1.48 μm/sec, in which a branched cell morphology was obtained, the former (runs 11 and 12) were performed with only a Perspex shield resting on the cell for insulation. While velocity variations due to draughts were not large, there was a tendency for λ_1 to decrease by cell tip splitting or by promotion of secondaries to the growth front (these processes being almost indistinguishable with this morphology), counteracting the general tendency for arms to be overgrown thus increasing λ_1. It was considered that thermal fluctuations might cause tip splitting and

so runs 13 and 14 were performed with the whole microscope carefully draught-shielded. Less tip splitting was observed and final λ_1 was significantly higher.

It is clear from the table that λ_1 was smaller in top growth than in base growth. This is discussed later. We define:

$$\Delta = \left(\frac{\lambda_1(\text{base}) - \lambda_1(\text{top})}{\lambda_1(\text{base})}\right) \times 100, \% \qquad (1)$$

for given R and alloy composition. Besides this difference, it was clear that growth on the cell top was much less "dendritic" (i.e. shorter secondary arms) than growth at the base for the same R. This is shown in Plates 18-19.

Initial secondary arm spacings were also measured in 9% CBr_4 runs. These also appear in Table IV.1 (i). There was some indication that initial λ_2 was higher, in a given run, for the primary arms growing at lower λ_1. (As shown in the upper table, there was considerable variation in λ_1 in any given run.) However, differences between top and base do not seem significant.

(2) <u>moving-plates stage</u>

A few experiments were performed with this stage, in which the vertical gradient is smaller and in the opposite sense (Table IV.1.(ii)). One cell was used for succinonitrile-15 wt.% CBr_4 studies while another was used for succinonitrile 7 wt.% camphor. In each case a normal primary was selected, growing within 5° of the horizontal G direction, and the cell was turned over and re-solidified to obtain λ_1 for top and base growth.

(d) Dendrite Growth Temperature

Dendrite primary tip temperature during steady-state growth in nominally pure succinonitrile was measured in a single thermocouple cell repeatedly solidified and re-melted. Results are given in Table IV.2, together with the order in which runs were carried out. The cell condition appeared to be unaffected by thermal degradation until run 10, when a large air bubble appeared during the long solidification time ($\sim$ 10 hours) required for this slow growth run. The result of this run is therefore dubious. The cell was then re-filled with succinonitrile for runs 11 and 12. The interface was apparently planar in slow growth runs but, as the liquid wets the glass walls which are $\sim 125\ \mu$ms apart, it might be more appropriate to consider such morphologies as two-dimensional cells. The term "ripples" in the table refers to an almost "planar" interface with gentle, nearly sinusoidal shape undulations of period $\sim 100\ \mu$ms. In run 7, the solid deposited in run 6 was remelted at steady state. Melting interface temperatures were similar when dendritically grown material was remelted although there was some indication of increased melting temperatures, up to 57°C, for fast remelting rates.

Tip temperatures could not simply be determined when interfaces reached the thermocouple bead, because of the local distorsion of the thermal field by the thermocouple, and because the bead virtually blocked the cell, causing the dendrites to slow down in a type of terminal transient. So, as shown in Fig. IV.11, simultaneous measurements of bead temperature and interface position were made for a

period of time while the interface was far from the thermocouple. The position-time graph was then extrapolated to find the time when the interface would have reached the position of the bead centre, had its motion been unaffected by the thermocouple. The bead temperature at this time represented the interface temperature. In rapid growth runs, there was insufficient time to carry out this procedure. Instead, a run was performed in which interface position alone was measured as a function of time, to find out the time Δt on Fig. IV.11. Then a second run was made to find the bead temperature at the time when the interface met the bead, and this was corrected to give the steady-state dendrite tip temperature from a knowledge of G and Δt. The measurement error is estimated as $\pm 0.3^{\circ}C$ for the first technique, $\pm 0.5^{\circ}C$ for the second. There was also an error due to thermal field distorsion of $\sim \pm 0.3^{\circ}C$, and an error of $\sim 0.2^{\circ}C$ due to the heating effect of illumination on the thermocouple (chap. III. (f)). (Maximum illumination was never used in this or any other observational experiments, although it was used in photography.) So the overall accuracy was, at worst, to $\pm 1.0^{\circ}C$: internal self-consistency suggests considerably better accuracy than this, as the graph (Fig. IV.12) shows.

Two methods were used to obtain the liquidus temperature of nominally pure succinonitrile alloy. Run 7 should have given an accurate melting interface temperature if the solid deposited in run 6 was homogeneous and if the melting interface was truly planar[25] (as it appeared to be in the microscope viewfield.) In view of these doubts, specimens

were frozen dendritically from one glass wall upwards (by contact with a cold surface) and then remelted on the isothermal stage (chap. II.(f)) in thermocouple cells until the last solid in contact with the bead remelted. This procedure should have avoided macrosegregation and obtained the liquidus temperature: the result was 55.5°C ±0.2°C (averaged), in reasonable agreement with the melting run. We take 55.6°C as an average value.

(e) Solidification in A Temperature Gradient

In this section we introduce a dimensionless parameter which has wide application in simplifying the presentation of theories of solidification and thus illuminating the interconnections between them. We define:

$$Q = \frac{-(1 - k)}{k} \frac{mc_0R}{D_LG} \qquad (2)$$

which is positive (since m is negative): c_0 (alloy composition) and the other parameters have their usual meanings. Parts of this work appeared in ref. 1 (where the notation was slightly different.) The applications are:

(i) interface stability[1]

According to constitutional supercooling theory, (I.18):

$$Q < 1 \qquad (3)$$

for stability. For the case of negligible latent heat and surface energy effects and $K_S = K_L$, perturbation analysis[31] obtains the same result.

(ii) <u>differential migration in dendritic solidification</u> (chap. VIII.(e)).

According to ref. 1:

$$\frac{\lambda_{2f}}{\lambda_{2i}} = \frac{kQ}{kQ - 1} \tag{4}$$

where λ_{2i}, λ_{2f} are initial, final values of spacing between two specific secondary arms neither of which melts off during solidification. According to the revised treatment of chap. VIII.(e) allowing for a dendrite growth undercooling:

(VIII.34)

$$\frac{\lambda_{2f}}{\lambda_{2i}} = \frac{k(Q - 1) + 1}{k(Q - 1)}$$

(iii) <u>TGZM and crystal growth</u> (chap. VIII.(d))

Assuming local equilibrium and planar growth, it is possible for some droplets to migrate faster than the crystal grows when (equation (VIII .27)):

$$Q < 1 \tag{5}$$

(iv) <u>dendrite tip temperature - theory of Burden and Hunt</u>[51]

As discussed in section (f), Burden and Hunt predicted (their equation 17)[51]:

$$\Delta T = \frac{GD_L}{R} - \frac{mRr}{D_L}(1 - k)c_\infty + \frac{2\Theta}{r}c \tag{6}$$

where ΔT is undercooling below the liquidus temperature, r the dendrite tip radius, c_∞ the bulk liquid composition, and Θ_c is defined in (I.2). Now, if the Peclet number:

$$p = \frac{Rr}{2D_L} \tag{7}$$

and the equilibrium freezing range (liquidus temperature minus solidus temperature):

$$\Delta T_0 = -mc_\infty \frac{(1 - k)}{k} \tag{8}$$

then (IV.6) may be rewritten:

$$\Delta T = \Delta T_0 \left(\frac{1}{Q} + 2kp\right) + \frac{2\Theta}{r} c \tag{9}$$

The first term in the brackets is the "plane wave" undercooling and the second is the "radial" diffusion undercooling, while $\Delta T_c = 2\Theta_c/r$ is curvature undercooling. If the minimum undercooling assumption applies, the "radial" undercooling equals the curvature undercooling (at least in the simple[45,51] theory). So:

$$\Delta T = \Delta T_0 \left(\frac{1}{Q} + 4kp\right) \tag{10}$$

in this case.

(v) <u>cellular microsegregation - theory of Flemings</u>[59]

As noted in chapter II.(a) (4), Flemings derived an expression for cellular microsegregation as an extension of theory similar to that of Burden and Hunt,[51] but neglecting the "radial" term. His result was:

$$c_S^* = kc_\infty \left[\frac{a}{k-1} + \left(1 - \frac{ak}{k-1}\right)(1 - f_s)^{(k-1)} \right] \qquad (11)$$

where:

$$a = + \frac{D_L G}{mRc_\infty} \qquad (12)$$

is a negative dimensionless parameter. (The book[159] erroneously defines a as a positive quantity (Flemings' (3 - 12)) but the paper[49] and the other equations in the book use negative a.) Equation (IV.11) becomes:

$$c_S^* = kc_\infty \left[\frac{1}{kQ} + \left(1 - \frac{1}{Q}\right)(1 - f_s)^{(k-1)} \right] \qquad (13)$$

in our notation.

(f) Discussion

The results suggest that dendritic λ_1 increases as R decreases, but that λ_1 decreases again as R falls further and cellular structures are formed. The former result has often been observed[55]: the latter has been obtained once,[52] but most work suggests that λ_1 continues increasing as R falls in the cellular region. It seems likely that our result is an artefact due to the prolonged relaxation towards a steady-state spacing in cell structures. Thermal instability may also play a part in reducing cell spacings in experiments. As the spacing between any two existing cells or dendrites never appeared to vary, spacings changed only by overgrowth (increasing λ_1) and tip splitting or promotion of sidearms to the growth front (decreasing λ_1). These two

processes must produce a more or less dynamic equilibrium steady-state spacing. As overgrowth is a process occurring gradually over, say, 30 seconds,[1] while tip splitting is much more instantaneous, it seems likely that tip splitting is promoted by thermal fluctuations, and hence λ_1 is higher in a thermally stable system as indicated by the results.

The result that λ_1 is higher in the 9% than the 12% CBr_4 alloy is anomalous.[55] Composition control in cell preparation was of uncertain effectiveness, but as dendritic growth persisted to lower R in the "12%" alloy it seems clear that the impurity content was genuinely higher in the "12%" than the "9%" alloy. It may be that λ_1 depends on cell thickness in this apparatus, and that the two cells used were of different thickness. The jump in λ_1 in the 118.5 μm/sec result, when a second row of dendrites appeared, is notable. It suggests that λ_1 is made artificially small when only one row of primary arms is present, and this effect may depend on cell thickness.

The clearest and most interesting result is the difference in λ_1 between top and base growing primary arms. Nine comparisons between top and base growth consistently obtained λ_1(top) about 30% smaller than λ_1 (base) (Table IV.1 (i)), with average scatter $\pm$7%, in succinonitrile-CBr_4 alloys. This effect appeared to be independent of R and unaltered by the slightly different type of primary arm at top and base in the 9% case. Two explanations appeared possible from the fixed-plates stage results. Firstly,

convection might have aided solute transport away from top-growing primary arms but not from base-growing arms, since the densities of succinonitrile and CBr_4 are 1.023 and 3.345 gm/cc respectively.[228] Therefore the diffusion field and primary spacing would be expected to be reduced in top-growing primaries. Secondly, because of the considerable positive vertical gradient, the vertical secondary arms from base-growing primaries would be expected to grow much more strongly than those from top-growing primaries, increasing the diffusion field and λ_1 in the former case. Plates 16 and 17 show that the vertical secondaries are indeed more extensive in base-growing primaries. To show which of these explanations is correct, the experiments of Table IV.1 (ii) were performed. Despite the reversal of the vertical temperature gradient, Δ in the CBr_4 alloy was apparently unaltered. However, experiments with camphor as solute (density = 0.981 gm/cc,[228] marginally lower than for succinonitrile) produced λ_1 (top) about 15% larger than λ_1 (base). These results indicate that the convection analysis is correct and that the vertical gradient has little or no effect. It seems surprising that convection is so important in the camphor alloy, where Δ is roughly half what it is for CBr_4 (and of opposite sign), though the density difference between succinonitrile and camphor is only about one-fiftieth of the density difference between succinonitrile and CBr_4. Closely parallel results were obtained by Hebditch and Hunt,[255] who found considerable convective macrosegregation in Pb-Sn alloys (high density difference) but also significant convective macrosegregation in Sn-Zn

(very low density difference). It may be that the establishment of convection cells is more important than the potential driving force for convection.

(2) Dendrite Growth Temperature

Our results will be compared to the Burden and Hunt[51] theory of cell and dendrite growth. Burden and Hunt treated the diffusion field as two superposed fields, a "radial" field at the dendrite tips identical to that occurring in isothermal dendritic growth[45,21] and a "plane wave" field introduced by the temperature gradient (Fig. IV.14). This latter field was calculated by matching the composition gradient in the mushy zone ($\partial c_L/\partial z \sim G/m$) to an exponential diffusion field ahead of the growth front. The undercooling attributable to this "plane wave" field was given by the first term in (IV.6) and (IV.9). As shown by (IV.9), when $Q \rightarrow 1$ (critical condition for planar-cell breakdown in constitutional supercooling theory), since $r \rightarrow \infty$, $\Delta T \rightarrow \Delta T_0$. Thus a planar interface grows at the solidus temperature and, if the radial field is negligible, the undercooling varies as Q^{-1} (or as R^{-1} in our experiments). Fig. IV.13 shows that measured undercooling does indeed vary as R^{-1} but does not fall to zero as R^{-1} goes to zero. Instead, dendrite tip undercooling never falls below 2.7°C which is much larger than the calculated uncertainty of $\pm$1.0°C in the results. There is also a considerable difference between results before and after cell re-filling. Run 11 was in fact very close to the planar-cell breakdown condition, so that although the

equilibrium freezing range was almost unaffected by re-filling ($7.5^{o}C$ before, about $6.7^{o}C$ after), the planar breakdown velocity was greatly altered ($\sim 0.6\,\mu m/sec$ before re-filling, $\sim 1.5\,\mu m/sec$ after). Taking, from (IV.6):

$$D_L = \frac{\Delta T_o . R_{crit}}{G} \qquad (14)$$

where R_{crit} is planar breakdown velocity, D_L is determined as 7.5×10^{-6} cm^2/sec (before re-fill), 2.7×10^{-6} cm^2/sec (after re-fill) if $G \sim 60^{o}C/cm$. Making a correction for increased G and reduced velocity normal to the interface because of the vertical gradient, these figures are reduced to $\sim 6.5 \times 10^{-6}$ cm^2/sec and $\sim 2.3 \times 10^{-6}$ cm^2/sec respectively. The discrepancy is unexplained but the agreement with $D_L \sim 3 \times 10^{-6}$ cm^2/sec from TGZM data (chap. VII.(a)) is fair.

The TGZM data also suggest a pure material melting point for succinonitrile which is very close to the alloy liquidus temperature, indicating low k. If k = 0.1 and $-m = 5^{o}C/wt.\%$, (IV.8) gives impurity content $c_\infty \sim 0.2$ wt.% for $\Delta T_o = 7.5^{o}C$. This is an entirely plausible result and so the large freezing range observed here must be regarded as reasonable. The high undercoolings at high R are less easily explained. Equation (IV.9) shows that high undercoolings would be found if the Peclet number were not small by comparison with unity. This seems to have occurred in the experiments of Jin and Purdy,[40,253] where ΔT was $\sim \frac{2}{3} \Delta T_o$ at high R. Unfortunately, tip radius was not

measured in this work. The experiments of Ross[218] (see section (a)) will be used as a guide. Since these experiments were performed, values for D_L (chap. VII.(a)) and σ[229] have been obtained and so we may also test the minimum undercooling criterion quantitatively. Taking $D_L \sim 3 \times 10^{-6}$ cm^2/sec, the Peclet number p is found to be 0.056 for succinonitrile-13.5 wt.% CBr_4, 0.125 for succinonitrile-2.2 wt.% CBr_4. This suggests the possibility of higher p in nominally pure succinonitrile so that our undercooling results seem plausible. Taking $k \sim 0.2$, $m \sim 0.6^{\circ}C$/wt.% in succinonitrile-CBr_4,[218] and using the Zener[45] formula:

$$r_{min} = \left(\frac{2\Theta_c D_L}{mRc_\infty (1 - k)}\right)^{\frac{1}{2}} \qquad (15)$$

for the tip radius at minimum undercooling, we calculate $r_{min} = 2.4\ \mu$ms for $c_\infty = 2.2$ wt.%, $R = 6\ \mu$m/sec. This compares with Ross's observed tip radius $r = 12.5\ \mu$ms for these conditions. As stated in section (a), Ross's results indicated a constant (r/r_{min}) and so our work has shown this ratio to be roughly equal to five. The importance of this comparison is that, unlike other comparisons reported in section (a), the observations were direct and tip radii could not have been enlarged by quenching artefacts. It is possible that errors in D_L, m and σ could have added up to a factor of five, but the indication is clearly against the proposition that dendrites grow at the minimum undercooling.

Table IV.1 Dendrite Spacing

(i) fixed-plate stage

Growth velocity R in μms/sec: spacing in μms. See text for definition of Δ. Plate spacing = 8.1 mms

Primary Spacing

	succinonitrile-9 wt.%CBr_4			succinonitrile-12 wt.%CBr_4		
R	top λ_1	base λ_1	Δ	top λ_1	base λ_1	Δ
1.48	-	-		125 (14)	202 (13)	38
"	-	-		85 (12)	116 (11)	27
2.96	-	-		136±17 (8)	191±30 (7)	23
5.92	206±18 (3)	239±29 (5)	14	164±18 (5)	225±30 (6)	27
11.85	164±50 (2)	254±55 (6)	35	147±10 (4)	205±26 (3)	23
"	-	-		153 (9)	184 (10)	
29.62	127±21 (1)	201±49 (7)	35	-	-	
59.25	122±15 (4)	174±3 (8)	30	112±31 (2)	138±21 (1)	26
118.5	142±2 (9)	-		-	-	

The numbers in brackets denote the order in which the experiments were carried out.

Secondary Spacing

R	top λ_2	base λ_2
5.92	43.0	37.6
11.85	21.2	20.5
29.6	13.2	14.5
59.2	9.0	9.7

(9% CBr_4, from above runs: "top" and "base" refer to primary position).

(ii) moving-plates stage

Horizontal G $\sim 43^{\circ}C/cm \pm 5\%$

Vertical G (stationary cell) $\sim -2^{\circ}C/cm$, from TGZM studies (upper plates covered with asbestos paper)

$\therefore$ vertical G $\sim -7^{\circ}C/cm$ for R = 7.85 μm/sec

$\sim -4^{\circ}C/cm$ for R = 3.0 μm/sec

(see chap. III (f).)

Plate spacing = 7.27 mms

(a) succinonitrile - 15 wt.% CBr_4. R = 3.0 μm/sec.

λ_1 (base) = 400 μms $\pm$ 91: λ_1 (top) = 265 μms $\pm$ 54, so Δ = 34%. Both measurements after 15 mins growth.

(b) succinonitrile - 7 wt.% camphor. R = 7.85 μm/sec.

λ_1 (base) = 230 μms after 4 mins. growth, 254 μms after 10 mins growth.

λ_1 (top) = 260 μms after 5 mins growth, 314 μms after 12 mins growth

$\therefore$ Δ(4 - 5 mins) $\sim -11\%$

Δ(10 - 12 mins) $\sim -18\%$

Table IV.2 Dendrite Tip Temperature

Runs (in order:)	1	2	3	4	5
Growth Velocity (μms/sec):	3.6	3.6	7.9	16.3	0.78
Dendrite Tip Temperature (^{o}C):	51.3	51.9	52.1	52.4	48.7
Growth Morphology:	branched cells	branched cells	dendrites	dendrites	ripples

Run	6	7	8	9	10	11	12
Velocity	0.52	1.6	47	109	0.25	1.6	3.6
Temperature	48.1	55.8	52.9	52.9	48.1	48.9	49.6
Morphology	"planar"	melting interface	dendrites	dendrites	"planar"	rippled	branched cells

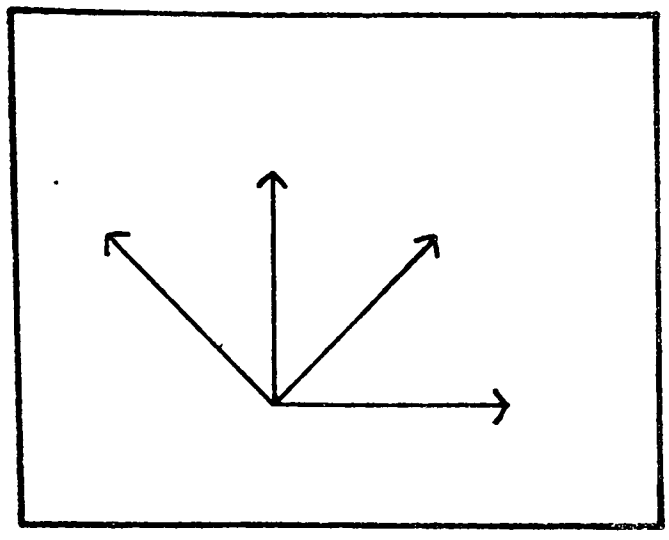


FIG. IV. 1. Growth directions in CBr_4 - borneol, from plate 17 of Ross (schematic).

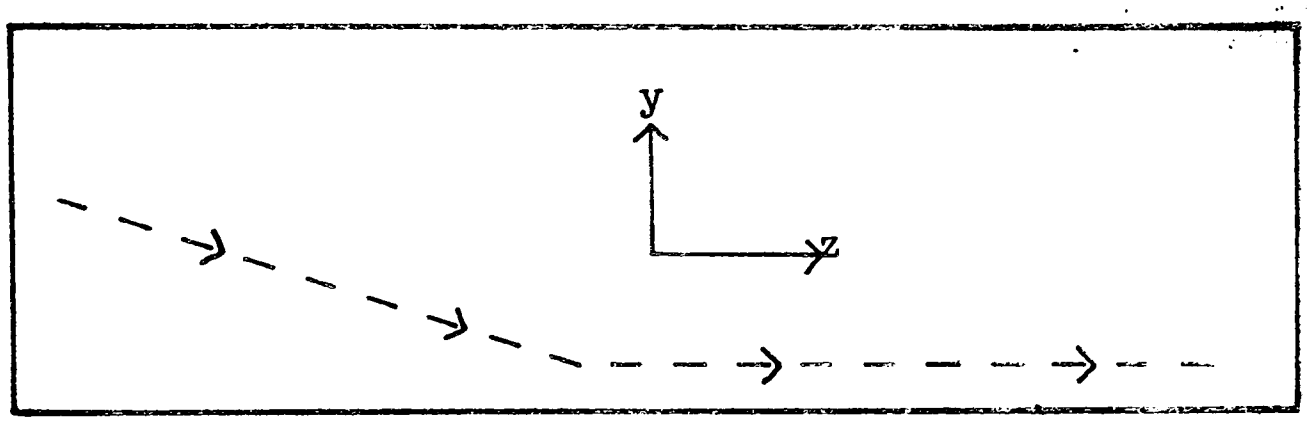


FIG. IV. 2. Showing why primary arms grow along specimen cell walls.

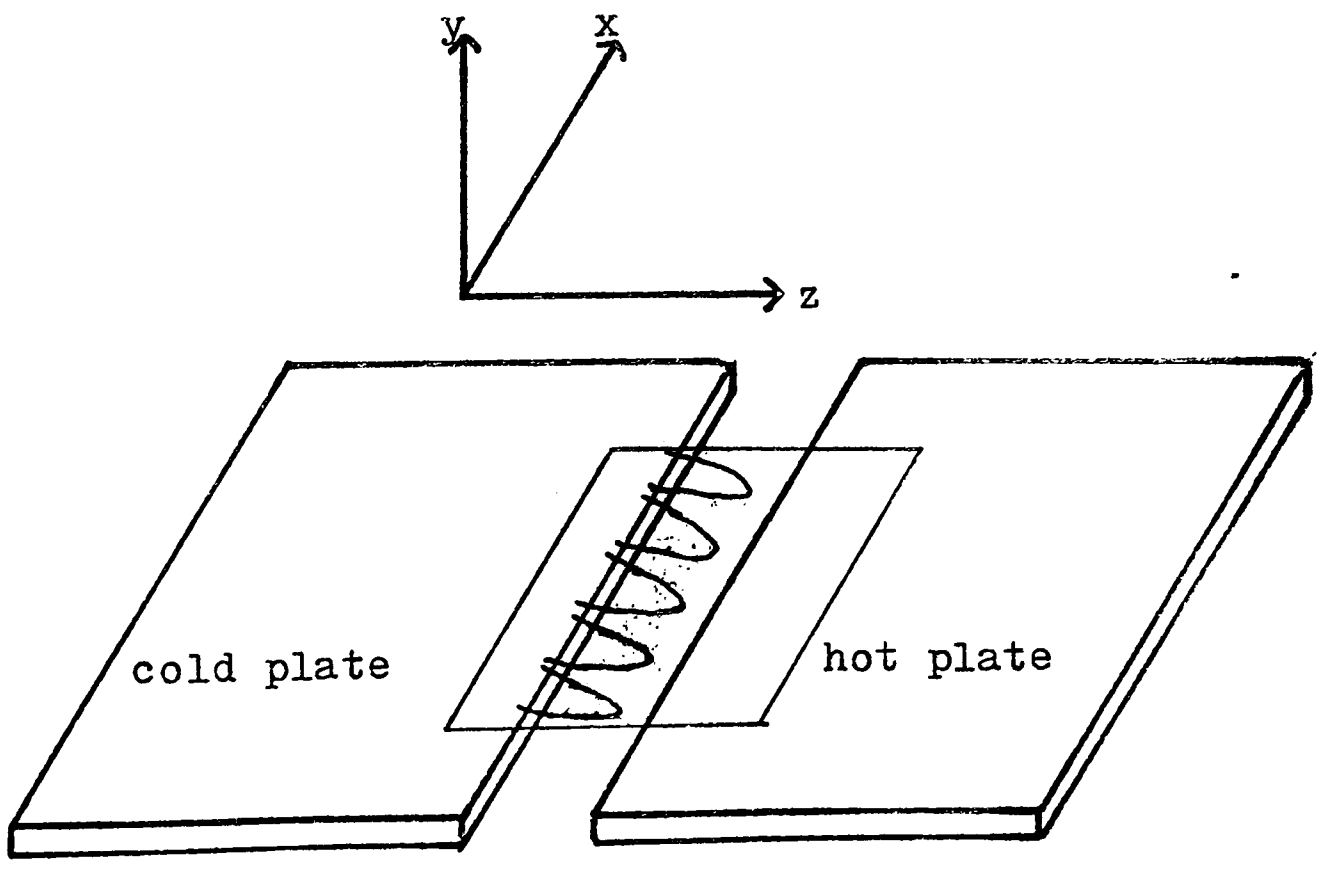


FIG. IV. 3. Co-ordinate system used.

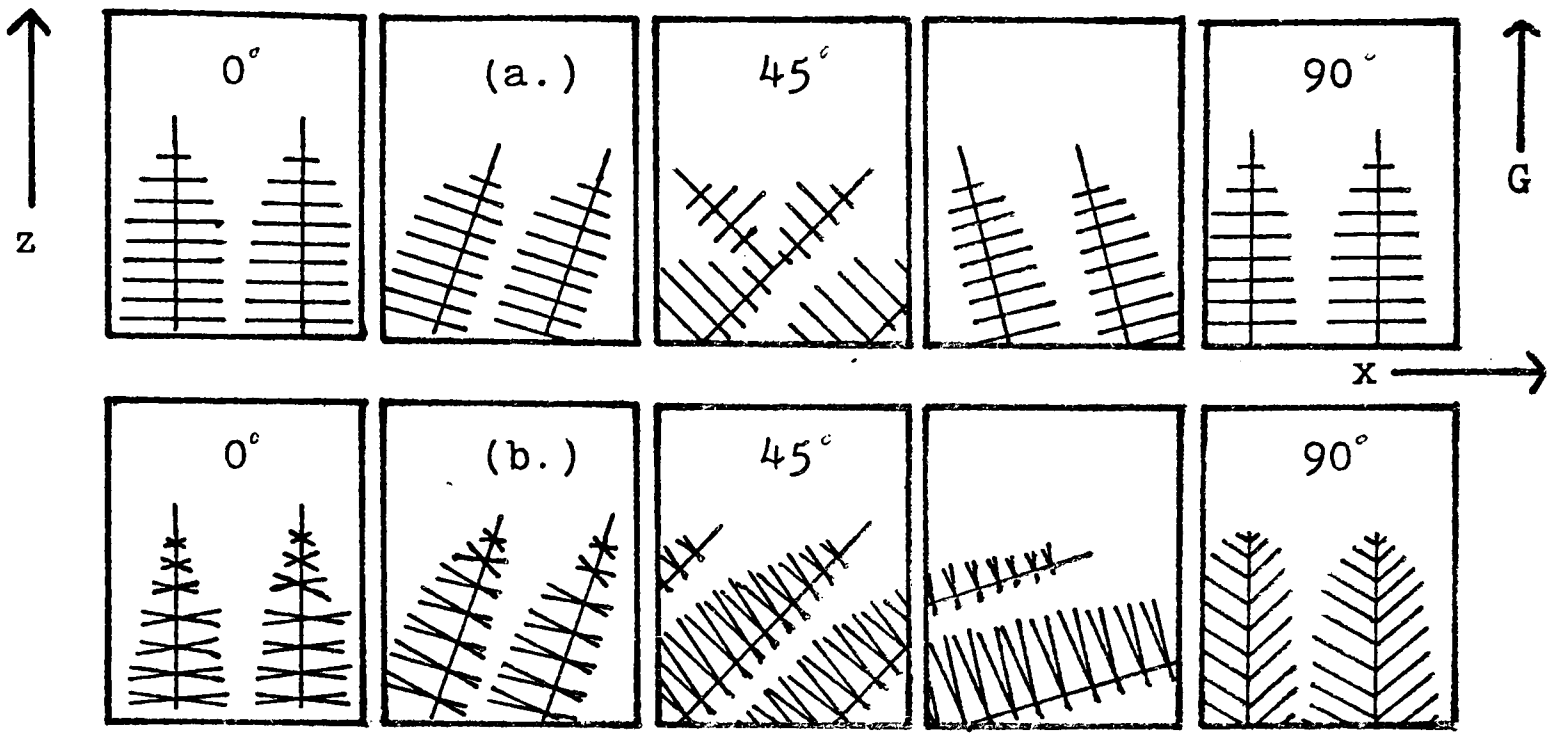


FIG. IV. 4. Schematic illustration of solidification morphology varying as cell is rotated through 90°. (a.) Type 1 grain. (b.) Type 2 grain.

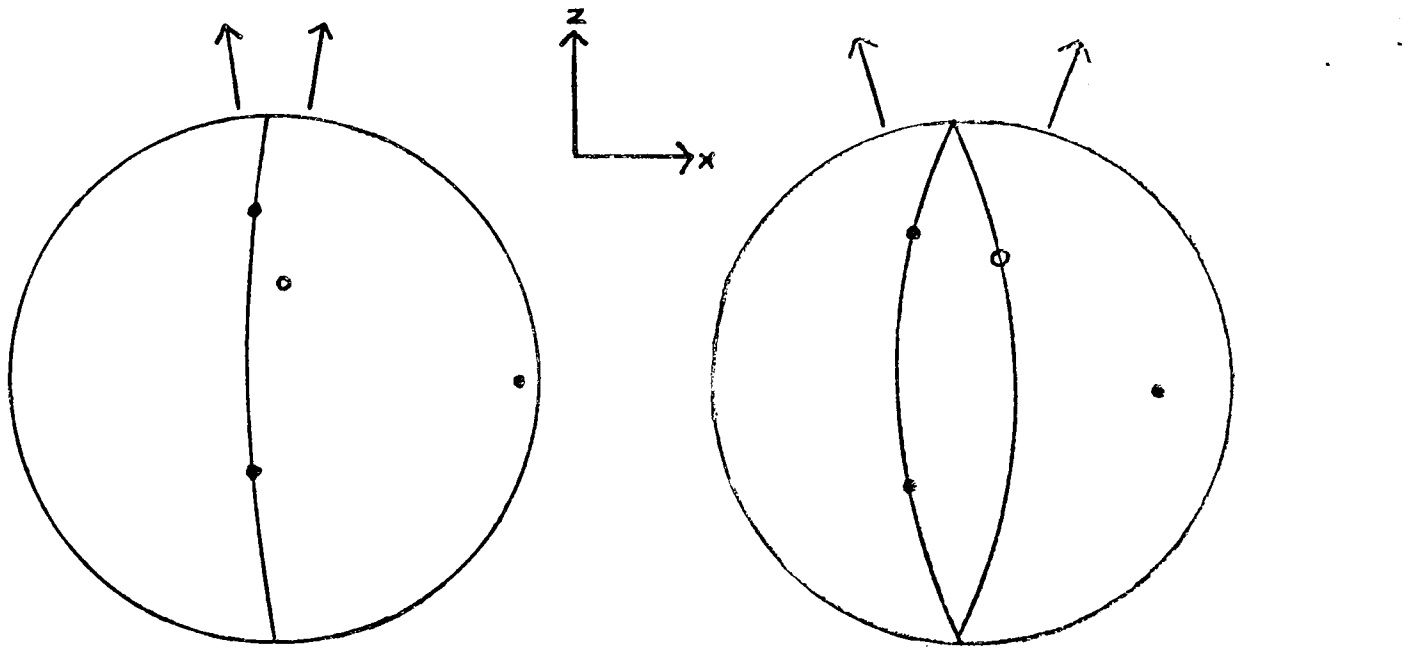


FIG. IV. 5. Stereographic projections in the x - z plane (a.) of type 2 grains (b.) of type 3 grains. •, ∘ represent ⟨100⟩ poles, ⟶ represent possible primary growth directions in the cell plane.

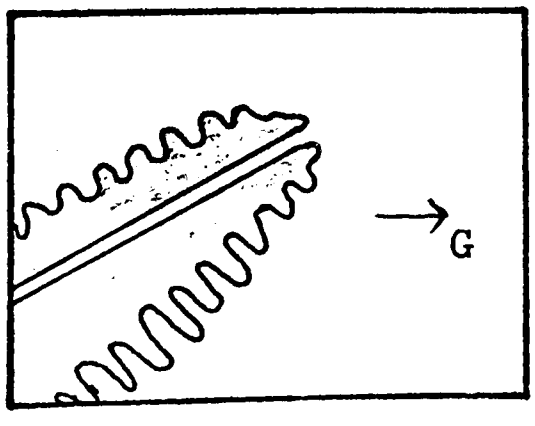


FIG. IV. 6. Schematic diagram of "split" primary dendrite in Type 4 grain.

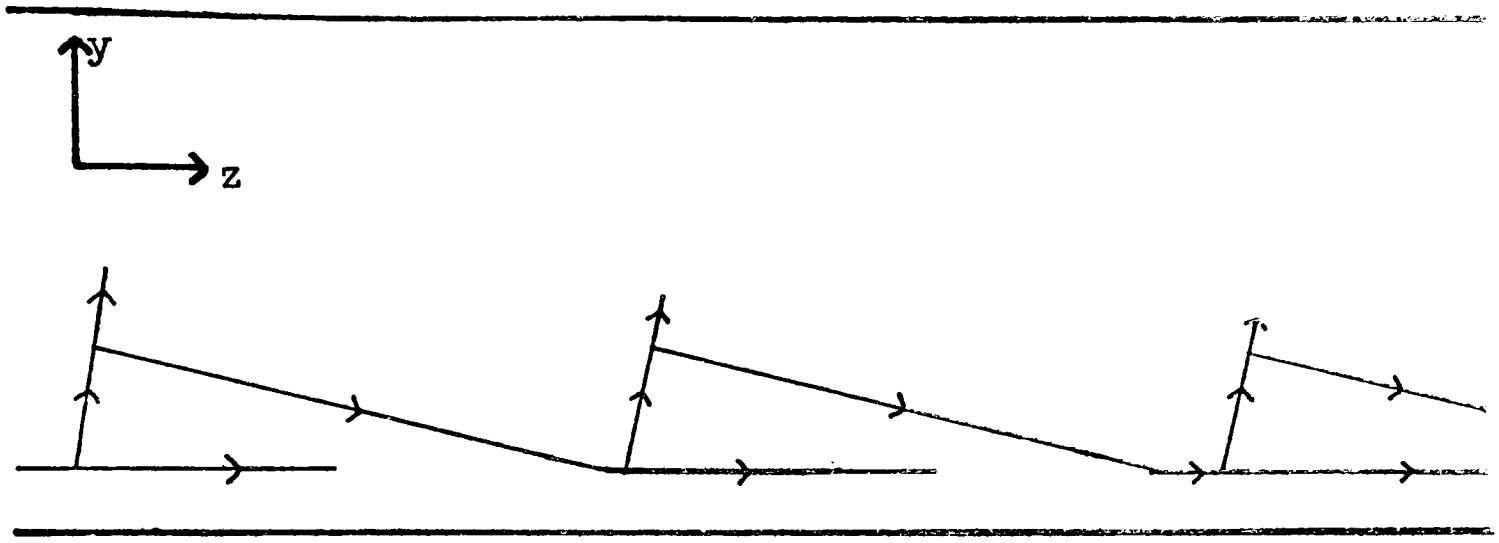


FIG. IV. 7. Formation of "double dendrite" structure (schematic.)

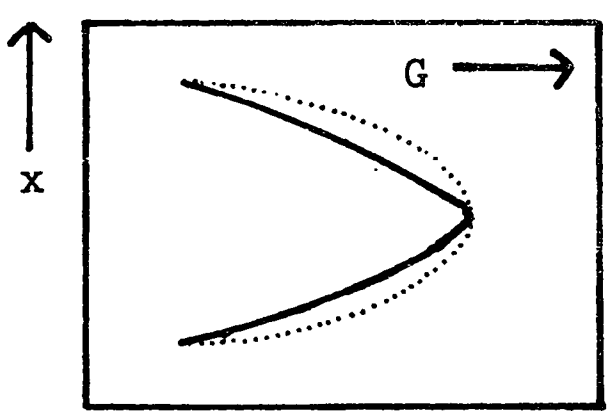
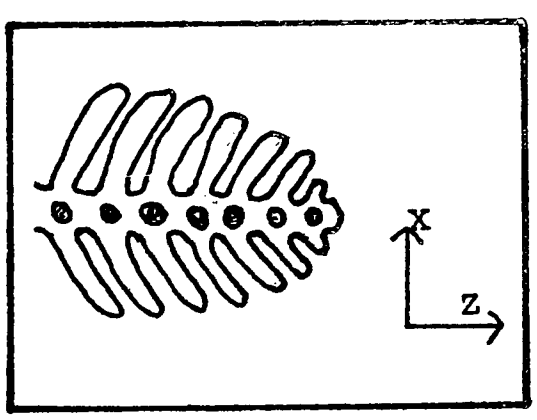


FIG. IV. 8. Dendrite tip shape in CBr_4, (solid line), as compared to parabola.



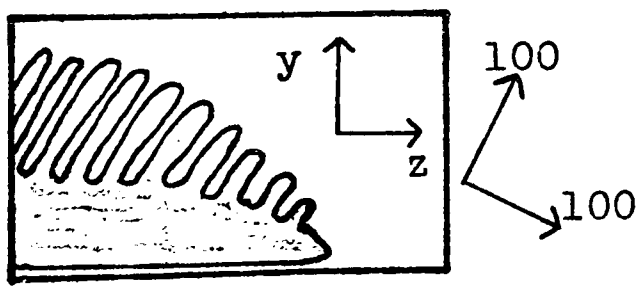


FIG. IV. 9. "Misoriented" dendrite (schematic)

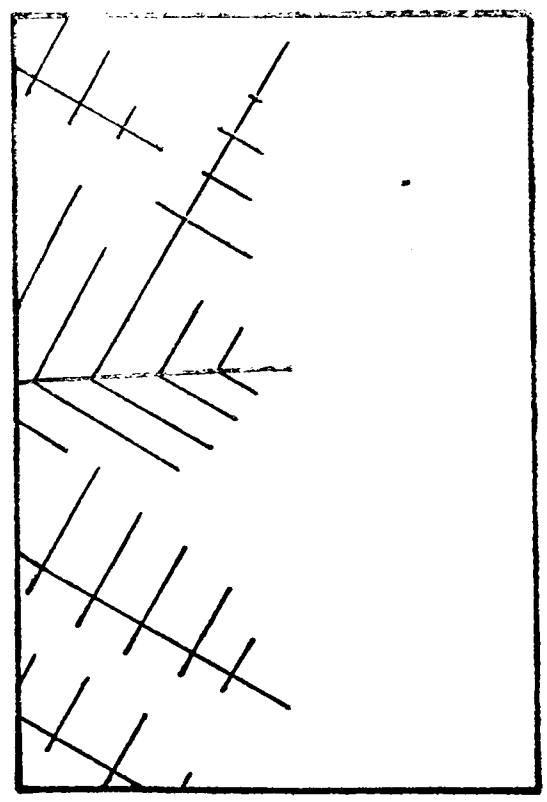


FIG. IV. 10. Structure seen in CBr_4- borneol alloy.

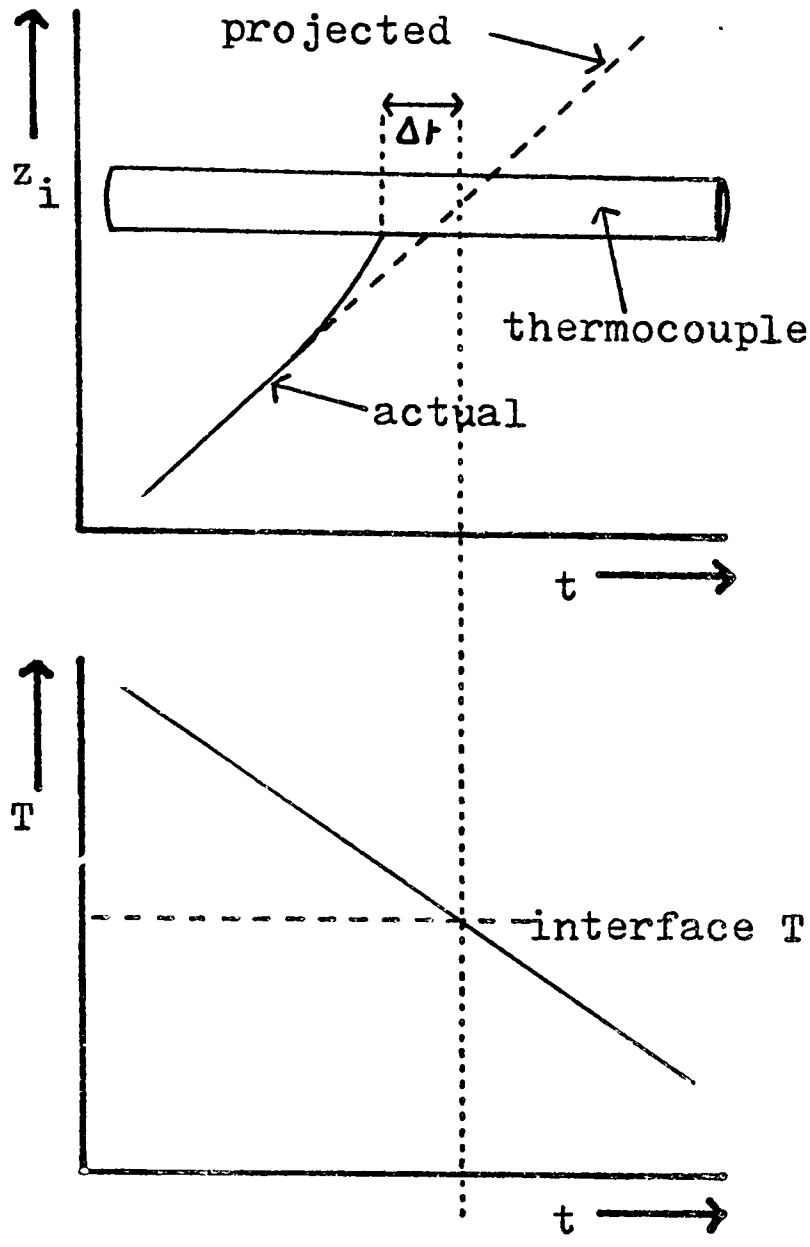


FIG. IV. 11. Measurement of interface temperature.

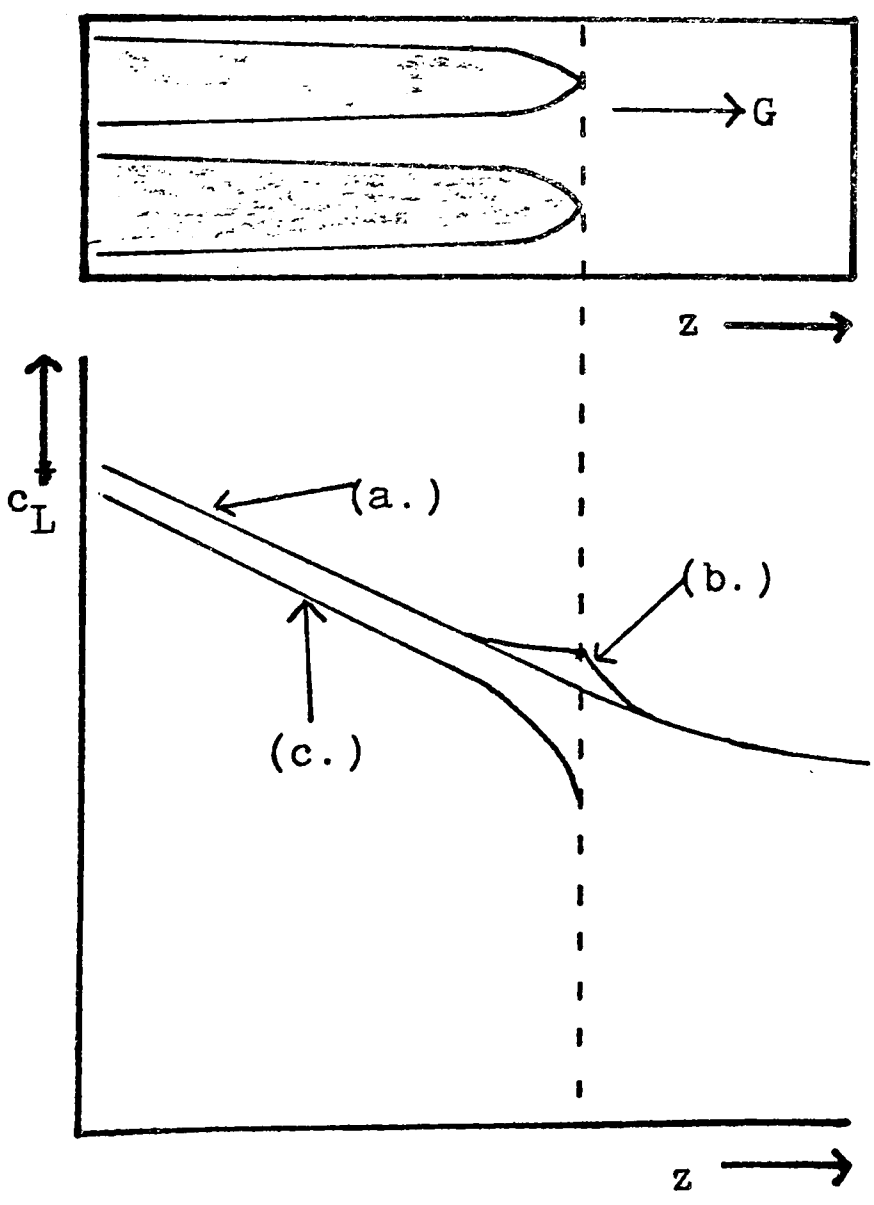


FIG. IV. 14. Dendrite growth temperature theory. (a.)"plane wave" term, (b.)plus "radial" term, from Burden and Hunt. (c.)actual c_L^* - z plot along dendrite side, assuming constant G.

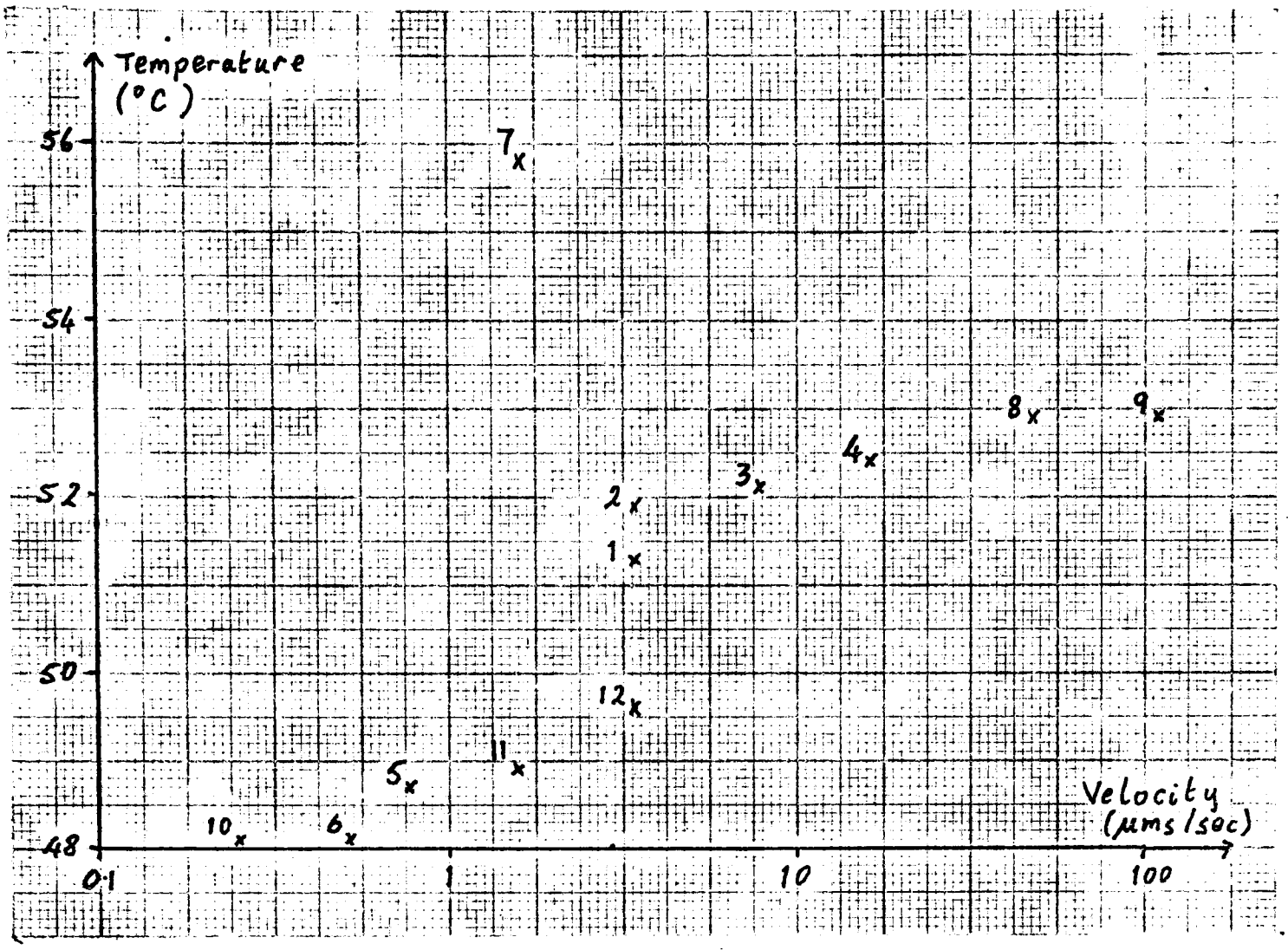


FIG. IV. 12. Dendrite tip temperatures in nominally pure succinonitrile.

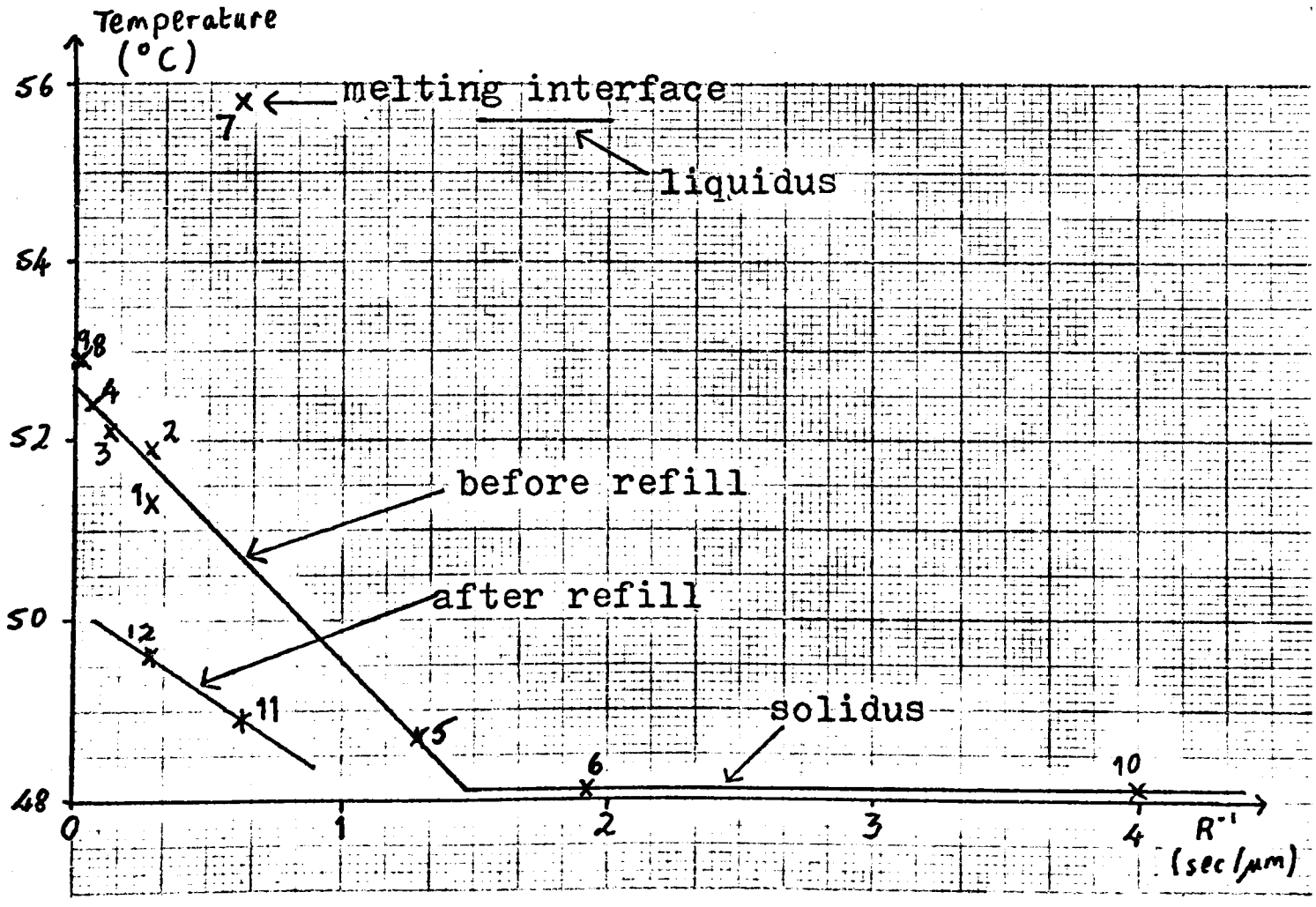


FIG. IV. 13. Re - plotted results of Fig. IV. 12.

Chapter V. A Model of Interdendritic Solidification

(a) Background

This work is a development of an established model for interdendritic solidification, as shown in Fig. V.1. Neighbouring dendrite arms are assumed to have parallel planar surfaces which approach each other as isothermal cooling takes place. Local equilibrium is assumed at the solid-liquid interface, fluid flow is neglected, and diffusion is assumed to be one-dimensional. Brody and Flemings[101] and others[103,93,94,63] used this model to analyze the effect of solid-state diffusion on micro-segregation (Chap II.(b)(4)), while Rohatgi and Adams[58] gave a geometrically similar model of liquid-state diffusion.

The interdendritic liquid was taken to be "completely mixed" by diffusion[49] in the microsegregation treatments. However, from equation (I.11), $v = 0$ if $(\partial c_L/\partial x) = 0$ at the interface and $D_S \rightarrow 0$. Solidification largely depends on the existence of concentration gradients in the liquid, and so the "complete mixing" assumption is not easy to justify. It will be replaced by a diffusion treatment in this work.

Brody and Flemings also assumed as an approximation:

$$\frac{\partial c_S^*}{\partial x} \sim \left(\frac{\partial c_S}{\partial x}\right)_t \qquad \text{(* denotes interfacial concentration)} \qquad (1)$$

in order to carry out an analytical treatment. In reality, solid-state diffusion makes $|(\partial c_S/\partial x)| < |(\partial c_S^*/\partial x)|$ and

the assumption (V.1) leads to an overestimate of the extent of homogenization, as was shown by comparison with numerical results for Al-Cu.[49] We will also use (V.1) in order to retain the flexibility of the analytical approach. Rohatgi and Adams, by contrast, took:

$$\frac{\partial c_L^*}{\partial t} = \left(\frac{\partial c_L}{\partial t}\right)_x \qquad (2)$$

which, as we will show, is also an approximation.

Finally, Brody and Flemings assumed arbitrarily that x^* varies linearly or parabolically with time, and obtained:

$$c_S^* = kc_0\left(1 - \frac{f_S}{1 - \alpha k}\right)^{k-1} \quad \text{(linear analysis)} \qquad (3)$$

$$c_S^* = kc_0\left(1 - (1 - 2\alpha k)f_S\right)^{\left(\frac{k-1}{1-2\alpha k}\right)} \quad \text{(parabolic, } dx^*/dt \propto t^{-\frac{1}{2}}\text{)} \qquad (4)$$

from their approximate analytical treatment, where $f_S = (x^*/\frac{1}{2}\lambda)$ is volume fraction solid (Fig. V.1) and $\alpha = 4D_S t/\lambda^2$. Kirkwood and Evans,[103] noting that the linear and parabolic assumptions had no physical basis, instead assumed a constant rate of heat extraction. The x^* - t relation, which provides a boundary condition to the solid-state diffusion problem, was thus obtained as part of the (numerical) solution.

(b) Basic Equations

In either phase, composition depends on x and t. Therefore:

$$dc = \left(\frac{\partial c}{\partial x}\right)_t dx + \left(\frac{\partial c}{\partial t}\right)_x dt \tag{5}$$

So, for any moving coordinate system X, (V.5) becomes:

$$\left(\frac{\partial c}{\partial x}\right)_X = \left(\frac{\partial c}{\partial x}\right)_t + \left(\frac{\partial c}{\partial t}\right)_x \left(\frac{\partial t}{\partial x}\right)_X \tag{6}$$

or $$\left(\frac{\partial c}{\partial t}\right)_X = \left(\frac{\partial c}{\partial x}\right)_t \left(\frac{\partial x}{\partial t}\right)_X + \left(\frac{\partial c}{\partial t}\right)_x \tag{7}$$

Thus, choosing X coordinates which move with the left-hand solid-liquid interface at $x = x^*$ in Fig.V.1, (V.6) becomes:

$$\left(\frac{\partial c}{\partial x}\right)_X = \left(\frac{\partial c}{\partial x}\right)_t + \left(\frac{\partial c}{\partial t}\right)_x \cdot \left(\frac{dt}{dx^*}\right) \tag{8}$$

while (V.7) becomes:

$$\left(\frac{\partial c}{\partial t}\right)_X = \left(\frac{\partial c}{\partial x}\right)_t \cdot \frac{dx^*}{dt} + \left(\frac{\partial c}{\partial t}\right)_x \tag{9}$$

where:

$$\left(\frac{\partial c}{\partial t}\right)_x = D\left(\frac{\partial^2 c}{\partial x^2}\right)_t \tag{10}$$

from Fick's second law. All these equations apply throughout each phase. Now, using the local equilibrium assumption, we may also write equations to introduce thermal considerations which apply only at the solid-liquid interface:

$$\left(\frac{\partial c^*}{\partial t}\right)_X = \left(\frac{\partial c^*}{\partial T}\right)_X \left(\frac{\partial T}{\partial t}\right)_X \tag{11}$$

$$= \frac{-F}{m} \text{ (liquid)}, \frac{-kF}{m} \text{ (solid)} \tag{11a}$$

where F is cooling rate. Alternatively, writing $dx^*/dt = v$,

$$\left(\frac{\partial c^*}{\partial x}\right)_X = \left(\frac{\partial c^*}{\partial t}\right)_X \left(\frac{\partial t}{\partial x}\right)_X \tag{12}$$

$$= \frac{-F}{mv} \text{ (liquid)}, \frac{-kF}{mv} \text{ (solid)} \tag{12a}$$

Equations of the form (V.11) or (V.12) may be substituted into (V.8) or (V.9), but the resulting equation is valid only at the solid-liquid interface. One such equation for each phase, and the solute conservation equation (I.11), are in principle sufficient to determine the three unknowns v, $(\partial c_L/\partial x)_{\text{interface}}$, $(\partial c_S/\partial x)_{\text{interface}}$. Combining (V.8) and (V.12) for the solid:

$$\frac{-kF}{mv} = \left(\frac{\partial c_S}{\partial x}\right)_t + \frac{D_S}{v}\left(\frac{\partial^2 c_S}{\partial x^2}\right)_t \tag{13}$$

Thus equation (V.1) results from neglecting the term containing D_S in (V.13). Combining (V.9) and (V.11) for the liquid:

$$\frac{-F}{m} = v\left(\frac{\partial c_L}{\partial x}\right)_t + D_L\left(\frac{\partial^2 c_L}{\partial x^2}\right)_t \tag{14}$$

and so equation (V.2) may be seen to result from neglecting the

first term on the right-hand side of (V.9) or (V.14). (By contrast, Okamoto et al[54] ignored the second term on the r.h.s. of (V.14) in their primary spacing theory (their equation 4). This must be a serious error.) The difference between $(\partial c_L^*/\partial t)_X$ and $(\partial c_L/\partial t)_x$ is demonstrated in Fig. V.2. We will first investigate the accuracy of the approximate equation (V.2) by solving (V.14) simultaneously with (I.11), neglecting solid-state diffusion.

Equations (V.13) and (V.14) apply only at the left-hand interface at $x = x^*$ in Fig. V.1: similar equations are required for the interface at $x = (\lambda - x^*)$. For this symmetrical, isothermal model, such equations may be obtained simply by reversing the signs of v, $(\partial c_L/\partial x)_t$. An important result of this is that $(\partial^2 c_L/\partial x^2)_t$ at $x = x^*$ equals $(\partial^2 c_L/\partial x^2)_t$ at $x = (\lambda - x^*)$.

(c) Liquid-State Diffusion

To solve (V.14), it is necessary to assume:

$$\left(\frac{\partial c_L}{\partial t}\right)_x = D_L\left(\frac{\partial^2 c_L}{\partial x^2}\right)_t = \text{constant (in space and time).} \quad (15)$$

This is physically possible if $(F/m + v(\partial c_L/\partial x)_t)$ is held constant, from (V.14). We shall see later that this is nearly, but not exactly, the same as holding F constant. It may be noted that the result $(\partial^2 c_L/\partial x^2)_{t,x=x^*} = (\partial^2 c_L/\partial x^2)_{t,x=\lambda-x}$ derived above from symmetry considerations, is a necessary precondition for the assumption (V.15).

Combining (V.14) with (I.11) and taking $D_S \rightarrow 0$:

$$D_L\left(\frac{\partial^2 c_L}{\partial x^2}\right)_t = \frac{-F}{m} + \frac{v^2 c_L^*(1 - k)}{D_L} \qquad (16)$$

From (V.15), the left-hand side of (V.16) is constant. So the right-hand side as a whole is also constant, and we may integrate:

$$D_L\left(\frac{\partial c_L}{\partial x}\right)_t = \left(\frac{-F}{m} + \frac{v^2 c_L^*(1 - k)}{D_L}\right)(x - \tfrac{1}{2}\lambda) \qquad (17)$$

the integration constant having been eliminated since, by symmetry,

$$\left(\frac{\partial c_L}{\partial x}\right)_t = 0 \quad \text{when } x = \tfrac{1}{2}\lambda. \qquad (18)$$

Further integration yields:

$$c_L(x = x') - c_L(x = \tfrac{1}{2}\lambda) = \left(\frac{-F}{m} + \frac{v^2 c_L^*(1 - k)}{D_L}\right)\left(\frac{(x' - \tfrac{1}{2}\lambda)^2}{2D_L}\right) \qquad (19)$$

with x' being any value of x within the liquid region. Rohatgi and Adams[58] obtained a similar equation to (V.19) (their A-3), although they implicitly assumed (V.2) and therefore obtained (dc_L/dt) in place of our $((-F/m) + (v^2 c_L^*(1 - k)/D_L))$ term in (V.19). They recognized their A-3 as an exact solution for the special case assumed in (V.15), and attempted to calculate the error involved in applying their A-3 when $(\partial c_L/\partial t)$ is not constant. Unfortunately, this latter calculation is incorrect. Their differentiation of A-3 with respect to time, "relating" $(\partial^2 c_L/\partial t^2)$ to the

variation of $(\partial c_L/\partial t)$ with position, is inadmissible because their A-3 is only valid when $(\partial^2 c_L/\partial t^2) = 0$.

Returning to (V.17) and substituting (I.11) into the left-hand side:

$$\left(\frac{(x^* - \tfrac{1}{2}\lambda)c_L^*(1 - k)}{D_L}\right)v^2 + c_L^*(1 - k)v\,\frac{-F}{m}(x^* - \tfrac{1}{2}\lambda) = 0 \tag{20}$$

Solving the quadratic equation:

$$v = \frac{D_L}{2(x^* - \tfrac{1}{2}\lambda)}\left[-1 \pm \left(1 - \frac{4F(x^* - \tfrac{1}{2}\lambda)^2}{D_L m c_L^*(1 - k)}\right)^{\frac{1}{2}}\right] \tag{21}$$

Defining:

$$p = \frac{-4F(x^* - \tfrac{1}{2}\lambda)^2}{D_L c_L^*(1 - k)m} \tag{22}$$

(V.21) may be expanded binomially, obtaining:

$$v = \frac{D_L}{2(x^* - \tfrac{1}{2}\lambda)}\left[-1 \pm (1 - \tfrac{1}{2}p - \tfrac{1}{8}p^2 - (1/16)p^3 \ldots)\right] \tag{23}$$

Taking the positive sign, and dropping p^3 and higher terms on the assumption $p \ll 1$ (to be discussed later):

$$v = \left(\frac{F(x^* - \tfrac{1}{2}\lambda)}{mc_L^*(1 - k)}\right)\left(1 - \frac{F(x^* - \tfrac{1}{2}\lambda)^2}{D_L m c_L^*(1 - k)}\right) \tag{24}$$

Now, if the calculation is repeated using the approximation (V.2) instead of the exact equation (V.14), the v^2 term in (V.16) and (V.20) disappears and (from (V.14) and (V.15)) F becomes constant. Then (V.20) becomes:

$$v = \left(\frac{F(x^* - \frac{1}{2}\lambda)}{mc_L^*(1 - k)}\right) \qquad (25)$$

By changing variables, (V.25) may be seen to be identical to (I.16) which, on integration, yields the familiar "complete mixing" or Scheil equation, (I.17). Comparing (V.24) and V.25), it is seen that when $p \ll 1$, the value of v obtained from the approximate approach is increased by a multiplying factor $(1 + \frac{1}{4}p)$ when the exact equation (V.14) is used. Thus, our model shows that the Scheil equation slightly underestimates f_s for a given c_L^*, but is a reasonable approximation, when $p \ll 1$. The model suggests that the Scheil equation may markedly underestimate f_s when p is not $\ll 1$ but obtains no accurate result in this case.

(d) Applications to Dendritic Growth

Dendritic growth analyses (e.g. Burden and Hunt[51,55]) show that (V.15) cannot apply near the growth front, when radial diffusion fields are much shorter-range than the primary spacing. From dimensional diffusion theory, the concentration disturbances due to dendritic growth should spread out laterally to a distance $\sim \sqrt{D_L t}$ in time t (Fig. V.3), and the radial diffusion fields should therefore overlap after an "initial transient time":

$$\theta_t = \frac{\lambda_1^2}{4D_L} \qquad (26)$$

Thus when $(4D_L\theta_f/\lambda_1^2) \gg 1$ (Brody and Flemings' criterion[49]), $\theta_t \ll \theta_f$ and so the initial transient takes up a negligible fraction of the local solidification time. After

this transient, the condition (V.15) is physically achievable (given the correct cooling curve, i.e. F almost constant). The other condition required to validate (V.25), that $p \ll 1$, may also be related to the initial transient. Defining:

$$\theta_d = \frac{-mc_L^*}{F} \quad \text{(at the dendritic growth front)} \tag{27}$$

equations (V.26), V.27) and (V.22) may be combined to give:

$$p = \left(\frac{4(1 - f_s)^2}{(1 - k)}\right)\left(\frac{\theta_t}{\theta_d + t}\right) \tag{28}$$

at time t after the passage of the dendritic growth front. The parameter θ_d represents the time taken to cool at rate F from the pure material melting point to the dendritic growth front temperature. The contents of the first bracket in (V.28) are fairly close to unity and so the ratio of time parameters in the second bracket determines p. When $\theta_t \ll \theta_d$, $p \ll 1$ for any t and so this condition for the validity of (V.25) is always fulfilled. However, when θ_t is not $\ll \theta_d$, p may be significant compared to unity even when t is considerably greater than θ_t and this may invalidate (V.25) for a large fraction of the total freezing time. This may occur in fairly pure materials. Approximating c_L^* at the growth front to equal the alloy composition c_0 and taking typical values $D_L \sim 10^{-5}$ cm^2/sec, $\lambda_1 \sim 100\mu$ms, $F \sim 1^\circ$C/sec, $(-m) \sim 5^\circ$C/% solute, we find from (V.26) and (V.27) that $\theta_d = \theta_t$ when $c_0 = 0.5\%$. If this is so, and $(1 - f_s)^2/(1 - k) = 1$, then (V.24) still predicts a 10% higher value for v than does (V.25) at the point when

$t = 9\theta_t$. So, when θ_t is not $\ll \theta_d$, equation (V.25) remains inaccurate for a considerable time after the initial transient has been completed. It should be noted, however, that (from (V.28)) $p \ll 1$, and (V.25) is approximately valid during the majority of the total freezing time provided that $\theta_t \ll \theta_f$.

Doherty and Melford[88] suggested a "duplex" model for dendritic solidification, combining a steady-state analysis (e.g. Nash and Glicksman[21]) for initial growth at the dendrite tips with a modified Brody and Flemings analysis[101] (i.e. the Scheil equation adapted to include solid-state diffusion) for the later stages of solidification. The present work suggests a more complex sequence (Fig. V.3):

(i) initial growth - fairly small interactions between neighbouring primary dendrite tips.[47,55]

(ii) initial transient - between $0 \leqslant t \leqslant \theta_t$ - meeting and overlap of diffusion fields from neighbouring primary arms.

(iii) stage when p not $\ll 1$ - exists between $0 \ll t \ll$ roughly 10 to 50 θ_t (depending on accuracy required) in cases where θ_t is not $\ll \theta_d$ - (V.25) underestimates rate of increase of fraction solid.

(iv) "modified Scheil equation" stage - (V.25) reasonably accurate - occupies most of the total freezing time if $\theta_t \ll \theta_f$, subject to the original assumptions (i.e. no convection, remelting, etc.).

A materials balance argument demonstrates why the modified Scheil equation can often apply quite accurately

during interdendritic solidification, despite the objections to the "complete mixing" assumption described in section (a). Equation (I.16) is exact when c_L is independent of x: equation (V.19) shows that the variation of c_L with x at a given time is often small compared to the variation of c_L with time throughout solidification. For instance, using the typical values for λ_1, D_L, F and m as chosen previously and neglecting the v^2 term, (V.19) gives $c_L(x = \frac{1}{4}\lambda) - c_L\ (x = \frac{1}{2}\lambda)$ $\sim 6 \times 10^{-2}\%$. A similar argument shows that the modified Scheil equation can apply in the general case where F varies considerably with time and so (V.15) cannot be assumed a priori. Assuming (V.19), c_L varies little with x at any time, therefore, in (V.15), $(\partial c_L/\partial t)_x$ must at least be roughly constant in space at a given time, and therefore (completing the virtuous circle) (V.19) and subsequent equations are approximately correct. Thus the solidification sequence described above is relevant for any cooling curve.

(e) Solid-State Diffusion

In this analysis, we accept equation (V.2) and hence deal with liquid-state diffusion by substituting (V.17) into (I.11) and neglecting the v^2 term. We are therefore describing stage (iv) in the solidification sequence of section (d). We also allow for solid-state diffusion in (I.11), using (V.13) with the important approximation (V.1):

$$vc_L^*(1 - k) = \frac{F}{m}(x^* - \tfrac{1}{2}\lambda) - \frac{D_s kF}{mv} \tag{29}$$

Assuming:

$$F = \text{constant} \tag{30}$$

and writing

$$c_L^* = \frac{-F(t + \theta_d)}{m} \tag{31}$$

(V.29) becomes:

$$(t + \theta_d)(1 - k)v^2 + (x^* - \tfrac{1}{2}\lambda)v - kD_s = 0 \tag{32}$$

or

$$v = \left(\frac{x^* - \frac{1}{2}\lambda}{2(t + \theta_d)(1 - k)}\right)\left[-1 \pm \left(1 + \frac{4k(1 - k)D_s(t + \theta_d)}{(x^* - \frac{1}{2}\lambda)^2}\right)^{\frac{1}{2}}\right] \tag{33}$$

The term $4k(1 - k)D_s(t + \theta_d)/(x^* - \frac{1}{2}\lambda)^2$ is dimensionless and roughly similar to $(4D_s t/\lambda^2)$. Such a term must be small compared to unity if the approximation (V.1) which we are using is to stand any chance of being valid. Therefore we may expand binomially and drop squared and higher terms:

$$v = \left(\frac{x^* - \frac{1}{2}\lambda}{2(t + \theta_d)(1 - k)}\right)\left[-1 \pm \left(1 + \frac{2k(1 - k)D_s(t + \theta_d)}{(x^* - \frac{1}{2}\lambda)^2}\right)\right] \tag{34}$$

Taking the negative sign (from comparison with (V.25)):

$$v = \frac{-(x^* - \frac{1}{2}\lambda)}{(1 - k)(t + \theta_d)} - \frac{kD_s}{(x^* - \frac{1}{2}\lambda)} \tag{35}$$

This can be made exact and solved (Appendix A), setting $x^* = x_0$ and $f_s = f_{s0}$ at $t = 0$ to allow for initial dendritic growth not describable by these equations. Defining:

$$\alpha' = \frac{4D_s t}{\lambda^2}, \quad \alpha_d = \frac{4D_s\theta_d}{\lambda^2} \quad (\text{and } ^{(49)}\ \alpha = \frac{4D_s\theta_f}{\lambda^2}): \tag{36}$$

the solution is:

$$c_s^* = k(c_L^*)_{(t=0)}\left[\frac{(1 - f_s)^2 + (\alpha' + \alpha_d)(2k(1 - k)/(3 - k))}{(1 - f_{s0})^2 + \alpha_d(2k(1 - k)/(3 - k))}\right]^{(k-1)/2} \tag{37}$$

which may be compared to (V.3) and (V.4) as derived by Brody and Flemings.[101] (Note that the equation is strictly not solved for c_s^* since this also appears in the α terms). When $c_L^*{}_{(t=0)} = c_0$, $f_{s0} \to 0$ and α', $\alpha_d \to 0$ because $D_s \to 0$, the Scheil equation is obtained from (V.37). The equation may also be written:

$$f_s = 1 - \left(\frac{c_s^*}{kc_L^*_{(t=0)}}\right)^{2/(k-1)} \left((1 - f_{s0})^2 + \alpha_d\left(\frac{2k(1 - k)}{3 - k}\right)\right)$$

$$+ (\alpha' + \alpha_d)\left(\frac{2k(1 - k)}{3 - k}\right) \qquad (38)$$

So far the only approximations made have been those incorporated into (V.29). To find the composition of the last liquid to freeze, we may approximate $f_{s0} \rightarrow 0$, $c_L^*{}_{(t=0)} = c_0$, and $\alpha_d(2k(1 - k)/(3 - k)) \ll 1$, to obtain:

$$c_L^*(\text{final}) = c_0\left[(\alpha + \alpha_d)\frac{2k(1 - k)}{(3 - k)}\right]^{(k-1)/2} \qquad (39)$$

or:

$$c_L^*(\text{final}) = (c_0)^{2/(3-k)}\left[\frac{-4D_s^m}{F\lambda^2} \cdot \frac{2k(1 - k)}{3 - k}\right]^{(k-1)/(3-k)} \qquad (40)$$

Equation (V.40) demonstrates that complete solidification cannot occur without solid-state diffusion unless k varies or a second solid phase appears. The equation may give a meaningless result $c_L^*(\text{final}) > c_L^*(\text{eutectic})$ when $f_s < 1$ at the eutectic. It may also give ridiculous results when α is not small compared to unity, because the assumption (V.1) overestimates solid-state diffusion. Complete solid-state homogenization, which in fact requires $\alpha \rightarrow \infty$, is represented by $c_L^*(\text{final}) = c_0/k$. It is instructive to find the α value for which (V.39) obtains a similar result. This is:

$$\alpha + \alpha_d = \left(\frac{3 - k}{2k(1 - k)}\right)(k)^{2/(1-k)} \qquad (41)$$

or, for example, $(\alpha + \alpha_d) \sim 0.16$ when $k = 1/5$! Clearly, then, the analysis is grossly overestimating solid-state homogenization for α values of this order.

The low α value obtained here does partially reflect the considerable homogenization which occurs in the last stages of solidification, when, from (V.25), $(dx^*/dt) \propto (x^* - \frac{1}{2}\lambda)$ for $D_s = 0$, so that a steep concentration gradient appears in the solid. Numerical calculations (e.g. Table V.2) show quite significant homogenization when $\alpha \gtrsim 0.05$. The present treatment, based on the assumption of constant cooling rate, makes reasonable allowance for the very slow solidification in the last stages, whereas the linear and parabolic solidification rate assumptions of Brody and Flemings do not. Nevertheless, the main reason for the result of (V.41) must be the inadmissibility of assumption (V.1) and we conclude that this type of analytic treatment must be unreliable except for very low α values (e.g. $< 10^{-2}$).

The importance of solid-state diffusion in the final stages of solidification may be demonstrated qualitatively. In (V.29), the solid-state and liquid-state diffusion terms contribute equally to the interfacial solute flux when:

$$(x^* - \tfrac{1}{2}\lambda) = \left(\frac{mc_L^*(1 - k)D_s k}{2F}\right)^{\frac{1}{2}} \qquad (42)$$

which, taking $(-m) = 5^\circ C/\%$ solute, $k = 0.2$, $c_L^* = 25\%$ solute, $F = 1^\circ C/sec$ and $D_s = 10^{-9}$ cm^2/sec, gives a liquid

pool width = $2(x^* - \frac{1}{2}\lambda) = 2\mu$ms. The interface velocity is then:

$$v = \left(\frac{-2D_s kF}{mc_L^*(1-k)}\right)^{\frac{1}{2}} \qquad (43)$$

After this point, liquid-state diffusion should become progressively less important as $(x^* - \frac{1}{2}\lambda)$ in (V. 29) decreases, and v should thus decrease somewhat. We will assume v constant after the time when (V.42) is true, and hence calculate the time taken in these final stages of solidification when solid-state diffusion dominates in (V.29) as:

$$mc_L^*(1-k)/2F \qquad (44)$$

representing 50 seconds or 50°C in our example. This must be a considerable fraction of the total freezing time. Thus, solid-state diffusion may be important in determining the non-equilibrium freezing range of an alloy (e.g. for solidification cracking analyses), although the present crude treatment finds that the "solid-state diffusion controlled freezing time" is independent of D_s.

(f) Microsegregation in Aluminium-Copper Alloys

Michael and Bever[104] cast sixteen Al-Cu specimens (2 - 5 wt.%Cu), measured their freezing times and determined the volume fraction of eutectic microsegregate by quantitative metallography. Bower, Brody and Flemings[49] measured the compositions at primary arm centres in fully solidified and quench-interrupted castings in Al-4½ wt.%Cu. Bower, Brody

and Flemings[49] and Kirkwood and Evans[103] compared these results to their numerical analyses of solid-state diffusion discussed in section (a). Both groups claimed to find good agreement between theory and experiment. Kirkwood and Evans[103] demonstrated that uncertainties in the diffusion data caused the main difficulties in making the comparison. We shall show that these uncertainties can be considerably reduced by checks on the self-consistency of the results, and hence re-examine the agreement between theory and experiments.

In their calculations, Bower, Brody and Flemings used actual diffusion data ((1) in Table V.1), but multiplied the measured λ values by a "correction factor" of 0.32 to obtain a better data fit. In terms of the relevant $\propto$ parameter, this is equivalent to multiplying D_0 by $(0.32)^{-2}$, as in (2) in Table V.1, and accepting the measured λ values. We will discuss their work in these terms. Diffusion data of Murphy, quoted by Kirkwood and Evans,[103] and data obtained by Young,[65] agree quite well with the corrected Brody and Flemings data as shown in Table V.1. Kirkwood and Evans used measured λ values without a correction factor: in discussing volume fraction eutectic, they made two sets of calculations assuming constant D_s values of 10^{-9} and 3×10^{-9} cm^2/sec.

Besides the uncertainties in diffusion data, major problems occur in choosing a single λ parameter to characterize the complex dendritic structure. The problems are largely overcome when the solid-state diffusion theory is applied to both dendrite centre composition and fraction eutectic measurements, since the theory is effectively

tested if both types of measurement can be fitted by the same D_s and λ data. Other factors which might cause homogenization would not affect the two types of measurement equally. Remelting, for instance, would homogenize the secondary arms and hence reduce the fraction eutectic while leaving the primary arm centre relatively unaffected. A significant growth temperature depression would affect the primary composition more than the fraction eutectic. Brody and Flemings showed that the growth temperature depression had much less effect on the primary arm centre composition than did solid-state diffusion, by performing quench-interrupted solidification experiments and thus observing the increase of dendrite centre composition after the initial growth.

Dendrite centre composition measurements were fitted to theory by Kirkwood and Evans with $D_s = 1.3 \times 10^{-9}$ cm^2/sec, and by Brody and Flemings with their corrected data for which $D_s = 1.7 \times 10^{-9}$ cm^2/sec at the eutectic temperature. These values agree with the diffusion data at the eutectic temperature and suggest that a constant value $D_s = 1.5 \times 10^{-9}$ cm^2/sec would be a reasonable choice for volume fraction eutectic calculations.

Table V.2 presents the volume fraction data of Michael and Bever,[104] together with the calculated results of Kirkwood and Evans, and additional calculations of our own which are asterisked. Clearly, the measured fraction eutectic is generally significantly lower than that predicted for $D_s = 1.5 \times 10^{-9}$ cm^2/sec. (The analysis by Bower, Brody and Flemings obtained broadly similar results, except for the 4.8 wt.% Cu points for which the calculated

% eutectic was much lower relative to measured % eutectic than in Kirkwood and Evans' data. The reason for this difference between the two groups' results is not clear). Figure V.4 demonstrates again that $D_s = 1.5 \times 10^{-9}$ cm^2/sec is a reasonable choice for the diffusion coefficient, since it shows no systematic variation of Δf_E (see Table V.2) with $\propto$. Had $D_s = 1.5 \times 10^{-9}$ cm^2/sec been too low a value, we should have found Δf_E greater for the specimens with high $\propto$, since more solid-state diffusion occurs in such specimens. Admittedly, there is considerable scatter in the Δf_E values at high $\propto$, probably because the freezing times, which were of the order of a few seconds, were not accurately measured. Nevertheless, Fig. V.4 shows that $D_s = 1.5 \times 10^{-9}$ cm^2/sec. is roughly the correct value to remove a systematic dependence of Δf_E on $\propto$ while $D_s = 3 \times 10^{-9}$ cm^2/sec is clearly too high. So the remaining discrepancies between theory and experiment appearing in Δf_E must be due to an unconsidered homogenization mechanism. Remelting, by coarsening and TGZM, is the obvious possibility. The "error factor" term in Table V.2 approximately gives the total homogenization (below Scheil equation predictions) divided by that attributable to solid-state diffusion with $D_s = 1.5 \times 10^{-9}$ cm^2/sec. The mean "error factor" is 4.2 and the mode is 3.4. Thus, only a quarter of the observed homogenization, in terms of fraction eutectic, is due to solid-state diffusion. On average, the calculations based on $D_s = 1.5 \times 10^{-9}$ cm^2/sec overestimated the volume % eutectic by $\sim$ 34% (i.e. average ($\Delta f_E \div$ measured % eutectic) = 0.34).

So the Scheil equation would have overestimated volume % eutectic by about 45% on average. The average value of Δf_E for the sixteen specimens is ~ 1.3 volume %, being slightly higher for the higher composition specimens.

Table V.1. Diffusion Data

$D_s = D_0 \exp - (Q/RT)$

(1) D_s quoted by Brody and Flemings (i.e. $D_0 = 0.084$ cm^2/sec, $Q = 32600$ cal/mole).

(2) The above data "corrected" by multiplying D_0 by $(1/0.32)^2$, so that $D_0 = 0.82$ cm^2/sec.

(3) D_s quoted by Kirkwood and Evans (i.e. $D_0 = 0.29$ cm^2/sec, $Q = 31120$ cal/mole)

(4) D_s from Young[65] ($D_0 = 0.39$ cm^2/sec, $Q = 31219$ cals/mole).

Temperature		821°K (eutectic)	850°K	900°K
D_s (x 10^{-9} cm^2/sec):	(1)	0.174	0.343	1.00
	(2)	1.70	3.36	9.81
	(3)	1.49	2.85	7.94
	(4)	1.88	3.61	10.10

Table V.2. Microsegregation Data.[104,103]

From Kirkwood[103]	*	*	*	*	*	*	*
wt % Cu	volume % eutectic: measured	calculated for D_s ($cm^2/sec \times 10^9$) of: = 1	= 3	= 1.5	= 0	Δf_E (%)	$\Delta f_E'$ (%) x 10^9	D_s (fit)	error factor	α
2.07	2.2	2.9	2.6	2.8	3.05	0.6	0.4	5.6	3.7	4.1×10^{-3}
2.07	1.5	2.6	1.7	2.4	3.05	0.9	0.2	3.4	2.3	1.5×10^{-2}
2.08	1.1	2.7	2.0	2.5	3.05	1 4	0.9	5.6	3.7	1.2×10^{-2}
1.96	0.5	0.6	0	(0.5)	(0.9)	(0.0)	(-0.5)	(1.5)	(1)	7.5×10^{-2}
2.94	3.6	4.7	4.5	4.7	4.8	1.1	0.9	12 0	8.0	4.1×10^{-3}
2.96	2.9	4.6	4.1	4.5	4.85	1.6	1.2	7.8	5.2	1.0×10^{-2}
2.97	2.8	4.5	4.0	4.4	4.75	1.6	1.2	7.8	5.2	1.1×10^{-2}
2.81	1.9	2.4	0.7	2.0	3.25	0.1	-1.2	1.6	1.1	7.5×10^{-2}
3.93	5.6	7.2	7.1	7.2	7.25	1.6	1.5	33.0	22.0	1.5×10^{-3}
3.96	5.4	7.0	6.4	6.9	7.3	1.5	1.0	6.3	4.2	1.1×10^{-2}
3.94	4.6	6.9	5.7	6.6	7.5	2.0	1.1	4.8	3.2	1.8×10^{-2}
4.06	2.8	5.5	3.2	4.9	6.65	2.1	0.4	3.4	2.3	7.5×10^{-2}
4.71	7.5	8.8	8.5	8.7	8.95	1.2	1.0	9.7	6.5	1.0×10^{-2}
4.79	7.5	8.8	8.0	8.6	9.2	1.1	0.5	4.3	2.9	2.0×10^{-2}
4.82	7.3	8.7	7.3	8.4	9.4	1.1	0.0	3.0	2.0	2.7×10^{-2}
4.80	4.0	7.5	5.2	6.9	8.65	2.9	1.2	4.0	2.7	7.5×10^{-2}

Notes: The calculated volume % eutectic for $D_s = 1.5 \times 10^{-9}$ cm^2/sec was obtained by linear interpolation between Kirkwood and Evans' calculations for $D_s = 1 \times 10^{-9}$ and 3×10^{-9} cm^2/sec. This procedure is reasonable if, as predicted by (V.29), homogenization varies linearly with D_s. This is approximately true when little solid-state diffusion occurs. Calculations for $D_s = 0$ obtained by a similar linear extrapolation

have been included to show how accurate this procedure is. The term Δf_E represents calculated volume fraction eutectic for $D_s = 1.5 \times 10^{-9}$ cm^2/sec minus the measured volume fraction eutectic. $\Delta f_E'$ is similar but for D_s taken as 3×10^{-9} cm^2/sec. $D_s(fit)$ is the value of D_s which, from linear extrapolation of the Kirkwood and Evans results, would be required to fit the measured volume % eutectic. "Error factor" = $D_s(fit) \div 1.5 \times 10^{-9}$ cm^2/sec. The $\propto$ parameter is calculated from the column "al^2" in Kirkwood and Evans,[103] assuming a freezing range of 100^oC and $D_s = 1.5 \times 10^{-9}$ cm^2/sec.

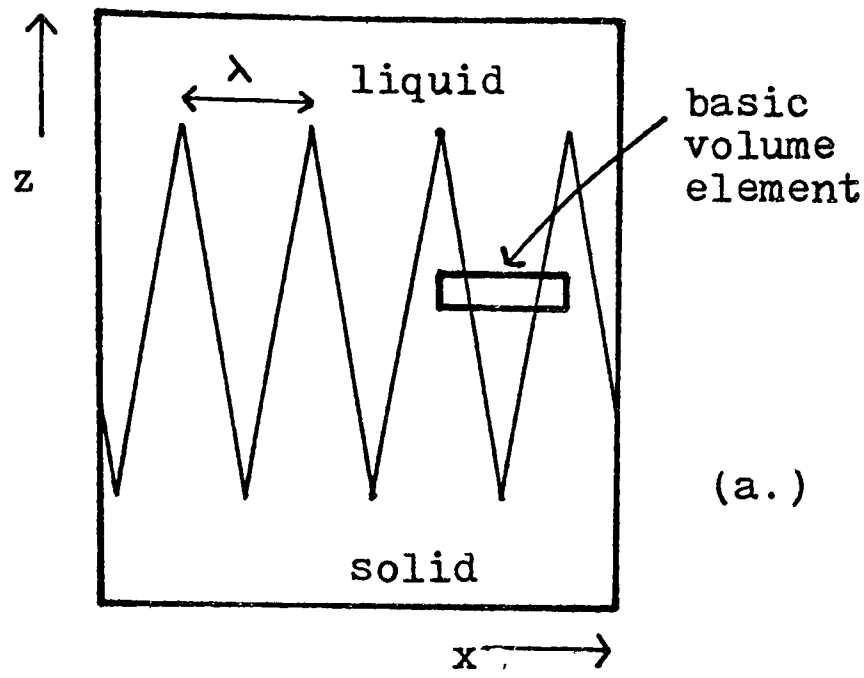
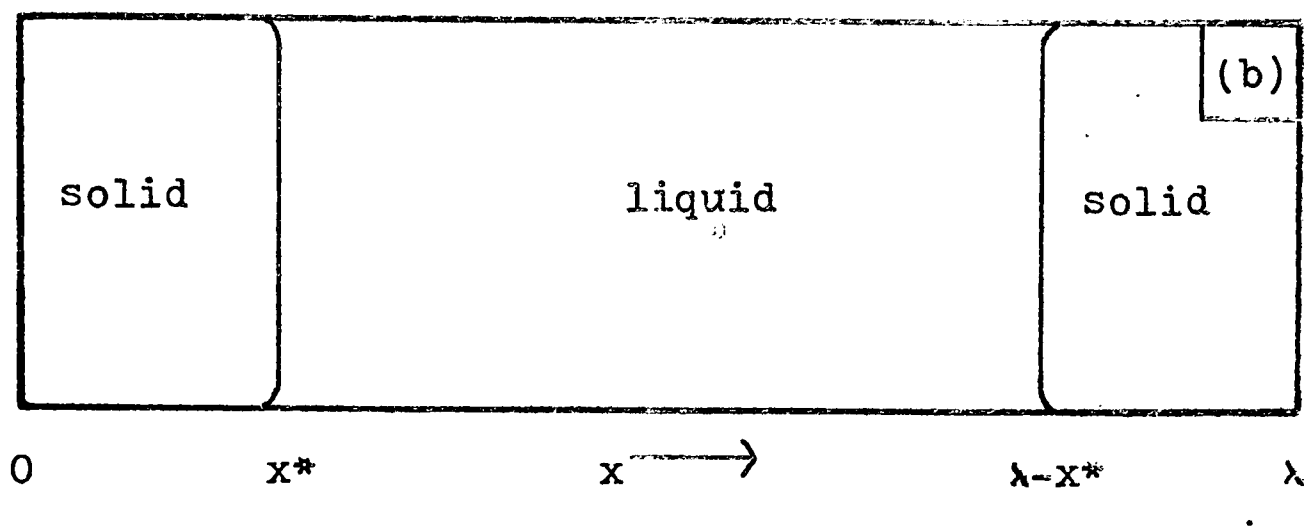


FIG. V. 1. Solidification model. (a.)The volume element used (schematic). (b.)The model.



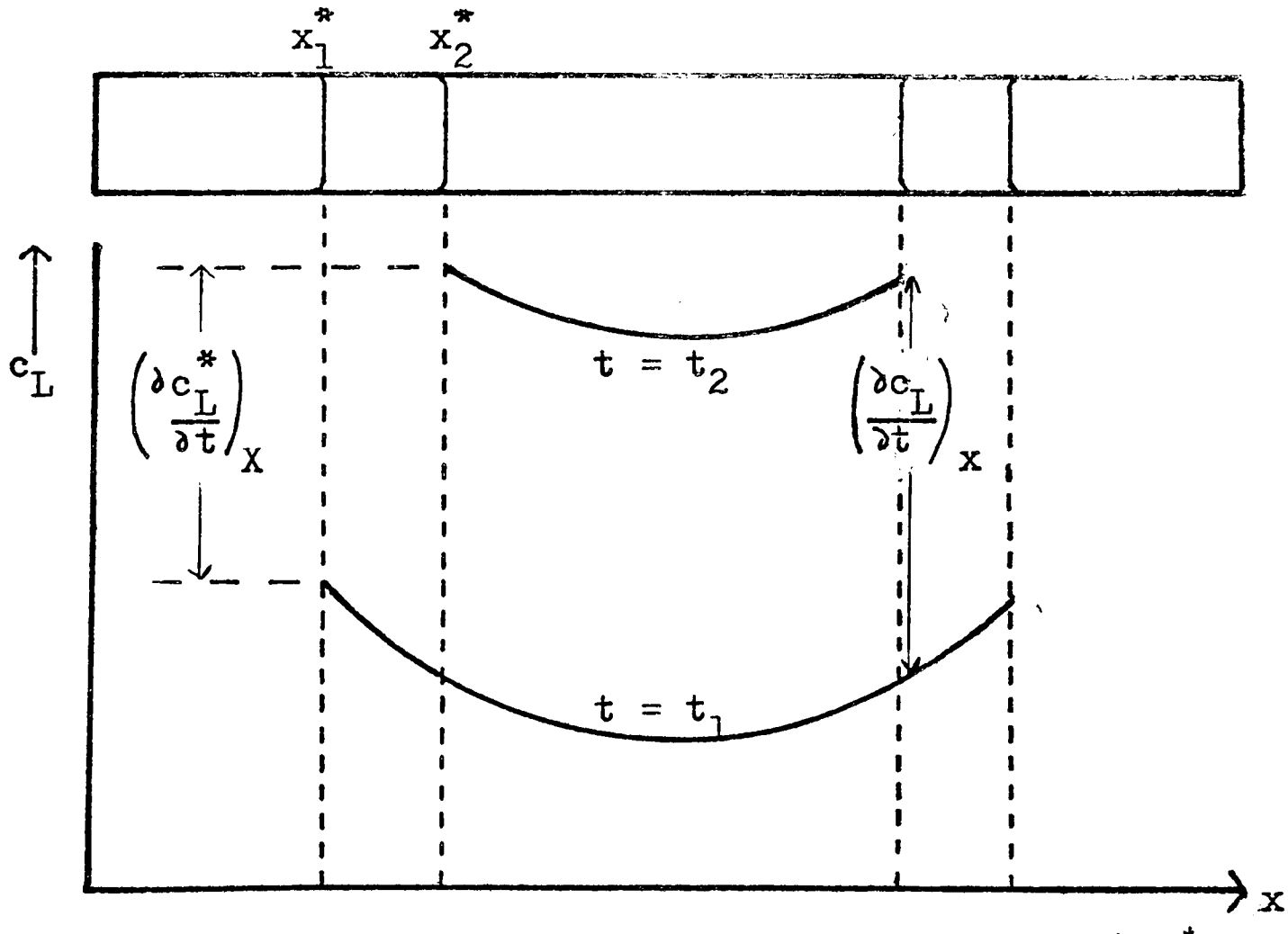


FIG. V. 2. Showing the difference between $(\partial c_L^*/\partial t)_X$ and $(\partial c_L/\partial t)_x$ (schematic). Interface is at x_1^* at $t = t_1$, x_1^* at $t = t_2$.

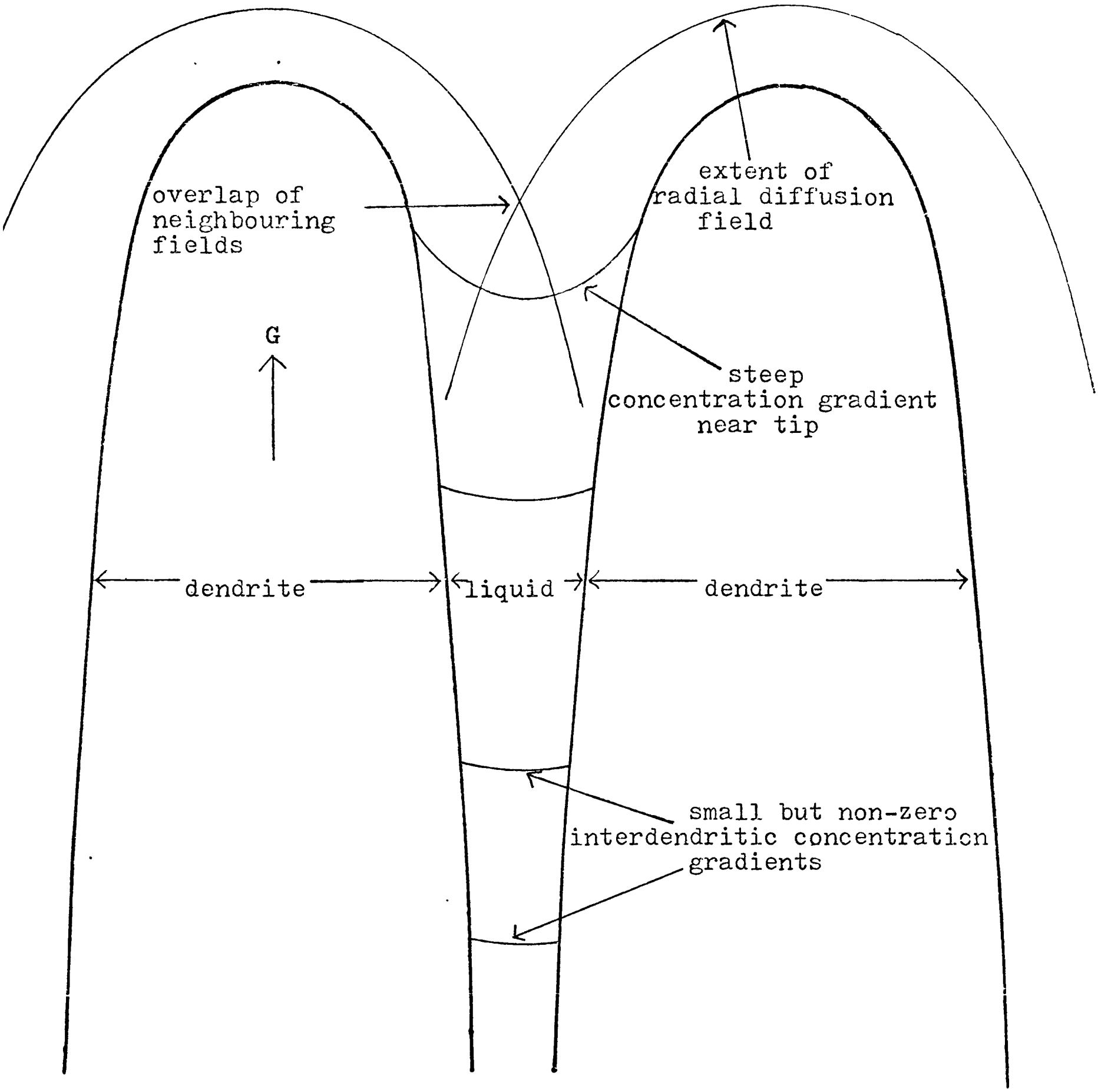


FIG. V. 3. Solute distributions during inter - dendritic solidification.

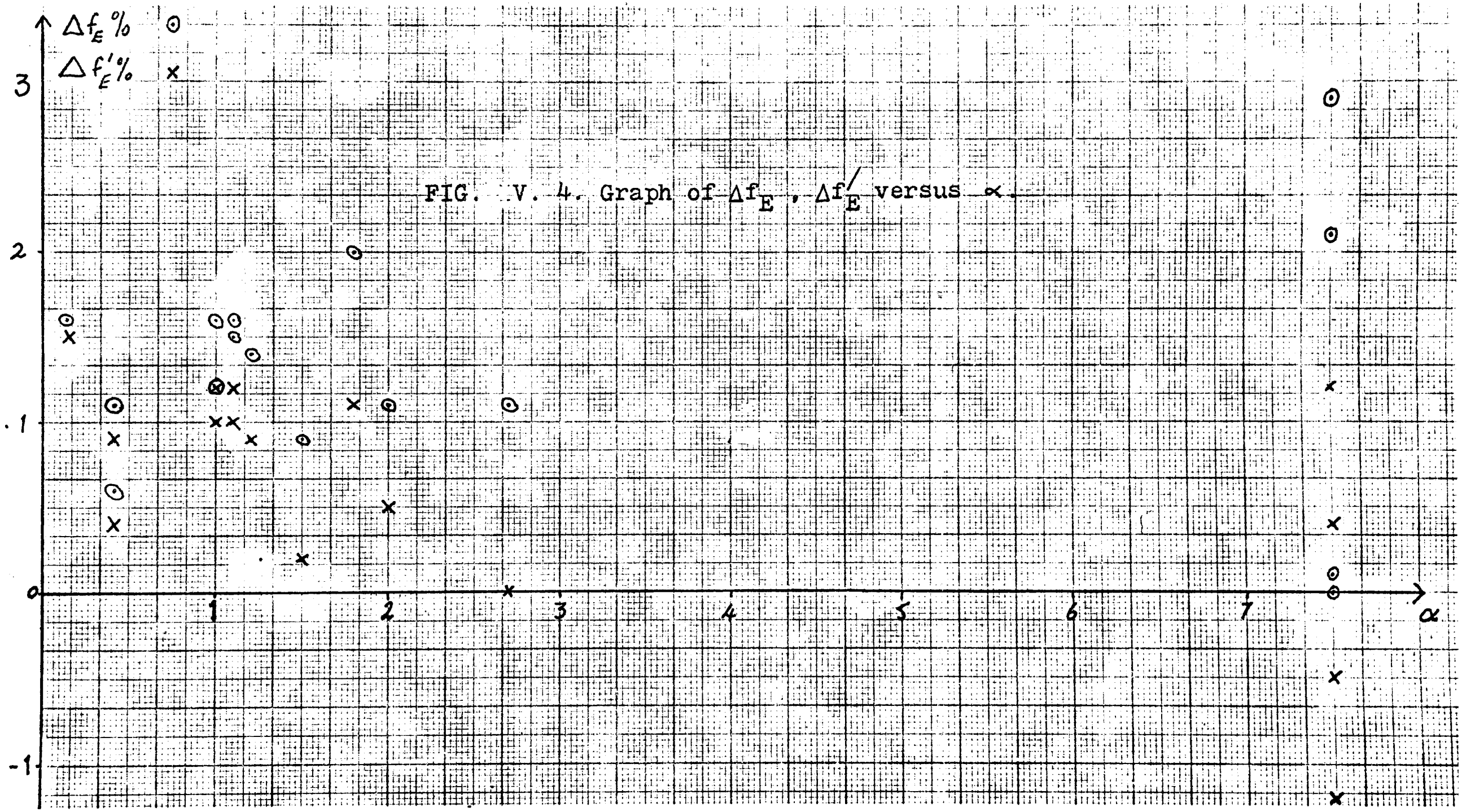


FIG. V. 4. Graph of Δf_E , $\Delta f_E'$ versus α

Chapter VI. "Temperature Gradient Zone Melting - Analysis"

Experimental and theoretical work on temperature gradient zone melting (TGZM) is presented in the following three chapters. The basic theory (this chapter) comes first, since the equations are required for calculations with experimental data (chapter VII). Various applications of the theory are discussed in chapter VIII and dislocation interactions are considered in chapter VII.

All the previous diffusion treatments, including our own,[1] have been based on simple assumed solute distributions. In the following section, the solute distribution during TGZM is calculated from first principles. Exact solutions are obtained only for a few special cases, but these solutions illustrate general behaviour and indicate good approximate solutions for a wide range of problems.

(a) Solute Distribution within Migrating Zones: Exact Solutions

(1) Basic Equations

We assume a planar zone perpendicular to the temperature gradient as shown in Fig VI.1. Three parallel z-type axes are defined in the temperature gradient direction (Fig. VII 13). The origin of the z axis is fixed to the specimen, while the origin of z_i moves with the interface of a migrating liquid region and the origin of z_p moves with the isotherms. If R is isotherm velocity, equal to dendrite growth velocity at steady state, while v is interface

velocity in the z direction:

$$R = \left(\frac{\partial z}{\partial t}\right)_{z_p} \quad \left(= -\left(\frac{\partial z_p}{\partial t}\right)_z\right) \tag{1}$$

$$v = \left(\frac{\partial z}{\partial t}\right)_{z_i} = \frac{dz^*}{dt} \tag{2}$$

where z^* is interfacial z coordinate. Following the procedure of Chapter V.(b), we may derive boundary conditions similar to (V.13) and (V.16) for each interface in Fig. VI.1. Adapting (V.9):

$$\left(\frac{\partial c_L}{\partial t}\right)_{z_i} = \left(\frac{\partial c_L}{\partial z}\right)_t \frac{dz^*}{dt} + \left(\frac{\partial c_L}{\partial t}\right)_z \tag{3}$$

in the bulk liquid. The derivation of interface equations in place of (V.11a) is more complex. Adapting (V.11):

$$\left(\frac{\partial c_L^*}{\partial t}\right)_{z_i} = \left(\frac{\partial c_L^*}{\partial T}\right)_{z_i} \left(\frac{\partial T}{\partial t}\right)_{z_i} \tag{4}$$

and, assuming a constant temperature gradient,

$$\left(\frac{\partial T}{\partial t}\right)_{z_i} = \left(\frac{\partial T}{\partial z}\right)_t \frac{dz^*}{dt} + \left(\frac{\partial T}{\partial z_p}\right)_z \left(\frac{\partial z_p}{\partial t}\right)_z = G(v - R) \tag{5}$$

Now, in (V.11), we used the local equilibrium assumption to specify $(\partial c_L^*/\partial T)_{z_i} = (1/m)$. In the present work, we use the less stringent restriction:

$$\Delta T_k = \text{constant} \tag{6}$$

for any given interface. Hence:

$$\left(\frac{\partial c_L^*}{\partial T}\right)_{z_i} = \frac{1}{m} \tag{7}$$

$$\therefore \quad \left(\frac{\partial c_L^*}{\partial t}\right)_{z_i} = \frac{G(v - R)}{m} \tag{8}$$

Combining (VI.3) and (VI.8):

$$\frac{G(v - R)}{m} = v\left(\frac{\partial c_L}{\partial z}\right)_t + \left(\frac{\partial c_L}{\partial t}\right)_z \tag{9}$$

replaces (V.14) at the interface in the liquid. Correspondingly:

$$\frac{kG(v - R)}{m} = v\left(\frac{\partial c_s}{\partial z}\right)_t + \left(\frac{\partial c_s}{\partial t}\right)_z \tag{10}$$

at the interface in the solid.

(2) Liquid-State Diffusion: Method of Chapter V.

In chapter V, an exact solution was found for the boundary condition (V.14) for the case $(\partial c_L/\partial t)_x$ = constant, equation (V.15). Such a solution was possible because the boundary conditions $c_L^*(x = x^*) = c_L^*(x = (\lambda - x^*))$ and $(\partial c_L/\partial t)_x\ (x = x^*) = (\partial c_L/\partial t)_x\ (x = (\lambda - x^*))$, implicit in (V.14), were compatible with the assumption (V.15). To investigate whether similar conditions can be fulfilled in TGZM, we rearrange (VI.9), using suffices m, f to denote the melting and freezing interfaces respectively:

$$\left(\frac{\partial c_L}{\partial t}\right)_z = \frac{-GR}{m} + v_f\left[\frac{G}{m} - \left(\frac{\partial c_L}{\partial z}\right)_t (z = z_f^*)\right] \text{ at } z = z_f^* \tag{11}$$

$$\left(\frac{\partial c_L}{\partial t}\right)_z = \frac{-GR}{m} + v_m\left[\frac{G}{m} - \left(\frac{\partial c_L}{\partial z}\right)_t (z = z_m^*)\right] \quad \text{at } z = z_m^* \tag{12}$$

and write the boundary conditions:

$$c_{Lf}^* = c + \frac{Gz_f^*}{m} + \frac{\Delta T_{kf}}{m} \tag{13}$$

$$c_{Lm}^* = c + \frac{Gz_m^*}{m} + \frac{\Delta T_{km}}{m} \tag{14}$$

where c is a constant.

There is only one simple solution for which $(\partial c_L/\partial t)_z$ is constant, but it is important. This is:

$$\left(\frac{\partial c_L}{\partial t}\right)_z = 0 \; : \; \left(\frac{\partial c_L}{\partial z}\right)_t = \frac{G}{m} \quad \text{everywhere} \tag{15}$$

under the conditions:

$$R = 0 \; ; \; \Delta T_{kf} = \Delta T_{km} = 0 \; : \; D_L = \text{constant.} \tag{16}$$

This solution is valid for any v_m or v_f, which (contrary to Tiller's statement[18]) may be large, unequal or time-dependent. For inclusions, extra terms $(\Delta T_c/m)$ are added to the right-hand sides of (VI.13) and (VI.14), and so the solution (VI.15) applies only with the additional restriction:

$$\Delta T_{cf} = \Delta T_{cm} = \text{constant} \tag{17}$$

This restricts the solution to spherical and cylindrical inclusions migrating without change of size or shape.

The solution (VI.15) is generally invalid if any of the restrictions (VI.16) is relaxed. If $R > 0$, c_L at a point must rise continuously and so the concentration profile is curved (Fig. VIII.13). If the ΔT_k terms are not zero, c_L at a point must also (in general) vary with time, as demonstrated in Fig. VIII.3. In these cases, the $(\partial c_L/\partial z)_t$ terms in (VI.11) and (VI.12) are unequal and so $(\partial c_L/\partial t)_z$ cannot generally be constant. If D_L is not constant along the liquidus line, the two equations in (VI.15) cannot be true simultaneously. A few special-case solutions can be found where $(\partial c_L/\partial t)_z$ is constant although some of the restrictions (VI.16) are removed: these solutions are obtained by a different method in the next section.

It is clear that the steady-state equation (I.14), commonly assumed when (VI.16) apply, is incorrect. A true steady state cannot be achieved unless c_{Lf}^* and c_{Lm}^* are held constant, and this only occurs if the specimen is cooled at the precise rate required to keep the migrating interfaces at constant temperature. The curved concentration profile and c_L (z) rising with time predicted by (I.15) may be contrasted with the linear concentration profile and constant c_L (z) of the exact solution (VI.15). Consequently (see chapter II(b)(2)) the first term on the right-hand side of (II.27) quoted from Jones's drop shape theory[144] should be removed. The supercoolings calculated by Hurle et al[129] for migrating zones do not exist, as c_L within planar zones always lies on the liquidus when (VI.16) apply. The morphological stability theories of TGZM[35,36] also require re-examination.

The solution (VI.15) represents a quasi-stationary diffusion field attained after an initial transient. The assumption (V.15) used here and in chapter V.(c) relies on the fact that, given $(\partial^2 c_L/\partial x^2)_t$ constant in space, $(\partial c_L/\partial t)_x$ is automatically constant in space and time because of Fick's second law (assuming D_L constant) and so a quasi-stationary diffusion field must be maintained. In the following section, we drop the assumption (V.15) and simply solve the diffusion equation (VI.3) on the assumption that a quasi-stationary solution exists.

(3) Liquid-State Diffusion: Quasi-Stationary Solutions

The assumption may be expressed as:

$$c_L = f(z_i) + g(t) \tag{18}$$

For compatibility with the two interfacial boundary conditions (VI.9), (VI.18) requires that:

$$v_f = v_m = \text{constant} \quad : \quad R = \text{constant} \tag{19}$$

Then, because of (VI.18), (VI.8) gives:

$$\left(\frac{\partial c_L}{\partial t}\right)_{z_i} = \left(\frac{\partial c_L^*}{\partial t}\right)_{z_i} = \frac{dg}{dt} = \frac{G(v - R)}{m} \tag{20}$$

$$\therefore \quad g = \frac{G(v - R)t}{m} + K \tag{21}$$

where K is constant. Now, from (VI.18),

$$\left(\frac{\partial c_L}{\partial z_i}\right)_t = \frac{df}{dz_i} \tag{22}$$

and since:

$$\left(\frac{\partial}{\partial z}\right)_t = \left(\frac{\partial}{\partial z_i}\right)_t \left(\frac{\partial z_i}{\partial z}\right)_t = \left(\frac{\partial}{\partial z_i}\right)_t \tag{23}$$

equations (VI.9), (VI.22) and (VI.23) give

$$\frac{d}{dz_i}\left(D_L \frac{df}{dz_i}\right) + v\frac{df}{dz_i} = \frac{G(v - R)}{m} \tag{24}$$

allowing for variable D_L. For a solution, $D_L(z_i)$ must be independent of time, or:

$$\left(\frac{\partial D_L}{\partial t}\right)_{z_i} = \left(\frac{\partial D_L}{\partial T}\right)_{z_i} \left(\frac{\partial T}{\partial t}\right)_{z_i} = 0 \tag{25}$$

If D_L varies with temperature, the restriction (VI.25) becomes

$$v = R \tag{26}$$

and, taking D_L to vary linearly with T,

$$D_L = D_{LO} + az_i \quad \text{where } a = dD_L/dz_i = G(dD_L/dT) \tag{27}$$

Then (VI.24) becomes:

$$(D_{LO} + az_i)\frac{d^2 f}{dz_i^2} + (v + a)\frac{df}{dz_i} = 0 \tag{28}$$

This is solved in Appendix B(a). Taking l = zone length and $z_i = 0$ at the freezing interface, the full solution for the case v = 0 is:

$$c_L = c_{Lf}^* + (c_{Lm}^* - c_{Lf}^*)\left[\frac{\ln(1 + az_i/D_{LO})}{\ln(1 + al/D_{LO})}\right] \qquad (B.9)$$

This solution is discussed in chapter VIII.(c). If D_L is constant, the restriction (VI.26) does not apply and (VI.24) becomes:

$$D_L \frac{d^2f}{dz_i} + v\frac{df}{dz_i} = \frac{G(v - R)}{m} \qquad (29)$$

This is solved in Appendix B(b). Taking $z_f^* = 0$ at $t = 0$, the boundary conditions (VI.13) and (VI.14) become:

$$f_f^* = c + \frac{\Delta T_{kf}}{m} \quad : \quad f_m^* = c + \frac{Gl}{m} + \frac{\Delta T_{km}}{m} \qquad (30)$$

and $K = 0$ in equation (VI.21). The solution for zone length l, freezing interface at $z_i = 0$, is given in (B.21). Combining this with (VI.21), the full solution is:

$$c_L = (c + \frac{\Delta T_{kf}}{m}) + (\frac{G(v - R)}{mv})(z_i + vt) + (\frac{(\Delta T_{km} - \Delta T_{kf})}{m} + \frac{GRl}{mv})$$
$$(\frac{(\exp(-vz_i/D_L)) - 1}{(\exp(-vl/D_L)) - 1}) \qquad (31)$$

or (using (VI.23)):

$$(\frac{\partial c_L}{\partial z})_t = \frac{G(v - R)}{mv} - (\frac{\Delta T_{km} - \Delta T_{kf}}{m} + \frac{GRl}{mv})(\frac{v}{D_L})(\frac{\exp(-vz_i/D_L)}{(\exp(-vl/D_L)) - 1}) \qquad (32)$$

(4) Solid-State Diffusion

Diffusion in the solid phase was not explicitly discussed in the previous two sub-sections. However, as will be shown

in (a)(5), solutions such as (B.9) or (VI.31) for the liquid phase actually impose very precise conditions for the behaviour in the solid phase. Thus, while the above solutions may be easily adapted to discuss diffusion in a planar solid zone $0 \leqslant z_i \leqslant l_s$ (Fig. VI.2), it must be noted that the solutions in the two phases are not generally applicable simultaneously.

Then in place of (VI.15):

$$\left(\frac{\partial c_s}{\partial t}\right)_z = 0 \quad ; \quad \left(\frac{\partial c_s}{\partial z}\right)_t = \frac{kG}{m} \quad \text{everywhere} \tag{33}$$

where:

$$R = 0 \quad ; \quad \Delta T_{kf}' = \Delta T_{km}' = 0 \quad : \quad D_s = \text{constant} \tag{34}$$

(see chapter VIII.(b) for definition of the $\Delta T_k'$ terms.)

In place of (B.9):

$$c_s = c_{sm}^* + (c_{sf}^* - c_{sm}^*)\left[\frac{\ln(1 + az_i/D_{sO})}{\ln(1 + al_s/D_{sO})}\right] \tag{35}$$

where:

$$D_s = D_{sO} + a_s z_i, \text{ where } a_s = G(dD_s/dt) \tag{36}$$

and:

$$v = R \quad ; \quad v_f = v_m = \text{constant} \quad : \quad R = \text{constant} \tag{37}$$

In place of (VI.31):

$$c_s = (c' + \frac{\Delta T_{km}'}{m}) + \left(\frac{kG(v - R)}{mv}\right)(z_i + vt) + \left(\frac{k(\Delta T_{kf}' - \Delta T_{km}')}{m}\right.$$

$$\left. + \frac{kGRl}{mv}\right)\left(\frac{(\exp(-vz_i/D_s)) - 1}{(\exp(-vl_s/D_s)) - 1}\right) \tag{38}$$

where:

$$v_f = v_m = \text{constant} \quad : \quad R = \text{constant}. \tag{39}$$

(5) Discussion

We have obtained exact solutions for diffusion in one phase during TGZM. As these apply only to special cases, approximate solutions will generally be required. We shall find that the exact solutions may be used to show what approximations are reasonable. Before the exact solutions are used in this way, we should consider the problem of describing diffusion in both phases simultaneously, the conditions pertaining to the use of quasi-stationary solutions, and morphological stability considerations.

The solute conservation equation (I.11), which links v, $(\partial c_L/\partial z)_t$ and $(\partial c_s/\partial z)_t$ at an interface, has not been used in these analyses. However, as v and $(\partial c_L/\partial z)_t$ have been allowed to vary independently in sub-sections (a)(2) and (3), $(\partial c_s/\partial z)_t$ at the interface has implicitly been fixed via (I.11): similarly, $(\partial c_L/\partial z)_t$ at the interface has been fixed in (a)(4). In principle, conditions in one phase may be adjusted arbitrarily in order to fulfil a condition such as (VI.19) for a diffusion solution in the other phase. For instance, for a specimen which is cooling ($R > 0$), the term $|D_L(\partial c_L/\partial z)_t|$ in (I.11) is higher for the freezing interface than for the melting interface (Fig. VIII.13). So, if $v_f = v_m$ as required by (VI.19), solute fluxes in the solid at these interfaces must be adjusted in compensation. Fluxes towards either interface are required: such fluxes would not generally be expected

in real situations (section (b)). So the conditions under which solutions (B.9) and (VI.31) are applicable may often be physically unrealistic, although they are always physically achievable. The solutions (VI.15) and (VI.33) are rather different, being valid for any v under the conditions (VI.16) and (VI.34) respectively, so that $(\partial c_L/\partial z)_t$ and $(\partial c_s/\partial z)_t$ remain independent variables. These solutions can therefore apply simultaneously: alternatively, one of these solutions may apply without specifying the behaviour in the other phase.

Quasi-stationary diffusion fields within a fixed region of space are generally attained after an initial transient. The associated relaxation time τ may be estimated from dimensional diffusion theory:

$$\tau_L \sim \frac{l^2}{D_L} \text{ (in liquid)} \quad ; \quad \tau_S \sim \frac{l_S^2}{D_S} \text{ (in solid)} \qquad (40)$$

In TGZM, the relevant region of space is not fixed, and so these formulae may not apply. As solid-state diffusion is generally slow, it may be more appropriate to take $\tau_S \sim (l_S/v)$.

It seems clear that, provided the interfaces remain planar, the initial solute distribution should relax towards the quasi-stationary distribution rather than away from it. This is demonstrated for solution (VI.15) in Fig. VI.3. However, a full stability treatment should consider the possibility of planar interface breakdown. The existing stability treatments[35,36] are suspect because they are

based on the assumption of the steady-state equation to describe the initial unperturbed state. As this does not represent the correct quasi-stationary solution, it must change with time and this may appear as the growth of the perturbation when the perturbed diffusion equation is solved. So the present treatments, which generally predict instability for planar zones, may be unduly pessimistic. For inclusions and dendrite sidearms, the curvature effect should act as an additional stabilizing factor.

(b) Solute Distribution Within Migrating Zones: Approximate Solutions.

We will derive approximate solutions from the exact solutions (VI.31) and (VI.38) which are reasonable under specified conditions. In the liquid phase, the diffusion coefficient is high and it may be reasonable to assume that the characteristic diffusion distance (D_L/v) is much greater than the zone length. Expanding exponentials in (VI.31), dropping v^4 and higher-order terms but making no other approximations, we may derive:

$$c_L = \left(c + \frac{\Delta T_{kf}}{m}\right) + \frac{G(v - R)t}{m}$$
$$+ \left(\frac{\Delta T_{km} - \Delta T_{kf}}{m}\right)\left(\frac{z_i}{l}\right)\left(\frac{1 - (vz_i/2D_L) + (v^2 z_i^2/6D_L^2)}{1 - (vl/2D_L) + (v^2 l^2/6D_L^2)}\right)$$
$$+ \left(\frac{Gz_i}{m}\right)\left[1 + \left(\frac{R(1 - z_i)}{2D_L}\right)\left(\frac{1 - (v(1 + z_i)/3D_L)}{1 - (vl/2D_L) + (v^2 l^2/6D_L^2)}\right)\right] \qquad (41)$$

Since $0 \ll z_i \ll 1$, our neglect of the higher-order terms in

the exponential expansion is reasonable if:

$$\frac{vl}{2D_L} \ll 1 \tag{42}$$

Then,if we assume (VI.42) and use the approximation:

$$\frac{1}{1+x} \sim 1 - x \quad \text{when } x \ll 1 \tag{43}$$

then (VI.41) becomes:

$$c_L = (c + \frac{\Delta T_{kf}}{m}) + \frac{G(v - R)t}{m} + (\frac{\Delta T_{km} - \Delta T_{kf}}{m})(\frac{z_i}{l})(1 + \frac{v(1 - z_i)}{2D_L})$$

$$+ (\frac{Gz_i}{m})\left[1 + (\frac{R(1 - z_i)}{2D_L})(1 + \frac{v(1 - 2z_i)}{6D_L})\right] \tag{44}$$

or, approximating further using (VI.42):

$$c_L = (c + \frac{\Delta T_{kf}}{m}) + \frac{G(v - R)t}{m} + (\frac{\Delta T_{km} - \Delta T_{kf}}{m})(\frac{z_i}{l})$$

$$+ (\frac{Gz_i}{m})(1 + \frac{R(1 - z_i)}{2D_L}) \tag{45}$$

If:

$$\frac{Rl}{2D_L} \ll 1 \tag{46}$$

then (VI.44) becomes:

$$c_L = (c + \frac{\Delta T_{kf}}{m}) + \frac{G(v - R)t}{m} + (\frac{Gl + \Delta T_{km} - \Delta T_{kf}}{m})(\frac{z_i}{l})(1 + \frac{v(1 - z_i)}{2D_L}) \tag{47}$$

Approximating further using (VI.42):

$$c_L = c + \frac{G(v - R)t}{m} + \frac{Gz_i}{m} \tag{49}$$

so that, using (VI.23):

$$\left(\frac{\partial c_L}{\partial z}\right)_t = \frac{G}{m} \tag{50}$$

These approximate solutions, being derived from (VI.31), are subject to the restrictions (VI.19). However, physical understanding allows us to show that they may still be good approximate solutions when the restrictions are removed. The dependence of $(\partial c_L/\partial z)_t$ on v in (VI.31) is ultimately derived from the inclusion of the first term on the right-hand side of (VI.3), which is similar to the first term on the right-hand side of (V.14). We have now shown that this term is small (equation (VI.45)) when $vl/2D_L \ll 1$, equation (VI.42). Obviously, this conclusion does not depend on the restriction $v_m = v_f$ = constant from (VI.19) and so equation (VI.45) may be applied without this restriction. Similarly, the dependence of $(\partial c_L/\partial z)_t$ on R (Fig. VIII.13) arises from the continuous increase in $c_L(z_i)$ with solidification. When $Rl/2D_L \ll 1$, (VI.47) shows that the curvature of the concentration profile required to give the correct rate of increase of $c_L(z_i)$ is negligible. This conclusion does not depend critically on the restriction R = constant from (VI.19) and so (VI.47) may be applied when R varies, except for violent thermal fluctuations.

In some cases, where diffusion in the solid is unusually rapid (e.g. carbon in iron) the above approximations may also apply in the solid phase. In general, however, it is likely that the opposite approximation to (VI.42):

$$\frac{vl_s}{D_S} \gg 1 \tag{51}$$

may be applied. In this case, $(\exp(- vl_S/D_S)) \ll 1$, Hence, the differential form of (VI.38) becomes:

$$\left(\frac{\partial c_S}{\partial z}\right)_t = \frac{kG(v - R)}{mv} + \left[\frac{k(\Delta T_{kf}' - \Delta T_{km}')}{m} + \frac{kGRl_S}{mv}\right]\left(\frac{v}{D_S}\right)\left(\exp\left(\frac{-vz_i}{D_S}\right)\right) \tag{52}$$

Thus, at $z_i = 0$, assuming local equilibrium:

$$\left(\frac{\partial c_S}{\partial z}\right)_t = \left(\frac{-kGR}{mv}\right)\left[\left(\frac{R - v}{R}\right) - \frac{vl_S}{D_S}\right] \tag{53}$$

and, taking $\left[(R - v)/R\right] \sim 1$ and approximating further using (VI.51):

$$\left(\frac{\partial c_S}{\partial z}\right)_t = \left(\frac{kGR}{mv}\right)\left(\frac{vl_S}{D_S}\right) \qquad \text{at } z_i = 0 \tag{54}$$

At $z_i = l_S$, assuming local equilibrium, (VI.52) gives:

$$\left(\frac{\partial c_S}{\partial z}\right)_t = \left(\frac{-kGR}{mv}\right)\left[\left(\frac{R - v}{R}\right) - \left(\frac{vl_S}{D_S}\right)\left(\exp\left(\frac{-vl_S}{D_S}\right)\right)\right] \tag{55}$$

This should be compared to (VI.53). When $p \ll 1$, the term $(p \exp(-p)) \ll 1$. So, again taking $\left[(R - v)/R\right] \sim 1$, we may approximate (VI.55) further:

$$\left(\frac{\partial c_S}{\partial z}\right)_t = -\left(\frac{kGR}{mv}\right)\left(\frac{R - v}{R}\right) \qquad \text{at } z_i = l_S \tag{56}$$

So, comparing (VI.54) and (VI.56):

$$(\frac{\partial c_S}{\partial z})_t (z_i = 0) \sim (\frac{-vl_S}{D_S})(\frac{\partial c_S}{\partial z})_t (z_i = l_S) \qquad (57)$$

and, using (VI.51), we thus show that the concentration gradient at the melting interface is much greater than that at the freezing interface. The use of these approximate solutions is discussed in the following chapters.

(c) Solute Distributions Outside Migrating Zones

The solutions in sections (a) and (b) may be applied to solid-state diffusion between two migrating liquid zones after the initial transient (Fig. VI.2), but not to solid-state diffusion associated with the migration of an isolated liquid zone or droplet (Fig. VI.4), or to solid-state diffusion with the morphology of Fig. VI.2. before completion of the initial transient. In this last case, as noted following (VI.40), the initial transient may persist until the solid zone has migrated a distance equal to its own thickness l_S. During this time, the liquid zones of Fig. VI.2 are probably best treated as isolated zones.

Our previous work (ref. 1, chapter VI.(g)) included a discussion of solid-state diffusion ahead of a planar melting interface, based on the assumption of the steady-state equation. Solid-state diffusion must occur when the melting interface composition c_{Sm}^* differs from the bulk solid composition far from the melting interface, $c_{S\infty}$ (Fig. VI.4.b). The "steady-state" solution is:[1]

$$D_S(\frac{\partial c_S}{\partial z})_t = -v_m(c_{Sm}^* - c_{S\infty}) \qquad (58)$$

at the melting interface, so that (I.14) gives:

$$v_m(c_L^* - c_{S\infty}) = -D_L\left(\frac{\partial c_L}{\partial z}\right)_t \text{ at melting interface} \qquad (59)$$

in agreement with Tiller's intuitive solution quoted following (II.14). We now see that, as in (b)(2), the steady-state solution is only exact if c_{Sm}^* is constant, or:

$$v_m = R \qquad (60)$$

To investigate how good an approximation (VI.58) is in other cases, we go back to equation (VI.10). For this to approximate the steady-state equation:

$$\frac{kG(v_m - R)}{m} \ll v_m\left(\frac{\partial c_S}{\partial z}\right)_t \text{ at melting interface} \qquad (61)$$

or, with (VI.58):

$$\frac{kG(v_m - R)D_S}{mv_m^2(c_S^* - c_{S\infty})} \ll 1 \qquad (62)$$

This represents the condition that $(\partial c_S^*/\partial t)_{z_i} \ll (\partial c_S/\partial t)_z$ and is fulfilled for high temperature gradients and low cooling rates.

The initial transient time associated with the establishment of this diffusion profile should be the length of the diffusion profile, $\sim (D_S/v_m)$, divided by the velocity v_m. Thus when $(D_S/v_m) \ll l_S$ in Fig. VI.2, (VI.59) rapidly becomes applicable while (VI.54) becomes applicable much later, after a time $\tau \sim (l_s/v_m)$.

For the case of Fig. VI.2., when $v_f = v_m$ = constant and $(D_S/v_m) \ll l_s$, it might be thought reasonable to use (VI.58) as an approximation after the transient period, with

$c_{s\infty}$ in front of the melting interface given by:

$$(c_{sf}^{*} - c_{s\infty}) = (\frac{l_s}{v_f})(\frac{\partial c_{sf}^{*}}{\partial t})_{z_i} \qquad (63)$$

This may be shown to give an identical value for $(\partial c_s/\partial z)_t$ at the melting interface to that predicted in (VI.54). The approximation (VI.63) is readily justifiable physically since, in Fig. VI.2, only a narrow region ahead of the melting interface is affected by solid-state diffusion, and the composition beyond this region is virtually constant and approximately as given by (VI.63). So the coincidence between (VI.63) and (VI.54) lends justification to the assumption that (VI.54) is valid in real situations after a transient $\tau_s \sim (l_s/v)$.

For diffusion behind the freezing interface, an approximate solution may be obtained by neglecting the second term of (VI.10). This is similar to the approximation (V.1), and overestimates solid-state diffusion behind an isolated migrating zone. The result derived is identical to (VI.56).

(d) TGZM of Droplets and Inclusions

In this section, our previous analyses are modified to deal with migrating inclusions. Firstly, we discuss the concept of "force" on a migrating droplet used by Nichols[121] and others (chap. II.(b)(7).)

(1) Force Models

Nichols claimed that the "force" model usefully simplified migration calculations, since driving force in a given situation and inclusion mobility by a selected

diffusion path were calculated independently, so that the migration velocity was simply determined by multiplying together the relevant mobility and force terms. However, our calculation method makes an entirely analogous separation between calculations of diffusive flux at the interface (sections (a) - (c)) and the term ($c_L^* - c_S^*$) in (I.11). Furthermore, we will show that the operative diffusion path during migration depends on the nature of the applied "force", so that not all combinations of "force" and "mobility" are valid.

At least four kinds of "force" may be distinguished. These are: (i). body forces - e.g. gravity, magnetism. These forces act on all the separate atoms in an inclusion and their effects on different types of atom need not necessarily be different. To preserve mechanical equilibrium, these forces must be balanced by a net force arising from stresses in the matrix:[126]

$$\vec{F} = -\int_S \sigma_{rr} \cos\Theta dS \qquad (64)$$

where F is the body force, $\int_S$ a surface integral over the inclusion surface, Θ the angle between F and the surface-normal, and σ_{rr} the radial dilatational stress at the interface. We may show that (VI.64) implies a difference in average curvature undercoolings between opposite ends of the drop when $\vec{F} \neq 0$. From Geguzin and Krivoglaz,[126] we quote the strss boundary conditions at the surface of a pore or liquid droplet:

$$\sum_j \sigma_{ij} n_j = -(p_L - p_\sigma) n_i \qquad (65)$$

where p_L is the pressure in the droplet and p_σ is the excess pressure due to the curvature effect. But since tangential stresses relax to zero at the surface, (VI.65) simplifies to:

$$\sigma_{nn} = -(p_L - p_\sigma) \qquad (66)$$

where σ_{nn} is dilatational stress normal to the interface, equal to σ_{rr} for a spherical droplet. Thus, when $\vec{F} = 0$, and surface energy σ is constant, (VI.64) and (VI.66) are satisfied for a spherical droplet. When $\vec{F} \neq 0$, the droplet is distorted and its curvature undercooling (related to p_σ) varies. An analytic treatment then becomes complex since $\sigma_{nn} \neq \sigma_{rr}$ but it should be clear that $(\int_S \Delta T_c \cos\theta \, dS) \neq 0$ and there is therefore a difference in average composition between opposite ends of the drop. This, and other effects of the body force, should generally cause migration. A simple argument demonstrates, however, that there is no simple relation between migration rate and body force. In a gravitational field, one factor causing migration is the sedimentation flux[192] (diffusion biased by gravity). This will be greater in an inclusion composed of 50% A stoms of mass m and 50% B atoms of mass 4m than in a similar inclusion with atom masses 2m and 3m, yet the body forces on the two inclusions are equal.

(ii). surface forces - e.g. intersecting dislocations, grain boundaries. These forces act on inclusion surfaces rather than the individual atoms, and cause migration via

surface distorsion. Equation (VI.64) is applicable with $\vec{F}$ = surface force.

(iii) diffusional "forces" - e.g. "force" due to the presence of a thermal gradient or electric field. The phenomenological theory of diffusion, which relates diffusion to energy gradients, allows us to express the effects of e.g. concentration gradients in dimensions of "force". However, (VI.64) does not apply and so these "forces" are quite different from body or surface forces.

(iv) elastic interactions - e.g. "force", measured as rate of change of elastic energy in the matrix with separation distance, between two liquid droplets. Again, this does not represent a mechanical force on the droplets since σ_{nn} must relax to the value given by (VI.66) at the drop surface so that, for a spherical droplet, σ_{nn} is constant over the surface. (VI.64) therefore does not apply to this "force" and the droplets remain undistorted. Also, since $\vec{F} = 0$ in (VI.64) (unless a body force is also present), there is no pressure gradient within the droplets. Consequently, liquid-state diffusion will not act to move the droplets relative to each other and so a combination of elastic "force" with liquid-diffusion "mobility" is not valid. Solid-state diffusion, resulting from chemical potential gradients in inhomogeneous stress fields,[126] will indeed occur but this form of migration will be very slow. Geguzin and Krivoglaz[126] postulated a curvature equation replacing σ_{nn} in (VI.66) with $(\frac{1}{3}\sigma_{ii})$ when surface equilibrium takes place by surface diffusion (chap. II (b)(7)). As $\sigma_{\theta\theta}$ and $\sigma_{\phi\phi}$ do not relax to zero at the drop surface this

equation would indicate that $p_{\sigma-}$ and hence ΔT_c are altered by elastic interactions. However, this type of equilibration seems likely only when surface diffusion is dominant.

The "force" model can give correct results and provide a convenient mental picture. But there are many pitfalls and a more direct diffusion analysis is always possible.

(2) Droplet Shapes

As in section (a) we first look for exact solutions to the diffusion equation in migrating droplets (Fig. VI.4). Unfortunately, the conditions for a quasi-stationary solution are very rigorous. As in (a)(2 - 4):

$$\left(\frac{\partial c_L}{\partial t}\right)_{z_i} = \text{constant} \tag{67}$$

but addtitionally, in all cases, constant shape requires:

$$v_n = v\cos\theta \quad \text{over the surface} \tag{68}$$

where v_n is interface velocity along the surface-normal, θ the angle between the surface-normal and the migration direction, and v the migration velocity. Now, (VI.67) and (VI.68) can be satisfied for a spherical droplet, but since, from (I.11):

$$v_n(c_L^* - c_s^*) = -D_L(\partial c_L/\partial n)_t + D_S(\partial c_s/\partial n)_t \tag{69}$$

and, from (VI.15):

$$\left(\frac{\partial c_L}{\partial n}\right)_t = \frac{G}{m} \cos\theta \tag{70}$$

this only occurs if:

$$\frac{-D_L G}{m(c_L^* - c_s^*)} + \frac{D_s(\partial c_s/\partial n)}{(c_L^* - c_s^*)\cos\theta} = \text{constant over the surface} \tag{71}$$

i.e. when there is no solid-state diffusion and D_L and $(c_L^* - c_s^*)$ are independent of temperature. In general, these conditions do not apply exactly and the droplet is therefore distorted.

Previous shape distortion analyses of interface kinetics assumed, in effect:[161,144]

$$\left(\frac{\partial c_L^*}{\partial z}\right)_t \text{ (on surface)} = \left(\frac{\partial c_L}{\partial z}\right)_t \text{ (in bulk)} \tag{72}$$

at a given z_i, as illustrated in Fig. VI.5. This ensures one-dimensional diffusion in the liquid and thus roughly ensures (VI.68) when solid-state diffusion fluxes are small compared to liquid-state fluxes and the fractional variations of D_L, $(c_L^* - c_s^*)$ and other parameters across the drop are small. We will use (VI.72) in a simple analysis.

As shown in Fig. VI.6, droplets with slow melting kinetics should be flattened in the migration direction while droplets with slow freezing kinetics should be elongated.[161,145] We shall consider three other possible causes of distorsion. In a $k < 1$ system, $(c_L^* - c_s^*)$ is lower at the melting interface which therefore tends to migrate faster.

The droplet then elongates until this factor is compensated by a higher solute flux, resulting from the curvature effect, at the freezing interface. If D_L increases with temperature, the droplet again elongates until the higher concentration gradient at the cold end compensates higher D_L at the hot end. The main effect of solid-state diffusion (see (VI.57)) is to retard the melting interface. We may assume (VI.58) at $z_i = 1$ (Fig. VI.4) provided that $(D_s/v_m) \ll$ drop radius. This tends to flatten the droplet until additional fluxes due to curvature are set up in the liquid, increasing v_m and reducing v_f.

We assume that the droplet is a prolate spheroid (ellipsoid of revolution) and hence calculate the compositions on the interface, c_{Lf}^* at $z_i = 0$, c_{Ls}^* at $z_i = \frac{1}{2}l$, and c_{Lm}^* at $z_i = 1$, using (I.2). Radii of curvature are calculated by Mellor[254] p. 181 (or see Jones[144]). The result is:

$$\left(\frac{c_{Ls}^* - c_{Lm}^*}{c_{Lf}^* - c_{Ls}^*}\right) = \frac{Gl + 4\Theta_c l^{-1}\varrho}{Gl - 4\Theta_c l^{-1}\varrho} \qquad (73)$$

assuming local equilibrium, where the shape distorsion parameter;

$$\varrho = q + q^{-1} - 2q^2, \text{ where } q = l/w \qquad (74)$$

and l is length, w width of the droplet. Now, if a steady state can be achieved, $v_m = v_f$. We first assume that this is possible, in which case (I.11) gives:

$$\frac{-D_{Lf}}{(c_{Lf}^{*} - c_{Sf}^{*})}\left(\frac{\partial c_L}{\partial z}\right)_t (z_i = 0) = \frac{-D_{Lm}}{(c_{Lm}^{*} - c_{Sm}^{*})}\left(\frac{\partial c_L}{\partial z}\right)_t (z_i = 1)$$

$$+ \frac{D_S}{(c_{Lm}^{*} - c_{Sm}^{*})}\left(\frac{\partial c_S}{\partial z}\right)_t (z_i = 1) \qquad (75)$$

where the solid-state diffusion term can be accounted for (from (VI.58) and (I.11)) by incorporation into the first term on the right of (VI.75):

$$\frac{D_{Lf}}{(c_{Lf}^{*} - c_{Sf}^{*})}\left(\frac{\partial c_L}{\partial z}\right)_t (z_i = 0) = \frac{-D_{Lm}}{(c_{Lm}^{*} - c_{Sm}^{*}) + (c_{Sm}^{*} - c_{S\infty}^{*})}$$

$$\times \left(\frac{\partial c_L}{\partial z}\right)_t (z_i = 1) \qquad (76)$$

and from (VI.27):

$$D_{Lf} = D_{Lm} - al \qquad (77)$$

and, assuming local equilibrium:

$$(c_{Lf}^{*} - c_{Sf}^{*}) = (c_{Lm}^{*} - c_{Sm}^{*}) - Gl(1 - k)/m \qquad (78)$$

Combining (VI.76 - 78):

$$\frac{(\partial c_L/\partial z)_t \ (z_i = 1)}{(\partial c_L/\partial z)_t \ (z_i = 0)} = \left(1 + \frac{Gl}{mc_{Lf}^{*}}\right)\left(\frac{1}{1 + al/D_{Lf}}\right)\left(1 + \frac{(c_{Sm}^{*} - c_{S\infty})}{(c_{Lm}^{*} - c_{Sm}^{*})}\right) \qquad (79)$$

Now, using (VI.72), approximately:

$$\left(\frac{\partial c_L}{\partial z}\right)_t (z_i = 0) = \frac{-2(c_{Lf}^* - c_{Ls}^*)}{l} : \left(\frac{\partial c_L}{\partial z}\right)_t (z_i = 1) = \frac{-2(c_{Ls}^* - c_{Lm}^*)}{l} \quad . \tag{80}$$

and so (VI.79) and (VI.80) may be combined with (VI.73) to obtain:

$$\left(\frac{Gl + 4\Theta_c l^{-1}\rho}{Gl - 4\Theta_c l^{-1}\rho}\right) = \left(1 + \frac{Gl}{mc_{Lf}^*}\right)\left(\frac{1}{1 + al/D_{Lf}}\right)\left(1 + \frac{(c_{Sm}^* - c_{S\infty})}{(c_{Lm}^* - c_{Sm}^*)}\right) \tag{81}$$

However, the steady state discussed here is not a physical possibility when solid-state diffusion and the differential migration effect represented by (VI.78) occur. To see this, consider Fig. VI.7 in which we ignore varying D_L and solid-state diffusion and consider only the differential migration effect. For a planar zone, (VI.50) applies and so the velocities of the planar melting and freezing interfaces, v_{mp} and v_{fp}, are different. Also, from (VI.50), $(\partial c_L/\partial t)_z = 0$. This is reasonable because, considering the zone migrating past a fixed position z, the composition $c_L(z)$ will be c_{Lm}^* at some time and c_{Lf}^* at a later time, and, as T(z) is constant and local equilibrium applies, these compositions will be equal. So it is necessary that the average value of $(\partial c_L/\partial t)_z$ should be zero. Now consider a cylindrical droplet of cross-section as shown in Fig.VI.7. Again, the average $(\partial c_L/\partial t)_z$ during drop migration past a point must be zero, yet if diffusion is one-dimensional from (VI.72) and $(\partial c_L/\partial z)_t$ varies with z_i as in (VI.79),

$c_L(z)$ must continually increase. So the steady state is not possible: instead, the drop expands in all directions and a positive $(D_L(\partial^2 c_L/\partial z^2)_t)$ term is roughly counterbalanced by a negative $(D_L(\partial^2 c_L/\partial x^2)_t)$ term to keep $(\partial c_L/\partial t)_z \sim 0$ within the droplet (Fig. VI.7). Thus, the curvature of the $c_L(z)$ plot along the central axis of the droplet is not as pronounced as predicted in (VI.79), but the curvature of the $c_L^*(z)$ plot versus z along the drop surface is greater than this and it is therefore not obvious whether the real shape distorsion is greater or less than as predicted by (VI.81). A simple argument will be used to investigate this question.

We now denote the actual composition at $z_i = \frac{1}{2}l$ and $x = \pm \frac{1}{2}l$ by c_{Ls}^*, while the composition at this point predicted by our steady-state treatment becomes $c_{Ls}^{*\prime}$. We write c_{Lc} for the drop centre composition at $z_i = \frac{1}{2}l$, $x = 0$ (see Fig. VI.7). To obtain a solution, we assume that $(\partial^2 c_L/\partial z^2)$ is constant along the axis $x = 0$ while $(\partial^2 c_L/\partial x^2)$ is constant on $z = 0$ and also assume that the droplet cross-section is almost circular. Then, we assume:

$$\left(\frac{\partial c_L}{\partial t}\right)_z = D_L \left(\frac{\partial^2 c_L}{\partial z^2}\right)_t + \left(\frac{\partial^2 c_L}{\partial x^2}\right)_t = 0 \qquad (82)$$

at the drop centre. This implies:

$$\tfrac{1}{2}(c_{Lf}^* + c_{Lm}^*) - c_{Lc} = c_{Lc} - c_{Ls}^* \qquad (83)$$

and also:

$$-J_f - J_m = 2J_s = K\left[\tfrac{1}{2}(c_{Lf}^{*} + c_{Lm}^{*}) - c_{Lc}\right] \tag{84}$$

where J is liquid-state diffusion flux at the interface along the outward surface-normal and K is a constant. When $(-J_f) = J_m$, $(v_m - v_f) = (v_{mp} - v_{fp})$: when $c_{Lc} = c_{Ls}^{*/}$ as in the steady-state treatment, $(v_m - v_f) = 0$. Consequently (provided $\Delta T_C \ll mc_L^{*}$, see (d)(3)) :

$$(v_m - v_f) = \left(1 - \frac{\tfrac{1}{2}(c_{Lf}^{*} + c_{Lm}^{*}) - c_{Lc}}{\tfrac{1}{2}(c_{Lf}^{*} + c_{Lm}^{*}) - c_{Ls}^{*/}}\right)(v_{mp} - v_{fp}) \tag{85}$$

Equations (VI.84), and (VI.85) are simultaneously satisfied when:

$$\tfrac{1}{2}(c_{Lf}^{*} + c_{Lm}^{*}) - c_{Lc} = \tfrac{1}{2}\left[\tfrac{1}{2}(c_{Lf}^{*} + c_{Lm}^{*}) - c_{Ls}^{*/}\right] \tag{86}$$

or, using (VI.83):

$$c_{Ls}^{*} = c_{Ls}^{*/} \tag{87}$$

This means that $(v_m - v_f)$ is half what it is for the planar case while the sides move out at velocity $\pm \tfrac{1}{4}(v_{mp} - v_{fp})$ along the x axis. (VI.87) shows that the steady-state analysis actually obtains the correct shape distorsion, equation (VI.81), if not for the correct reasons. (The shape distorsion parameter ρ in (VI.74) is incorrect for cylinders, however.)

A similar analysis may be carried out for distorted spherical droplets. Then, an extra $(\partial^2 c_L/\partial y^2)$ term appears on the right of (VI.82) and so a multiplying factor 2

appears on the right of (VI.83), while the centre of (VI.84) becomes $4J_s$ and (VI.85) is unchanged. Then the coefficient in front of the square brackets in (VI.86) alters from $\frac{1}{2}$ to $\frac{2}{3}$ but (VI.87) is again obtained, validating (VI.81) for real droplets. Now $(v_m - v_f) = \frac{1}{3}(v_{mp} - v_{fp})$: a general result is that an n-dimensional droplet changes in length at (1/n) times the rate for an equivalent planar zone.

Similar arguments may be used to validate (VI.81) approximately for droplets shrinking because of solid-state diffusion ahead of the melting interface (shrinking will generally occur, because $c_{\zeta\infty} > c_{Sm}^*$ implies the existence of superheated solid in most cases). The solid-state diffusion term in (VI.81) is, however, rather crude because (VI.58) only applies at $z_i = 1$ and diffusion over the rest of the melting interface has been glossed over. There will also be increased solid-state diffusion when (D_S/v_m) is significant or large by comparison with drop radius.

(3) Droplet Velocities

In this section, we consider the effects of solid-state diffusion ahead of the melting interface, and of interfacial curvature, on droplet migration velocities. From the above analysis (because of the assumption that $(\partial^2 c_L/\partial z^2)$ is independent of z_i), the droplet centre-of-mass velocity:

$$\bar{v} = \tfrac{1}{2}(v_m + v_f) = \tfrac{1}{2}(v_{mp} + v_{fp}) \qquad (88)$$

provided that $\Delta T_c \ll mc_L^*$ for the droplet. Thus the drop as a whole is retarded by solid-state diffusion when

$c_{Sm}^* > c_{S\infty}$. The effect of interfacial curvature is shown in Fig. VI.4. From sub-section (1), the curvature effect cannot alter the average concentration gradient across a droplet, even when it is distorted from spherical: however, curvature does act to increase $c_L^*(1 - k)$ and hence reduce the migration velocity (see (I.11)). From (I.4),

$$c_L^* = \frac{-\Delta T}{m} - \frac{4\Theta_c}{lm} \tag{89}$$

where ΔT is undercooling below the pure material melting point: k is assumed independent of droplet size (Appendix C). For a hypothetical droplet where $\Theta_c \to 0$ and $c_{Sm}^* = c_{S\infty}$, (I.11) and (VI.15) give:

$$\bar{v}_0 = \frac{+D_L G}{\Delta T(1 - k)} \tag{90}$$

In terms of $\bar{v}_0$, the actual drop velocity $\bar{v}$, from (VI.59), (VI.88) and (VI.89), is:

$$\left(\frac{\bar{v}}{\bar{v}_0}\right) = \left(\frac{1}{1 + 4\Theta_c/l\Delta T}\right)\left(\frac{1}{1 + (c_{Sm}^* - c_{S\infty})/2\Delta T(1 - k)}\right) \tag{91}$$

The first term on the right of (VI.91) is $1/(1 - (\Delta T_c/mc_L^*))$ and thus shows the reason for the assumption preceding (VI.85). The curvature effect thus introduces a size-dependent drop retardation which might be confused with the effects of "normal growth" kinetics, equation (II.18). (See chapter VII). The retardation by solid-state diffusion is largely independent of size, given the assumption $(D_S/v_m) \ll \frac{1}{2}l$

used to derive (VI.91): however, if this assumption is not valid, increased retardation occurs especially for small drops.

(4) Droplet Size Changes.

Assuming (VI.15), (I.11) and (VI.59) give:

$$\frac{v_{fp}}{v_{mp}} = \frac{c_{Lm}^{*} - c_{S\infty}}{c_{Lf}^{*}(1 - k)} \qquad (92)$$

for a planar zone. This is equivalent to equation (11) of Tiller.[18] Tiller's fig. 5, plotted from this, is however misleading. Much of the graph (where v_f/v_m is predicted to be far from unity) implies "compositions" outside the range 0 - 100%. When $c_{Sm}^{*} = c_{S\infty}$ in (VI.92), the zone expands in size but its solute content can be shown to remain constant. When $c_{Sm}^{*} > c_{S\infty}$ the solute content continually decreases. (VI.92) allows for differential migration ((VI.58)) which tends to expand the drop, as well as solid-state diffusion which does the opposite. If $R \neq 0$ and we take the case $v_m = R$, the droplet migrates with the isotherms and so its composition remains constant. In the previous case, zone expansion due to differential migration (VI.78) arose from the decrease in $c_L^{*}(z_i)$ with time. So when $v_m = R$, this effect is cancelled out by the effect of cooling the material and, provided $c_{S\infty} < c_{Sf}^{*}$, the zone always shrinks. As the zone composition is constant, we may equate the rate of loss of solute from the zone to the rate of zone shrinkage multiplied by composition:

$$v_f c_{Sf}^* - v_m c_{S\infty} = (v_f - v_m) c_{Lf}^* \tag{93}$$

or:

$$\frac{v_f}{v_m} = \left(\frac{c_{Lf}^* - c_{S\infty}}{c_{Lf}^* - c_{Sf}^*}\right) \tag{94}$$

Relating shrinkage rate $(v_f - v_m)$ to migration velocity:

$$\frac{(v_f - v_m)}{v_m} = \frac{c_{Sf}^* - c_{S\infty}}{c_{Lf}^* (1 - k)} \tag{95}$$

As shown in sub-section (3), the shrinkage rate of an n-dimensional drop is $\sim(1/n)$ times the above value for a planar zone. For a nearly spherical droplet:

$$v_f = v_{fp} - \tfrac{1}{3}(v_{fp} - v_{mp})$$

$$v_m = v_{fp} - \tfrac{2}{3}(v_{fp} - v_{mp})$$

$$\bar{v} = v_{fp} - \tfrac{1}{2}(v_{fp} - v_{mp}) \tag{96}$$

ignoring the curvature effect. Thus the rate of shrinkage, $(v_f - v_m)$, is comparable in magnitude to the droplet retardation $(\bar{v}_0 - \bar{v})$ discussed in sub-section (3). So drop retardation by solid-state diffusion should be experimentally distinguishable from all the other possible explanations (e.g. interface kinetics[18]) by the occurrence of size changes.

(e) TGZM With Varying Temperature

When terms such as c_L^*, D_L in (I.11) vary with temperature, TGZM velocity becomes time-dependent. Of the solutions in section (a), only (VI.15) applies for varying velocity and this does not apply when $R \neq 0$. However, the results (VI.45) and (VI.50) show that when $(vl/2D_L) \ll 1$ the solute distribution within the zone is approximately independent of v so that these results may be used when v varies. We proceed to obtain distance-time relations for TGZM in these situations.

Results in this section strictly apply to a single interface, one side of a planar zone, assuming local equilibrium, constant D_L, and no solid-state diffusion.

(1) Static TGZM (i.e. R = 0).

Assuming (VI.15), with (I.11):

$$v = \frac{-D_L G}{m c_L^* (1 - k)} \tag{97}$$

The boundary conditions are (from (VI.13), (VI.14)):

$$c_L^* = c + \frac{G z^*}{m} : \quad z^* = 0 \text{ at } t = 0 \tag{98}$$

Combining (VI.97) and (VI.98) and integrating:

$$\int_0^{z^*} (c + \frac{Gz^*}{m})dz^* = \int_0^{t} \frac{-D_L G dt}{m(1 - k)} \qquad (99)$$

$$\therefore \quad cz^* + \frac{Gz^{*2}}{2m} = \frac{-D_L G t}{m(1 - k)}$$

So:

$$\text{average velocity} = \frac{z^*}{t} = \frac{-D_L G}{m(c + (Gz^*/2m))(1 - k)} \qquad (100)$$

where $(c + Gz^*/2m)$ is the arithmetic mean of the initial and final c_L^*.

(2) TGZM During Solidification

The exact solution (VI.15) is now replaced by the approximate solution (VI.50) and so (VI.97) applies approximately. From (VI.8):

$$d = \int v dt = \int (\frac{m}{G})(\frac{v}{v - R})\, dc_L^* \qquad (101)$$

Substituting for v from (VI.97) and integrating:

$$d = \frac{D_L}{R(1 - k)} \ln(\frac{c_2 + D_L G/Rm(1 - k)}{c_1 + D_L G/Rm(1 - k)}) \qquad (102)$$

where d is distance moved by the interface (on the z scale) and c_1, c_2 represent the initial and final values of c_L^* respectively. (This result may alternatively be obtained by setting up a linear differential equation $v^{-1} = (dt/dz^*)$ = fn(t) + fn(z^*) + constant, which may be made exact

and solved.) In earlier work, we assumed:[1]

$$v \ll R \tag{103}$$

as an approximation. On this assumption, the v term may be removed from the denominator and the simpler result:

$$d = \frac{D_L}{R(1 - k)} \ln\left(\frac{c_2}{c_1}\right) \tag{104}$$

is obtained in place of (VI.102). As v = (R/Q) at the solidus temperature from (IV.5), (VI.103) is often valid.

Equation (VI.45) provides a more accurate description of the solute distribution during solidification than does (VI.50). It gives:

$$\left(\frac{\partial c_L}{\partial z}\right)_t = \frac{G}{m}\left(1 + \frac{Rl}{2D_L}\right), \quad z_i = 0 \tag{105}$$

$$\left(\frac{\partial c_L}{\partial z}\right)_t = \frac{G}{m}\left(1 - \frac{Rl}{2D_L}\right), \quad z_i = l. \tag{106}$$

Then, replacing (VI.97):

$$v_f = \frac{-D_L G}{m c_{Lf}^{*}(1 - k)}\left(1 + \frac{Rl}{2D_L}\right) \tag{107}$$

$$v_m = \frac{-D_L G}{m c_{Lm}^{*}(1 - k)}\left(1 - \frac{Rl}{2D_L}\right) \tag{108}$$

In the absence of solid-state diffusion, the average velocity $\frac{1}{2}(v_f + v_m)$ is thus given by (VI.97), and (VI.102) applies to the zone centre. Calculations of the individual distances d_f and d_m travelled by the freezing and melting interfaces would, however, require simultaneous solutions to (VI.107) and (VI.108), since l is a variable. The implications of these results are discussed in chapter VIII.(e).

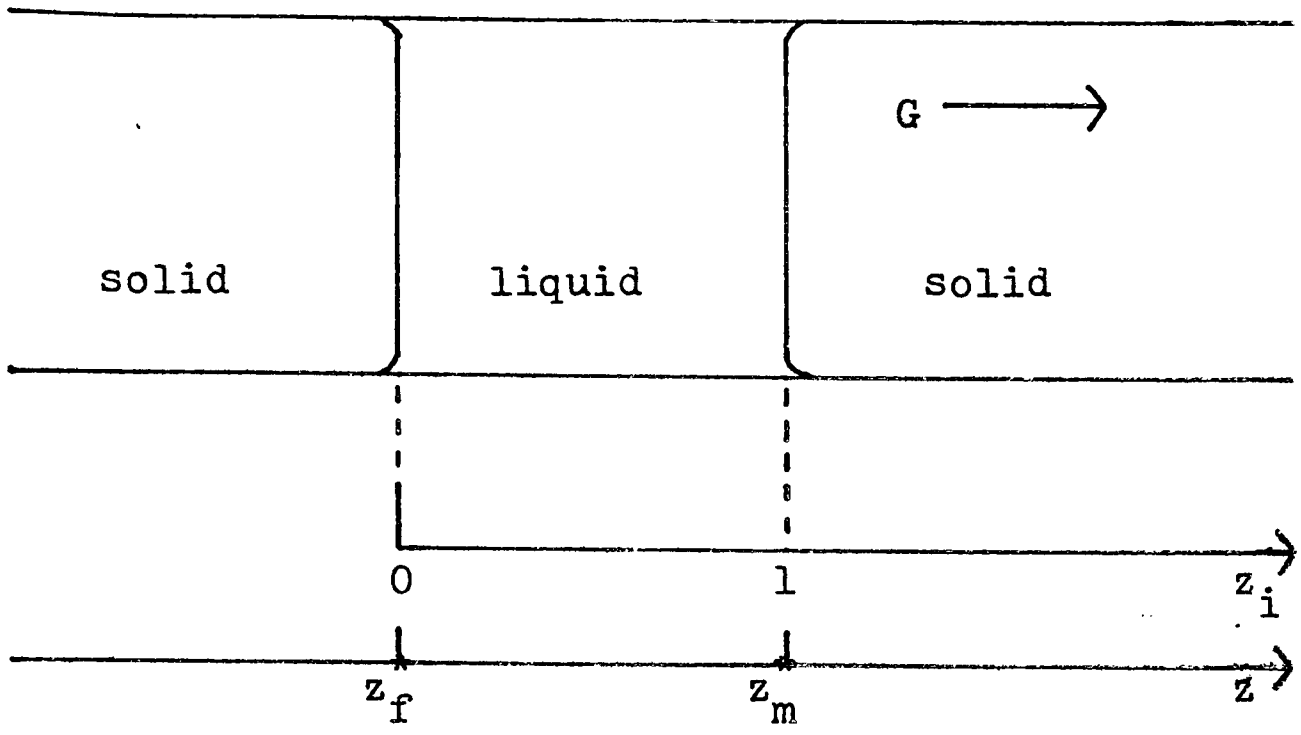


FIG.VI.1. TGZM model.

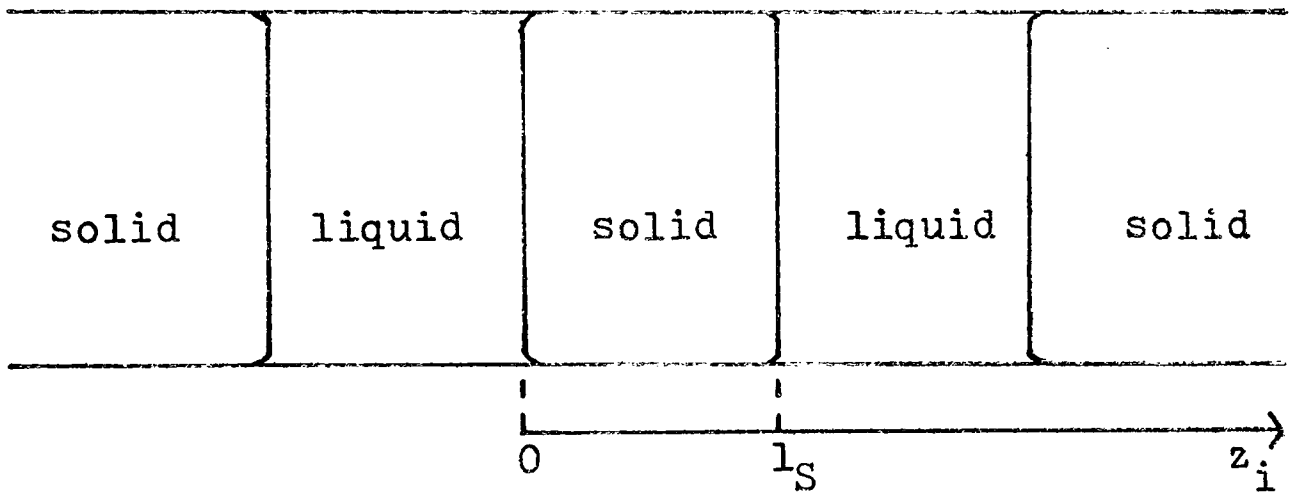


FIG.VI. 2. TGZM model for solid - state diffusion (section (a)(4).)

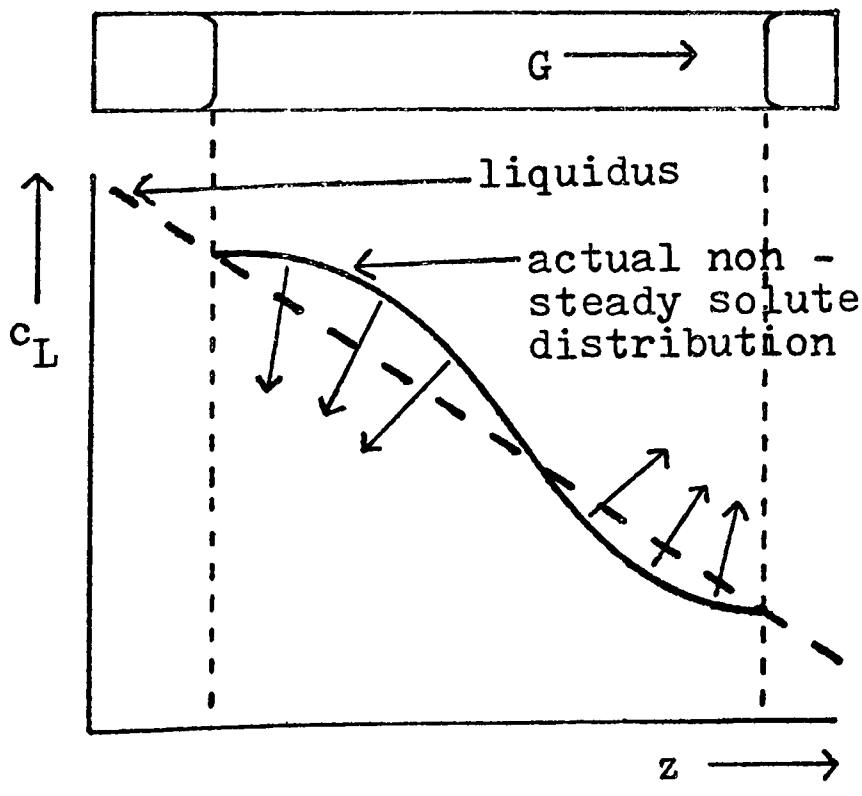


FIG.VI. 3. Showing that a transient solute distribution tends towards (VI. 15).

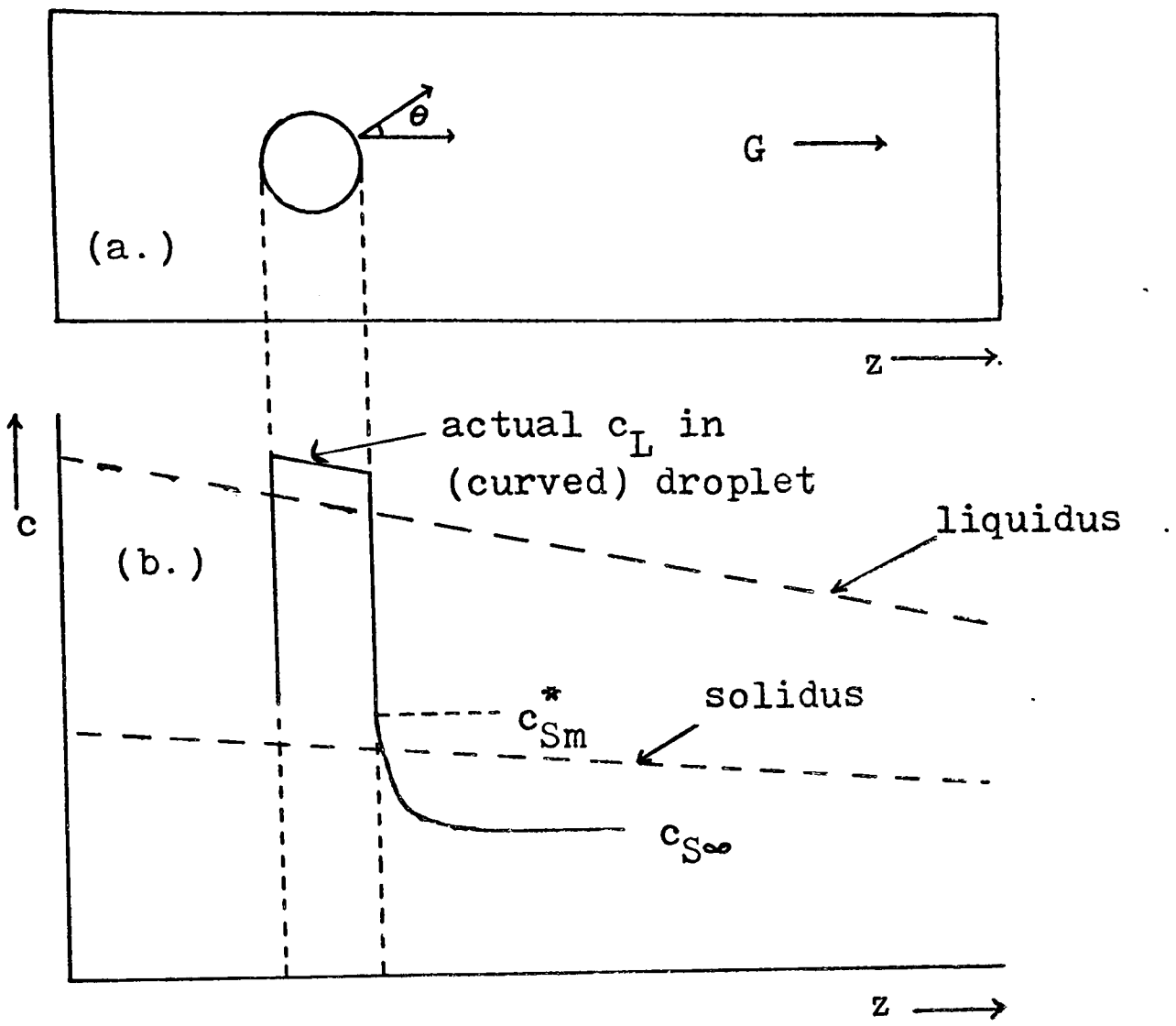


FIG. VI. 4. Solid-state diffusion and effect of interface curvature on droplet TGZM.

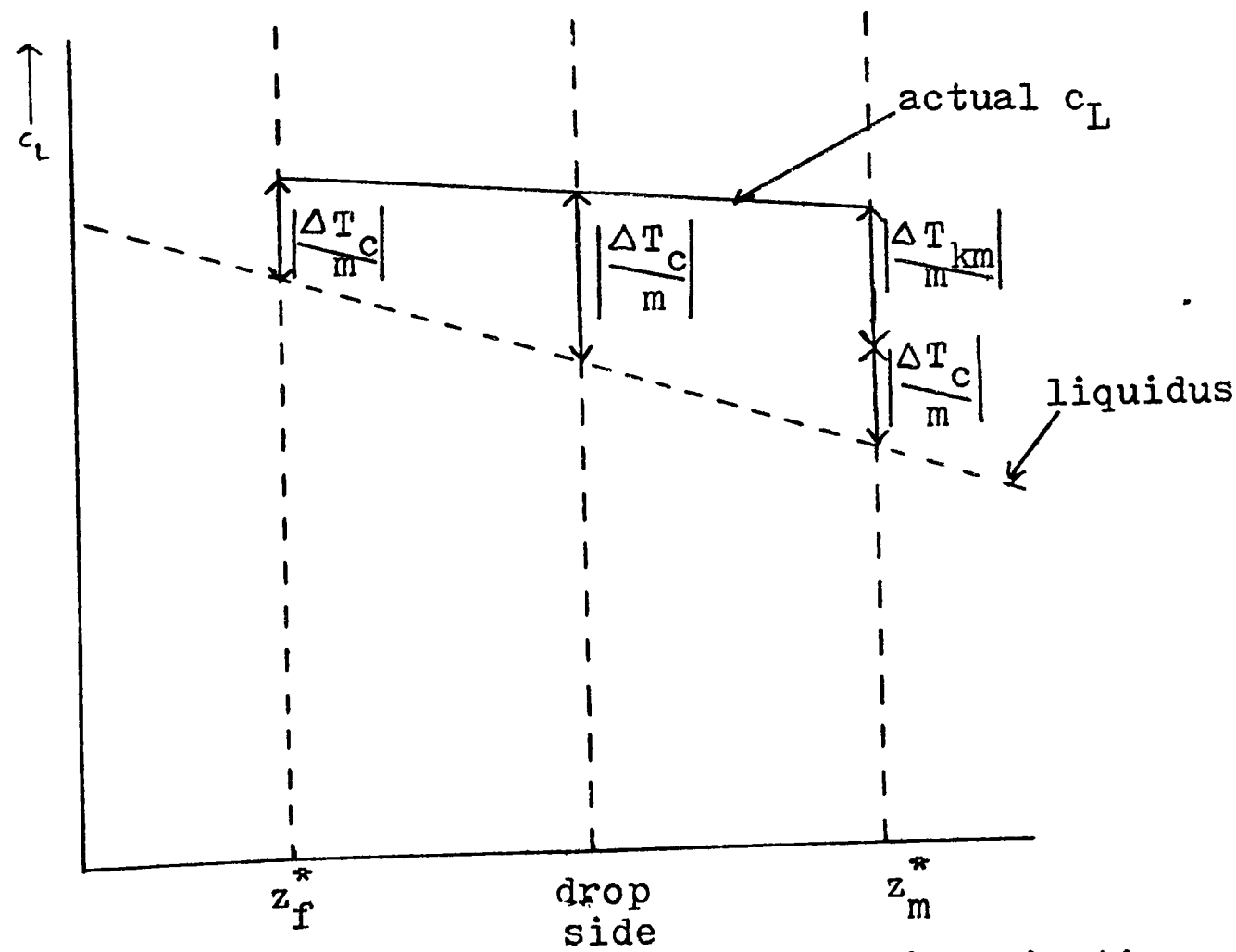


FIG. VI. 5. Showing how slow melting kinetics distorts droplet shape.

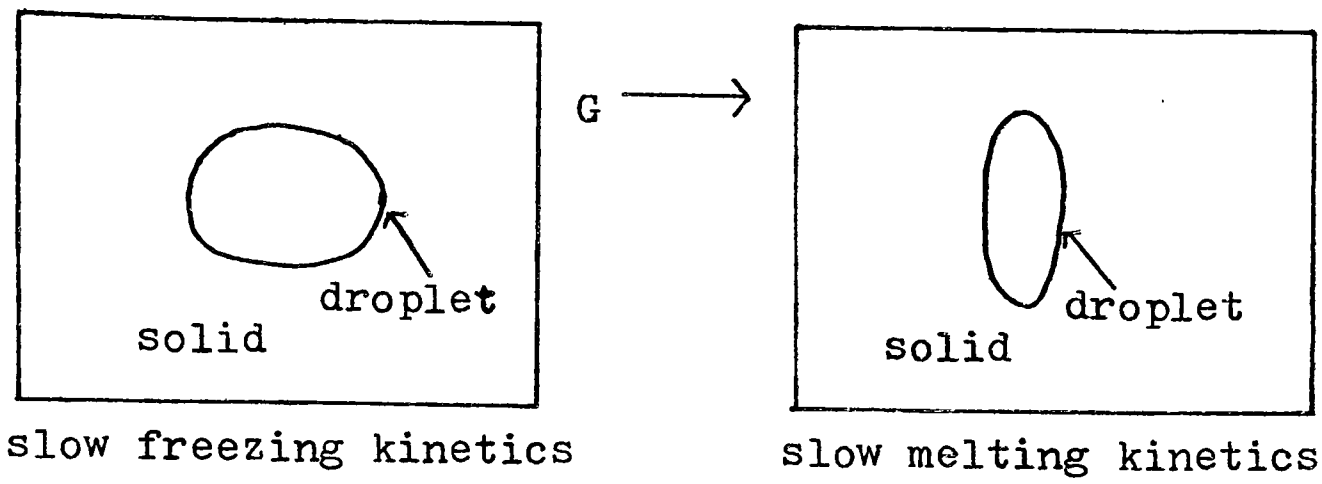


FIG. VI. 6. Drop shape distortions

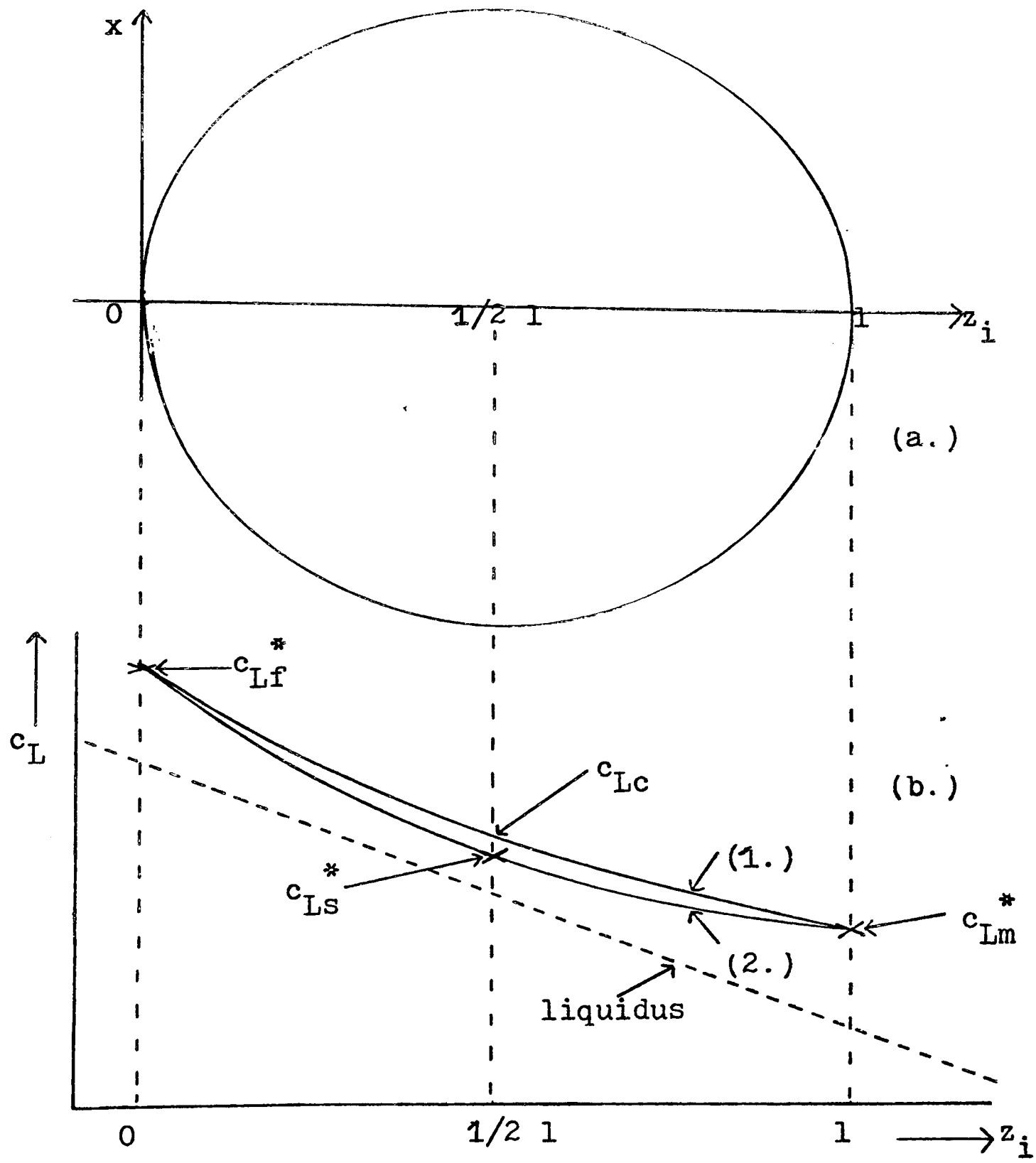


FIG. VI. 7. Solute distributions in distorted droplets, (1.)along z_i axis (2.) following the interface from $z_i = 0$ to $z_i = 1$.

Chapter VII. Temperature Gradient Zone Melting - Experimental

(a) Measurements of Diffusion Coefficients

The basic TGZM equation (II.14) suggests that D_L can be measured only if m is known. This appears to rule out measurements on nominally pure materials in which the solute and its phase diagram are unknown. However, the problem is largely overcome by rearranging (II.14). Differentiating v^{-1}:

$$\frac{dv^{-1}}{dc_L^*} = \frac{-m(1 - k)}{D_L G} \qquad (1)$$

assuming D_L, G, m and k are independent of temperature. So, with (II.12):

$$\frac{dv^{-1}}{dz} = \frac{-(1 - k)}{D_L} \qquad (2)$$

Thus, if v is measured as a function of position in the temperature gradient, it is not necessary to measure m or even G to determine D_L. Furthermore, as $v^{-1} \rightarrow 0$ at the pure material melting point, extrapolation of the v^{-1} - z graph to the z axis should yield a value for melting point if the thermal field is known. As the alloy liquidus and solidus temperatures can be measured in solidification studies (chapter IV), k for an ideal, straight-line phase diagram may then be found from:

$$k = \frac{T \text{ (pure material melting point)} - T \text{ (liquidus)}}{T \text{ (pure material melting point)} - T \text{ (solidus)}} \qquad (3)$$

(1) Early results

Results on succinonitrile (Fig. VII.1) gave $(D_L/1 - k) = 3.3 \times 10^{-6}$ cm^2/sec, while results on droplets and dendrite sidearms in camphene (with R = 0 at the time of measurement) gave $(D_L/1 - k) = 5.9 \times 10^{-6}$ cm^2/sec and 5.8×10^{-6} cm^2/sec respectively. Scatter was $\pm$ 8% in droplet studies and $\pm$ 12% in sidearm studies. The camphene results agree well with those of Jones and Chadwick.(150) The succinonitrile results were measured from about 3 - 9°C below the pure material melting point. All experiments involved a temperature gradient G ~ 50°C/cm in the horizontal direction as given by Fig. III.11 (ii) (approximately). Drop velocity was measured optically, using the "x 32" objective and graticule scale, in the horizontal plane. (The vertical migration component can be ignored since (VII.1) and (VII.2) apply either to the principal thermal gradient direction or to any resolved component, provided only that v and z are measured in the same direction.) Studies on cells containing thermocouples (which are unreliable because of the field distorsion, as discussed in chap. III(f)) suggested a pure material melting point of ~ 55.2°C by extrapolation of the v^{-1} - z plot in succinonitrile to the z axis. However, one run suggested that the v^{-1} - z graph curves at low alloy content, indicating an increase in D_L and extrapolating to a slightly higher temperature ~ 56°C

at $v^{-1} \rightarrow 0$. In any event, it is seen from (VII.3) and the measured T (liquidus) = 55.6°C, T (solidus) = 48.1°C (chap. IV.(d)) that k in succinonitrile is quite small. Glicksman's[229] value of 58.1°C for the pure material melting point indicates k = 0.25 in conjunction with our results: Glicksman measured k = 0.15 in his own succinonitrile sample. Taking k ~ 0.2, a value $D_L \sim 3 - 4 \times 10^{-6} cm^2/sec$ is indicated for succinonitrile, in fair agreement with the dendrite growth temperature results (chap. IV.(f)).

The experiments of section (d) indicate a somewhat lower $D_L/1 - k \sim 2.0 \times 10^{-6}$ cm^2/sec averaged over Fig. VII.6, but as the $v^{-1} - z_p$ graph clearly curves in this case, indicating varying D_L, m or k, the simple analysis given here is not really adequate. The lower value is plausible because of the higher impurity content and lower temperature (section (d)).

(2) Later results

The experiments of section (e)(2) allowed a re-determination of D_L in succinonitrile. The analyzed 52.4°C run yielded $(D_L/1 - k) = 2.96 \times 10^{-6}$ cm^2/sec, with v^{-1} extrapolating to zero at 55.4°C. The analyzed 49.5°C run did not yield an accurate result because of the greater scatter, but the result obtained was $(D_L/1 - k) = 2.9 \times 10^{-6}$ cm^2/sec in good agreement with the 52.4°C run and the previous work.

(b) Bi-phase Droplets

Gas bubbles were sometimes observed to appear inside migrating liquid drops in succinonitrile. Such bubbles, usually occupying one-hundredth or less of the drop volume, did not appear to alter the drop TGZM velocity. Biphase drops with a greater gaseous fraction were produced on warming up a specimen containing gas bubbles entrapped in solid. A string of liquid drops could be formed by the appearance of liquid at the gas-solid interface, growth of the liquid region, migration of the liquid up the temperature gradient and breakaway of the liquid from the stationary gas bubble (Fig. VII.2), the process occurring repetitively. Finally, biphase drops consisting of perhaps 90% gas surrounded by a thin liquid film were observed to migrate at about half the velocity of a fully liquid droplet.

These observations parallel the results of Hoekstra et al,[134] where biphase liquid-solid droplets were postulated with the solid merely acting as an inert particle to be pushed along, and hence reducing the migration rate. The reversed migration direction found by other investigators[181,182,167] of gas-liquid droplets was not observed here. Presumably the vapour pressure, or its temperature dependence, is much smaller in succinonitrile than in the systems previously studied (see chap. II.(b)(7)).

During TGZM, gas bubbles remained at the cold end of biphase drops, even when the microscope was tilted to bring the hot plate above the cold plate. This indicates

that the viscous drag on the gas bubble exceeded the gravitational upthrust, so that the gas was "pushed" by the solid-liquid interface. A simple calculation, assuming Stokes' law for viscous drag and taking gas bubble radius = 2 μms, TGZM velocity = 2×10^{-5} cm/sec, indicates that the viscous force exceeds gravitational upthrust if viscosity exceeds 0.4 poise. The viscosity of succinonitrile is not known, but that of glycerine is 46 poise at 0°C (though that of water is 2×10^{-2} poise) so that our result is plausible.

(c) Liquid Film Instability

As noted in chap. IV.(b), liquid succinonitrile wets the glass in our experiments and so a liquid film would be expected to exist above and below the solid for a considerable distance behind the main interface (Fig. VII.3). This was confirmed by studies of droplets migrating at an angle to the cell plane and hence reaching the lower surface of the solid. In droplets close to the main interface, a second ring would suddenly appear inside the drop indicating the onset of coalescence with the liquid layer. (The second ring arises from the formation of a second section of curved vertical solid-liquid interface (Fig. VII.4), as explained in chapter III. (g)). In droplets further from the bulk liquid, no second ring would appear but the drop contrast would gradually fade, indicating spreading of the drop over a solid-air or solid-glass interface.

At the upper surface of the solid, an entirely opposite phenomenon sometimes occurred. The upper liquid layer became unstable and droplets developed from it, migrating

down into the solid. Such droplets, most having reached the configuration of Fig. IV.4 in the process of breakaway from the upper liquid layer, are shown in Plate 20. This form of instability may be understood by reference to Fig. IV.5, where a hemispherical depression in the solid-liquid interface is postulated. The vertical gradient acts to make c_L^* at the centre of the depression lower than c_L^* away from the depression, although the curvature effect counteracts this. If c_L^* is lower at the depression, solute flows to the depression causing further melting and eventual release of a drop into the solid. The vertical gradient (assumed positive i.e. hot at base) promotes instability at the upper liquid layer only, as observed in succinonitrile. A simple stability treatment shows that hemispherical depressions continue melting if:

$$G_{vert.}r - \frac{2\theta_c}{r} > 0 \qquad (4)$$

(see (I.2)) where r is depression radius, G_{vert} the vertical thermal gradient. Taking $G_{vert} = 10^{\circ}C/cm$ and $\theta_c = 6.23 \times 10^{-6}\,^{\circ}C/cm$ for succinonitrile using Glicksman's[229] data, (VII.4) predicts that depressions of radius greater than ~10 μms may grow, in good agreement with experiment.

(d) TGZM During Solidification

The experiments described here were designed to show whether or not an interdendritic liquid pool in a solidifying specimen undergoes TGZM at substantially the same velocity as a liquid droplet in a solid specimen held stationary in

a similar thermal gradient at a similar temperature. To this end, the apparatus was developed so that the alteration of the thermal field due to solidification (as compared to the static situation) was small and measureable (chap. III(f)), and dendritic growth in thin cells was characterized to show what types of grain produced "normal" growth features relatively unaffected by the cell walls (chap. IV.(b)) The concurrent theoretical development (chap. VI.(e)) indicated that if the pools between secondary arms were approximately planar, TGZM during solidification would indeed be similar to "static" TGZM provided that $(Rl/2D_L) \ll 1$, where l is liquid pool width parallel to the temperature gradient.

As in chapter VI, three parallel z-type axes are defined parallel to the horizontal thermal gradient G. Axes z, z_i and z_p are fixed to the specimen cell, the interface of a migrating liquid region, and the heating plates respectively, with $z_p = 0$ at the cold plate edge (Fig. VII.13). Unfortunately, there was no full measurement of the thermal field in these experiments, but the plate temperature settings (94.8°C and 20.0°C), and measured temperature at the hot plate edge 72.3°C, have been marked on Fig. III.11 and from these the horizontal temperature gradient may be estimated as $\sim$ 50 - 60 °C/cm, plate spacing being 7.84 mms as in run (ii) of Fig. III.11.

A nominally 5.95 wt.% camphor in succinonitrile alloy was made up (this solute being preferred to CBr_4 because of evidence of bromine evolution at high temperature in the latter case.) Three series of droplet velocity measurements

were made, each covering a range of z_p determined by focusing on the cold plate edge and then moving the stage under the lens with the lateral traverse, using the graticule scale to measure distance covered. There were systematic differences between measured velocity values at a given z_p in the different runs indicating a temperature difference $\sim 0.4^{\circ}C$ at given z_p between the highest and lowest temperature run. Two runs were carried out by direct observation, timing successive drops migrating against the graticule scale, and the other was photographic. The results appear in Fig. VII.6 (see also (a)(1)). No significant ($\gtrsim$ 5%) variations of drop velocity with size were seen, but in consideration of section (e)(1) only larger drops, radius $\gtrsim 5\,\mu$ms, were used in these measurements. Dust particles were used as reference marks in the photographic run. Surprisingly, these did suggest a small bodily displacement of the cell up the temperature gradient (by $\sim 5\,\mu$ms as compared to drop migration distances $\sim 125\,\mu$ms). How such a displacement could have occurred is not clear and it seems possible that sparingly soluble dust particles on the inside walls of the cell themselves migrated slowly. It was decided to correct the velocity measurements on the assumption that a real cell displacement had occurred, thus introducing a possible 4% error if the assumption was wrong.

The cell used in these static TGZM runs was also used in a solidification experiment. It was necessary to select a steady-state growth velocity large enough to produce dendrites, but small enough not to affect the thermal field

($T - z_p$ plot) significantly. In the eventual experiment, the velocity was 3 μm/sec and the dendrite tip position at z_p = 3260 μms from the cold plate edge. Now, from (VIII.27), it may be seen that for given D_L, G, m and k, the critical velocity for planar-cell breakdown R_c equals the TGZM velocity at the alloy solidus temperature. From Fig. VII. 6, the TGZM velocity at the dendrite tip temperature is approximately 0.31 μm/sec. This is likely to be nearer the alloy liquidus temperature than the solidus temperature: from chapter IV.(e), Q must be $\gtrsim$ 10 and is probably nearer (10/k), perhaps 25 - 50. As suggested by this, fully dendritic growth was obtained.

A fixed area was photographed during solidification at one-minute intervals: three such photographs are shown in Plate 21 (a) - (c). Individual secondary arms were identified and labelled throughout solidification from the sequence of photographs. A large fixed dust particle is labelled with a vertical line in Plate 21. Its contrast changes during the run because, as solidification proceeded, the focus height was raised to follow upward secondary growth from the base-growing primary, a "normal" arm from a type 2 grain (chap. IV.(b)). The distance migrated between Plate 21 (a) and 21 (c), for a section of solid-liquid interface starting at the centre of Plate 21 (a), was obtained from the average of several film measurements (Fig. VII.7). These measurements were taken only from liquid pools separating two sidearms which were nearest neighbours throughout solidification, avoiding spurious results arising from melting-off of small sidearms and

consequent thickening of neighbours. Measurements were taken from contrast features representing the secondary-primary junction (arrowed, arm 6, plate 21 (c)), to avoid effects from the upward and slightly forward elongation of sidearms during solidification. These showed an actual migration distance of 75 μms (accuracy $\sim \pm$ 15%), with an expansion of the scale of structure along the z axis or differential migration (chap. VIII,(c) and (e)) of about 4%. Eight observed dust particles, seven of which were stationary with respect to each other, indicated the absence of specimen displacement to accuracy $\pm$ 3 μms, as indicated by the marked particle.

Immediately following the photograph (c) of Plate 21, the motor was switched off. After the photographic "static" TGZM run had been carried out on droplets generated by coarsening of the grown dendrites, the distance to the cold-plate edge was measured optically. Hence (taking into account the motor over-run, Table III.(4)), it was ascertained that z_p at the centre of the final photograph was 1592 μms. Hence, because the solidification run at 3 μm/sec lasted 480 sec, z_p at the centre of Plate 21 (a), was 3032 μms. Now, on the assumption that TGZM velocity in "static" droplet migration is identical to that in solidifying interdendritic liquid pools, equation (VI.101) may be written:

$$d = \int_{z_{p2}}^{z_{p1}} \left(\frac{v}{R - v}\right) dz_p \qquad (5)$$

where z_{p1} represents the position at the centre of plate 21(a) 3032 μms, and z_{p2} represents the position reached by the

migrating pool in Plate 21 (c): v is taken from the results of Fig. VII.6, and so d represents a "predicted" migration distance during the solidification run. If the assumption v (static TGZM) = v (solidification TGZM) is correct, then d (predicted from static TGZM measurements and (VII.5)) should equal d (solidification photographs). This indirect form of comparison was necessary because of the rapid variation of v with z_p during solidification, mainly because of the c_L^* term in (VI.97).

Initially, (VII.5) was integrated numerically with z_{p2} taken at the centre of Plate 21(c.), 1592 μms. The area under the graph $(v/(R - v))$ versus z_p was calculated by Simpson's rule (e.g. Stephenson[256] p. 232), using 50 μm intervals and allowing for smaller end sections as triangles, obtaining d = 81 μms. The above z_{p2} value is however incorrect, as the arm actually migrated to the right of the photographed viewfield. Taking z_{p2} = 1592 + 81 μms, from the previous calculation, a first-iteration value of z_{p2} = 1673 μms was obtained. Using this value to repeat the numerical integration obtained an iterated predicted d = 78 μms. As the total accuracy was assessed at $\pm$20%, further iteration was unnecessary. Thus, within the experimental accuracy, the predicted and observed migration distances agreed well.

One possible important source of error was the distorsion of the T - z_p field during solidification. Taking G $\sim$ 50°C/cms, the cell cooled through about 7°C at a rate (= GR) of $\sim$ 1.5 x 10^{-2} °C/sec. The graph of Fig. III.14 indicated that when the cell was cooling at such a rate,

it was roughly $\frac{1}{2}^{o}$C above its final equilibrium temperature at given z_p. On this basis (admittedly an approximate argument as the cell cooled under different circumstances in the experiments of Fig. III.14), the relevant z_p range from Fig. VII.6 to use in the calculations of (VII.5) should have been $\frac{1}{2}^{o}$C further up the thermal gradient, i.e. approximately 3132 - 1770 μms. Using these figures a revised predicted d of 82 μms (5% increased) was obtained. The agreement with measured d remained well within experimental error.

Taking inter-secondary pool width to average 5 μms, with $D_L \sim 3 \times 10^{-6}$ cm^2/sec, the factor $(Rl/2D_L)$ in equations (VI.107 - 108) is calculated as 0.025. On this basis, v_f should exceed v_m by 5%, or more if v_m is reduced by solid-state diffusion. The results of Fig. VII.7 actually indicate that v_m exceeds v_f, i.e. that the liquid pools widen during freezing. This does in fact occur, at the primary-secondary junction where measurements were made, because of "blunting" of the liquid pool root due to the curvature effect.[1,64] The calculation of $(Rl/2D_L) \ll 1$ does however confirm that solidification TGZM should be similar to static TGZM in this experiment. These results have been published.[257]

An interesting effect was noticed in a preliminary solidification run (Plates 22 - 24). One sidearm, arrowed, was distended by migration past a large dust particle fixed to the cell base.

(e) TGZM Velocity and Droplet Size.

The local equilibrium assumption is commonly accepted for solidification phenomena at all but the fastest velocities in nonfaceted materials:[2,7,207] thus the observed size dependence of droplet TGZM velocity in camphene,[150] albeit rather uncertain because of the experimental error, is surprising. As shown in chap. II.(e), the implied interface-kinetic effect is really several orders of magnitude greater than theory predicts. Similar results by McLean[177,176] on a metallic system are equally puzzling, although the suggested incompatibility[176] between these results and interface-kinetic explanations is not proved: the measured μ_2 appears fully compatible with data on other systems (Table II.3) and the observation[176] that dendritic growth data in pure aluminium rule out such large kinetic effects may be irrelevant since McLean's work relates to a liquid lead-solid aluminium interface several hundred ^{o}C below the aluminium melting point. Our incomplete experimental programme on nominally pure succinonitrile, summarized below, confirms the existence of size effects in some cases. As will be seen, certain interface-kinetic explanations are possible but other possibilities also exist.

(1) fixed-plates stage

One series of droplet photographs in nominally pure succinonitrile was taken using this apparatus, and measurements of migration distance were made for nineteen droplets, using a sequence of photographs to label drops

as in section (d). From the plate spacing 9.49 mms and estimated plate temperatures of 75°C and 15°C, G was estimated as 40°C/cm ± 25%. Results showed a small velocity dependence on size, a greater dependence on temperature within the photographed viewfield, and a tendency for drops to shrink while migrating, probably due to plate cooling during the experiment because of lack of temperature control. Results were first plotted against initial position (z_p), establishing $(D_L/1 - k) \sim 5.9 \times 10^{-6}$ cm^2/sec by the method of section (a), with the average temperature about 8½°C lower than the temperature at which $v^{-1} \to 0$, i.e. about 46.5°C (see section (a)). Then, deviations from the average $v - z_p$ graph were measured and plotted against drop size for individual droplets. This showed a reduction in velocity at low diameter with a roughly constant velocity at high diameter. Averaging freezing and melting interfaces, the average drop velocity was found to tend towards $\sim 2.8 \times 10^{-5}$ cm/sec at the high-diameter limit, with the velocity of a 5 μms diameter droplet reduced about 4½% below this.

(2) moving-plates stage

Five series of droplet photographs in nominally pure succinonitrile were taken using plate temperatures differing by 7.1°C, plate spacing 7.27 mms, as shown in Fig. III.15, but with slightly different absolute plate temperatures. Only two have been analyzed in detail. In all the runs, the camera was centred on z_p = 6119 μms

(where a low vertical gradient was obtained, chap. III.(f)). Two runs with plate temperatures 55.2°C and 48.1°C (giving an observation temperature ~ 52.4°C), and one run with plate temperatures 53.8°C and 46.7°C (giving observation temperature ~ 51.0°C) seemed qualitatively similar in that small or negligible size dependence of velocity occurred. Two runs with plate temperatures 52.3°C and 45.2°C giving observation temperature ~49.5°C, and plate temperatures 50.9°C, 43.8°C giving observation temperature ~ 48.1°C, were similar in that velocity variations of 10-20% were common and droplets did not migrate exactly along the thermal gradient direction. Two runs were analyzed fully, one at observation temperature 52.4°C and one at 49.5°C, as representing each of these types of behaviour.

In the 52.4°C run the variation of v with z_p was dominant. So drop positions (average of front and back position with respect to "cold" edge of film) were measured to plot v^{-1} against z_p for seventy-six droplets, not including drops on the grain boundary in the viewfield (Plate 25) or drops which coalesced during the run. From this graph, a line was drawn by eye to account for the variation but displaced somewhat to low v^{-1} in an attempt to guess $(v^{-1})_{l \to \infty}$, the value of v^{-1} extrapolated to infinite drop size. Thus, for each drop, actual v^{-1}, and guessed $(v^{-1})_{l \to \infty}$ from the graph, were known. A second graph of l^{-1} versus $1 - ((v^{-1}{}_{l \to \infty} / v^{-1}$ actual) was then plotted (Fig. VII.8). Circled points represent average values of

$1 - (v^{-1})_{\infty}/v^{-1}$ for all drops in a size range spanning $0.34\ \mu ms^{-1}$. The estimated measurement error of $\pm 1\%$ in the v^{-1} parameter is shown. (An error $\sim \pm 10\%$ in l^{-1} may also be estimated). The line drawn shows the predicted size effect on the basis of the curvature effect alone (sub-section (3)). While most drops do fall within the scatter band, a few do not. As noted in section (g), the grain boundary appeared to migrate at the same speed as the droplets. One droplet close to the boundary on the hot side (about $30\ \mu ms$ away) migrated 8% slower than the mean: two droplets similarly close to the boundary on the cold side migrated 5% and 3% faster than the mean. Re-checks showed that these results could not be attributed to inaccuracies in measurements. Drop positions in the lateral (x) direction were also measured. Again, most drops migrated parallel to the z axis (in the film plane) within measurement error. A vertical gradient of $\sim +0.8^{o}C/cm$ did exist but was fairly small by comparison with the horizontal gradient $\sim 8^{o}C/cm$.

In the $49.5^{o}C$ run, by contrast, the size effect was dominant. So a first graph of v versus l^{-1} was plotted in order to "correct" drop velocities by linear extrapolation to infinite size. These "corrected" velocities were then plotted out to estimate the $(v^{-1})_{l \to \infty}$ versus z_p relationship. From this second graph, calculated $(v^{-1})_{l \to \infty}$ values for each drop were obtained. Finally, a third graph of l^{-1} versus $1 - ((v^{-1})_{l \to \infty}/v^{-1}$ actual) was plotted (Fig. VII.9) as in the previous case. The effect of this procedure was to

remove from the results any scatter introduced by variations of z_p from drop to drop. Clearly, extensive scatter remained, an order of magnitude greater than measurement error, and smaller drops migrated more slowly by 30% or more. Insofar as a definite relation could be determined from Fig. VII.9, the graph was linear, or perhaps slightly curved towards reduced retardations for the larger droplets. It was notable that despite the extensive scatter, there seemed to be a cut-off point of 0.1 in the parameter containing v^{-1} below which no drops were found despite the fact that the linear extrapolation met the axis at 0.04. This suggests that the linear extrapolation may have been incorrect: an alternative curve-fit is drawn on the figure. Lateral drop position measurements showed severe scatter in migration direction, droplets deviating equally to right and left of the z direction by up to 10 - 15 degrees: smaller drops showed greater deviations and greater scatter in deviation. Indeed, the variation in lateral velocity was closely similar to the variation in velocity along z shown in Fig. VII.9. Droplets in this run were much less spherical than previously (Plate 26), even excluding the droplets on grain boundaries which were excluded from the total of fifty-three used in measurements. It was noted that although not all drops were elongated along the migration direction (some, indeed, were flattened), those most retarded for their size were most elongated, and those migrating e.g. to the left were elongated to point in that direction (Fig. VII.10). Drop sizes were here measured on photographs of differing focus **height** to improve

accuracy (chap. III. (g)). In both this run and the last, few drops changed size significantly and there was no evidence of overall freezing or melting.

(3) discussion - curvature effect.

As discussed in chapter VI.(d)(3), the curvature effect creates a size dependence of drop velocity. The theoretical line on Fig. VII.8 was drawn using (VI.91), taking the undercooling below the pure material melting-point, mc_L^*, as 4^oC and using Glicksman's [229] surface energy data. The results are consistent with this, but evidence for the size effect is flimsy. The predicted retardation of a 5 μm size drop is 0.6%, and would be about 0.25% for the sub-section (1) run and 0.4% at 49.5^oC. So this effect is minor or negligible in the latter two cases.

(4) discussion - interface kinetics

Following a treatment similar to Tiller's[18] (chap.II. (b)(5)), but without specifying the kinetic mechanism:

$$v = \left(\frac{-D_L G}{\Delta T_s (1 - k)}\right)\left(1 - \left(\frac{|\Delta T_{kf}| + |\Delta T_{km}|}{Gl}\right)\right) \quad (see\ (I.2)) \qquad (6)$$

and it follows from this that:

$$\left(1 - \frac{\bar{v}^{-1})_{l \to \infty}}{v^{-1}(actual)}\right) = \left(\frac{|\Delta T_{kf}| + |\Delta T_{km}|}{G}\right) l^{-1} \qquad (7)$$

Hence the sum $\Delta T_k = \Delta T_{kf} + \Delta T_{km}$ can be found from graphs such as Fig. VII. 8 or 9. A linear graph implies that ΔT_k is independent of drop size (and thus of drop velocity).

If v increases with ΔT_k, the graph should be concave to the 1^{-1} axis. In Fig. VII.9 the reverse may be true, indicating that ΔT_k is lower when v is high. The result of sub-section (1) gives $\Delta T_k = 9 \times 10^{-4}$ °C at v = 2·8 x 10^{-5} cm/sec, T = 46.5°C. The linear plot of Fig. VII.9 gives $\Delta T_K = 1.9 \times 10^{-3}$ °C at V = 3 to 6 x 10^{-6} cm/sec, T = 49.5°C. From Fig. VII.8, the maximum credible slope of the data fit is 2½ times that of the theoretical line, indicating a possible $\Delta T_k < 8 \times 10^{-5}$ °C at v ~ 2 x 10^{-5} cm/sec, T = 52.4°C (assuming the curvature effect acts as predicted). Comparison of the first two runs discussed here again suggests ΔT_k decreases as v increases. Such a kinetic law has not bee previously suggested, but it could be rationalized on the basis of impurity adsorption at the interface, with less impurity retained at high v. Indeed, the absence of facets and occurrence of erratic migration also point to adsorption effects at the lower temperatures: other kinetic effects would presumably cause systematic deviation in migration direction, or no deviations. Our results are notably similar to those of Jones and Chadwick,[150] though our photographic technique reduces measurement error by an order of magnitude. When Jones[144] eliminated interface kinetics as a possible cause of drop elongation in camphene (chap II.(b)(5)), he assumed $\mu_f \sim \mu_m$: his figures show that if instead $|\Delta T_{kf}| \gg |\Delta T_{km}|$ was assumed, the elongation effect would be explained. Jones later gave such an argument to explain results on ice.[145] As similar elongations occur here, and in tin-bismuth[239] and sodium-potassium,[212] the phenomenon appears widespread. It is not easy to see why only the freezing interface

should be affected by adsorption. An alternative explanation may be given in terms of dislocation dragging.

(5) <u>discussion - dislocations</u>

Doherty and Strutt[176] argued that migrating droplets could be slowed or stopped by intersecting dislocations. They calculated that droplets of radius 0.05 - 0.10 μms in McLean's[177] system could be held immobile by a single dislocation, in good agreement with observations. They also compared the results of Cline and Anthony on TGZM[161] and drop shape relaxation[160] to show that apparently, $(|\Delta T_{kf}| + |\Delta T_{km}|) \sim 10(|\Delta T_{km}| - |\Delta T_{kf}|)$ although $|\Delta T_{km}| \gg |\Delta T_{kf}|$ would be expected in this system. In fact, as noted in chap. II.(b)(5), a very similar anomaly arises when Cline and Anthony's data on steady-state drop shapes is considered. Doherty and Strutt found that equivalent drag effects on the freezing interface would be produced by an excess density of dislocations $\sim 1 - 3 \times 10^{12}$ m^{-2}, a figure they considered high but plausible. It may be remarked that, as a drop sweeps through crystal and picks up dislocations which cannot easily break free again without an increase in length and energy, one may expect a high density of excess dislocations to build up on the freezing interface. This excess density might easily be orders of magnitude greater than the average dislocation density.

Dislocations exert a surface force (chap. VI.(d)(1)) on droplets, which must be compensated by differences in curvature undercooling across the drop. Such excess curvature

undercoolings, or "dislocation undercoolings" ΔT_{dis}, affect concentration gradients in droplets in exactly the same way as do the kinetic undercoolings postulated in the preceding sub-section, and so the values quoted there may equally apply to ΔT_{dis} if this explanation is correct. One attraction of the dislocation hypothesis is its ready explanation of droplet elongations. We have noted that Jones's calculations can be adapted to fit the drop retardation[150] and elongation[144] in camphene using the same interface-kinetic parameters provided that melting kinetics is negligible. It therefore follows that equal ΔT_{dis} values would also fit both sets of data. Calculation of the density of dislocations required is much simplified by a formula $\sigma \sim (1/40)Gb$ due to Kotze and Kuhlmann-Wilsdorf[258]; this removes the need to estimate shear modulus G. We obtain a dislocation density $\sim 10^{13}$ m^{-2} to fit the elongation data[144] on camphene, which seems reasonable.

It is necessary to suggest why most drops at 52.4°C were unaffected by dislocations. An intriguing speculation is that dislocations and grain boundaries, acting as liquid tubes and films, may themselves undergo TGZM. Grain boundaries were observed to migrate thus at 52.4°C but not 49.5°C (section (g)): insofar as a low-angle boundary is a dislocation array, we may even claim evidence for dislocation TGZM. Srivastava and Silcox[259] observed migration of sessile dislocations in the thermal gradient provided by beam heating in the electron microscope. Their explanation in terms of climb in a nonconservative vacancy flux due to thermotransport is plausible but deserves

further study. Migrating dislocations would not then drag droplets. Exceptions would occur when short dislocation lines ran between drops and grain boundaries, as a drag effect would then still occur irrespective of dislocation TGZM (Fig. VII.11). This could explain the few anomalous drops migrating at unusual velocities at 52.4°C.

The graph of Fig. VII.9 can be reasonably well explained on a dislocation model. As thermal "force" varies as l^3 while the number of dislocations attached to a drop might perhaps vary as l^2, the drop retardation might vary as l^{-1}. The dislocation model also accounts easily for the scatter and lateral migration results.

Doherty and Strutt[176] suggested a direct test for the dislocation model: if the migration direction is reversed by reversing the thermal gradient, droplets should initially migrate faster. We attempted to apply this test, setting the hot plate to 46.9°C and the cold plate to 44.5°C and allowing ~ 200 μms migration, then resetting the hot plate to 42.1°C. As this lowered the observation temperature, migration velocity was reduced: the clearest indication of dislocation drag would thus have been a reversed size effect (small drops migrating fastest). In fact the size effect appeared to be unaltered (i.e. small drops still slowest.) It is possible that, because of the vertical gradient, especially the transient vertical gradient induced by a change in plate temperature, droplets did not retrace their original paths. It might also be that the cooling and solidification caused extensive plastic deformation and dislocation rearrangement, nullifying the drag effect. Nevertheless, the result leaves us without a convincing explanation for our observations and further work is clearly needed.

(f) Solidification at Gas Bubbles in Liquids

Wilcox[182] observed "vapour growth" of solid camphor from the edge of a gas bubble in the liquid. Iwai[260] made similar observations of ice whiskers growing from air bubbles in water-saturated silicone oil, starting when an ice fragment hit the bubble. We have made similar observations on camphor, confirming that the growth occurs only when solid meets the bubble. Growth was curved, non-crystallographic, and occurred by motion of solid camphor away from the bubble, with the growth tip stationary at the liquid-gas interface. Interestingly, growth occurred with pulsations in the bubble surface and often ended with the solid tip "spat out" rapidly from the bubble into the bulk liquid.

The phenomenon deserves further study because the "vapour growth" explanation begs some questions. It is generally thought that solid-vapour surface energy always exceeds the sum of solid-liquid and liquid-vapour surface energies so that the proposed "vapour growth" model implies disequilibrium at the intersection points of the three interfaces. Shih and Li[230] have recently proposed that such disequilibrium is necessary to explain grain growth observations. It might be that rapid deposition of solid keeps the tip within the bubble, while the surface energy imbalance is necessary to provide the force pushing the solid bodily away from the bubble. This would explain the observed instability of growth, tips being "spat out" when the deposition rate falls too low.

(g) Grain Boundary TGZM

The grain boundary in Plate 25 appeared to migrate up the thermal gradient at roughly the same speed as the liquid droplets. As it also straightened out during observations, no exact velocity comparison is possible. The drops on the boundary, while elongating along it, appeared to have equal curvatures on either side of the boundary and thus did not seem to be dragging the boundary. By contrast, the boundaries in Plate 26 at lower temperature (visible mainly via cusps in intersecting drops) appeared immobile. An intermediate case was observed in succinonitrile-CBr_4 alloy, using a glass tube ~ 70 μms diameter inside a cell. Most grain boundaries within the tube were wetted by liquid, but one was not: this boundary migrated at about four-fifths of the speed of liquid boundaries, without a change in its orientation (Fig. VII.12). It was therefore of low angle and energy. In this case, the liquid regions near the tube walls (see figure) clearly were dragging the boundary and the contribution of thermal migration is therefore uncertain.

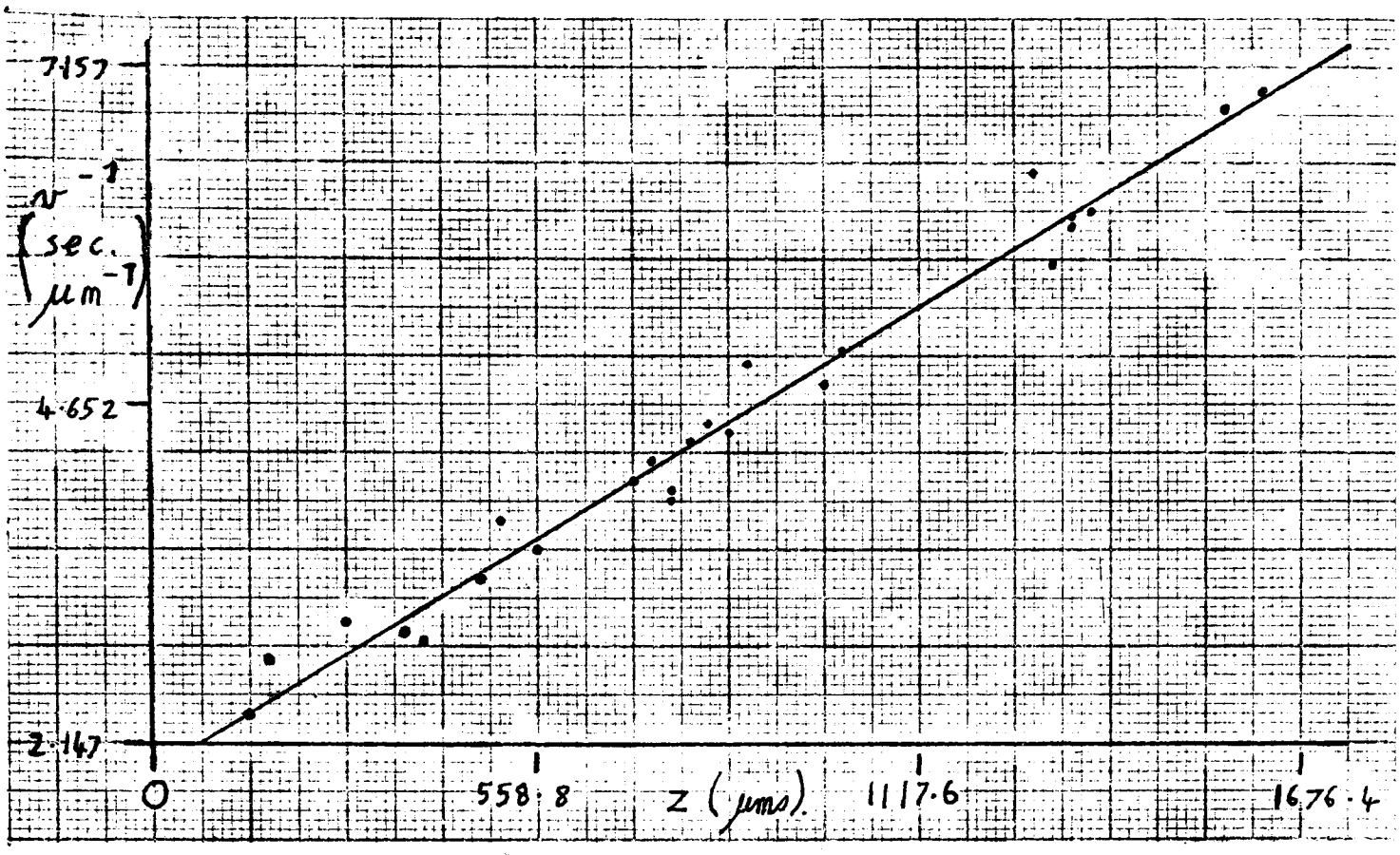


FIG. VII. 1. Graph of v^{-1} versus z for nominally pure succinonitrile.

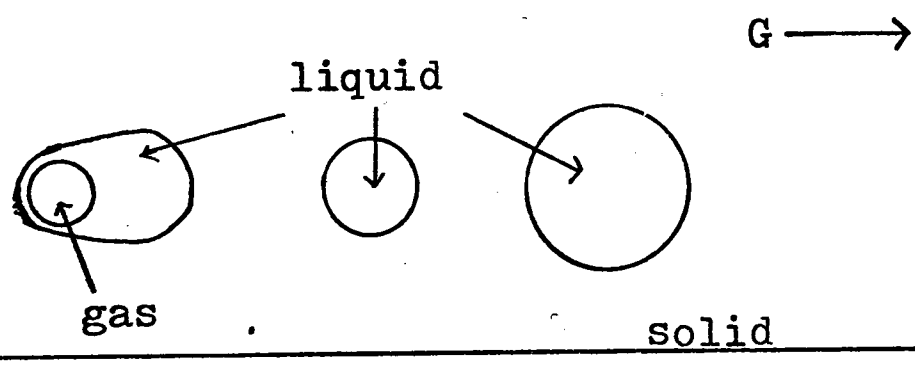


FIG. VII. 2. Liquid drops emerging from a gas bubble.

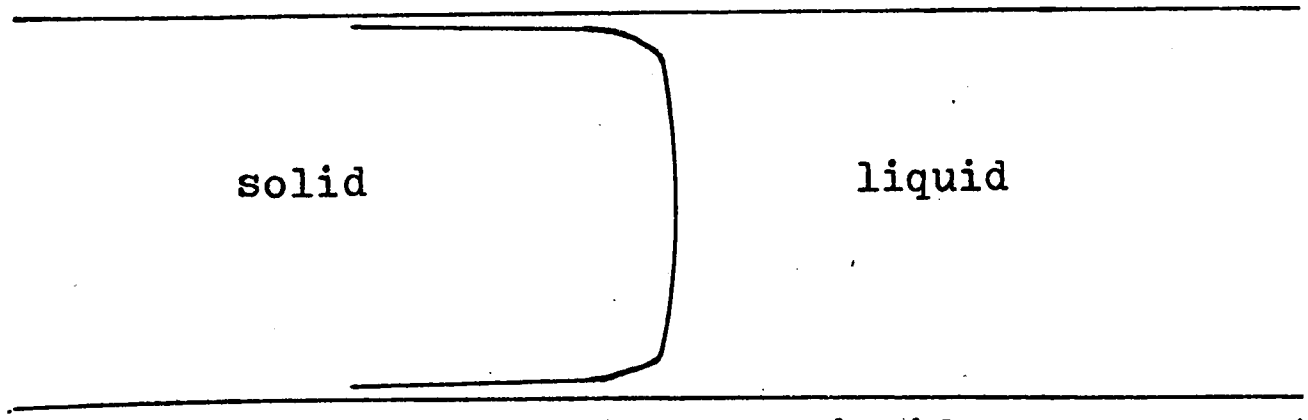


FIG. VII. 3. Showing the liquid layers near the walls of a specimen cell.

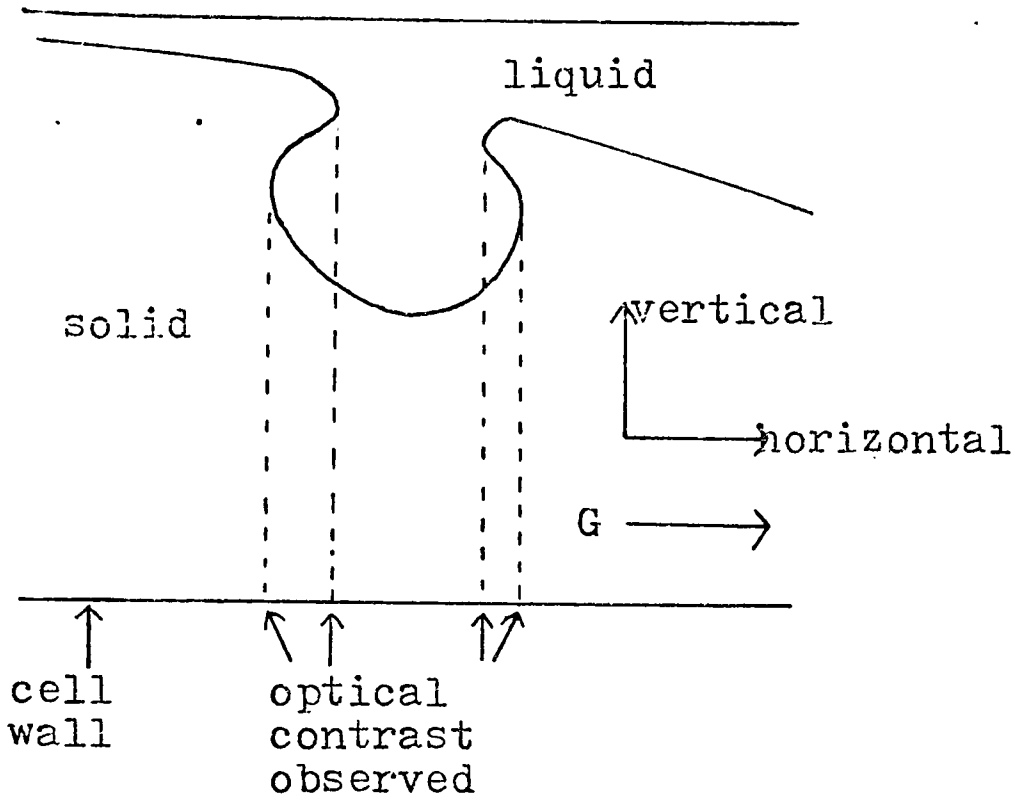


FIG. VII. 4. Showing why a double ring is observed when a liquid drop coalesces with, or breaks free from, a liquid layer.

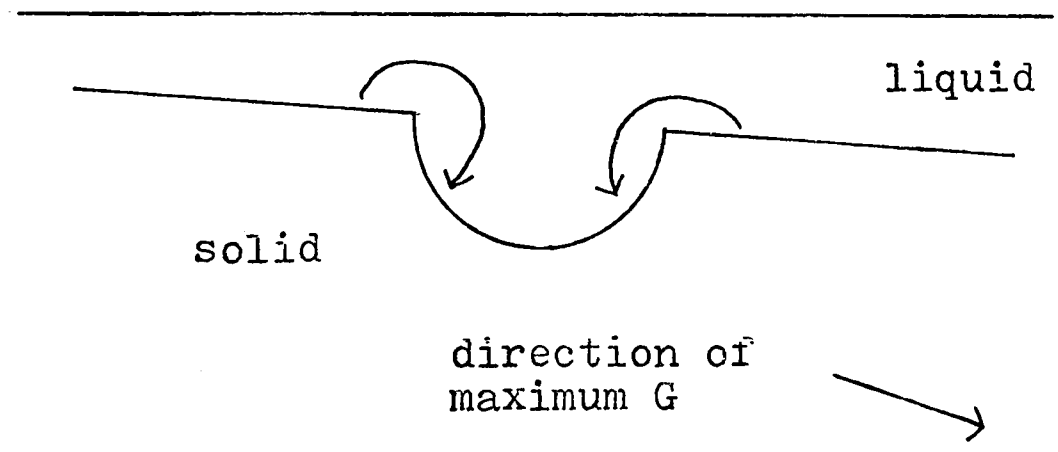


FIG. VII. 5. Upper liquid layer instability. Solute flows towards the depression, down the vertical component of the thermal gradient.

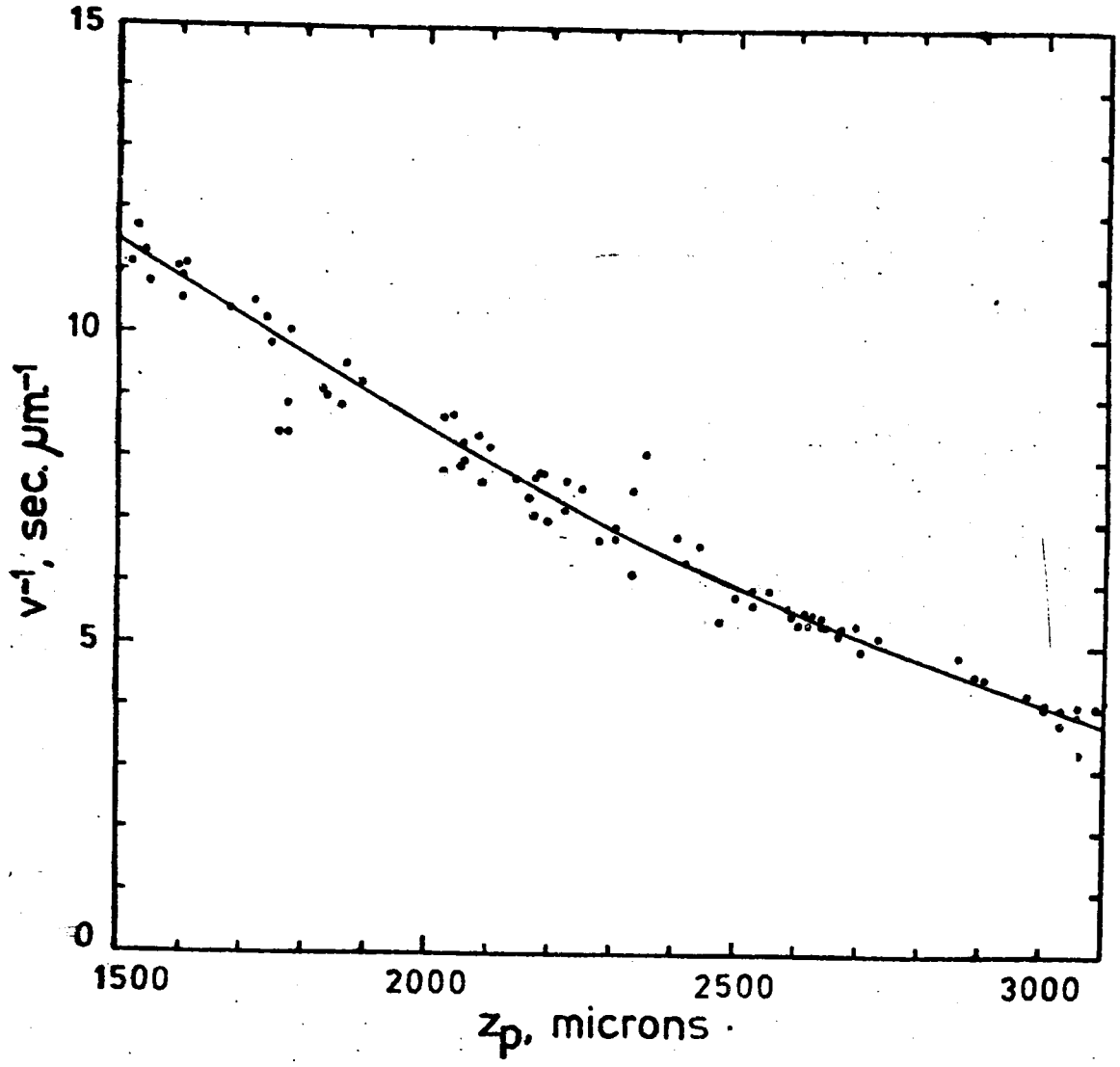


FIG. VII. 6. Graph of v^{-1} versus z_p for drops in succinonitrile - 6 wt. % camphor.

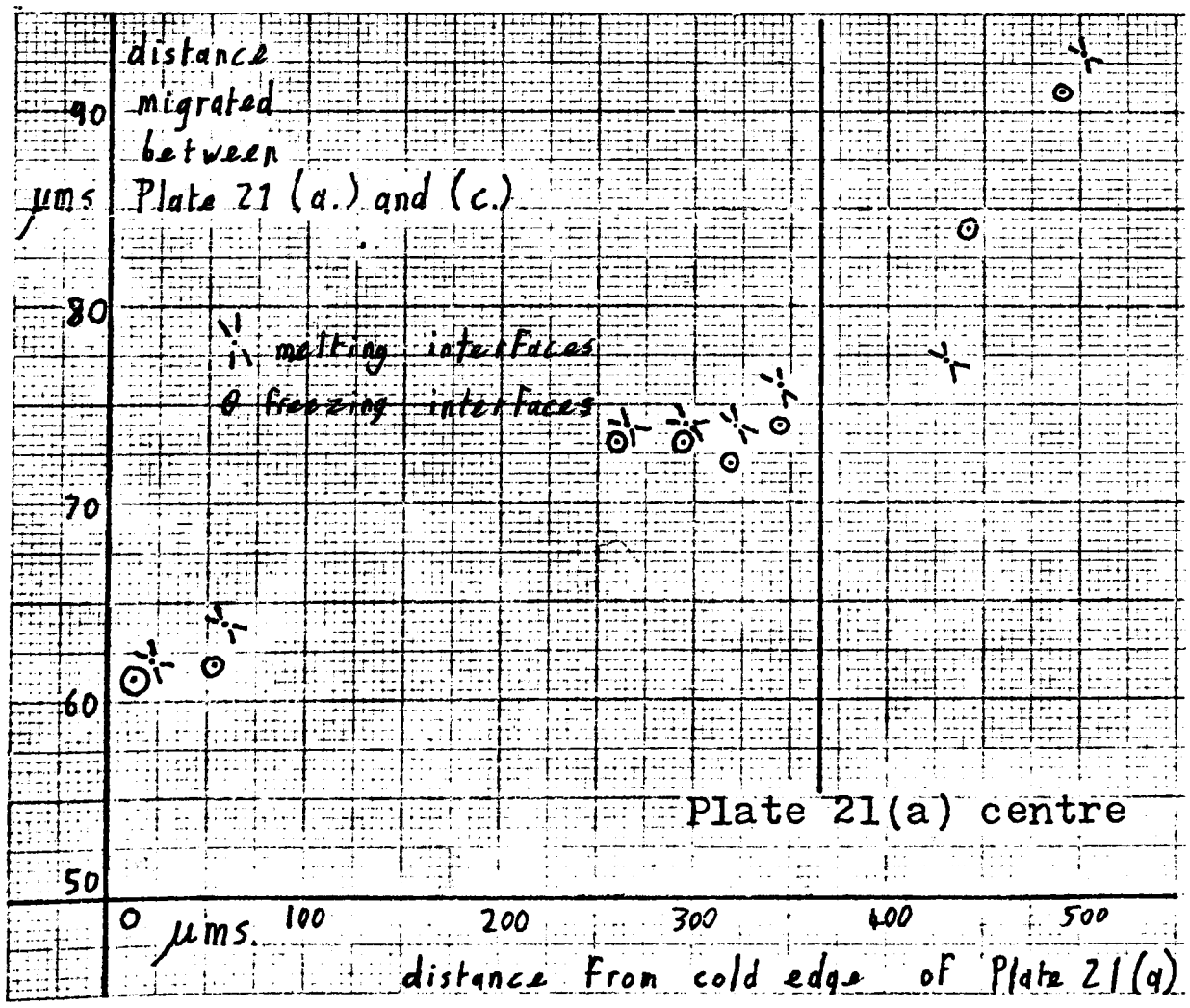


FIG. VII. 7. Measurements of distances migrated from Plate 21.

FIG. VII. 8. l^{-1} versus $(v^{-1})_{l\to\infty}/v^{-1}$, high - temperature run.

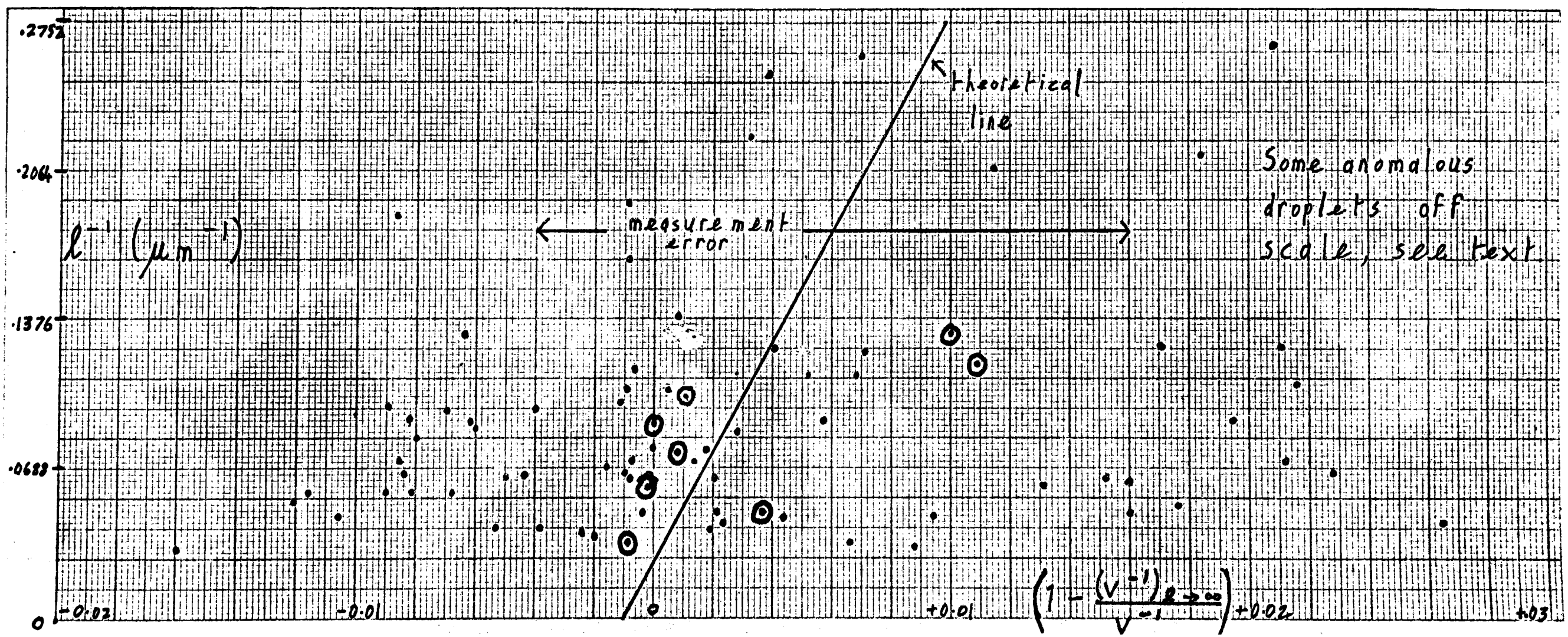
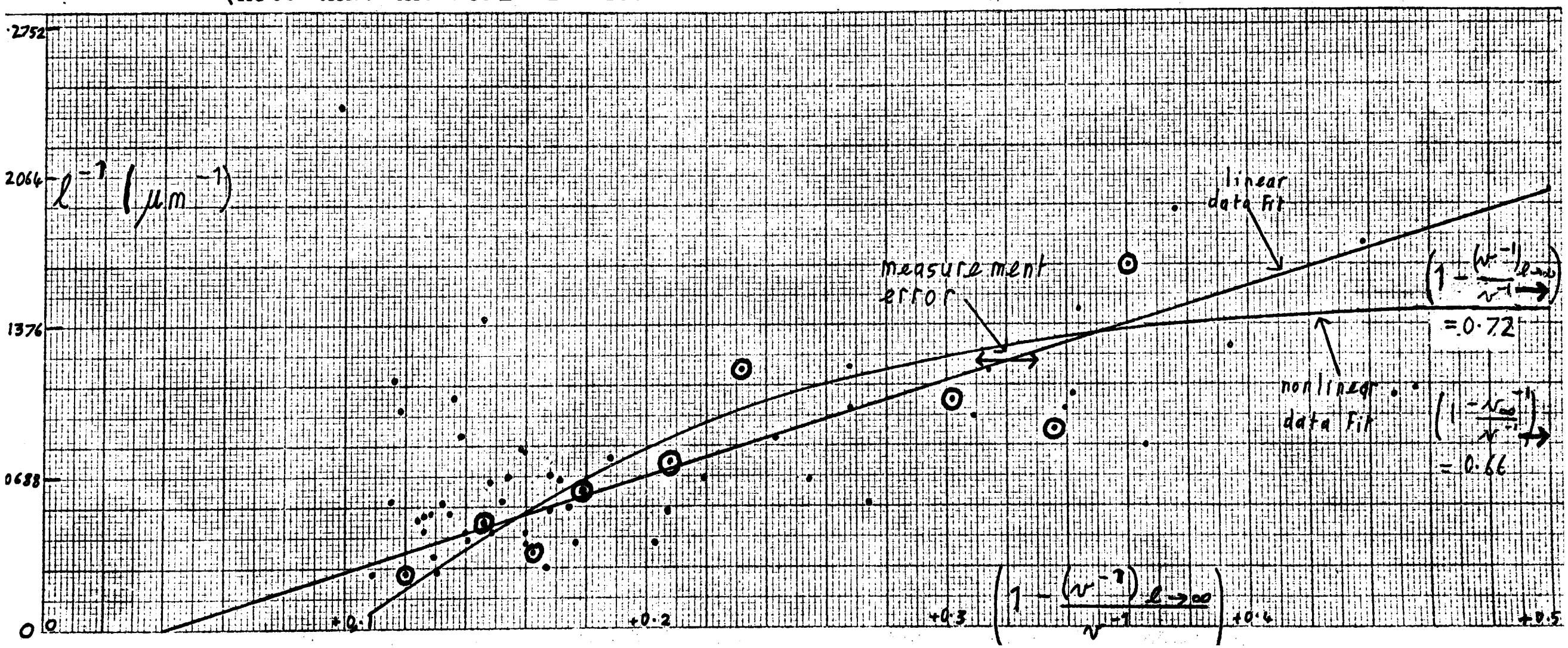


FIG. VII. 9. l^{-1} versus $(v^{-1})_{l\to\infty}/v^{-1}$, low - temperature run.
(note that the scale is different from FIG. VII. 8)



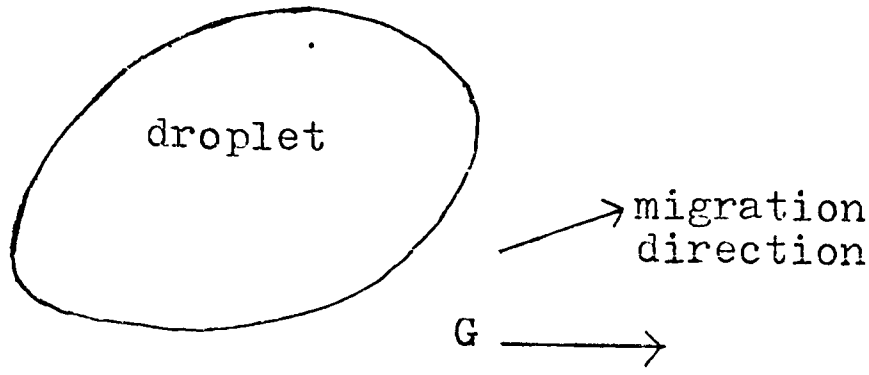


FIG. VII. 10.

Observations of shape distortion in drops, section (e.)

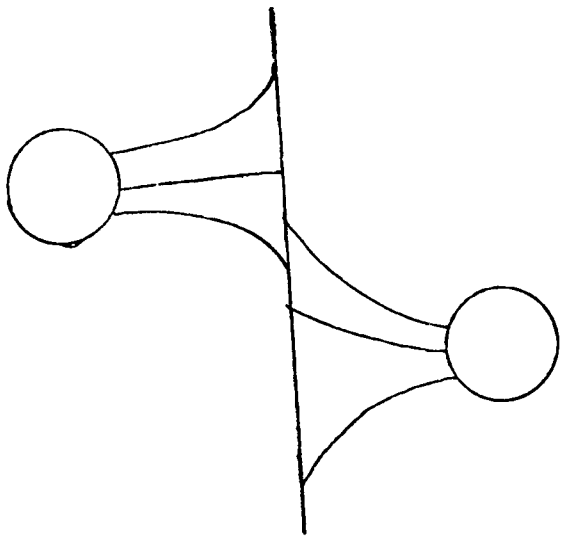


FIG. VII. 11.

Dislocations "attracting" droplets to grain boundary (schematic)

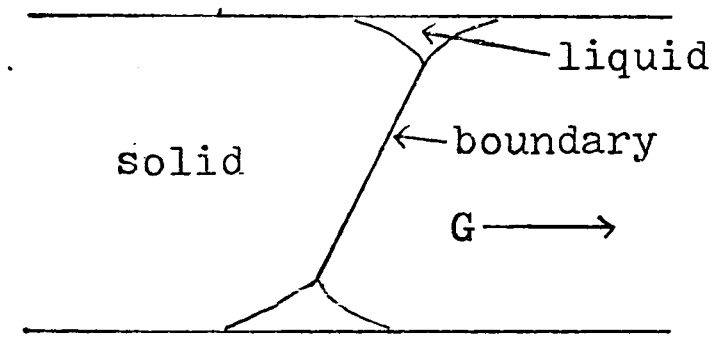


FIG. VII. 12.

Low - angle boundary in glass tube (section (g.)).

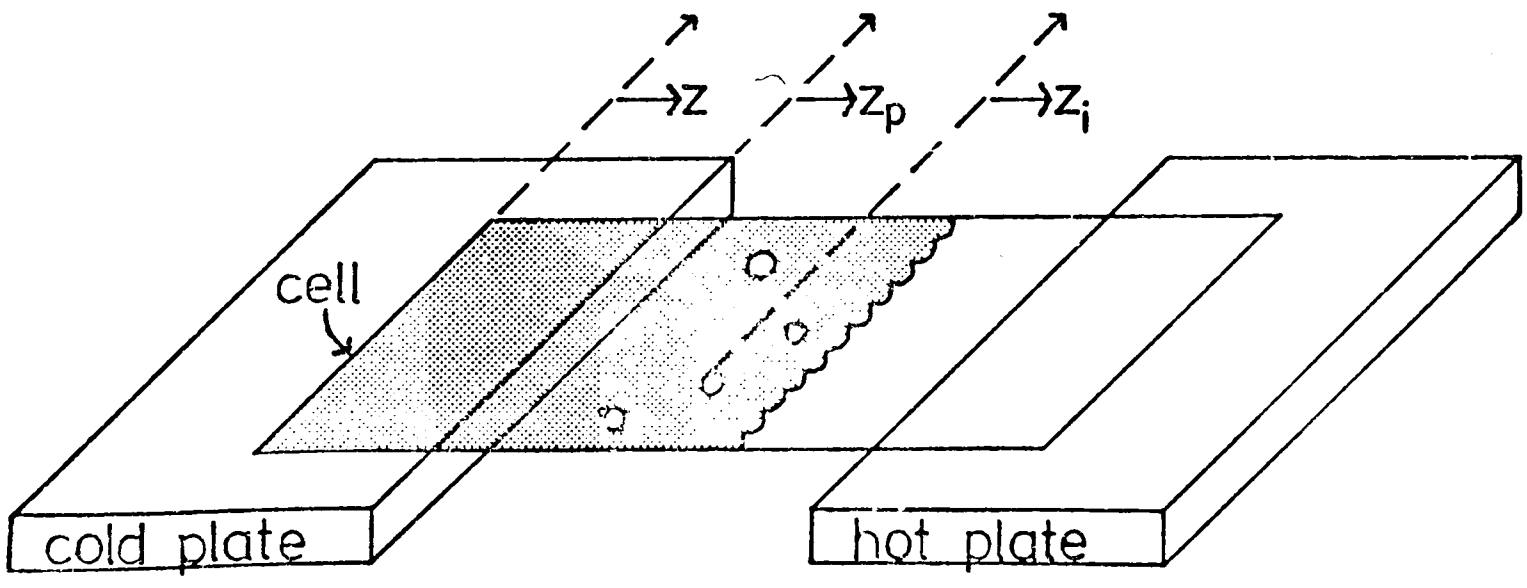


FIG. VII. 13. Definition of co-ordinates.

Chapter VIII. Temperature Gradient Zone Melting - Theoretical Applications.

This chapter provides a physical interpretation of the results obtained in chapter VI and a discussion of the consequences of TGZM in various situations.

(a) Diffusion Versus Heat-Flow "Control"

Standard texts (e.g. refs 5, 59, 81) commonly describe phase transformation as "diffusion-controlled" in alloys and"heat-flow-controlled" in pure materials, provided that local equilibrium is maintained at the interface. The texts do not specify what degree of purity is required of a "pure" material, and in view of the low thermal conductivity of organic materials,[231,229] it has been suggested[209] that thermal interactions are of importance in alloyed organics.

TGZM appears to be a particularly suitable process to consider in a theoretical study of this question. When an infinite slab zone migrates in a unidirectional thermal field (Fig. VIII.1), the interfacial heat conservation equations (I.10) point the way to the thermal field solution of Tiller:[18]

$$G_L = \frac{K_s}{K_L} G_\infty - \frac{v\Delta H_f}{K_L} \qquad (II.9)$$

where v_f and v_m are assumed equal, G_L is constant within the zone and $G_s = G_\infty$ is constant within the solid. Clearly,

from (I.10), G_s remains constant and G_L decreases as the $(v\Delta H_f/K_L)$ term increases. The migration velocity is given by an adaptation of (VI.50) combined with (I.11):

$$v = \frac{-D_L G_L}{mc_L^*(1 - k)} \tag{1}$$

assuming local equilibrium and neglecting solid-state diffusion. Combining (II.9) and (VIII.1):

$$v = \frac{-D_L K_s G_\infty}{mc_L^*(1 - k)K_L - D_L \Delta H_f} \tag{2}$$

So, if we define v_0 as the velocity predicted if the latent heat term in (II.9) is ignored:

$$\frac{v}{v_0} = \frac{mc_L^*(1 - k)K_L}{mc_L^*(1 - k)K_L - D_L \Delta H_f} \tag{3}$$

The consequences of (VIII.2) and (VIII.3) are shown in Fig. VIII.2. As temperature increases towards the melting-point and c_L^* falls towards zero, v_0 tends to infinity (if local equilibrium is still maintained), but the actual velocity v falls increasingly below v_0 as G_L is reduced by the latent heat term: v tends towards an upper limit $(k_s G_\infty/\Delta H_f)$ obtained by setting $G_L \to 0$ in (II.9), at which point the migration can be said to be entirely heat-flow controlled. In general, both heat flow and diffusion affect the TGZM velocity, but an arbitrary criterion to describe the "transition" to heat-flow control at low c_L^* might be taken as:

$$v = \tfrac{1}{2}v_0 \tag{4}$$

or:

$$-mc_L^*(1 - k) = \frac{D_L \Delta H_f}{K_L} \tag{5}$$

where:

$$\Delta H_f \text{ (per unit volume)} = \frac{T}{M}\rho \Delta S_f \text{ (per mole)} \tag{6}$$

where ρ is density, M molecular weight, and $(\Delta S_f(\text{molar})/R)$ is commonly near unity for metals and the organic analogues.(15,207) For a hypothetical "typical" metal, we take $T = 1000^oK$, $\rho = 10$ gm/cm, M = 100 gms, $(\Delta S_f(\text{molar})/R) = 1$, and as $R = 8.31$ joules/mole/^oK, $\Delta H_f \sim 10^3$ joule/cm^3. Then, if $D_L = 3 \times 10^{-5}$ cm^2/sec and $K_L = 1$ joule/sec/cm/^oK, $(-mc_L^*(1 - k)) = 0.03^oC$. So when $k \sim 0$ and $m \sim 3^oC$/wt %, $c_L^* = 0.01\%$ for the transition from diffusion to heat-flow control. Accepting this value, (VIII.3) shows that $v = 0.99v_0$ when $c_L^* = 1\%$ and the error in ignoring the latent heat term is even smaller for higher c_L^*. For a typical organic analogue, $T = 300^oK$, $\rho = 1$gm/cm,(226) M = 100 gms, ΔS_f (molar)/R = 1 and so ΔH_f is much lower, ~ 25 joules/cm^3. Then, if $D_L = 3 \times 10^{-6}$ cm^2/sec (chapter VII) and $K_L = 2 \times 10^{-3}$ joule/sec/cm/^oK (Glicksman(229)), then $(-mc_L^*(1 - k)) = 0.04^oC$. This is essentially similar to the result for metals and shows that low K_L in organics is compensated by low ΔH_f and D_L.

From (VIII.1), the condition $v = \frac{1}{2}v_0$ is identical to $G_L = \frac{1}{2}G_s$. From (I.10) taking $K_L \sim K_s$, this occurs when:

$$v = \frac{K_L G_s}{2\Delta H_f} \qquad (7)$$

for any solidification process. This condition is satisfied, using previous figures, when $v = 5 \times 10^{-4}\ G_s\ ^{o}C/sec$ for the typical metal or $v = 4 \times 10^{-5}\ G_s\ ^{o}C/sec$ for organics. Thus if $G_S \sim 20 - 25^{o}C/cm$, the fairly severe distorsion of of the thermal field implied by $G_S = 2G_L$ occurs at $v \sim 10^{-2}$ cm/sec in metals, $v \sim 10^{-3}$ cm/sec in organics. So, sharp changes in G at the interface may occur in rapid dendritic growth, especially in organics (see chapter IV). The transition between diffusion and heat flow "control" occurs at similar solute contents in metals and organics, but at somewhat lower velocities in organics as these have lower D_L values.

However, the problem of heat flow versus diffusion "control" need not always be a simple question of the magnitude of the latent heat term, as it is in TGZM. The thermal diffusivity

$$D_{th} = \frac{K}{\rho c_p} \qquad (8)$$

where K is thermal conductivity and c_p is specific heat, determines the scale and speed of thermal interactions: being unrelated to ΔH_f, but incorporating c_p, this should not be related to the previous discussion. For organics, we take[(226)] c_p = 2 joules/gm ^{o}C, K and ρ as before, giving $D_{th} = 10^{-3}$ cm^2/sec. For metals, we take c_p = 0.4 joules/gm ^{o}C, ρ and K as before, to obtain D_{th} = 0.25 cm^2/sec. Therefore,

$$\frac{D_{th}}{D_L} \sim 10^4 \text{ (metals)}, \quad \sim 3 \times 10^2 \text{ (organics)} \qquad (9)$$

So, while the ratio is somewhat lower for organics than for metals, it is not as low as the figure ~10 suggested by Glicksman[209] and there seems no reason to attribute special importance to thermal interactions in organics on the basis of this ratio.

The only other calculations known to the author which relate latent heat to solute effects in a diffusion treatment are those of James and Sekerka.[257] These authors discussed the "thermal wave" produced when a solid-liquid system is subjected to thermal oscillations. This much more complex analysis showed that latent heat and solute terms were roughly equal when $c_0 = 0.01\%$ in good agreement with our treatment.

(b) Interface Kinetics in TGZM

From (VI.32), the exact solution for R = 0, slow interface kinetics, is:

$$\left(\frac{\partial c_L}{\partial z}\right)_t = \frac{G}{m} - \left(\frac{\Delta T_{km} - \Delta T_{kf}}{m}\right)\left(\frac{v}{D_L}\right)\left(\frac{\exp(-vz_i/D_L)}{(\exp(-vl/D_L)) - 1}\right) \qquad (10)$$

When $(vl/2D_L) \ll 1$, from (VI.48):

$$\left(\frac{\partial c_L}{\partial z}\right)_t = \frac{G}{m} + \frac{\Delta T_{km} - \Delta T_{kf}}{lm}, \text{ approximately.} \qquad (11)$$

which is the linear concentration gradient assumed by Tiller.[18] Fig. VIII.3 shows the full solutions schematically. Assuming ΔT_{kf} positive and ΔT_{km} negative, $c_L(z)$ must decrease

as the zone passes a fixed point and so $(\partial^2 c_L/\partial z^2)$ is negative. Qualitatively similar behaviour should occur when the restrictions (VI.19) are relaxed. It is of interest to examine whether our exact solution materially alters the "size effect" equations (II.18-23) as derived by Tiller.[18] As is clear from the approximation (VI.47), marked changes in the concentration gradients would only be expected when $(vl/2D_L)$ is significant compared to unity. Now, if, from (VIII.11):

$$\left(\frac{\partial c_L}{\partial z}\right)_t \ll \frac{G}{m} \qquad (12)$$

then, in TGZM,

$$v \ll \frac{-D_L G}{m c_L^* (1 - k)} \qquad (13)$$

Defining the distance between the interface under study and the position at which the temperature equals the pure material melting-point, z':

$$z' = -\frac{m c_L^*}{G} \qquad (14)$$

So, from (VIII.13) and (VIII.14):

$$\frac{vl}{2D_L} \ll \frac{l}{2z'(1 - k)} \qquad (15)$$

Thus, unless the droplet is within a few of its own diameters from the point at which the temperature reaches

the pure material melting-point, $(vl/2D_L)$ must be << 1. So, the assumption of a linear concetration gradient in Tiller's analysis, leading to (II.18-23), is seen to be a very good approximation except for a restricted range of special cases.

However, some of Tiller's other assumptions are not so clearly justified. As indicated in chapter I, equations such as (I.5 - 7) do not have rigorous theoretical justification, and both theory and experiment[13,14,130] suggest a wider range of kinetic behaviour. Our discussion of the results of Hamaker and White[157](chapter II.(b)(5)) illustrates the difficulties involved in finding which kinetic equation fits the data best. The literature survey would indicate that erratic behaviour is the most clear-cut indicator of interface kinetics governed by dislocations, and that stationary small droplets suggest a two-dimensional nucleation mechanism (since, alone of the kinetic laws, this mechanism implies negligible velocities at finite drop sizes.) Unfortunately, the results of chapter VII indicate that dislocation dragging can cause erratic droplet motion or prevent motion even when local equilibrium is maintained at the interface. Droplets, in particular, do not entirely behave as predicted by Tiller.[18] From (VI.68), it can easily be shown that $(\partial c_L^*/\partial z)$ along the surface of a spherical drop is not linear unless (I.5) applies or local equilibrium can be assumed. Any other kinetic law must cause a shape distorsion, in addition to that considered by Cline and Anthony[161] and Jones,[144] and this may possibly affect the migration velocity. The work of Cline and Anthony[161,164] demonstrates how

size-dependent shape distorsions affect velocity when $K_s \neq K_L$. Perhaps the most serious fault, however, is the assumption that k is unaltered by the departure from equilibrium (chap I.(b)).

Figure VIII.4 shows the possibilities for non-equilibrium melting given by a free energy-composition curve: this should be compared with Fig. I.1 for non-equilibrium solidification. It is clear that thermodynamics allows a much greater range of possible compositions to the growing phase than to that being consumed. In particular, while ΔT_{kf} must be positive in TGZM (since, as noted in (I.4), terms such as ΔT_c, ΔT_k refer to an equation connecting liquid composition with temperature), ΔT_{km} need not, in fact, be negative. Indeed, it appears possible from Fig. VIII.4 that $(\partial c_L/\partial z)$ might be greater than (G/m) due to a positive ΔT_{km}, leading to the intuitively unappealing result that slow interface kinetics at the melting interface may increase the drop migration velocity. While a binary interface-kinetic theory[2,20] might in fact rule out such a possibility, thermodynamics does not. So the TGZM studies summarized in Table II.3 provide rather different information from that obtained in solidification studies. Most of the μ values measured in Table II.3 refer to melting kinetics. So, the general result that slow interface kinetics retards droplets rather than increasing their velocities (except possibly in the experiments of Mkavsky and Weinstein[205]) is significant. It indicates that the range of liquid compositions forming at the melting interface (Fig. VIII.4) is to the right of c_L (eq.) This range includes c_L^* values for which μ_A and μ_B

both decrease on melting, and values for which μ_B increases, but not values for which μ_A increases. The theory of Langer and Sekerka,[20] by contrast, suggests that all three of these situations (i.e. both μ values decrease, only μ_A decreases, only μ_B decreases) can occur, depending on disequilibrium due to diffusion across the interface.

We have not applied Langer and Sekerka's theory to TGZM, but we may use the idea of disequilibrium due to diffusion to rationalize the TGZM results. At the melting interface, as it is almost always true that $c_{sm}^* > c_{s\infty}$, there is a flux of B atoms towards the solid in both phases (Fig. VI.4) and a corresponding flux of A towards the liquid. Diffusion and interface motion thus combine to transport A atoms into the liquid and we might expect $\mu_{AL} < \mu_{AS}$. On the other hand, while interface motion also brings B atoms into the liquid, diffusion acts in the opposite direction and the occurrence of $\mu_{BL} > \mu_{BS}$ seems possible. So this very speculative argument does at least concur with the results. An experimental test of these ideas might be to study μ_m as a function of $(c_{Sm}^* - c_{s\infty})$. In any event, besides the terms ΔT_k, ΔT_c determined from a $T - c_L$ relation such as (I.4), comparable terms $\Delta T_k'$, $\Delta T_c'$ are required to describe the $t - c_s$ relation:

$$\Delta T = \frac{-m}{k} c_s + \Delta T_c' + \Delta T_k' \qquad (16)$$

and, as ΔG_k (labelled ΔG in Fig. I.1) depends on both ΔT_k and $\Delta T_k'$, it may be incorrect to use (I.5 - 7) in

binary systems as in Tiller's[18] treatment.

A further problem in connection with melting kinetics may be the shortness of the solid-state diffusion profile. For instance, if $D_s = 10^{-9}$ cm^2/sec and $v = 10^{-3}$ cm/sec, the diffusion length $(D_s/v) = 100$ Å. The continuum theory of diffusion may be inappropriate for such situations, and interface kinetics may be indistinguishable from diffusion. This provides an additional reason for questioning the suggestion[150] that, as a result of the principle of microscopic reversibility, $|\mu_f| = |\mu_m|$.

(c) Fibre Coarsening - Theory of McLean[124]

McLean[124] (II.(b)(2) and (7)) discussed solid-state coarsening in a thermal gradient on the basis of differential thermal migration, by volume diffusion, resulting from a temperature-dependent diffusion coefficient. Such a coarsening mechanism might be particularly important in highly perfect lamellar structures where most of the other postulated solid-state coarsening mechanisms are geometrically impossible. However, we will show that substantial modifications are required in the light of the work of chapter VI. In the following, McLean's equations will be designated by the prefix M.

Considering diffusion of B atoms in a matrix α, McLean wrote:

$$f = -\eta kG \qquad \text{(M-1)}$$

where

$$\eta = \frac{Q^*}{kT} + \frac{T}{c_{B\alpha} m_\alpha} \qquad \text{(M-2)}$$

where f is the "force" on each B atom, Q^* the heat of transport, $c_{B\alpha}$ the concentration of B in the α phase of a two-phase mixture, and m_α the gradient of the α phase solvus. The "force" gives rise to a diffusive flux, the atom drift velocity being:

$$v_\beta = \frac{D_\beta}{kT} f_\beta \qquad (M\text{-}3)$$

and, with interface velocity v given by:

$$v = \frac{-c_{B\alpha} v_\beta}{(c_{B\beta} - c_{B\alpha})} \qquad (M\text{-}4)$$

a solution was obtained. In (M-2), the first term on the right represented thermotransport while the second represented normal diffusion down a concentration gradient, similar to TGZM as discussed in the rest of this thesis but due to solvus rather than liquidus composition varying with temperature. Dropping the thermotransport term for simplicity, and combining (M.1-4), we find:

$$v = \frac{GD_\beta}{m_\alpha (c_{B\beta} - c_{B\alpha})} \qquad (17)$$

Comparing this with (II.14) shows that McLean assumed:

$$\left(\frac{\partial c_{B\beta}}{\partial z}\right)_t = \frac{-G}{m_\alpha} \qquad (18)$$

everywhere in the beta phase, in spite of the concurrent assumption that D_β varies with temperature. On this assumption, McLean found that v should be higher at the hot end of a β zone (he assumed no diffusion in the α phase)

because of the higher D_β (see (M-3), (M-4)). However, Appendix B(a) suggests that (VIII.18) is incorrect, and that (from (B.10)), the diffusive flux ($D_\beta(\partial c_{B\beta}/\partial z)$) is constant across the β zone. Then, from (VIII.17), if ($c_{B\beta} - c_{B\alpha}$) varies negligibly with temperature as assumed by McLean, v should in fact be the same at the hot end as at the cold end of a β zone.

To understand the significance of (B.10), we consider zone migration past a fixed point z'. The composition $c_L(z')$ will be c_{Lm}^* at some time and c_{Lf}^* at a later time: now, when R = 0 and local equilibrium is maintained, these compositions $c_{LM}^*(z')$, $c_{Lf}^*(z')$ will be equal (Fig. VIII.5). Therefore, the average $(\partial c_L/\partial t)_z$ during the passage of the zone will be zero. Whereas (B.10) guarantees $(\partial c_L/\partial t)_z = 0$ at all times, (VIII.18) would imply a continuous decrease in $c_L(z')$ when D_β varies with temperature, and thus cannot be correct. These results highlight the problems involved in making valid approximations in this field. If (al/D_{LO}) is small in (B.10), i.e. if the change in D_L across the zone is much less than D_{LO}, then expansion of (B.10) to first order suggest a linear concentration gradient as assumed by McLean. The approximation seems very accurate, but, as the calculation sets out to find a small difference $(v_m - v_f)$ between two large quantities, small errors in v can give very large errors in $(v_m - v_f)$.

Bearing this in mind, we must now show that (B.10) does not entirely prove the equality of interface velocities at opposite ends of a zone in which all the diffusion occurs, in the general case. (B.10) applies only when v = 0 and

it can indeed be argued that the conclusion $(\partial c_L/\partial t) = 0$ is embodied in the assumption of a stationary diffusion solution with $v = 0$. We must therefore examine whether non-zero v introduces any new factors.

From Fig. VIII.5, it may be seen that although the average $(\partial c_L/\partial t)_z$ is zero (averaged over the complete zone passage), $(\partial c_L/\partial t)_z$ is not generally zero at any given time. The value of $c_L(z')$ is kept nearly constant by the downward curvature of the c_L - z plot, so that higher $(\partial c_L/\partial z)$ at the cold end balances higher D_L at the hot end: but, precisely because of this downward curvature, $c_1(z')$ is not exactly constant. We would like to have an exact solution to see how important this variability of c_L is. The best that can be achieved is to make the physically invalid assumption that D_L varies only with z_i. In reality (see (VI.25)) $D_L(z_i)$ must be time-dependent if $T(z_i)$ is not constant, and no solution is obtainable. By assuming D_L varies only with z_i, we do at least obtain D_L varying across a migrating zone and the solution (Appendix B(c)) predicts downward curvature of the c_L - z plot. The solution does indicate a difference between v_f and v_m but, as shown in the Appendix, such a difference is much smaller that that predicted by McLean provided that $(al/D_{LO}) \ll 1$. Thus, without relying on the precise results of Appendix B(c) (which though mathematically exact, is physically inexact) we may conclude that the velocities of opposite ends of a β zone are essentially equal under the conditions of McLean's analysis (D_β varying with T, $(al/D_{\beta O}) \ll 1$ with l as β zone length, no diffusion in α phase).

At first sight, this conclusion seems to invalidate the entire McLean analysis. However, we have only considered one particular β zone. From (B.10), the diffusive flux in the zone depends on the diffusion coefficient at its cold end, D_{LO}. Thus, two zones at different temperatures have differing D_{LO} values, different diffusion fluxes, and hence different migration rates. On the assumption $(al/D_{LO}) \ll 1$, we may expand the logarithm in (B.10) and drop cubic and higher terms to obtain:

$$D_L \frac{dc_L}{dz_i} = \frac{D_{LO}(c_{Lm}^* - c_{Lf}^*)}{l(1 - (al/2D_{LO}))}$$

$$\sim \frac{D_{LO}(1 + (al/2D_{LO}))(c_{Lm}^* - c_{Lf}^*)}{l}$$

$$= \frac{D_{Lc}(c_{Lm}^* - c_{Lf}^*)}{l} = \frac{D_{Lc}G}{m} \qquad (19)$$

where D_{Lc} is the diffusion coefficient at the zone centre. If we now write the equivalent expression for solid-state migration (e.g. replacing D_{Lc} with$D_{\beta c}$), we obtain (neglecting thermotransport).

$$v_0 = \frac{GD_\beta(z = 0)}{m_\alpha(c_{B\beta} - c_{B\alpha})} \qquad (20)$$

for a β zone centred on z = 0 and:

$$v_{(-1)} = \frac{GD_\beta(z = (-1))}{m_\alpha(c_{B\beta} - c_{B\alpha})} \qquad (21)$$

for a β zone centred on z = (-1). (Fig. VIII.6).
Assuming an Arrhenius relationship $D_\beta = D_0 \exp(-Q/kT)$

(see (B.11 - 12)), (VIII.20) and (VIII.21) give:

$$\frac{dl}{dt} = v_0 - v_{(-1)} = v_0(1 - \exp(-\alpha l)) \qquad (22)$$

where $\alpha = (QG/kT^2)$. This is the same as (M - 8) except that l refers to the centre-to-centre separation of β zones rather than the width of a single β zone as assumed by McLean. It is interesting that, from our treatment, the β zone in which all the diffusion occurs migrates without change of size while the α zone expands. Presumably, both zones expand in the general case where diffusion occurs in both zones. Thus, our analysis shows that (M-8) is qualitatively reasonable and fails only in its assessment of the relative rates of thickening of zones of different phase.

Proceeding with the analysis, McLean wrote:

$$\frac{dr}{dt} = \frac{\mu}{2} v_0(1 - \exp(-2\alpha r)) \qquad (M\text{-}11)$$

for cylindrical and spherical inclusions, where r is inclusion radius and μ was stated to equal unity. (M-11) was derived simply by substituting 2r for l in (M-8) (note that $dr/dt = \frac{1}{2}dl/dt$). However, as shown in chapter VI.(d)(2), migrating n-dimensional zones grow or shrink at (1/n) times the rate for an equivalent planar zone and so μ should be $\frac{1}{2}$ for cylinders, $\frac{1}{3}$ for spheres. McLean also gave an integrated form of (M-11), numbered (M-12), and proceeded to make two approximations:

when $2 \propto r \ll 1$, $\frac{dr}{dt} = \frac{1}{2}\mu v_0 \propto r$ (M-11a)

and:

when $\propto v_0 t \ll 1$, $r = r_0(1 + \mu \propto v_0 t)$ (M-12a)

These equation predict quite different r - t relations. The approximation $2 \propto r \ll 1$ is equivalent to $(v_0 - v_{-2r}) \ll v_0$ and thus seems reasonable. However, the approximation $\propto v_0 t \ll 1$ implies, from (M-12a), $r \sim r_0$. In other words, this approximation applies only to short times and small amounts of coarsening, and is therefore valid only when it is not useful. Unfortunately, McLean's final equation:

$$r(z) = r_0(1 + \mu \propto v_0 t \exp(\propto z)) \qquad \text{(M-16)}$$

was derived from (M-12a) and hence perpetuates this error. If we instead use (M-11a), putting $\mu = \frac{1}{2}$ for cylinders and dropping the other $(\frac{1}{2})$ on the right-hand side with is an arithmetic error, we obtain:

$$r(z) = r_0 \exp(\tfrac{1}{2} v_0 \propto t \exp(\propto z)). \qquad (23)$$

in place of (M-16). McLean found experimentally that $\log_{10}(r - r_0)$ was linearly proportional to z, as predicted by (M-16) but not by the corrected equation (VIII.23). It is difficult to apply our theory to McLean's results since the author did not state r_0, or the units of $(r - r_0)$: however, the fibre size was said to have doubled during coarsening.[262] Now, (M-11a) shows that dr/dt doubles when r doubles, while

(M-12a) ignores the increase in r and may thus underestimate the coarsening rate by a factor of about two. This error, in fact, roughly cancels out the error in setting $\mu = 1$ instead of $\frac{1}{2}$ for fibre coarsening and suggests that (M-16) could be a reasonably good approximation (i.e. within a factor of 2 - 3). From (M-16), McLean found $\alpha = 1.77\ mm^{-1}$ and obtained reasonable values for Q. What this implies is merely that $(dr/dt) \propto D_\beta^n$ with n = 1 (M-11a) is the correct form and that, for instance, $n = \frac{1}{3}$ as obtained from an Ostwald ripening analysis is not correct. It should also have been possible to obtain D_0 from the experimental data and thus check the theory more quantitatively.

Assuming $\alpha = 1.77\ mm^{-1}$ and that $r = 2r_0$ after coarsening, (M-12a) suggests that the distance a fibre migrated, $v_o t$, was of the order of 500 μms. This compares with an initial size of ~ 1 - 10 μms and shows that, if the mechanism is correct, the fibres migrated $\sim 10^2$ times their own diameters. The scale of this effect indicates a diffusional macrosegregation which could be more important than the coarsening effect, perhaps removing all the fibres from a $\frac{1}{2}$mm layer at the cold end of the specimen.

However, a rough quantitative check which may now be made casts doubt on these ideas. Migration of 500 μms in 4 hours implies $v \sim 3 \times 10^{-6}\ cm^2/sec$. The diffusion data quoted by McLean give $D_s \sim 5 \times 10^{-11}\ cm^2/sec$ to $\sim 3 \times 10^{-10}\ cm^2/sec$ within the temperature range of interest (1470 - 1570°K). Taking $G = 1.7 \times 10^3\ °K/cm$ in these experiments,[262] using McLean's suggested $m = 820°K/mole\%$[124] and approximating $(c_{B\beta} - c_{B\alpha}) \sim 100$ mole %, equation (VIII.17) gives:

$$v \sim \frac{1.7 \times 10^{3} \cdot 10^{-10}}{820 \cdot 100} \sim 2 \times 10^{-12} \text{ cm}^2/\text{sec.}$$

It seems possible that m_α could be 100 times smaller: this would bring the predicted v to $\sim 10^{-10}$ cm^2/sec. It is also possible that thermotransport, neglected in our calculations, dominates over normal diffusion and indeed McLean's suggested Q^* value, substituted into (M-2), gives $(Q^*/kT) \sim 7$ (thermotransport term) while $(T/c_{B\alpha}\, m_\alpha) \sim (2/c_{B\alpha})$ (normal diffusion term) assuming McLean's original value for m_α. However, this is increased to $\sim(200/c_{B\alpha})$ with our suggested lower m_α and if this is so, the additional thermotransport contribution cannot be of major importance. Consequently $v \sim 10^{-10}$ cm^2/sec is a maximum value possible from theory, but is four orders of magnitude too small to explain the results. We conclude that the coarsening observed by McLean was not due to differential fibre migration by volume diffusion.

(d) TGZM During Crystal Growth

It is argued here that TGZM presents a hazard in the growth of high-perfection single crystals, in that it may spread liquid droplets containing contaminants throughout the crystal while the crystal grows. The following, largely theoretical arguments for this hypothesis have been previously presented:[273] subsequently, Seidensticker and Hopkins[188] reached similar conclusions from an experimental study.

To avoid microsegregation, liquid entrapment and high dislocation densities, it is essential to avoid cellular and

dendritic growth in the production of high-quality crystals (see e.g. refs. 130, 188, 263). This imposes an upper limit to permissible growth rates (e.g. refs 184, 264). As discussed in chapter I (d), the earliest and simplest theory to predict this upper limit was the constitutional supercooling theory[30] and the later, more rigorous work of Mullins and Sekerka[31] and others does not generally modify the predictions by more than a factor of two (see e.g. Dismukes et al[265]). In practice, planar interfaces in isothermal non-metallic crystal growth often appear to be more stable than these theories predict: for a discussion of possible reasons see e.g. Tiller et al.[264] Recently, Jackson and Hunt[266] showed that the temperature dependence of interface-kinetic effects can be an important stabilizing factor. In this work, we will use the constitutional supercooling analysis to predict the permissible range of crystal growth rates, while bearing in mind that faster non-dendritic growth may be possible. Fig. VIII.7 demonstrates the principles of the constitutional supercooling analysis. If line (ii) represents the actual composition profile ahead of the advancing solid-liquid interface, the liquid ahead of the interface is below the liquidus composition (i.e. supercooled). Thus if a bump grows ahead of the main interface, its interfacial composition should (roughly) follow the liquidus and so the local concentration gradients near the bump will be steep and the bump will grow rapidly, causing instability. Since the liquidus slope is:

$$\left(\frac{\partial c_L^*}{\partial z}\right) = \frac{G}{m} \tag{24}$$

stability is predicted when:

$$\left(\frac{\partial c_L}{\partial z}\right)_{\text{interface}} \gg \frac{G}{m} \tag{25}$$

(note that m is negative). Combining (VIII.24) and (VIII.25) and neglecting solid-state diffusion:

$$R_g \ll \frac{-D_L G}{m c_L^* (1 - k)} \tag{26}$$

where R_g is the crystal growth rate. (In steady-state growth, R_g equals the isotherm velocity , R, and $c_L^* = (c_\infty/k)$, and (VIII.26) becomes identical to (I.18)).

If R_g is kept within the range specified by (VIII.26) and liquid contaminants are not otherwise introduced, a good crystal may be achieved. However, some growth techniques (e.g. unseeded flux growth, or the Bridgman method) involve an initial stage of rapid dendritic growth after nucleation before the main crystal is grown by controlled slow cooling. Liquid droplets can also form on the crystal outer surface when contaminants from the crucible or atmosphere form low melting-point compounds with the crystal material.[187,188,267] In both these cases, liquid contaminants are originally confined to a restricted region which can generally be discarded after the crystal has been grown. However, if the droplets migrate through the crystal along the temperature gradients set up during the growth process, the crystal may

become imperfect throughout even though (VIII.26) is satisfied during most or all of the growth process. For the contaminated region to expand and cover the whole crystal, droplet migration velocities must be of the same order as the crystal growth rate. Comparing (II.14) to (VIII.26), it may be seen that this is likely to be true. In fact, if D_L, G, m and k are constants and the maximum permissible value of R_g is R_c:

$$\frac{v}{R_g}\ (\text{TGZM}) = \frac{c_L^*(\text{growth front})}{c_L^*(\text{droplet})} \times \frac{R_c}{R_g} \qquad (27)$$

Figure VIII.8 shows the basic reason for this result. Given G, m constant, the concentration gradient in a droplet (assuming local equilibrium) equals the maximum permissible concentration gradient at the growth front. Thus a droplet placed just behind the growth front would migrate at a velocity R_c and would usually catch up with the growth front and merge with the bulk liquid. In practice, R_g is likely to be, say, $\frac{1}{2}R_c$ (i.e. small enough to prevent instability when transient increases in growth rate occur[184] but large enough to grow crystals in a reasonable time.) For droplets in the solid, the factors D_L, $(c_L^*)^{-1}$, (m^{-1}) generally decrease with falling temperature so that colder drops migrate at velocities lower than R_c. The results of these variations are shown schematically in Fig.VIII.9, where the solid lines refer to the local equilibrium case. The coldest drop does not migrate fast enough to keep up with the isotherms, and thus slows down and

probably stops. The hottest drop also fails to spread the final contaminated area by centimetre-scale distances because it soon merges with the bulk liquid. However, the centre drop, where v = R, migrates at constant speed and temperature and is thus potentially able to traverse the entire crystal as it grows. The dotted lines show the influence of interface kinetics: this lessens the chances of finding drops with v = R, but does not remove them (for the conditions of Fig. VIII.9, such drops do still exist, close to the growth front.)

Thus,we have shown that contaminant droplets in regions of the crystal where thermal gradients exist are likely to migrate fast enough to follow the growth front for centimetre-scale distances. However, drops may shrink in size as they migrate and thus disappear in much shorter distances. Since (when k is constant and < 1), c_{sm}^* is almost certainly greater than $c_{s\infty}$, the solute content of the crystal being dissolved is lower than that of the re-deposited material, c_{sf}^* (Fig. VIII.9). Thus the drop loses its solute to the solid as it migrates, and therefore shrinks in size.

To estimate how far a droplet can migrate before vanishing, we use a simple model. The drop is assumed to migrate at the isotherm velocity, so that its composition is constant. It is assumed initially to be a planar zone so that no lateral solid-state diffusion occurs. The original crystal is assumed to be completely pure (if this is not true, drops shrink more slowly). Then the shrinkage rate of the droplet can be simply obtained from

a materials balance: the total solute content of the drop (per unit area in the plane of the planar zone), lc_L^*, changes at a rate determined by the net rate of solute loss to the solid. So:

$$c_L^* \frac{dl}{dt} = v_m c_{S\infty} - v_f c_{Sf}^* \tag{28}$$

and, with $c_\infty = 0$, $v_m \sim v_f$, $(c_{Sf}^*/c_L) \sim k$:

$$\frac{dl}{dt} = -kv \tag{29}$$

The drop therefore vanishes after a time:

$$t = -l_0 \Big/ \left(\frac{dl}{dt}\right) \tag{30}$$

where l_0 is the initial diameter. During this time it migrates a distance

$$d = vt \tag{31}$$

So, combining (VIII,29 - 31):

$$\frac{d}{l_0} = \frac{1}{k} \tag{32}$$

Typical l_0 values might be expected between $\sim$ 5 - 100 μms. Taking l_0 = 10 μms, we find that d = 1 mm for k = 10^{-2} and d = 1 cm for k = 10^{-3}. Clearly, these results rule out

long-distance migration in most metallic alloys, but not in electronic materials where covalent bonding leads to very restricted miscibility and $k \sim 10^{-4} - 10^{-6}$ in many cases. There are many faults in the simple analysis given above but the main one is, in fact, our assumption of constant k. When k is less than $10^{-2} - 10^{-3}$, the solidus is generally retrograde (Fig. VIII.10).[268-270] This may be explained using free energy-composition curves (Fig. VIII.11). As temperature falls, the entropy contribution to the G - c curve becomes less important and so the shape of the curve changes. When bonding between different atomic species is weak as in low k alloys, two minima appear in the G - c curve as temperature falls and move towards the pure A and pure B composition, reaching them at absolute zero. So the equilibrium solid composition must move either towards pure A or pure B at low temperatures and this generally leads to a retrograde solidus. Interatomic compounds with limited existence ranges such as Ga As often behave similarly.[266] Departures from stoichiometry require differing vacancy concentrations on the different atomic sub-lattices and, since there are less vacancies at low temperatures, the existence ranges shrink. The importance of retrograde solidi may be seen from (VIII.28). If c_{sf}^{*} is actually lower than $c_{s\infty}$, as is likely when the solidus is retrograde, droplets expand while migrating. Therefore, distances covered in TGZM when $k \sim 10^{-2} - 10^{-3}$ are probably unlimited

(for thermodynamic solidus calculations at low k, see Hall[269]). We conclude that when $k \lesssim 10^{-2} - 10^{-3}$, and liquid drops are present in part of the crystal subjected to thermal gradients, the whole crystal is likely to be contaminated during its growth.

In (VIII.31), (d/l_0) should be increased by a factor of three for a three-dimensional droplet, but reduced somewhat if (D_S/v) is not $\ll 1$ (chapter VI.(d)(3)), and increased when the crystal composition $c_{S\infty}$ is significant. Drop survival may also be prolonged if other drops migrate along the same path as can be seen from Fig. VIII.9. So (VIII.31) may perhaps underestimate (d/l_0) by a factor of around 3 - 10 when k is constant.

The first experimental observation of TGZM in growing crystals was made by Bardsley, Boulton and Hurle,[184] who found doped solute trails of typical length 500 μms, width 20 - 40 μms, deposited behind migrating drops in Czochralski-grown gallium-doped germanium. In this material, k varies between 0.05 - 0.09 and so (VIII.31 suggests $(d/l_0) \sim 12$. This agrees well with our estimate $(d/l_0) \sim 12 - 25$, identifying d as the length and l_0 as the width of solute trails in the published photographs. Bardsley et al[184] adjusted their growth conditions to make about 50% of the crystal non-dendritic, so that the average growth rate must have been $\sim 1 - 2\ R_c$ for the dendritically grown regions. The actual growth rate was subject to low-frequency periodic variations (due to melt convection, or crystal rotation) and these induced longitudinal striations

in the crystal. (Fig. VIII.12). The solute trails also exhibited longitudinal striations, but at roughly twice the frequency of the striations in the rest of the crystal. If we assume that striations are formed when a thermal pulse reaches the crystal, the striation spacing should be proportional to the rat of deposition of solid. So the observations indicate that TGZM velocity was roughly half the crystal growth rate R_g, and so not far from R_c. This is consistent with theoretical predictions and incidentally suggests that, despite faceting, interface kinetics cannot greatly have reduced TGZM velocity or increased R_c.

Bardsley and Cockayne[271] subsequently observed similar solute trails in a garnet, and Bardsley et al[263] included useful micrographs in a review. Goodman[187] first studied TGZM due to contamination on a silicon surface. Tufton[267] noted that liquid droplets commonly form on the surface during Czochralski growth of gallium arsenide, run down the surface under TGZM and/or gravity, and commonly stick on striation facets but sometimes reach the growth front and cause harmful twin formation. Seidensticker and Hopkins[188] found droplet contaminants within the bulk of Czochralski-grown garnet crystals, in a region up to 5 mms deep at the shoulder of the crystal. They found that reducing R_g and increasing G had no effect on the occurrence of these inclusions and concluded that they could not have formed during dendritic growth. They therefore considered the possibility of surface-contaminant droplets penetrating the crystal by TGZM and obtained direct experimental evidence that this could occur in their system. We share their conclusion

that TGZM is likely to be important in many crystal growth processes.

(e) TGZM During Dendritic Solidification

Much of our work in this area has been adequately covered in chap. VI of our earlier thesis.[1] This account will be largely restricted to later developments.

We must first modify the earlier treatment of coarsening by differential TGZM during solidification. As explained,[1] the hotter of two sidearms migrates faster throughout solidification, increasing λ_2. However, each sidearm migrates an equal distance, so the greater migration of the hotter arm while both exist equals the distance migrated by the cold arm when first formed before the second arm exists. So:

$$\frac{\lambda_2 \text{ (final)} - \lambda_2 \text{ (initial)}}{\lambda_2 \text{(final)}} = \frac{v(\text{TGZM, initially})}{R} \qquad (33)$$

with v(TGZM) being approximately determined by (II.14) with c_L^* applying to the growth front. This was earlier taken as the liquidus composition. However, Burden and Hunt[51] (and chap. IV.(e)) showed that high undercoolings occur when Q is not far above unity, which is when differential migration is important. If, instead, c_L^* is taken as $(c_0 - GD_L/mR)$ to include the "plane wave" undercooling and the analysis of ref. 1 is repeated, (VIII.33) gives:

$$\frac{\lambda_{2f}}{\lambda_{2i}} = \frac{k(Q - 1) + 1}{k(Q - 1)} \qquad (34)$$

where λ_{2f}, λ_{2i} are final, initial secondary spacings respectively. Now $(\lambda_{2f}/\lambda_{2i})$ is positive for all $Q > 1$, becoming infinite for $Q = 1$. Consequently the inter-secondary pool never migrates as fast as a dendrite tip grows, and TGZM does not directly cause the cell-dendrite transition as suggested in ref. 1.

As shown by (VI.107 - 108), the fractional difference between freezing and melting interface velocities during interdendritic TGZM is (Rl/D_L), if solid-state diffusion is neglected. This is a small fraction in our experiments (chap. VII.(d)) and, as $\lambda_2 \propto D_L^{\frac{1}{3}}$ from a simple extension of Greenwood's coarsening theory,[66] it should tend to be smaller in metals where D_L can be 10 - 100 times higher, though it may be larger for higher R. It is notable that, from chapter VII.(d), migration distances in TGZM can be two or three times the secondary arm spacing even for Q values ~ 25 - 50 which are high enough to make the "plane wave" undercooling,(chap. IV.(e)), quite small. So the importance of remelting and consequent homogenization by TGZM "persists" to higher Q than the plane wave undercooling. However, Q values in commercial castings may be larger still. To investigate the extent of remelting in such cases, rather than using (VI.108), we may note that (VI.97) gives the average distance migrated by the melting and freezing interfaces, while the difference between distances migrated must be some fraction of the final secondary spacing λ_{2f}.

Consequently extensive remelting occurs if $(d/\lambda_{2f}) \gtrsim 1$, while much less remelting occurs if (d/λ_{2f}) is small although, as $l \rightarrow 0$ in the final stages of solidification, (VI.108) shows that some remelting is almost inevitable at that stage. Rough calculations were made using published thermal data[49,88,95,272] to estimate G and R, and taking $D_L = 3 \times 10^{-5}$ cm^2/sec, λ_{2f} as in Al-4½% Cu from the graph of Bardes and Flemings.[62] The results for (d/λ_{2f}) ranged from about 2 in big (2½ - 4 ton) steel ingots to about 0.2 in small aluminium castings. As these values fell close to $(d/\lambda_{2f}) \sim 1$ it would really be necessary to use more accurate λ_{2f} and diffusion data to find when extensive remelting occurs. Nevertheless, some conclusions can be drawn. Low thermal conductivity, leading to higher thermal gradients, is important: considerably more TGZM can thus be expected in steels than in aluminium alloys, copper-base and nickel-base alloys being intermediate. Despite the lower thermal gradients in big ingots, more TGZM occurs because of the greater local solidification time available. As migration distance varies as D_L^1 while λ_{2f} varies as $D_L^{\frac{1}{3}}$, high diffusion coefficient also increases the possibility of extensive remelting. In comparing the possible homogenizing effects of remelting by coarsening and TGZM, it should be noted that if λ_2 increases roughly as (time)$^{\frac{1}{3}}$ during solidification, this represents only an increase ~x 1.25 in λ_2 in the last half of the solidification time, implying that less than 20% of the secondary arm material then remelts. Thus it may be seen that homogenization by TGZM should often be as important, and sometimes should be much more important, than homogenization by coarsening.

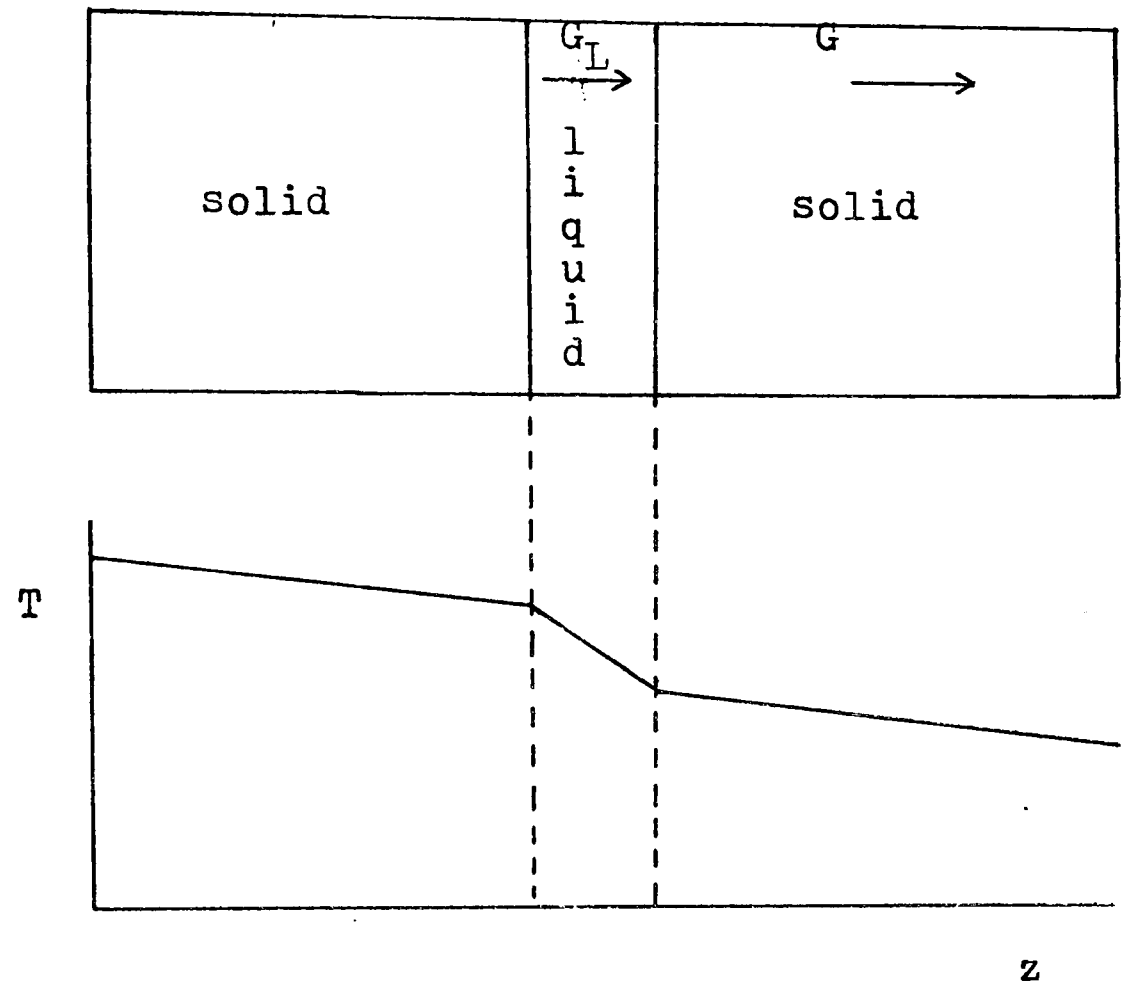


FIG. VIII. 1. TGZM of a slab zone.

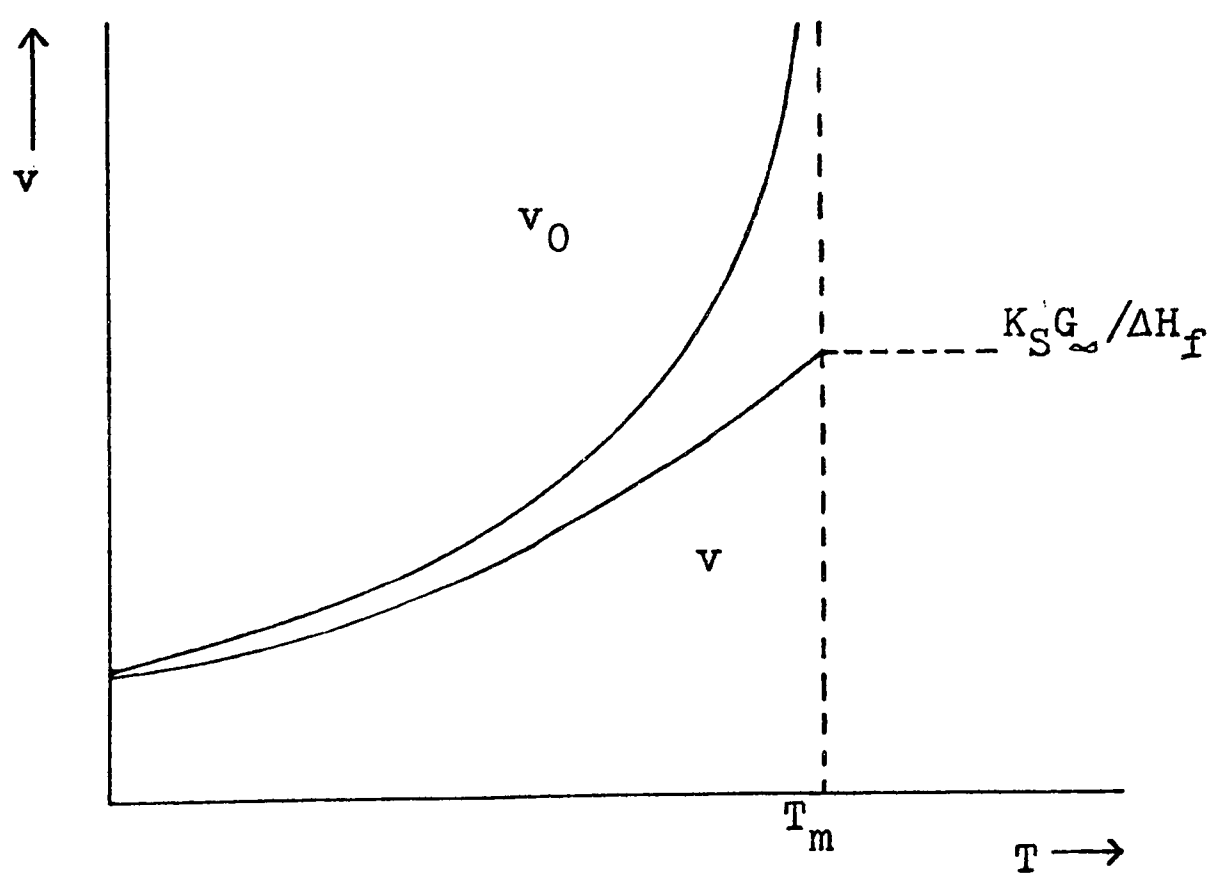


FIG. VIII. 2. TGZM velocity as a function of temperature (chap. VIII (a.))

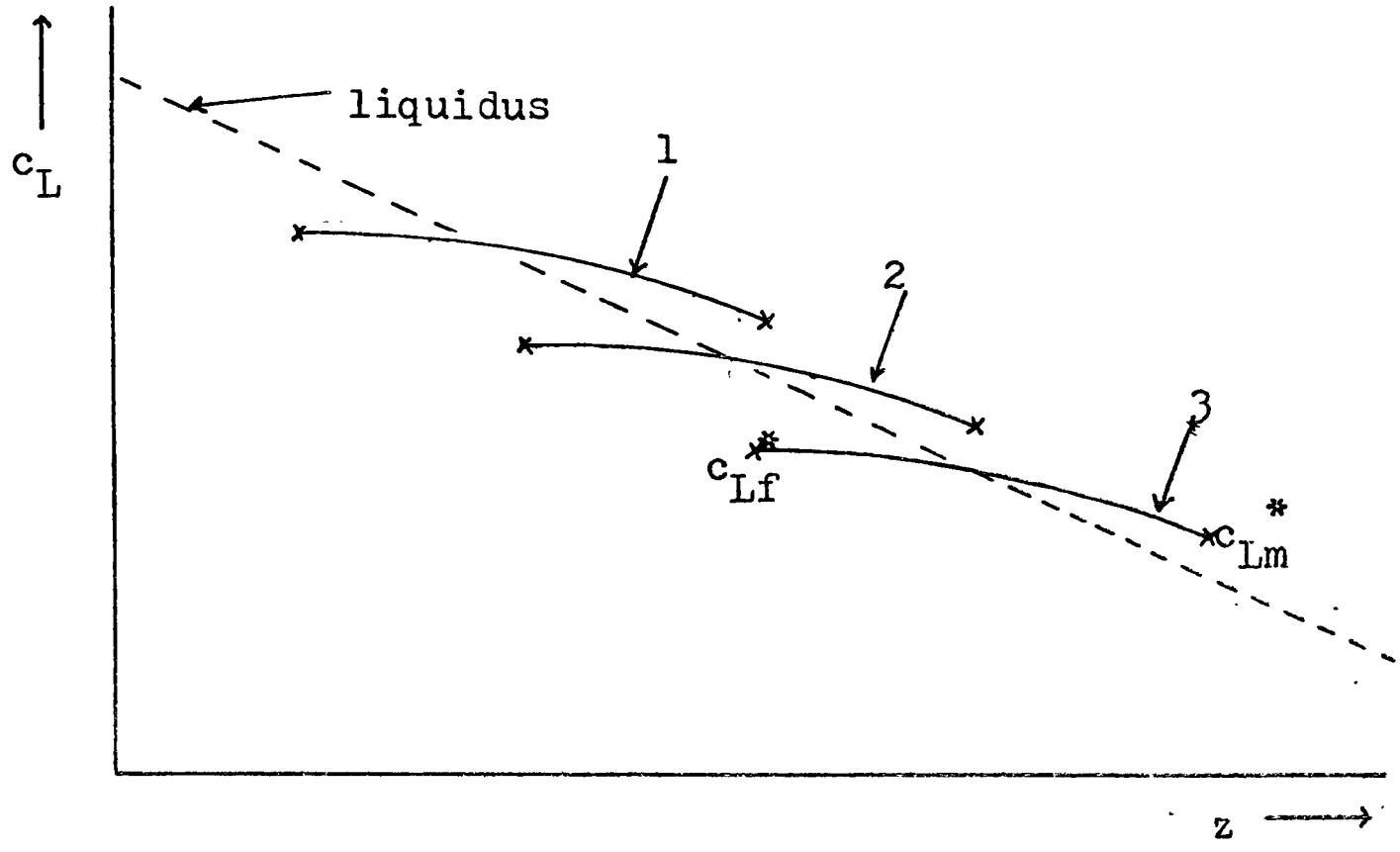


FIG. VIII. 3. TGZM and interface kinetics. 1,2,3, refer to zone positions at successive times.

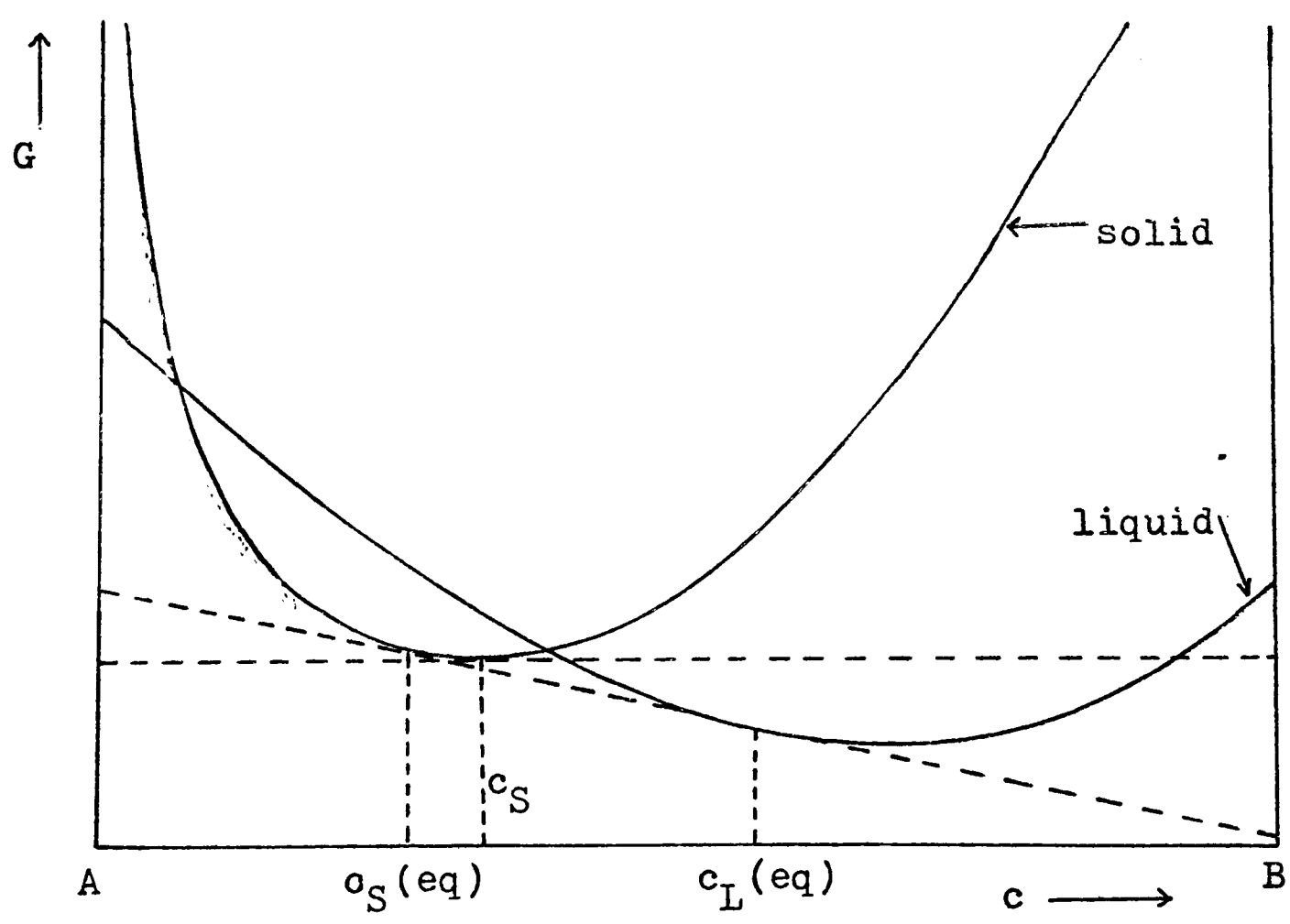


FIG. VIII. 4. G - c curves for non - equilibrium melting.

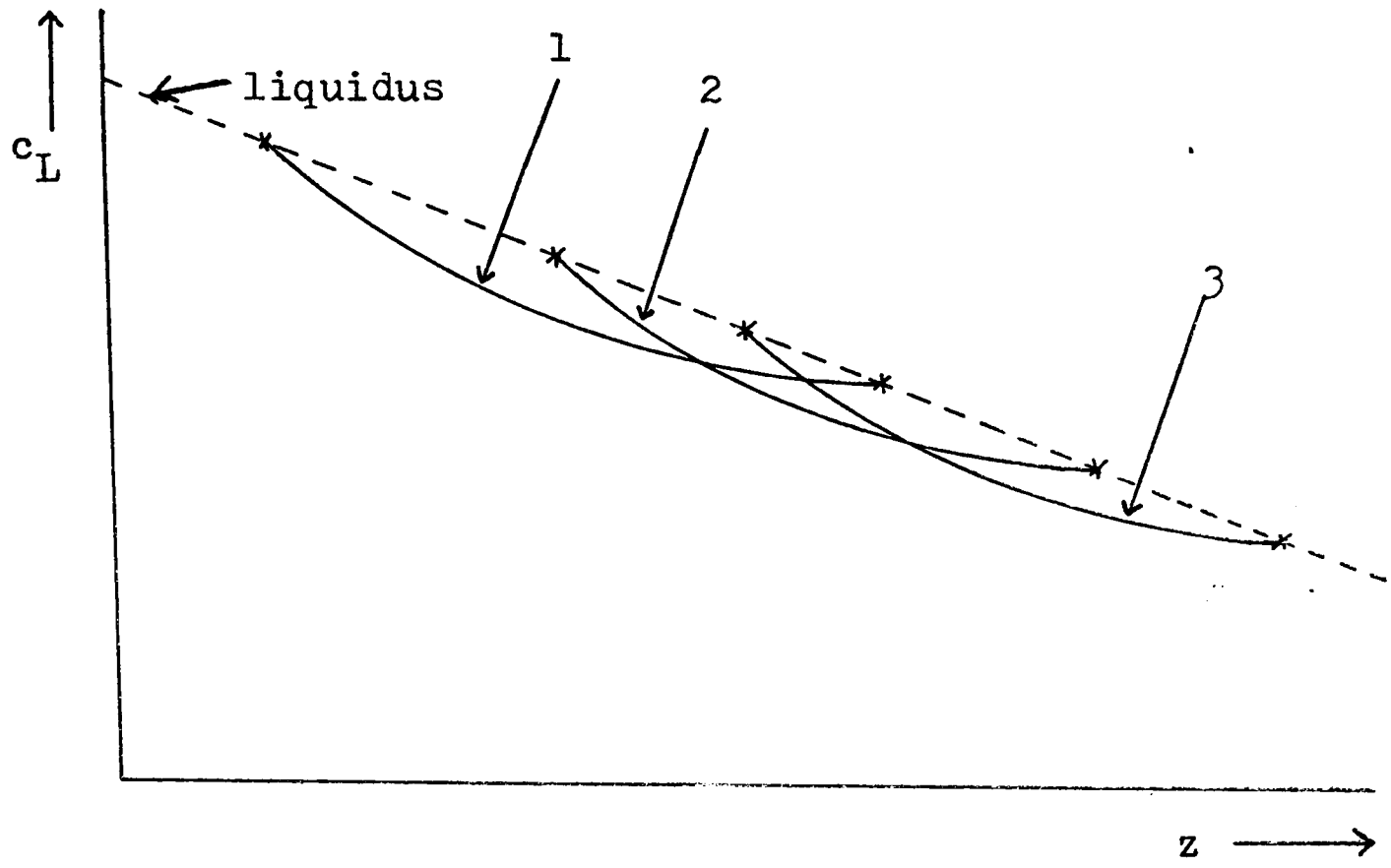


FIG. VIII. 5. TGZM with variable D_L. Curves 1,2,3 represent the solute distributions in a migrating zone at successive times.

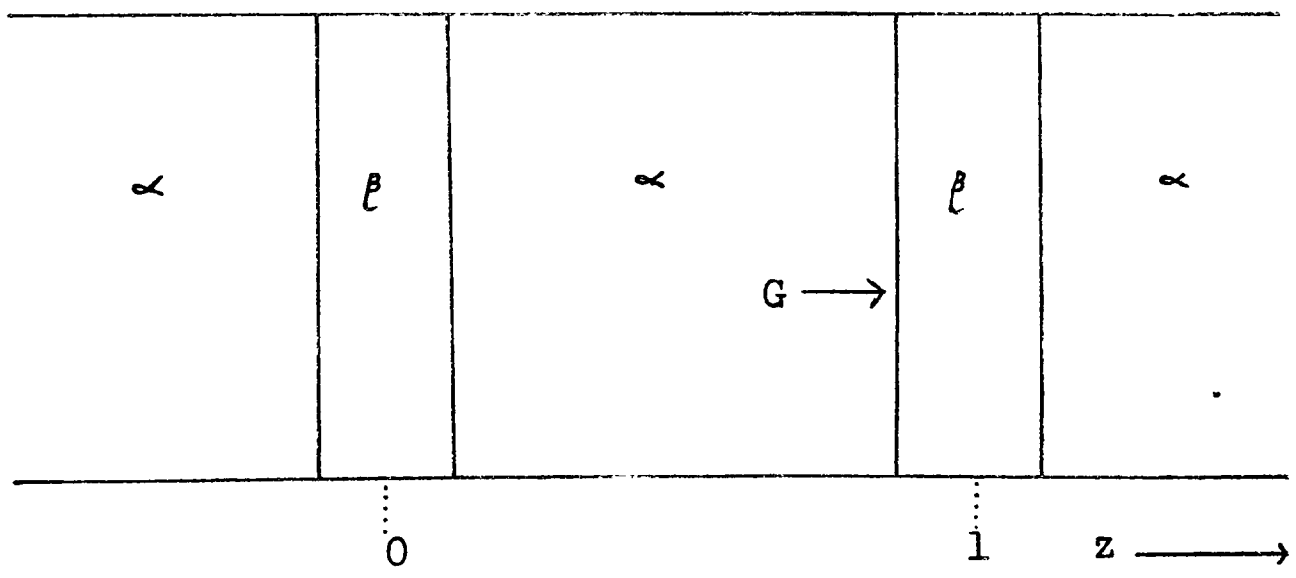


FIG. VIII. 6. TGZM in the solid state (amended notation of Mc Lean, see chap. VIII. (c.))

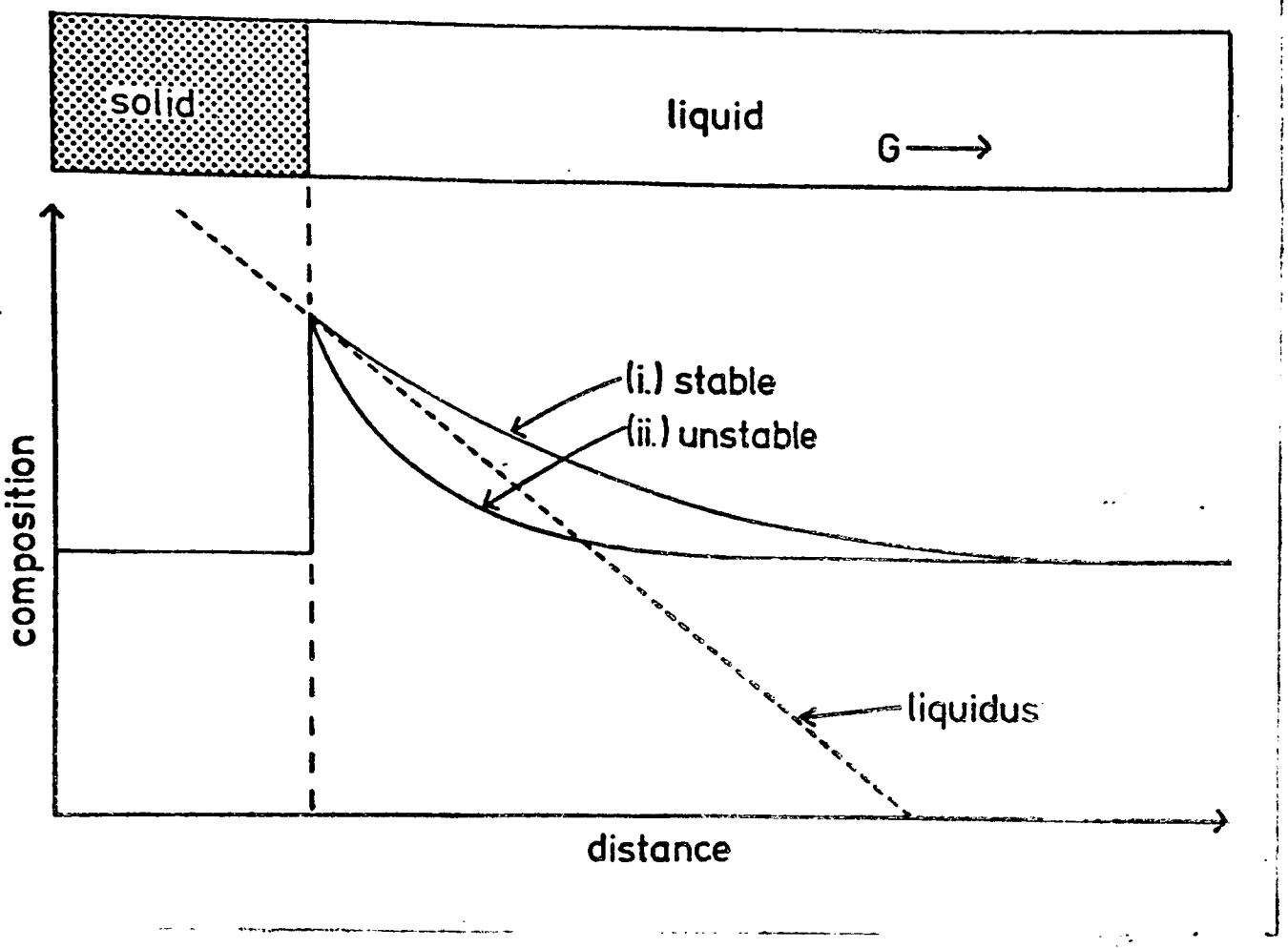


FIG. VIII. 7. Principles of the constitutional supercooling analysis.

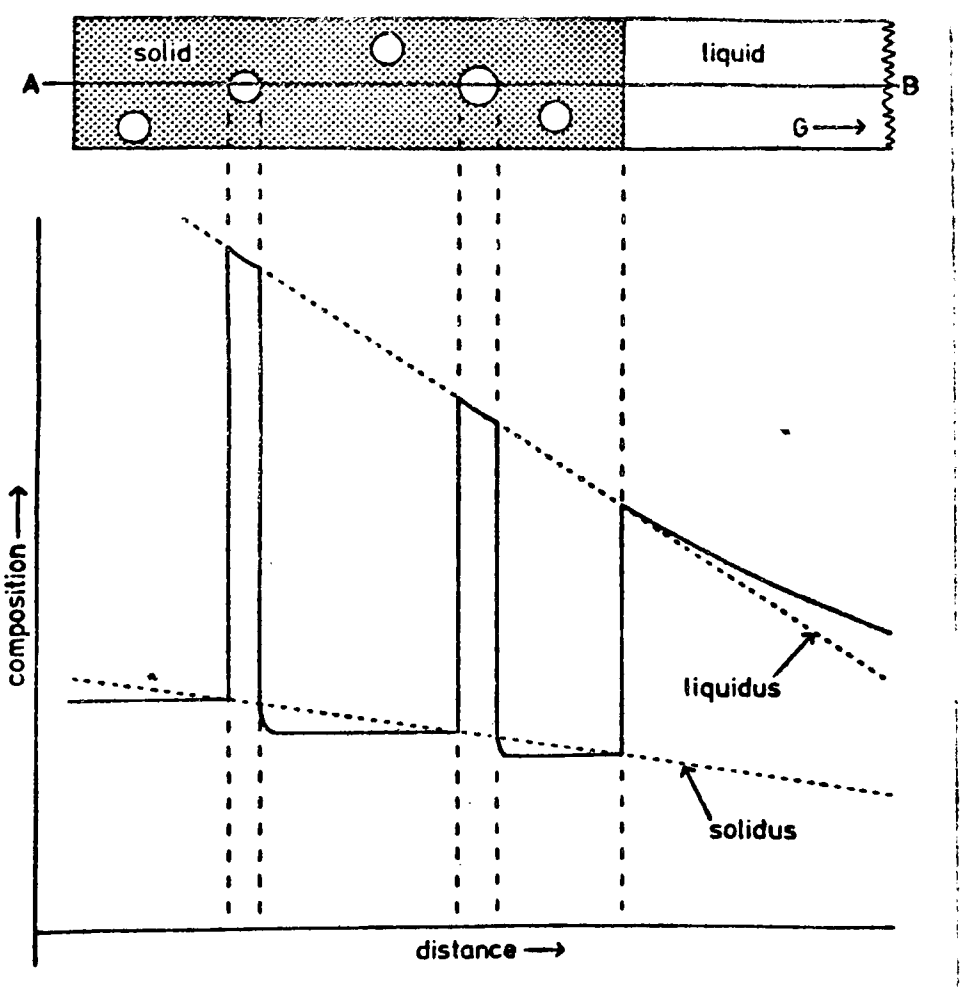


FIG. VIII. 8. TGZM in a growing crystal (schematic).

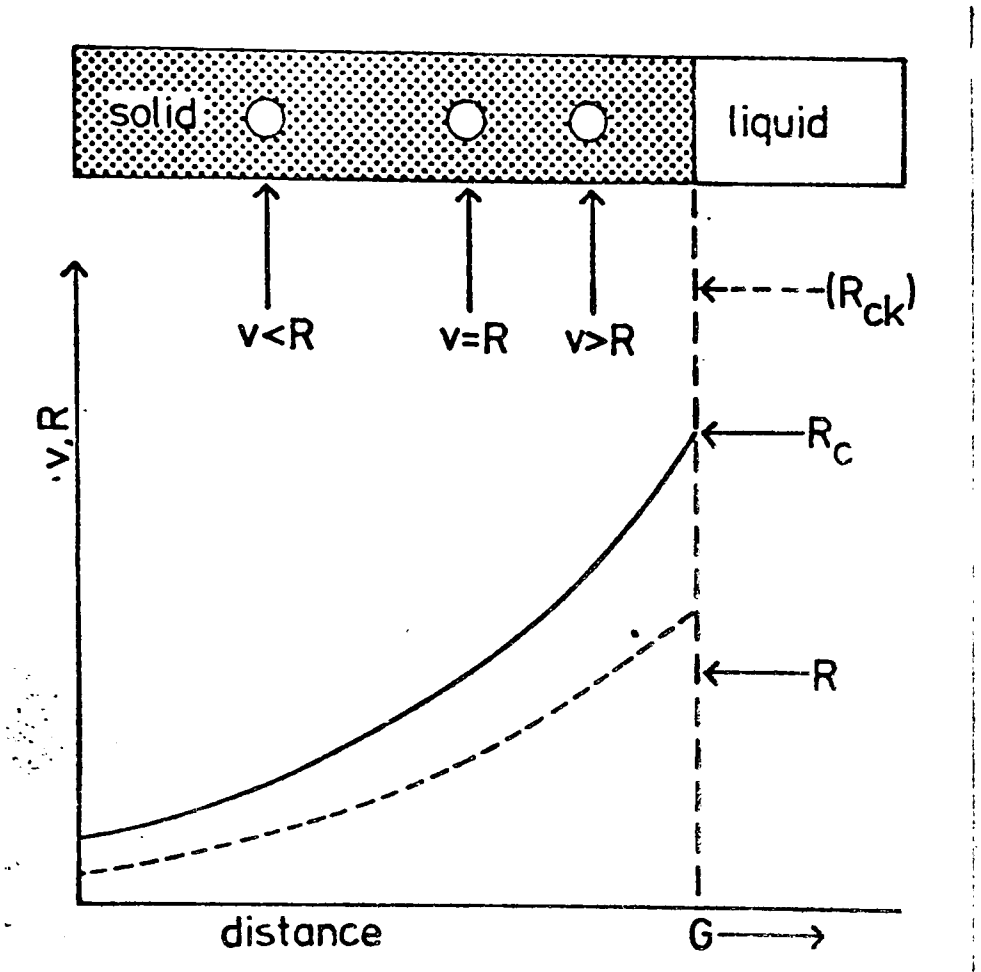


FIG. VIII. 9. Comparing TGZM velocity and crystal growth velocity.

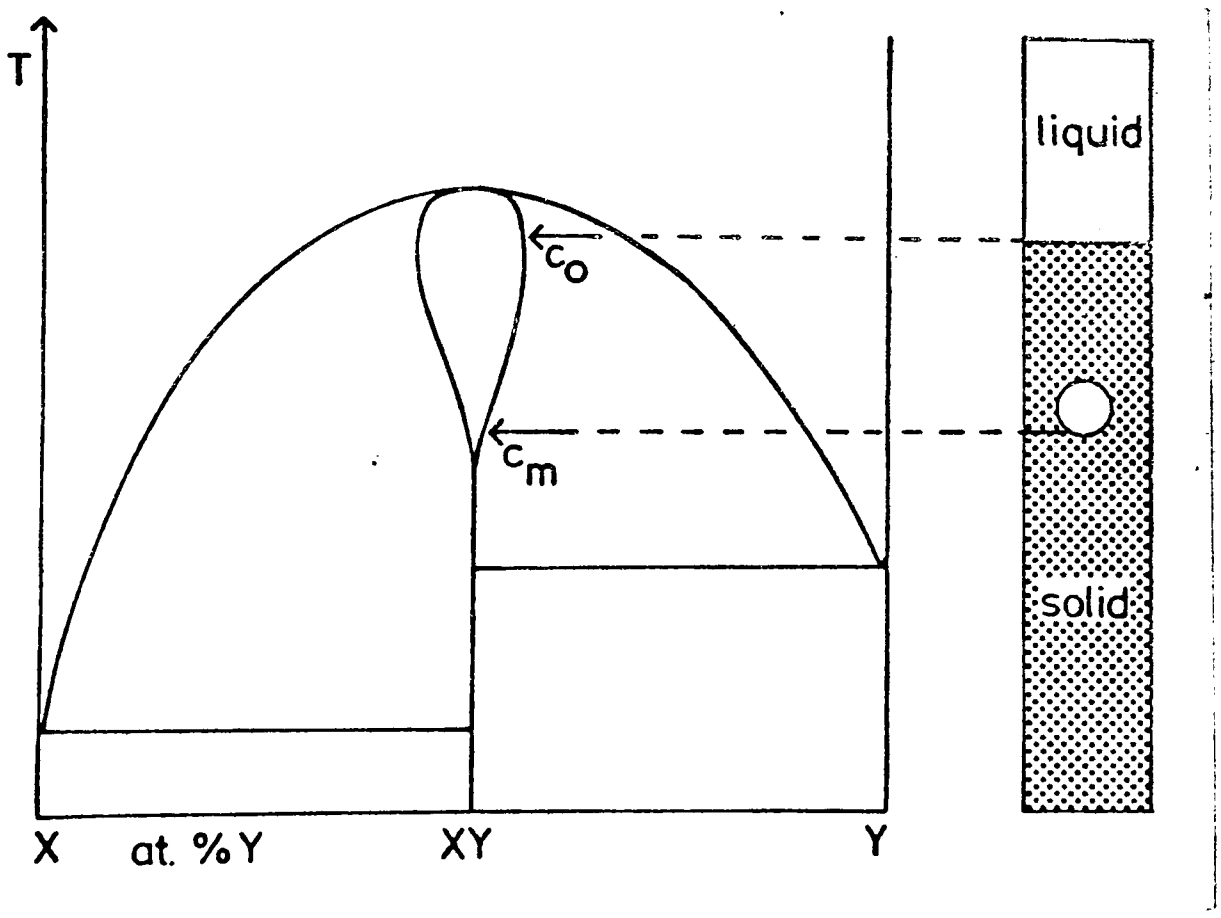


FIG. VIII. 10. Retrograde solidus in an interatomic compound XY.

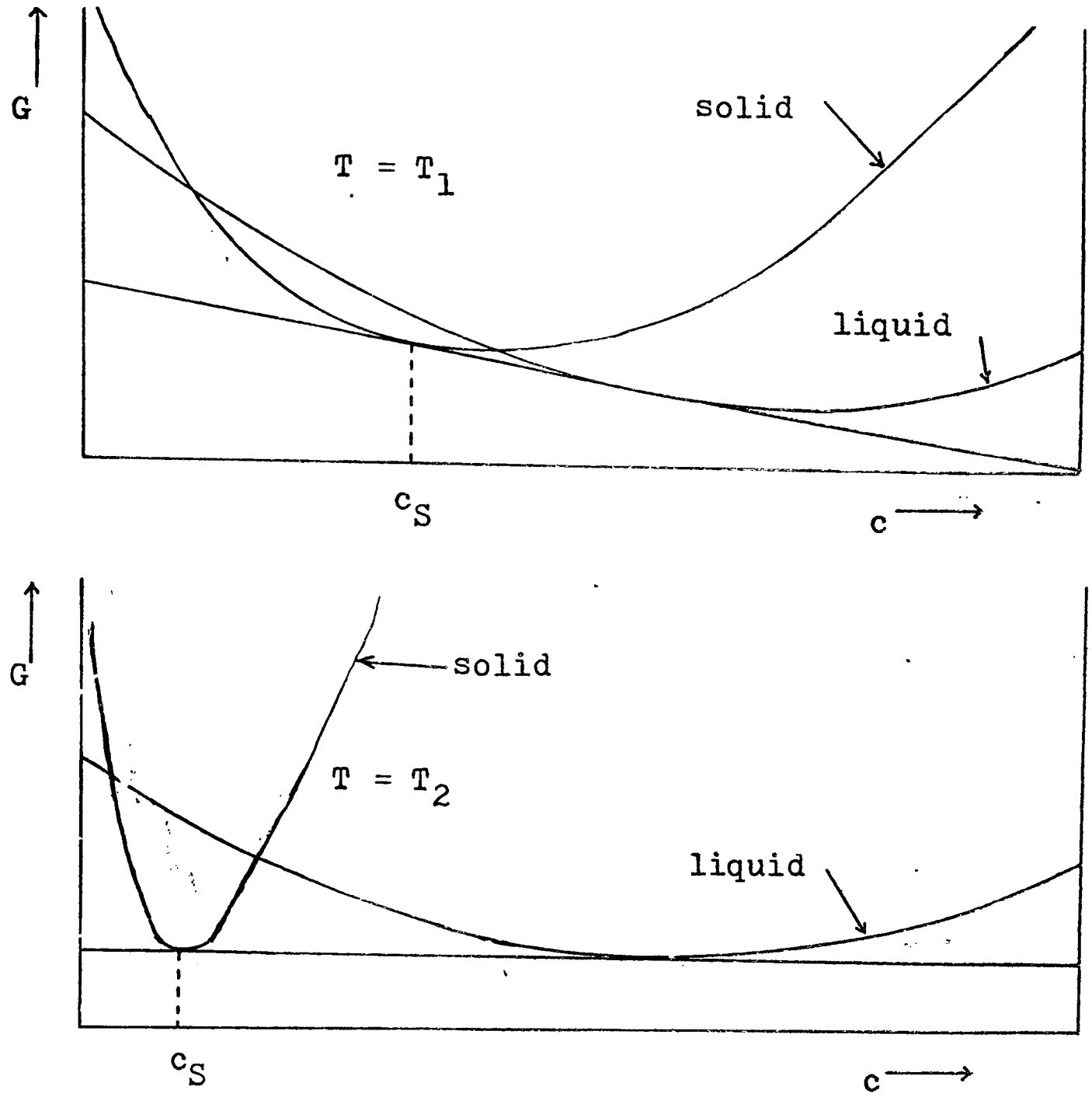


FIG. VIII. 11. G - c curves for T_1 and T_2 ,where $T_1 > T_2$,showing why retrograde solidi occur.

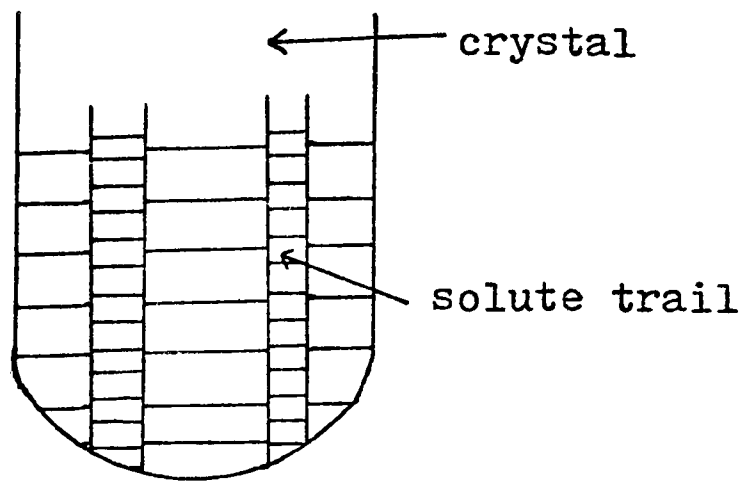


FIG. VIII. 12. Striated crystal and solute trails as observed by Bardsley et al.

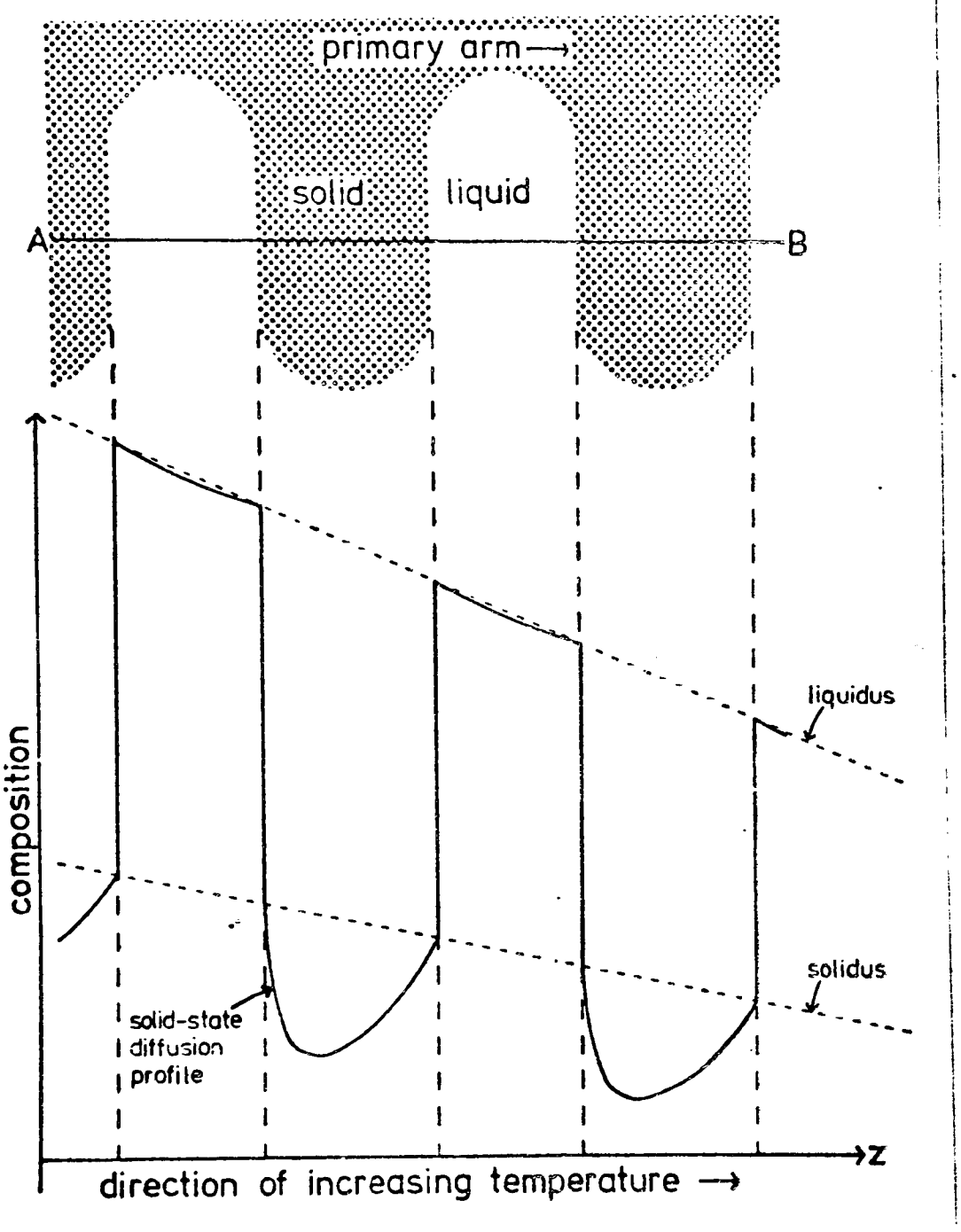


FIG. VIII. 13. Solute distribution caused by TGZM during dendritic solidification.

Summary and Conclusions

1. A temperature gradient microscope stage was designed for fixed area viewing, with moveable heating plates for solidification. Improvements made the thermal field controllable and reproducible, with reduced vertical heat flow.

2. Dendritic structures in thin specimen cells were characterized. Structures depended largely on grain orientation with respect to the cell walls, but there were differences between different non-faceting organic materials.

3. Dendrite spacings in thin cells were measured. It was shown that convection could affect primary spacing by up to 30%. Thermal fluctuations appeared to be important for cellular structures, which adjusted slowly to a steady-state spacing.

4. Dendrite tip temperatures were measured as a function of growth rate. Low velocity measurements agreed well with theory but undercoolings at high velocity were larger than expected. This was tentatively attributed to growth at high Peclet number rather than minimum undercooling.

5. A dimensionless parameter was introduced to unify theories of dendritic growth, interface stability and TGZM.

6. An analysis of interdendritic liquid-state diffusion was improved and integrated with the more intuitive "complete mixing" approach.

7. An analytical treatment of solid-state diffusion during solidification[49] was marginally improved but shown to remain very approximate.

8. Microsegregation calculations[103] were re-assessed, showing that solid-state diffusion accounts for only one-quarter of the observed homogenization during solidification of aluminium-copper.

9. Solute distributions during temperature gradient zone melting were derived analytically. Exact solutions were obtained for a number of special cases, illuminating general behaviour during migration in static specimens, migration during solidification, and the effects of interface kinetics and varying diffusion coefficient. The exact solutions were used to derive and justify approximate solutions of wider application. Commonly assumed solute distributions were proved incorrect.

10. Differing types of "force" on migrating inclusions were discussed. Inclusion retardations and shape distorsions were analyzed.

11. TGZM migration distances in static specimens and during solidification were calculated.

12. Liquid diffusion coefficients of succinonitrile and camphene were measured in TGZM.

13. Gas bubbles in migrating liquid drops were shown to act as inert particles in succinonitrile, in contrast to other systems.

14. TGZM during solidification was compared experimentally to TGZM of droplets in static situations. Velocities at equal temperatures in the two situations were found to be equal within experimental error of 20%.

15. Detailed studies on droplet TGZM in succinonitrile showed a considerable size dependence of migration velocity and variable migration direction at lower temperatures. High-temperature measurements were generally explicable on the basis of a small size dependence due to the curvature effect. Two plausible explanations were found for low-temperature results. It was shown that if interface kinetics caused the size-dependence, it was necessary to assume an adsorption effect affecting mainly the freezing interface, subject to considerable scatter and with kinetic undercooling increasing slowly or decreasing as velocity increased. An alternative explanation in terms of dislocation dragging by migrating droplets was shown to be plausible, offering better explanations for many results, but a specific test of this idea was unsuccessful and cast considerable doubt on its validity.

16. It was suggested that dislocations and grain boundaries can migrate like liquid regions in a thermal gradient. Evidence for such migration was presented for grain boundaries in succinonitrile.

17. TGZM theory was used to assess the relative importance of diffusion and heat flow for transformations in nearly pure materials.

18. Interface kinetics in TGZM was discussed, showing that our solute distribution analysis did not affect the validity of previous treatments but that melting kinetics presented some special features.

19. McLean's[124] theory of fibre coarsening by TGZM was corrected in several respects and shown not to explain his experimental results adequately.

20. Theoretical arguments were given to show that TGZM could result in contamination of large areas of growing high-quality crystals. Several experimental studies were shown to corroborate this hypothesis.

21. Some additional notes on TGZM and microsegregation during dendritic solidification were given to amend and extend earlier work,[1] including a discussion of commercial castings.

References

1. D.J.Allen, Part II Thesis "Dendrite Coarsening", Oxford University, 1973.

2. J.C.Baker and J.W.Cahn, in "Solidification", A.S.M. Seminar Book, Metals Park, Ohio, 1971, pp. 33 - 58.

3. K.Denbigh, "Principles of Chemical Equilibrium", Cambridge Univ. Press, 1955. (a) p.196: (b) p.125.

4. C.Herring, in "The Physics of Powder Metallurgy", ed. W.E.Kingston, McGraw-Hill, New York, 1951.

5. J.W.Christian, "Theory of Transformations in Metals and Alloys", Pergamon, 1965, pp. 80 - 94.

6. D.Turnbull, in "Thermodynamics in Physical Metallurgy", A.S.M. Cleveland, Ohio, 1950, pp. 282 - 306.

7. K.A.Jackson, D.R.Uhlmann, and J.D.Hunt, J.Cryst. Gth., 1 (1967) pp. 1 - 36.

8. D.P.Woodruff, Phil.Mag., 18 (1968) pp.123 - 127.

9. M.Volmer and M.Marder, Z.Physik.Chem., 154 (1931) p.97.

10. F.C.Frank, Discussions Faraday Soc., 5 (1949) p.48.

11. W.B.Hillig and D.Turnbull, J.Chem.Phys., 24 (1956) p.914.

12. W.K.Burton, N.Cabrera, and F.C.Frank, Phil.Trans.Roy.Soc. (London) Series A, 243 (1951) p.299.

13. P.Bennema and G.H.Gilmer, in "Crystal Growth", ed. P.Hartman, North-Holland, Amsterdam, 1973, chapter 10, pp.263 - 327.

14. D.Elwell and H.J.Scheel, "Crystal Growth from High-Temperature Solutions", Academic Press, London, 1975.

15. K.A.Jackson, "Liquid Metals and Solidification", A.S.M., Cleveland, 1958, pp. 174 - 186.

16. J.W.Cahn, Acta Met., 8 (1960) pp. 554 - 562.

17. J.W.Cahn, W.B.Hillig, and G.W.Sears, Acta Met., 12 (1964) pp. 1421 - 1439.

18. W.A.Tiller, J.Appl.Phys., 34 (1963) pp.2757 - 2762.

19. J.C.Baker and J.W.Cahn, Acta Met., 17 (1969) pp. 575 - 578.

20. J.S.Langer and R.F.Sekerka, Acta Met., 23 (1975) pp.1225 - 1237.

21. G.E.Nash and M.E.Glicksman, Acta Met., 22 (1974) pp. 1283 - 1290.

22. G.S.Cole, in "Solidification", A.S.M. Seminar Book, Metals Park, Ohio, 1971, pp. 201 - 274.

23. S.R.de Groot, "Thermodynamics of Irreversible Processes", North-Holland, Amsterdam, 1951.

24. W.A.Tiller, K.A.Jackson, J.W.Rutter and B.Chalmers, Acta Met. 1 (1953) pp.428 - 437.

25. J.D.Verhoeven and E.D.Gibson, Met.Trans., 2 (1971) pp. 3021 - 3026.

26. V.G.Smith, W.A.Tiller and J.W.Rutter, Can.J.Phys., 33 (1955) pp. 723 - 745.

27. E.Scheil, Z.Metallk., 34 (1942) pp.70 - 72.

28. J.A.Burton, R.C.Primm and W.P.Slichter, J.Chem.Phys., 21 (1953) pp.1987 - 1991.

29. M.A.Audero and H.Biloni, J.Cryst.Gth., 12 (1972), pp.297 - 308.

30. J.W.Rutter and B.Chalmers, Can.J.Phys., 31 (1953) p.15.

31. W.W.Mullins and R.F.Sekerka, J.Appl.Phys., 35 (1964) p. 444.

32. R.F.Sekerka, Proc.Int.Conf. on Crystal Growth, Boston, 1966, pp. 691 - 702.

33. D.P.Woodruff, Phil.Mag., 17 (1968) pp.283 - 294.

34. H.S.Chen and K.A.Jackson, J.Cryst.Gth., 8 (1971) pp.184 - 190.

35. R.G.Seidensticker, Proc. Int.Conf. on Crystal Growth, Boston, 1966, pp.733 - 737.

36. R.T.Delves, Phys.Stat.Sol., 20 (1967) pp.693 - 704.

37. G.Horvay and J.W.Cahn, Acta Met., 9 (1961) pp.695 - 705.

38. M.H.Burden, D.Phil. Thesis "Factors Affecting Grain Size in Castings", Oxford University, 1973.

39. D.D.Double, D.Phil.Thesis "Imperfections in Eutectic Crystals", Oxford University, 1971.

40. I.Jin and G.R.Purdy, J.Cryst.Gth., 23 (1974)pp.29 - 36.

41. W.Oldfield, Mat.Sci.Eng., 11 (1973) pp. 211 - 218.

42. D.M.L.Bartholomew, D.Phil. Thesis "Studies in Microsegregation", Oxford University, 1974.

43. F.A.Nichols, J.Mat.Sci., 11 (1976) pp. 1027 - 1032.

44. T.Z.Kattamis, J.C.Coughlin and M.C.Flemings, Trans. A.I.M.E., 239 (1967), pp. 1504 - 1511.

45. C.Zener, Trans. T.M.S. - A.I.M.E. 167 (1946) p.550.

46. G.P.Ivantsov, Growth of Crystals, New York, 1958, pp.76 - 85.

47. G.W.Scherer and D.R.Uhlmann, J.Cryst.Gth. 30 (1975) pp. 304 - 310.

48. M.Tassa and J.D.Hunt, J.Cryst.Gth., 34 (1976) pp.38 - 48.

49. T.F.Bower, H.D.Brody and M.C.Flemings, Trans, A.I.M.E., 236 (1966), pp. 624 - 634.

50. M.H.Burden and J.D.Hunt, J.Cryst. Gth., 22 (1974) pp. 98 - 109.

51. M.H.Burden and J.D.Hunt, J. Cryst. Gth., 22 (1974) pp.109 - 116.

52. R.M.Sharp and A.Hellawell, J.Cryst.Gth., 11 (1971) pp. 77 - 91.

53. G.F.Bolling and D.Fainstein-Pedraza, Acta Met., 22 (1974) pp.1033 - 1040.

54. T.Okamoto and K.Kishitake, J.Cryst.Gth., 29 (1975) pp.137 - 146.

55. J.D.Hunt, to be published.

56. H.Jacobi and K.Schwerdtfeger, Met.Trans.A, 7A (1976) pp.811 - 820.

57. G.J.Davies, "The Solidification of Metals", I.S.I. Publication 110 (1968), pp. 66 - 69.

58. P.K.Rohatgi and C.M.Adams, Trans. A.I.M.E., 239 (1967) pp. 1737 - 1746.

59. M.C.Flemings, "Solidification Processing", McGraw-Hill, New York, 1974.

60. G.F.Bolling and W.A.Tiller, J.Appl.Phys., 31 (1960) p.2040.

61. L.F.Donaghey and W.A.Tiller, "The Solidification of Metals", I.S.I. Publication 110 (1968) pp.87-92.

62. B.P.Bardes and M.C.Flemings, Mod. Castings, 74 (1966) pp.100-106.

63. E.A.Feest and R.D.Doherty, Met.Trans., 4 (1973) pp.125 - 136.

64. K.P.Young and D.H.Kirkwood, Met. Trans. A, 6A (1975) pp.197 - 205.

65. K.P.Young, Ph.D.Thesis, "Dendrite Morphology and Microsegregation in Aluminium-Copper Alloys", Sheffield University, 1972.

66. G.W.Greenwood, Acta Met., 4 (1956) pp.243 - 248.

67. I.M.Lifschitz and V.V.Slyozov, J.Phys.Chem.Solids, 19 (1961) pp.35 - 50.

68. C.Wagner, Z.Elektrochem., 65 (1961) pp.581 - 591.

69. G.W.Greenwood, "The Mechanism of Phase Transformations in Crystalline Solids", Inst. Metals Monograph, 33 (1969) pp. 103 - 110.

70. M.Kahlweit, in "Physical Chemistry: An Advanced Treatise", eds H.Eyring, D.Henderson and W.Jost, Academic Press, 1970, vol. X, pp. 719 - 759.

71. T-M. Ahn and J.K.Tien, J.Phys.Chem.Solids, 37 (1976) pp.771 - 775.

72. A.J.Ardell, Acta Met., 20 (1972) pp.61 - 71.

73. M.Kahlweit, Scripta Met., 2 (1968) pp.251 - 254.

74. A.A.Chernov, Sov.Phys.Cryst.1 (1956) pp.460 - 463.

75. M.O.Klia, Sov.Phys.Cryst., 1 (1956) pp.456 - 459.

76. K.A.Jackson, J.D.Hunt, D.R.Uhlmann and T.P.Seward, Trans. A.I.M.E., 236 (1966) pp.149 - 158.

77. J.J.Reeves and T.Z.Kattamis, Scripta Met., 5 (1971) pp. 223 - 229.

78. N.J.Whisler and T.Z.Kattamis, J.Mat.Sci., 7 (1972) pp.888 - 894.

79. N.J.Whisler and T.Z.Kattamis, J.Cryst.Gth., 15 (1972) pp.20 - 24.

80. T.Z.Kattamis and M.C.Flemings, Trans. A.I.M.E., 233 (1965), pp.992 - 999.

81. B.Chalmers, "Principles of Solidification", Wiley, New York, 1964.

82. S.V.Subramanian, C.W.Haworth and D.H.Kirkwood, J.I.S.I., 206 (1968) pp.1027 - 1032.

83. P.J.Ahearn and M.C.Flemings, Trans. A.I.M.E., 239 (1967) pp. 1590 - 1593.

84. L.R.Morris and W.C.Winegard, J.Cryst.Gth., 6 (1969) pp.61 - 66.

85. K.Chien and T.Z.Kattamis, Z.Metallk., 61 (1970), pp.475 - 479.

86. S.V.Subramanian, C.W.Haworth and D.H.Kirkwood, J.I.S.I. 206, (1968) pp.1124 - 1130.

87. D.Clayton, T.Smith and J.Brown, J.Inst.Met., 60 (1971) pp.224 - 228.

88. R.D.Doherty and D.A.Melford, J.I.S.I., 204 (1966), pp. 1131 - 1143.

89. D.A.Melford and D.A.Granger, "The Solidification of Metals", I.S.I.Publication 110, 1968, pp.289 - 294.

90. H.Thresh, M.Bergeron, F.Weinberg and R.K.Buhr, Trans. A.I.M.E., 242 (1968) pp.853 - 858.

91 F.Weinberg and R.K.Buhr, "The Solidification of Metals", I.S.I. Publication 110, 1968, pp.295 - 304.

92. T.Z.Kattamis, Z.Metallk., 61 (1970) pp. 856 - 860.

93. M.C.Flemings, D.R.Poirier, R.V.Barone, and H.D.Brody, J.I.S.I., 208 (1970), pp.371 - 381.

94. J.I.Nurminen and H.D.Brody, in "Titanium: Science and Technology", eds. R.I.Jaffee and H.M.Burte, vol.3 (1973) pp.1893 - 1914.

95. F.Weinberg and E.Teghtsoonian, Met.Trans., 3 (1972) pp. 93 - 111.

96. P.Dauncey, Ph.D. Thesis "Microsegregation in Binary Alloys", Sussex University, 1974.

97. H.Åström, B.Loberg, B.Bengtsson and K.E.Easterling, Metal Sci., 10 (1976) pp. 225 - 234.

98. D.J.Allen and J.D.Hunt, Met.Trans.A, 6A (1975) pp.1117 - 1118.

99. E.T.Turkdogan and R.A.Grange, J.I.S.I., 208 (1970) pp.482 - 494.

100. G.Forward and J.F.Elliott, Met.Trans. 1 (1970) pp. 2889 - 2898.

101. H.D.Brody and M.C.Flemings, Trans. A.I.M.E., 236 (1966), pp.615 - 623.

102. G.W.Swartzbeck and T.Z.Kattamis, J.Mat.Sci., 9 (1974) pp.635 - 643.

103. D.H.Kirkwood and D.J.Evans, "The Solidification of Metals", I.S.I. Publication 110, 1968, pp.108 - 111.

104. A.B.Michael and M.B.Bever, Trans.A.I.M.E., 200 (1954), pp. 47 - 56.

105. J.A.Horwath and L.F.Mondolfo, Acta Met., 10 (1962) pp.1037 - 1042.

106. R.E.Spear and G.R.Gardner, Trans. A.F.S., 71 (1963) pp.209 - 215.

107. T.Z.Kattamis and M.C.Flemings,**Trans.**A.I.M.E., 236 (1966), pp. 1523 - 1532.

108. T.Z.Kattamis, U.T.Holmberg, and M.C.Flemings, J.Inst.Met., 95 (1967), pp.343 - 347.

109. H.Matyja, B.C.Giessen and N.J.Grant, J.Inst.Met.,96 (1968) pp.30 - 32.

110. G.R.Kotler, K.W.Casey, and G.S.Cole, Met.Trans., 3 (1972) pp.723 - 726.

111. L.Backerüd and L.Liljenvall, J.Inst.Met., 100 (1972), pp.357 - 366.

112. J.E.Northwood and T.Homewood, Metallurgia and Metal Forming, 41(9)(1974) pp.254 - 261.

113. A.Suzuki, T.Suzuki, Y.Nagaoya and Y.Iwata, Nippon Kinzoku Gakkaishi, 32 (1968) pp.1301 - 1305.

114. T.Edvardsson, H.Fredriksson, and I.Svensson, Metal Sci., 10 (1976) pp.298 - 306.

115. T.Z.Kattamis, J.Cryst.Gth, 18 (1973) pp.45 - 53.

116. T.Okamoto, K.Kishitake, and I.Bessho, J.Cryst.Gth. 29 (1975) pp.131 - 136.

117. W.G.Whitman, Am.J.Sci., 11 (1926) pp.126 - 132.

118. W.G.Pfann, Trans. A.I.M.E., 203 (1955) pp.961 - 964.

119. A.A.Chernov, Sov.Phys.J.E.T.P., 4 (1956 - 57) pp.585 - 586.

120. G.A.Wolff and A.I.Mlavsky, in "Crystal Growth: Theory and Techniques", ed.C.H.L.Goodman, Plenum, New York, 1974, vol. 1, pp.193 - 232.

121. F.A.Nichols, J.Nuclear Mat., 30 (1969) pp.143 - 165.

123. P.S.Ho, J.Appl.Phys., 41 (1970) pp.64 - 68.

123. D.R.H.Jones, Metal Sci., 8 (1974) pp.37 - 40.

124. M.McLean, Scripta Met., 9 (1975) pp.439 - 446.

125. J.Biersack and W.Diez, Phys.Stat.Sol.27 (1968) pp.139 - 144.

126. Ya.E.Geguzin and M.A.Krivoglaz, "Migration of Macroscopic Inclusions in Solids", Consultants Bureau, New York, 1973.

127. W.G.Pfann, "Zone Melting", 2nd edn, Wiley, New York, 1966, chap. 10, pp.254 - 268.

128. W.R.Wilcox, Ind.Engng.Chem., 60(3)(1968) pp.13 - 23.

129. D.T.J.Hurle, J.B.Mullin and E.R.Pike, J.Mat.Sci., 2 (1967) pp.46 - 62.

130. J.C.Brice, "The Growth of Crystals from Liquids", North-Holland, Amsterdam, 1973.

131. H.S.Carslaw and J.C.Jaeger, "Conduction of Heat in Solids", Clarendon Press, Oxford, 1959, p. 427.

132. Ya.E.Geguzin, S.S.Simeonov, and V.M.Mostovoi, Sov. Phys. Solid-State, 13 (1971) pp.79 - 84.

133. D.T.J.Hurle, J.B.Mullin, and E.R.Pike, Phil.Mag.,9 (1964) pp.423 - 434.

134. P.Hoekstra, T.E.Osterkamp, and W.F.Weeks, J.Geophys. Res., 70 (1965) pp.5035 - 5041.

135. M.P.Watson, Part II Thesis "Studies in Temperature Gradient Zone Melting", Oxford University, 1976).

136. J.H.Wernick, J.Chem.Phys., 25 (1956) pp.47 - 49.

137. J.H.Wernick, Trans. A.I.M.E. 209 (1957) pp.1169 - 1173.

138. J.D.Harrison, J.Appl.Phys., 36 (1965) pp.3811 - 3815.

139. D.R.H.Jones, J.Cryst.Gth., 20 (1973), pp. 145 - 151.

140. W.A.Tiller, J.Cryst.Gth., 6 (1969) pp. 77 - 85.

141. R.G.Seidensticker, J.Geophys.Res., 71 (1966) pp.2180 - 2181.

142. D.R.H.Jones, Phil.Mag. 25 (1972) pp.97 - 103.

143. R.M.Jordan, D.Phil.Thesis, "Studies of Composite Materials Materials Grown In-Situ", Oxford University, 1970.

144. D.R.H.Jones, Phil.Mag., 30 (1974) pp. 195 - 201.

145. D.R.H.Jones, J.Cryst.Gth., 26 (1974) pp.177 - 179.

146. V.N.Lozovskii, Sov.Phys.Jnl, 14(2)(1971) pp.1623 - 1627.

147. M.E.Osinovskii, Sov.Phys.Solid State, 13 (1971) pp.3079 - 3082.

148. F.V.Wald and R.O.Bell, J.Cryst.Gth., 30 (1975) pp.29 - 36.

149. V.N.Lozovskii and V.P.Popov, Sov.Phys.Cryst., 15 (1970) pp.116-121.

150. D.R.H.Jones and G.A.Chadwick, Phil.Mag., 24 (1971) pp.1327 - 1345.

151. V.N.Lozovskii and G.S.Konstantinova, Sov. Phys. Cryst. 16 (1972) pp.935 - 937.

152. P.G.Shewman, Trans.A.I.M.E., 230 (1964) pp.1134 - 1137.

153. R.G.Seidensticker, J.Electrochem.Soc., 113 (1966) pp.152 - 156.

154. D.R.H.Jones, J.Cryst.Gth., 16 (1972)pp.187 - 194.

155. M.A.Wright, J.Electrochem.Soc., 112 (1965) pp.1114 - 1116.

156. M.Kumagawa, M.Ozeki and S.Yamada, Jap. J.Appl.Phys., 9 (1970) pp.1422 - 1423.

157. R.W.Hamaker and W.B.White,J.Appl.Phys. 39 (1968) pp.1758 - 1765.

158. R.W.Hamaker and W.B.White, J.Electrochem.Soc.116 (1969) pp.478 - 482.

159. T.R.Anthony and H.E.Cline, Phil.Mag., 22 (1970) pp.893 - 901.

160. H.E.Cline and T.R.Anthony, Aca Met., 19 (1971) pp. 175 - 180.

161. T.R.Anthony and H.E.Cline, J.Appl.Phys., 42 (1971) pp.3380-3387.

162. H.E.Cline and T.R.Anthony, Acta met., 19 (1971) pp.491 - 495.

163. T.R.Anthony and H.E.Cline, Phil.Mag.,24 (1971) pp.695 - 703.

164. H.E.Cline and T.R.Anthony, J.Appl.Phys.,43 (1972) pp.10 - 15.

165. H.E.Cline and T.R.Anthony, J.Cryst.Gth., 13 - 14 (1972) pp.790 - 794.

166. H.E.Cline and T.R.Anthony, Phil.Mag., 24 (1971) pp.1483 - 1494.

167. T.R.Anthony and H.E.Cline, Acta Met., 20 (1972) pp.247 - 255.

168. T.R.Anthony and H.E.Cline, J.Appl.Phys., 43 (1972) pp.2473 - 2476.

169. H.E.Cline and T.R.Anthony, J.Appl.Phys. 43 (1972) pp.4391 - 4395.

170. T.R.Anthony and H.E.Cline, Acta Met., 21 (1973) pp.117 - 122.

171. H.E.Cline and T.R.Anthony, Acta met., 21 (1973) pp.547 - 557.

172. T.R.Anthony and H.E.Cline, J.Appl.Phys., 47 (1976) pp. 2316 - 2324.

173. H.E.Cline and T.R.Anthony, J.Appl.Phys., 47 (1976) (pp.2325 - 2331.

174. H.E.Cline and T.R.Anthony, J.Appl.Phys., 47 (1976) pp.2332 - 2336.

175. M.F.Ashby and R.M.A.Centamore, Acta Met., 16 (1968) pp.1081 - 1092.

176. R.D.Doherty and T.R.Strutt, J.Mat.Sci., 11 (1976) pp. 2169 - 2173.

177. M.McLean and M.S.Loveday, J.Mat.Sci., 9 (1976) pp.1104 - 1114.: see also errata, p.2069.

178. C.A.Knight, Can.J.Phys., 40 (1962) pp.1681 - 1682.

179. C.A.Knight, J.Geol., 70 (1962) pp. 240 - 246.

180. C.A.Knight and N.C.Knight, Science, 150 (1965) pp.1819 - 1821.

181. W.R.Wilcox, Ind.Engng.Chem., 61(3) (1969) pp. 76 - 77.

182. W.R.Wilcox, Separation Sci, 4 (1969) pp. 95 - 109.

183. W.A.Tiller, J.Appl.Phys., 36 (1965) pp.261 - 263.

184. W.Bardsley, J.S.Boulton and D.T.J.Hurle, Solid-State Electronics, 5 (1962) pp.395 - 403.

185. V.N.Lozovskii, P.S.Popov and V.P.Popov, Sov.Phys.Jnl. 11 no. 6 (1968) pp.56 - 57.

186. I.F.Nicolau, J.Mat.Sci., 5 (1970) pp. 623 - 639.

187. C.H.L.Goodman, Solid-State Electronics, 3 (1961) pp. 72 - 74.

188. R.H.Hopkins, R.G.Seidensticker and A.M.Stewart, J.Cryst. Gth 33 (1976) pp.223 - 231.

189. R.S.Wagner, Met.Sci.Conf., 19 (1962) p.239.

190. W.A.Tiller, J.Appl.Phys., 34, (1963) pp.2763 - 2767.

191. W.R.Wilcox and P.J.Shlichta, J.Appl.Phys., 42 (1971) pp.1823 - 1827.

192. W.R.Wilcox, J.Cryst.Gth. 13 - 14 (1972) pp. 787 - 789.

193. R.S.Barnes and D.J.Mazey, Proc Roy.Soc.Lond.Series A, 275 (1963) pp.47 - 57.

194. G.K.Williamson and R.M.Cornell, J.Nuclear Mat., 13 (1964) pp.278 - 280.

195. M.E.Gulden, J.Nuclear Mat., 23 (1967) pp.30 - 36.

196. L.E.Willertz and P.G.Shewmon, Met.Trans., 1 (1970) pp. 2217 - 2223.

197. K.Y.Chen and J.R.Cost, J.Nuclear Mat. 52 (1974) p.59.

198. W.Diez and J.Biersack, Phys.Stat.Sol., 32 (1969) pp.247 - 261.

199. W.Diez, Phys.Stat.Sol. (A), 1 (1970) pp. K139 - K143.

200. T.R.Anthony and R.A.Sigsbee, Acta Met., 19 (1971) pp.1029 - 1035.

201. D.R.H.Jones and G.J.May, Acta Met., 23 (1975) pp.29 - 34.

202. D.R.H.Jones, J.Mat.Sci., 10 (1975) pp.563 - 566.

203. W.D.Kingery and W.H.Goodnow, in "Ice and Snow: Properties, Processes, and Applications" ed. W.D.Kingery, M.I.T.Press, Cambridge, 1963, chap. 19.

204. H.Steen, D.Phil.Thesis "The Solidifcation of Some Metal-Non-Metal Eutectics", Oxford University, 1973.

205. A.I.Mlavsky and M.Weinstein, J.Appl.Phys., 34 (1963) pp.2885 - 2892.

206. Ya.E.Geguzin, S.S.Simeonov, and E.A.Eivasor, Sov. Phys. Solid State, 9 (1967) p. 1123.

207. K.A.Jackson and J.D.Hunt, Acta Met., 13 (1965) pp.1212 - 1215.

208. J.D.Hunt, K.A.Jackson and H.Brown, Rev.Sci.Instrum., 37 (1966) p. 805.

209. M.E.Glicksman, in "Solidification", A.S.M. Seminar Book, Metals Park, Ohio, 1971, pp. 155 - 200.

210. M.E.Glicksman and R.J.Schaefer, Acta Met., 14 (1966) pp. 1126 - 1129.

211. E.W.J.Miller and J.Beech, Metallography 5 (1972) pp.298 - 300.

212. D.P.Woodruff and A.J.Forty, Phil.Mag.15 (1967) pp. 985 - 993.

213. M.E.Glicksman and C.L.Vold, Acta Met., 15 (1967) pp.1409 - 1412.

214. J.A.Blodgett, R.J.Schaefer, and M.E.Glicksman, Metallography, 7 (1974) pp. 453 - 504.

215. R.J.McDonald and J.D.Hunt, Trans. A.I.M.E., 245 (1969) pp. 1993 - 1997.

216. R.J.McDonald and J.D.Hunt, Met.Trans., 1 (1970) pp.2027 - 2029.

217. M.H.Burden and J.D.Hunt, Metal Sci., 10 (1976) pp. 156 - 158.

218. K.A.Ross, B.Sc. Thesis "Dendritic Growth", Oxford University, 1967.

219. M.J.Green, Part II Thesis "Dendritic Growth", Oxford University, 1968.

220. P.Burnell, Part II Thesis "Dendritic Growth", Oxford University, 1971.

221. D.R.H.Jones, Rev.Sci.Instrum., 41 (1970) pp.1509 - 1511.

222. D.R.H.Jones, private communication.

223. R.R.Jennison, Part II Thesis "Phase Transformations in Transparent Materials", Oxford University, 1969.

224. J.Timmermans, J.Phys.Chem.Solids, 18 (1961) pp.1 - 8.

225. C.A.Wulff and E.F.Westrum, J.Phys.Chem., 67 (1963) pp.2376 - 2381.

226. "Handbook of Physics and Chemistry", ed. R.C.Weast, 55th edn, CRC Press, Cleveland, Ohio, 1974.

227. "Landolt-Bornstein Zahlenwerte und Funktionen", Springer, Berlin, 1964.

228. "Crystal Data Determinative Tables", eds. J.D.H.Donnay and H.M.Ondik, 3rd edn., Am.Cryst.Assn., 1972, vol.1.

229. R.J.Schaefer, M.E.Glicksman, and J.D.Ayers, Phil,Mag. 32 (1975) pp.725 - 743.

230. K.K.Shih and J.C.M.Li, J.Mat.Sci. 11 (1976) pp.1571 - 1574.

231. D.R.H.Jones, Phil Mag., 27 (1973) pp.569 - 584.

232. J.D.Hunt and K.A.Jackson, Trans.A.I.M.E., 236 (1966) pp.843 - 852.

233. K.A.Jackson and J.D.Hunt, Trans. A.I.M.E., 236 (1966) pp.1129 - 1142.

234. C.M.Potter, Part II Thesis "Hot-tearing in a Nickel-Based Superalloy "Oxford University, 1974.

235. D.R.H.Jones and G.A.Chadwick, Phil. Mag., 22 (1970) pp.291 - 300.

236. R.J.Schaefer and M.E.Glicksman, Met.Trans., 1 (1970) pp. 1973 - 1978.

237. L.R.Morris and W.C.Winegard, J.Cryst.Gth., 1 (1967) pp. 245 - 246.

238. W.R.Wilcox, Trans.A.I.M.E., 245 (1969) pp.1443 - 1448.

239. K.G.Davis, Met.Trans., 5 (1974), pp. 1993 - 1998.

240. D.E.Ovsienko, G.A.Alfintsev and V.V.Malsov, J.Cryst. Gth., 26 (1974) pp. 233 - 238.

241. C.J.Simpson, C.J.Beingessner, and W.C.Winegard, Trans. A.I.M.E., 239 (1967) pp.587 - 588.

242. R.Rudman, J.Cryst.Gth., 6 (1970) pp.163 - 166.

243. M.Tassa, private communication.

244. R.P.Loveland, "Photomicrography - A Comprehensive Treatise", Wiley, New York, 1970, pp.431,ff.

245. J.H.Richardson,"Optical Microscopy for the Materials Sciences", Dekker, New York, 1971, pp.203,ff. and p.3.

246. R.M.Sharp and A.Hellawell, J.Cryst.Gth., 6 (1969) pp.253 - 260.

247. S.-K.Chan, H.-H.Reimer, and M.Kahlweit, J.Cryst.Gth., 32 (1976) pp.303 - 315.

248. J.D.Hunt, private communication.

249. T.F.Bower and M.C.Flemings, Trans.A.I.M.E. 239 (1967) pp.1620 - 1625.

250. R.M.Sharp and A.Hellawell, J.Cryst.Gth., 8 (1970) pp.29 - 32.

251. J.D.Verhoeven, Met.Trans., 2 (1971) pp.2673 - 2680.

252. M.Hämäläinen,J.Cryst.Gth., 1 (1967) pp.125 - 130.

253. I.Jin and G.R.Purdy, J.Cryst.Gth. 23 (1974) pp.37 - 44.

254. J.W.Mellor, "Higher Mathematics", Longmans, London, 1916.

255. D.J.Hebditch and J.D.Hunt, Met.Trans., 5 (1974) pp.1557 - 1564.

256. G.Stephenson "Mathematical Methods", Longmans, London, 1961.

257. D.J.Allen and J.D.Hunt, Met.Trans.A, 7A (1976), pp.767 - 770.

258. I.A.Kotzé and D.Kuhlmann-Wilsdorf, Appl.Phys.Letts., 9 (1966) p.96.

259.O.N.Srivastava and J.Silcox, Phil.Mag., 18 (1968) pp.503 - 518.

260. K.Iwai, J.Cryst.Gth., 34 (1976) pp.319 - 324.

261. D.W.James and R.F.Sekerka, J.Cryst.Gth., 1 (1967) pp.67 - 72.

262. M.McLean, private communication.

263. W.Bardsley, J.B.Mullin and D.T.J.Hurle, "The Solidification of Metals", I.S.I. Publication 110 (1968) p.93.

264. S.O'Hara, L.A.Tarshis, W.A.Tiller, and J.P.Hunt, J.Cryst.Gth., 3 - 4 (1968) pp. 555 - 561.

265. J.P.Dismukes and W.M.Yim, J.Cryst.Gth., 22 (1974) pp.287 - 294.

266. K.A.Jackson and J.D.Hunt, to be published.

267. P.Tufton, private communication.

268. C.D.Thurmond and J.D.Struthers, J.Phys.Chem., 57 (1953) pp.831 - 835.

269. R.N.Hall, J.Phys.Chem.Solids, 3 (1957) pp.63 - 73.

270. R.M.Logan and D.T.J.Hurle, J.Phys.Chem.Solids, 32 (1971) pp. 1739 - 1753.

271. W.Bardsley and B.Cockayne, Proc.Int.Conf. on Crystal Growth, Boston, 1966, pp. 109 - 113.

272. R.W.Ruddle, "The Solidification of Castings", 2nd ed., no.7, Institute of Metals, London, 1957.

273. D.J.Allen and J.D.Hunt, B.A.C.G.Conference, Edinburgh, 1975.

274. W.A.Tiller and B.K.Jindal, Acta Met., 20 (1972) pp.543 - 556.

275. G.Lesoult and M.Turpin, Mém.Sci.Rev.Mét., 66 (1969) p.659.

276. J.D.Hunt, to be published.



PLATE 1. Fixed - plates stage.

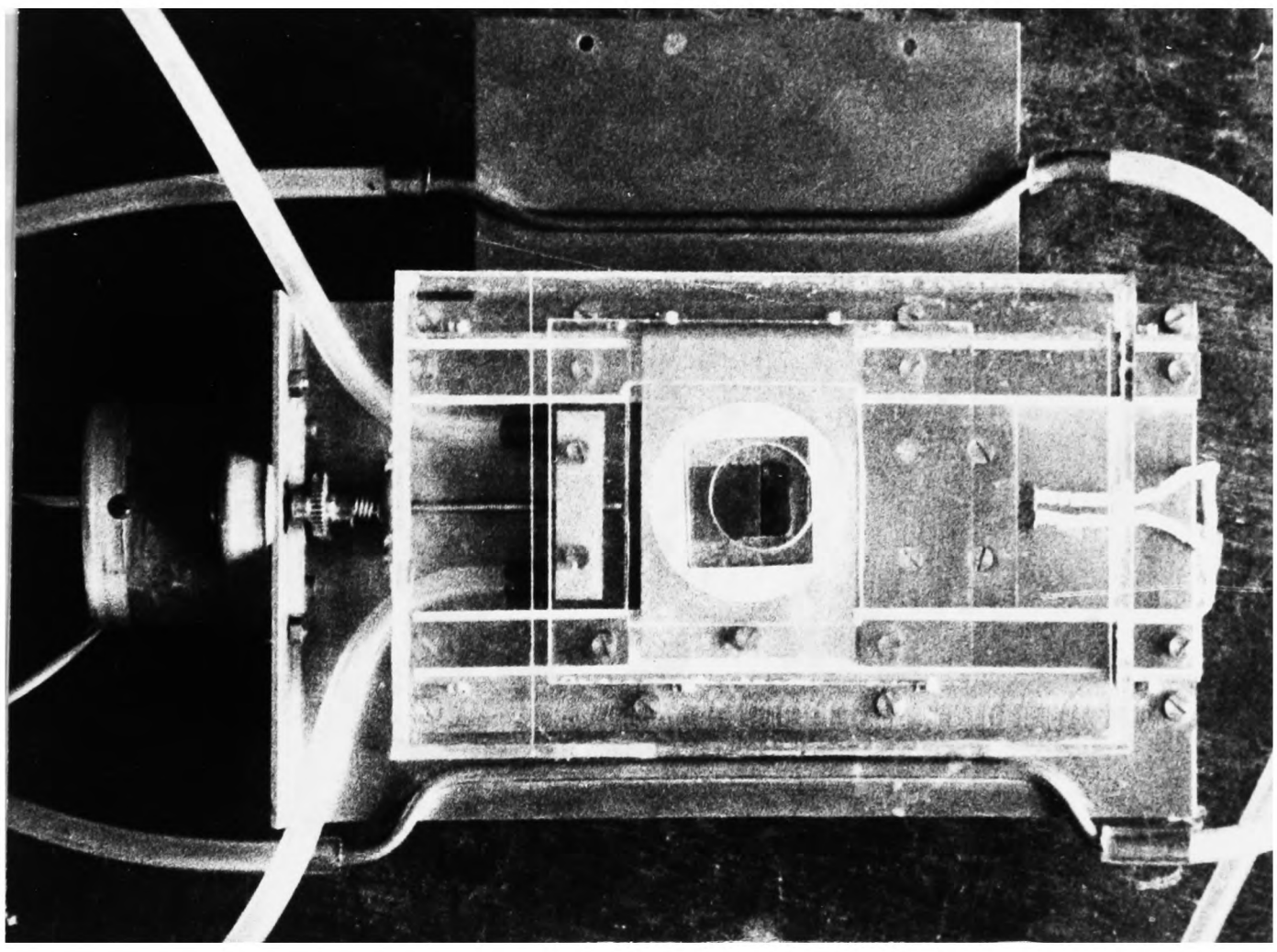


PLATE 2. Moving - plates stage.
(as originally built)



PLATE 3. Dendrite in glass tube. (x 634)

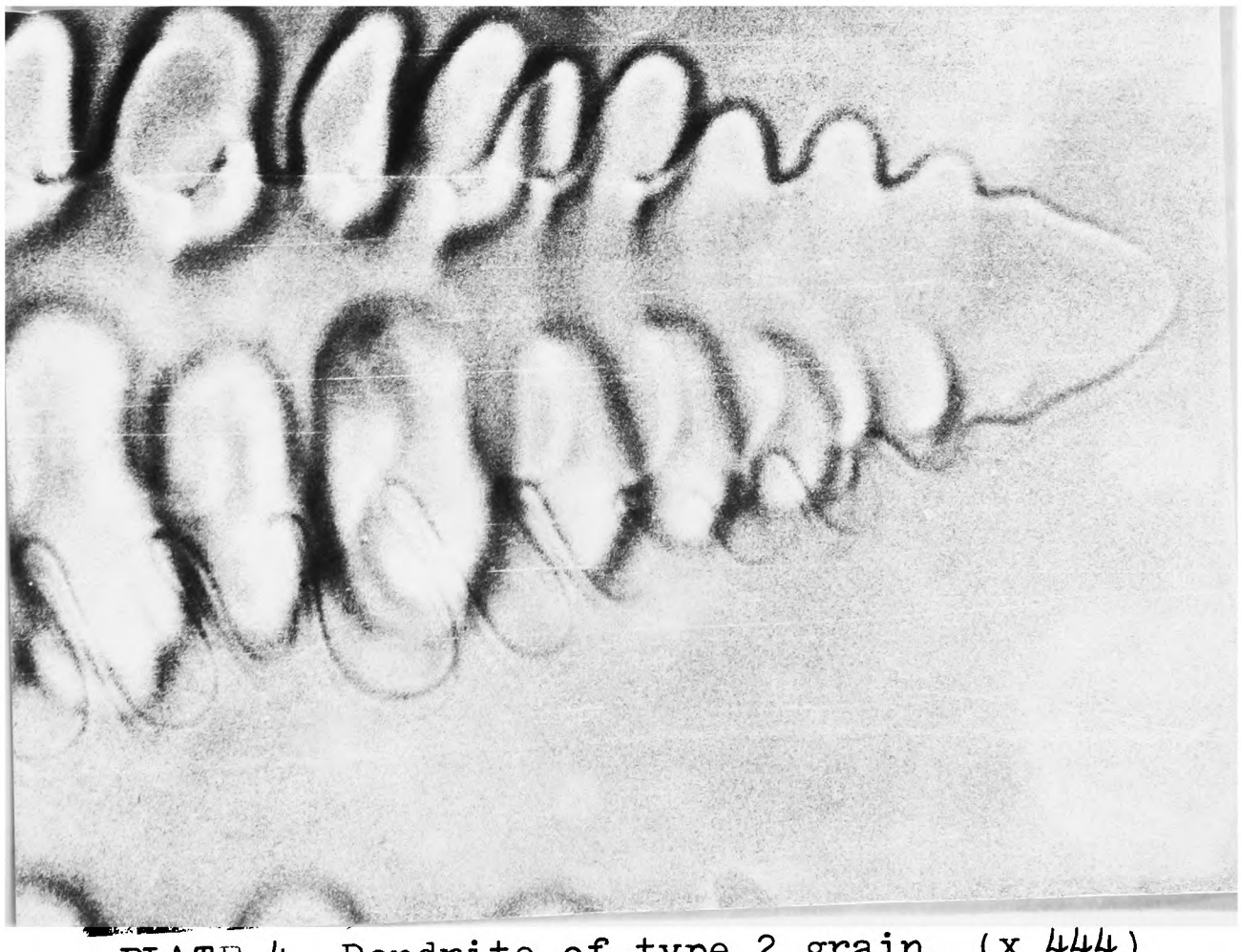


PLATE 4. Dendrite of type 2 grain. (x 444)
(9% CBr_4 - succinonitrile)

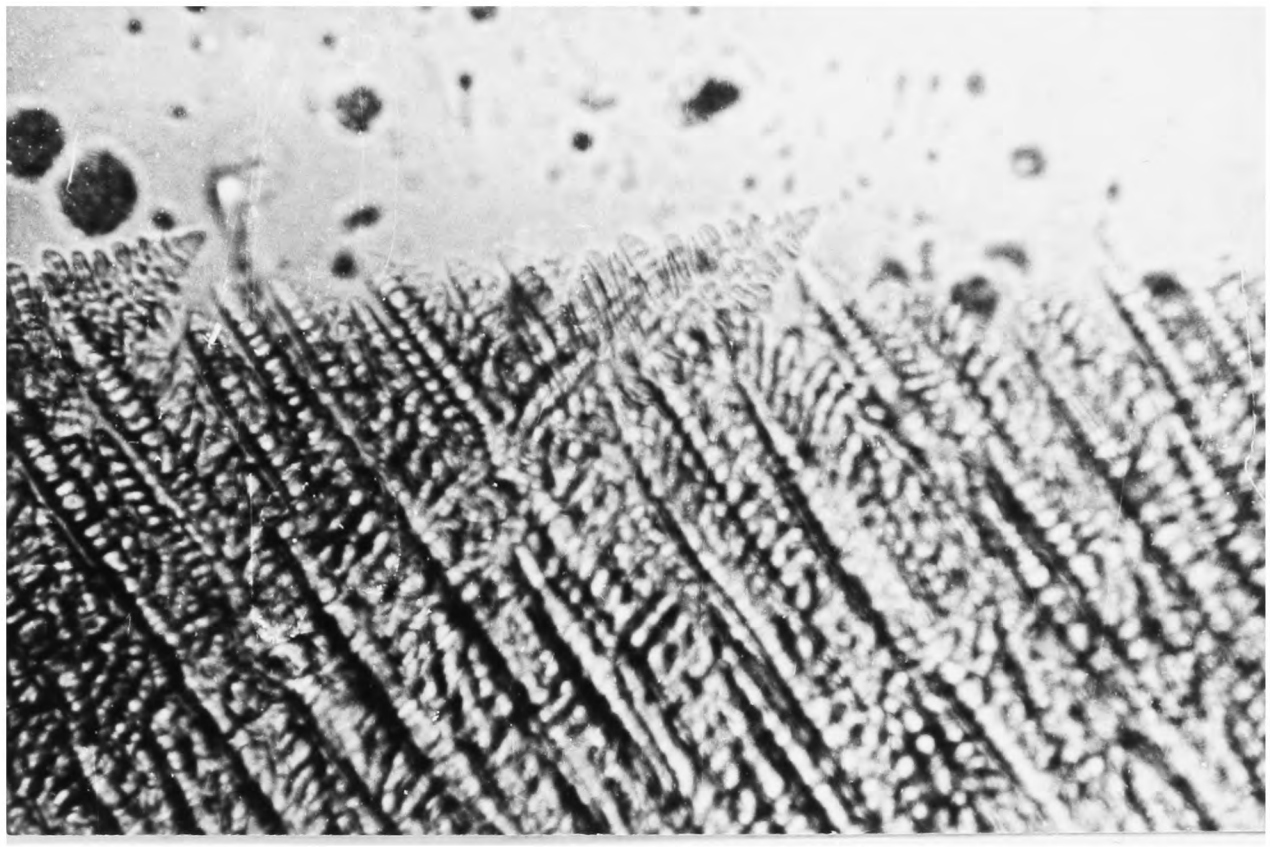


PLATE 5. Type 2 grain. (x 138)
(9% CBr_4 - succinonitrile)

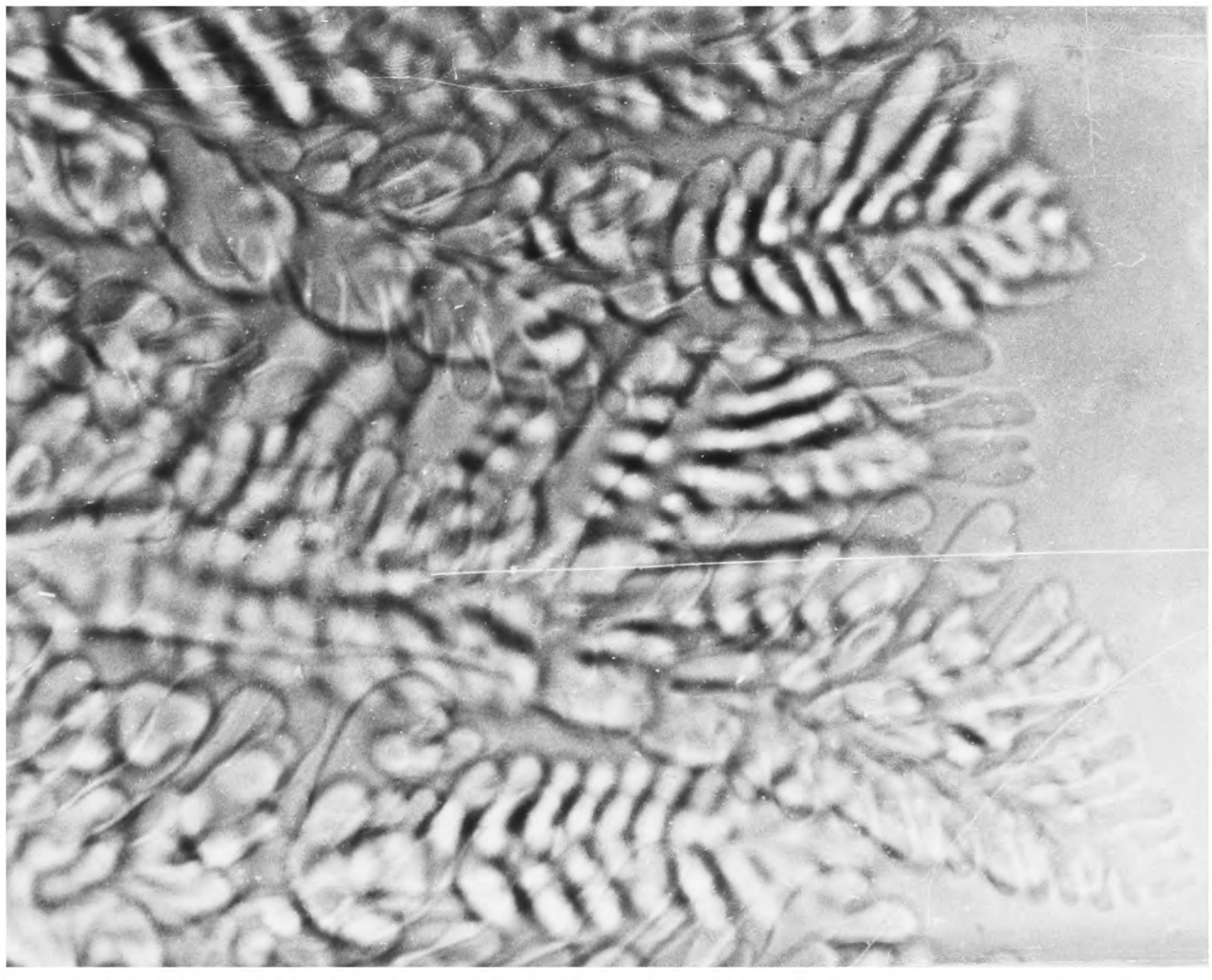


PLATE 6. Type 3 grain. (x 302)
(6% camphor - succinonitrile)

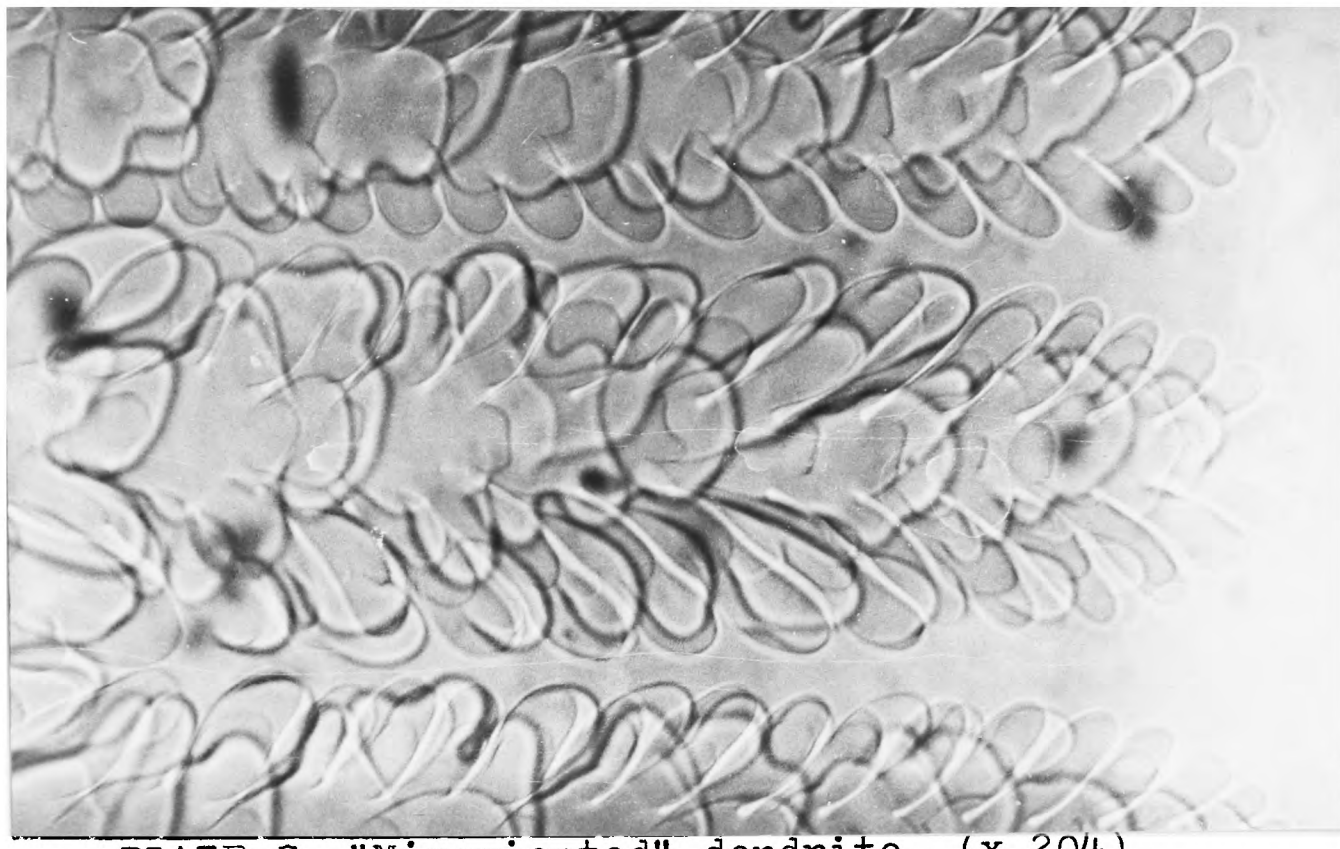


PLATE 7. "Misoriented" dendrite. (x 204)
(7% camphor - succinonitrile)

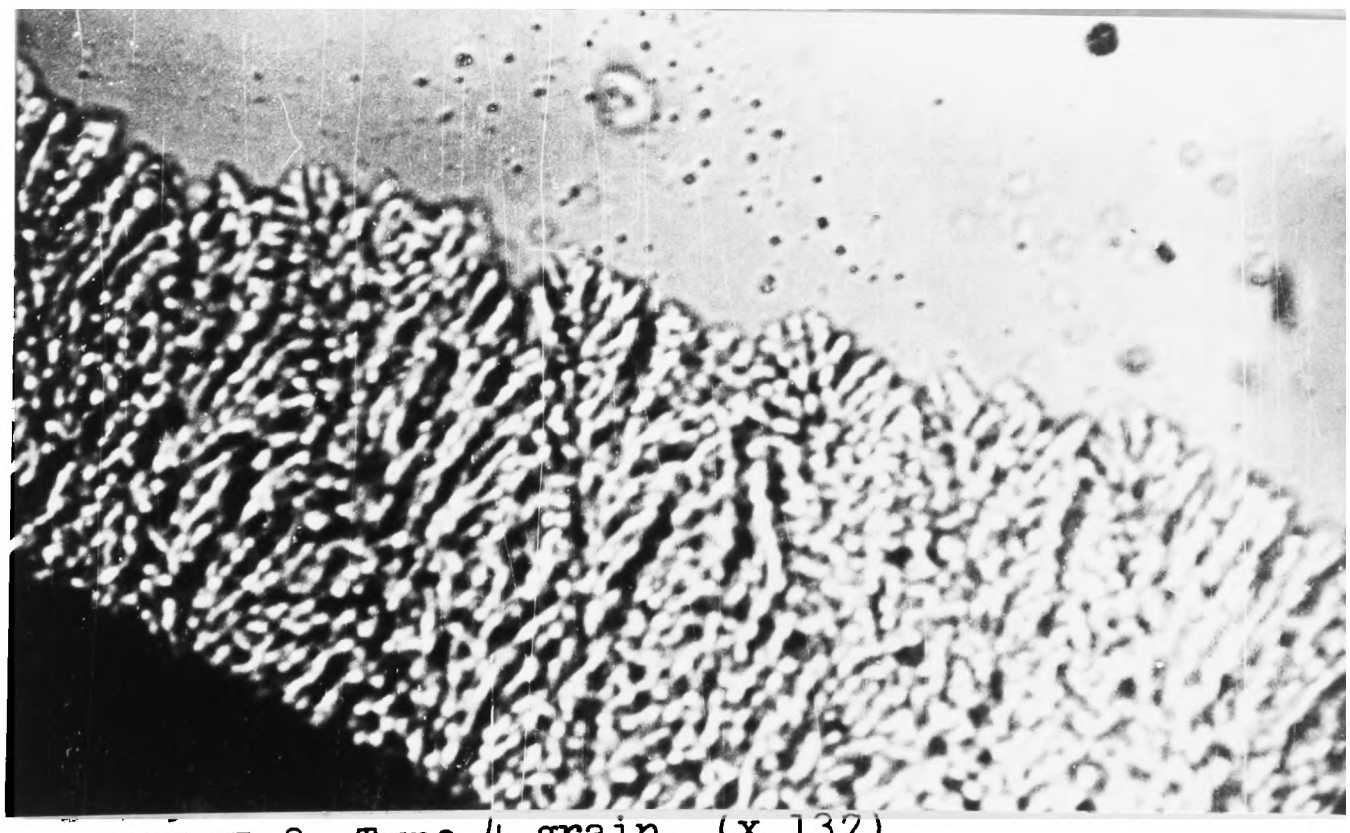


PLATE 8. Type 4 grain. (x 137)
(9% CBr_4-succinonitrile)

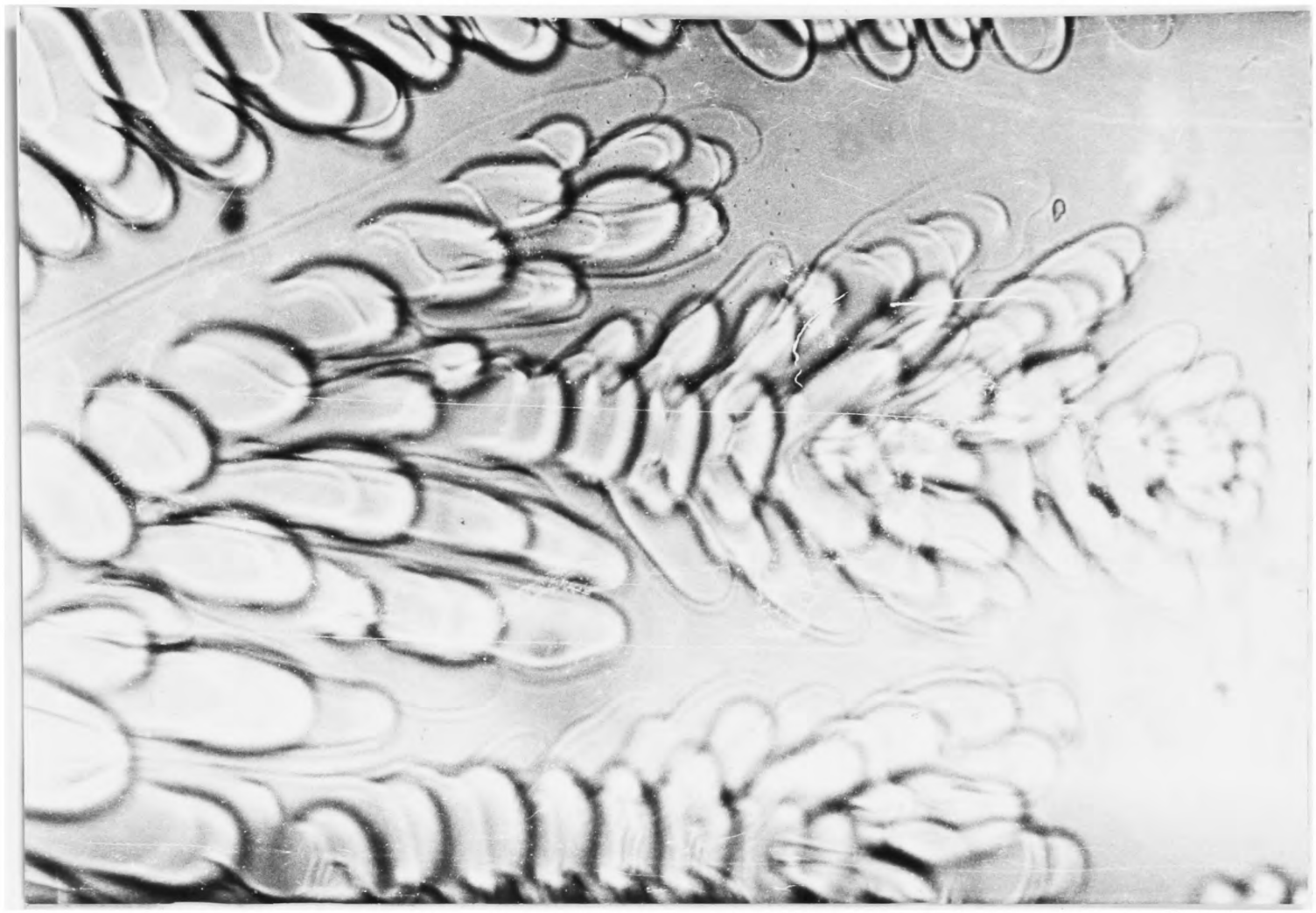


PLATE 9. Transient "misoriented" dendrites. (x 242)
("pure" succinonitrile)

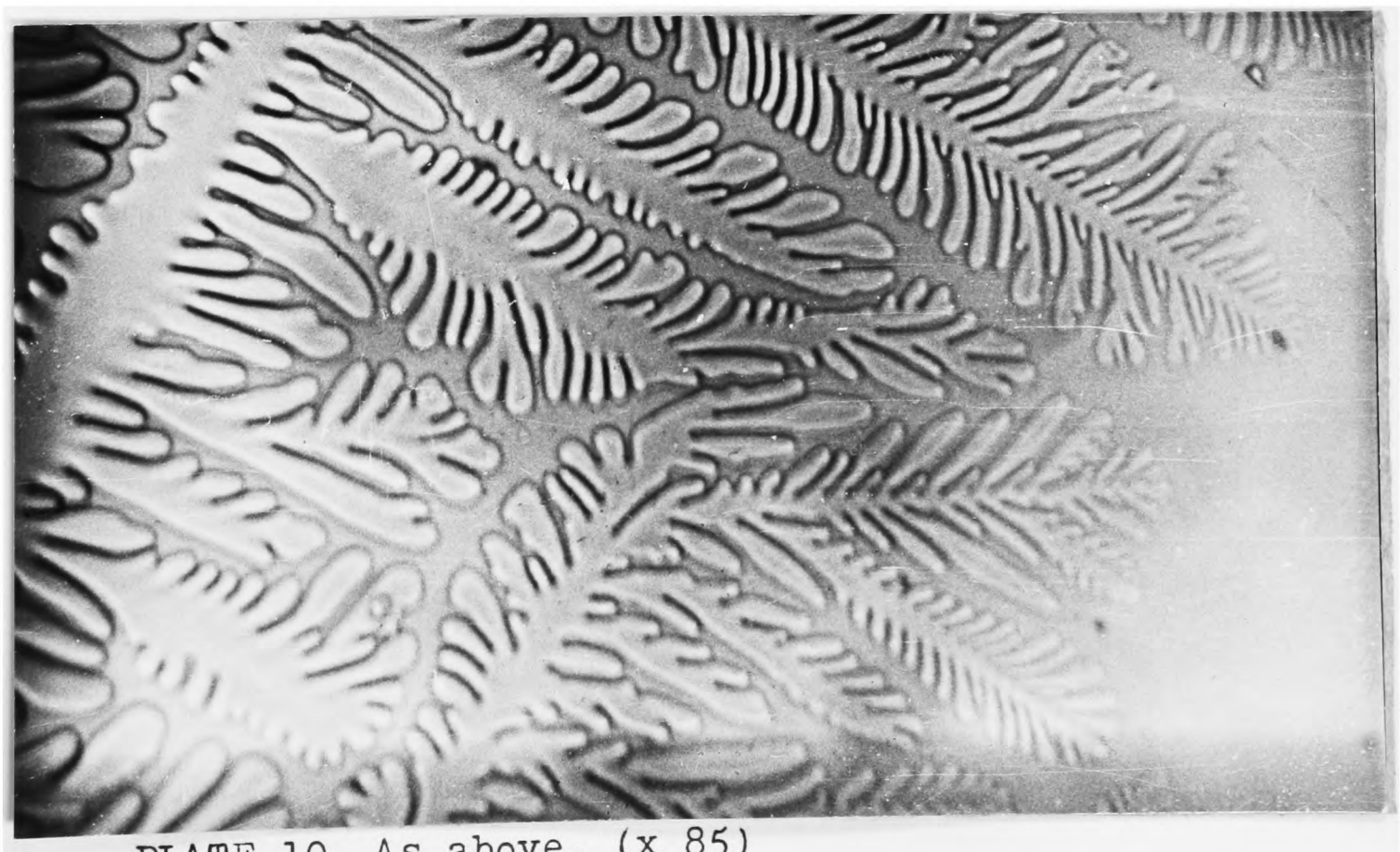


PLATE 10. As above, (x 85)

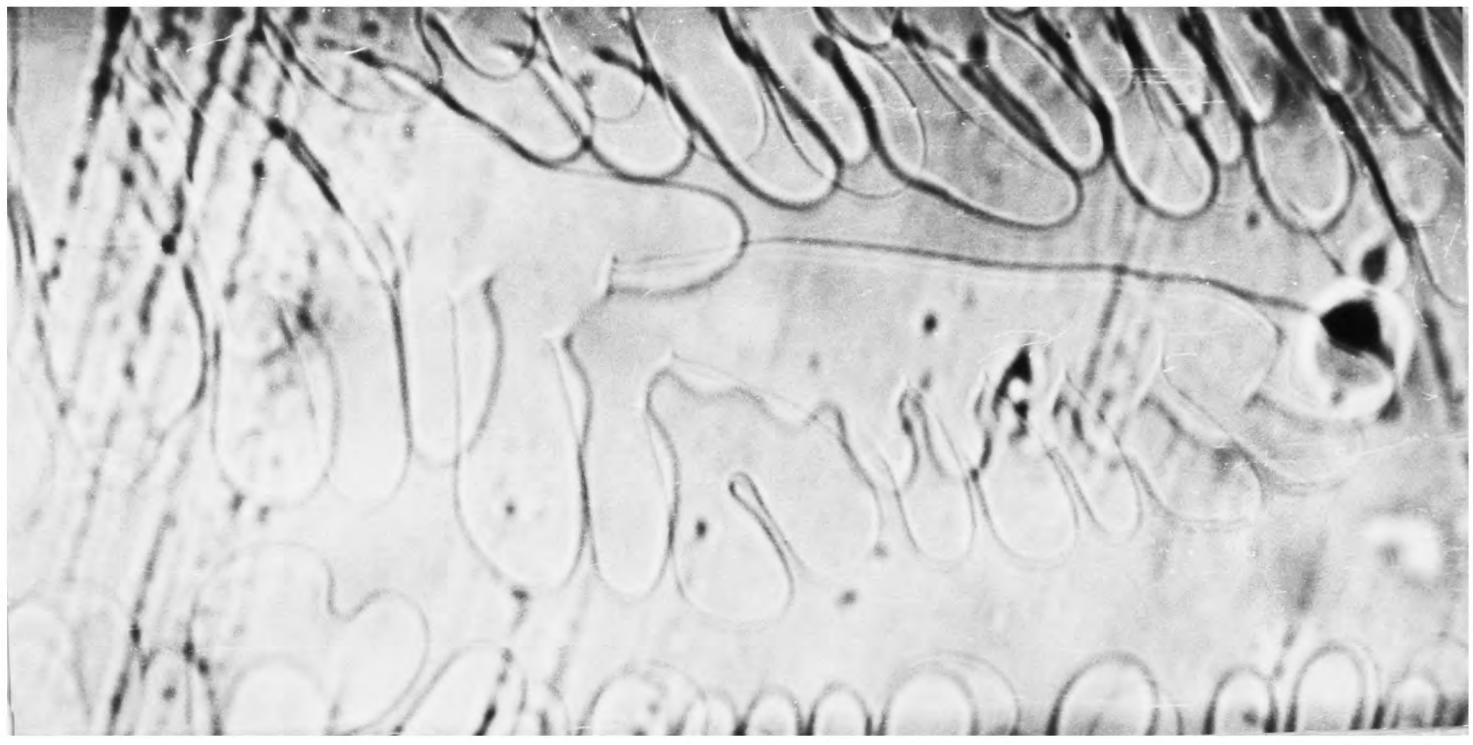


PLATE 11. Transient "misoriented" sidearm (x 437)

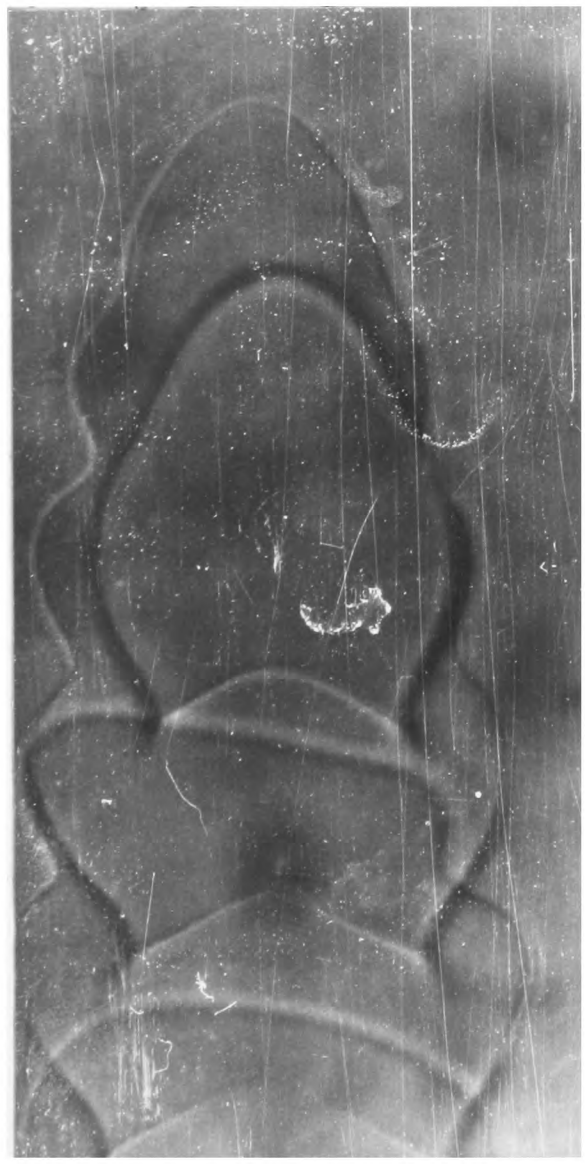


PLATE 12.
"Double" dendrite (x 359)

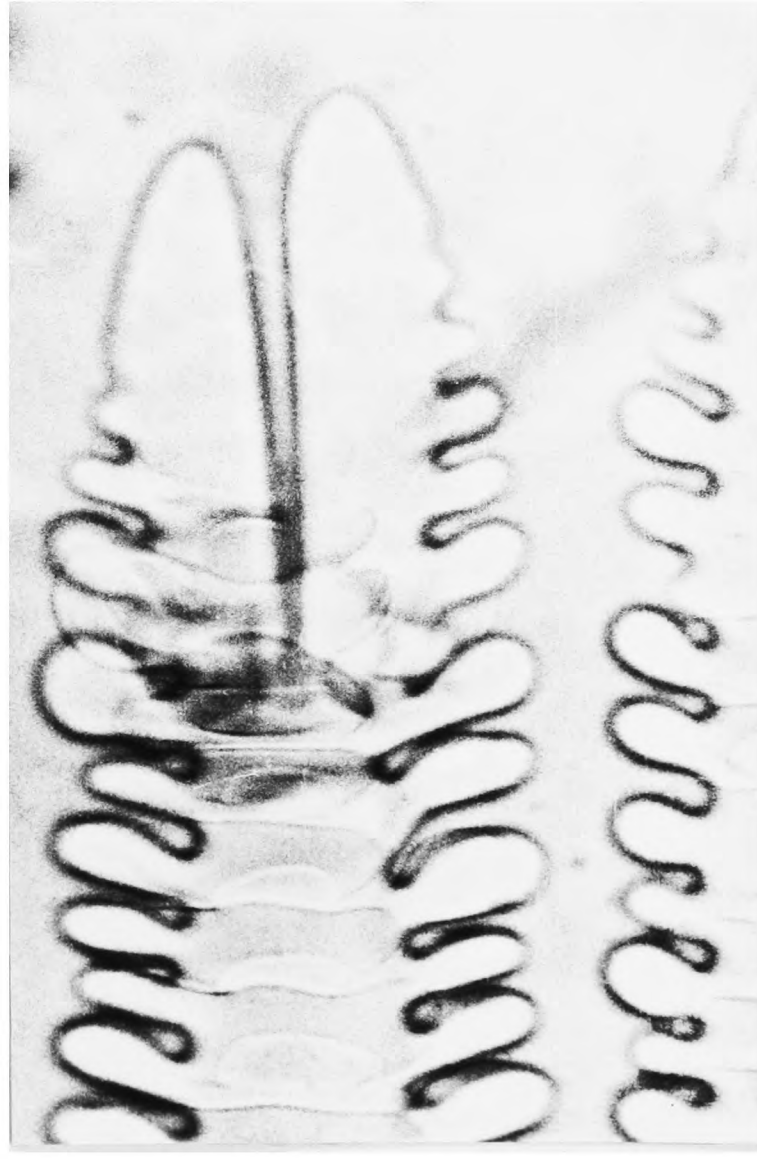


PLATE 13.
Tip splitting (x 318)

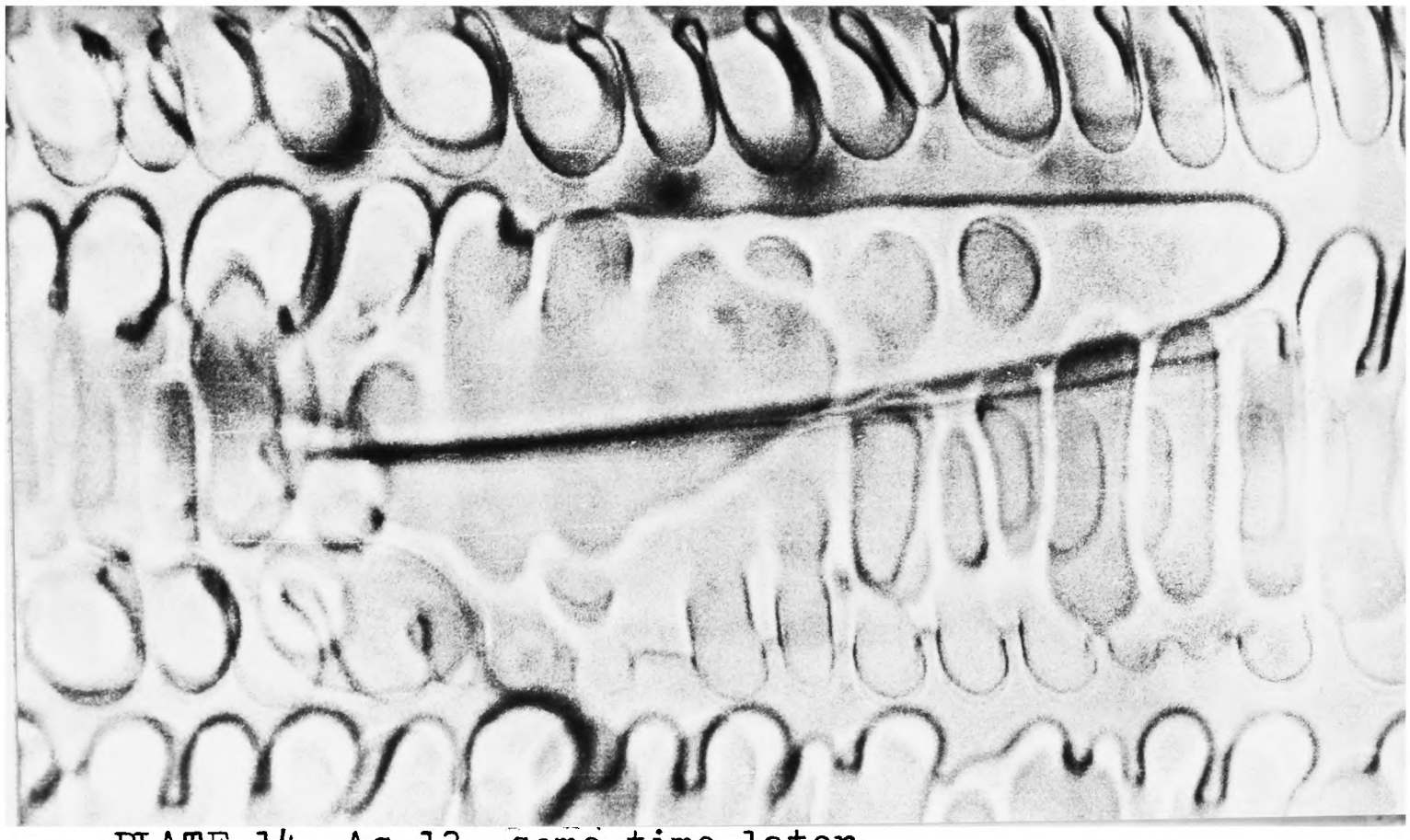


PLATE 14. As 13, some time later.

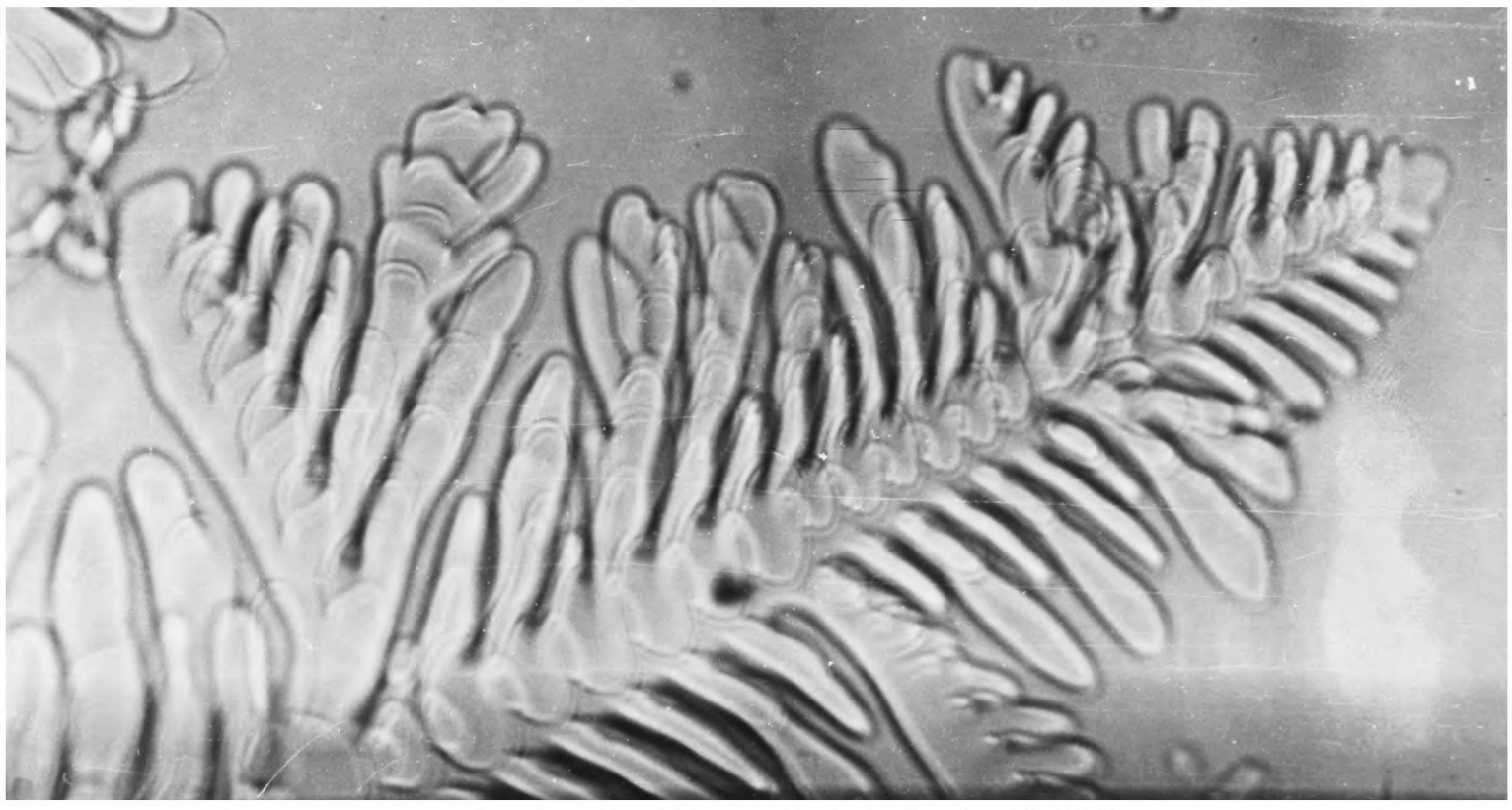


PLATE 15. "Misoriented" dendrite. (x 212)
("pure" succinonitrile)

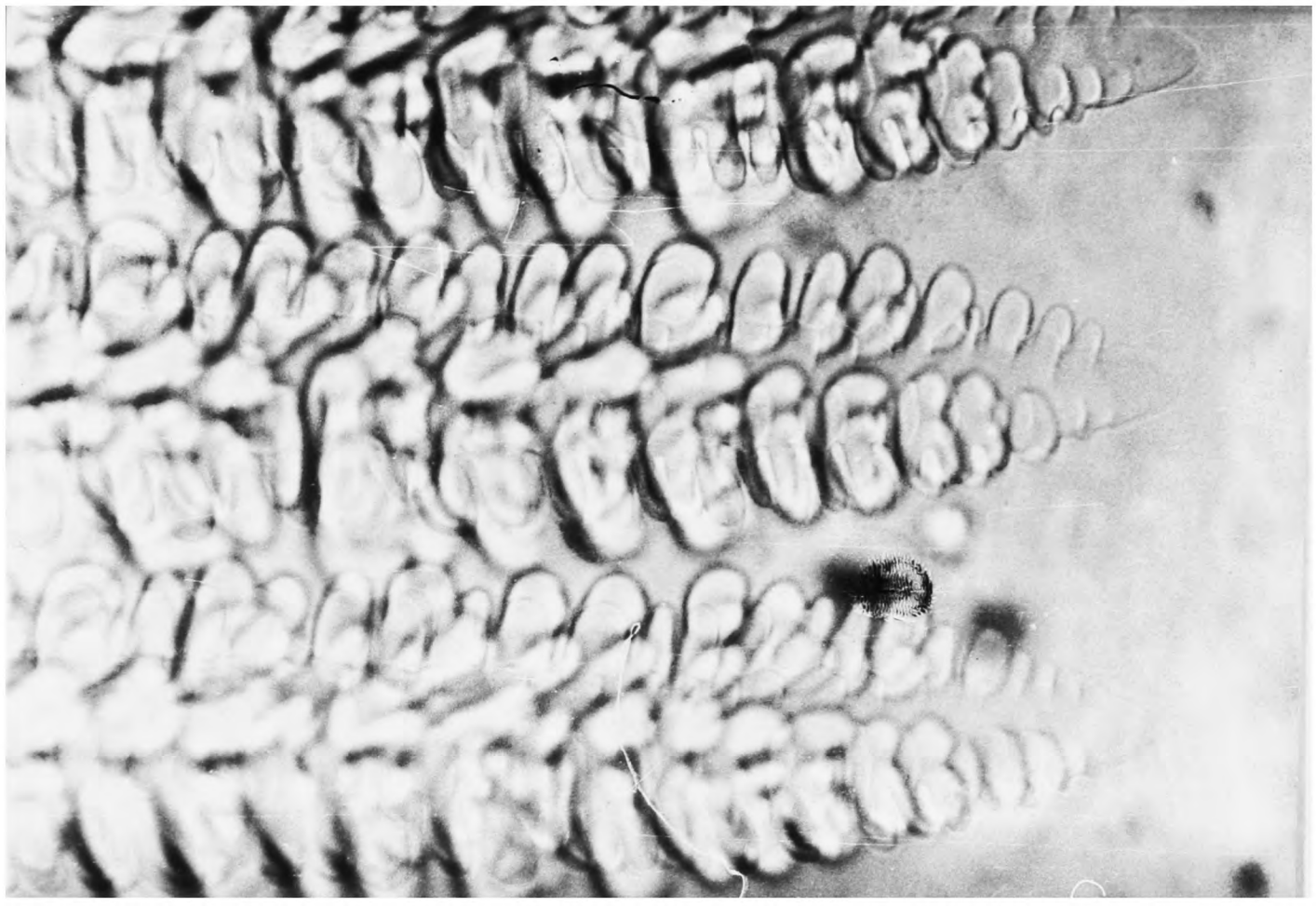


PLATE 16. R = 29.5 μm/sec., growth at top of cell. (x 242) (9% CBr_4 - succinonitrile). Type 2.

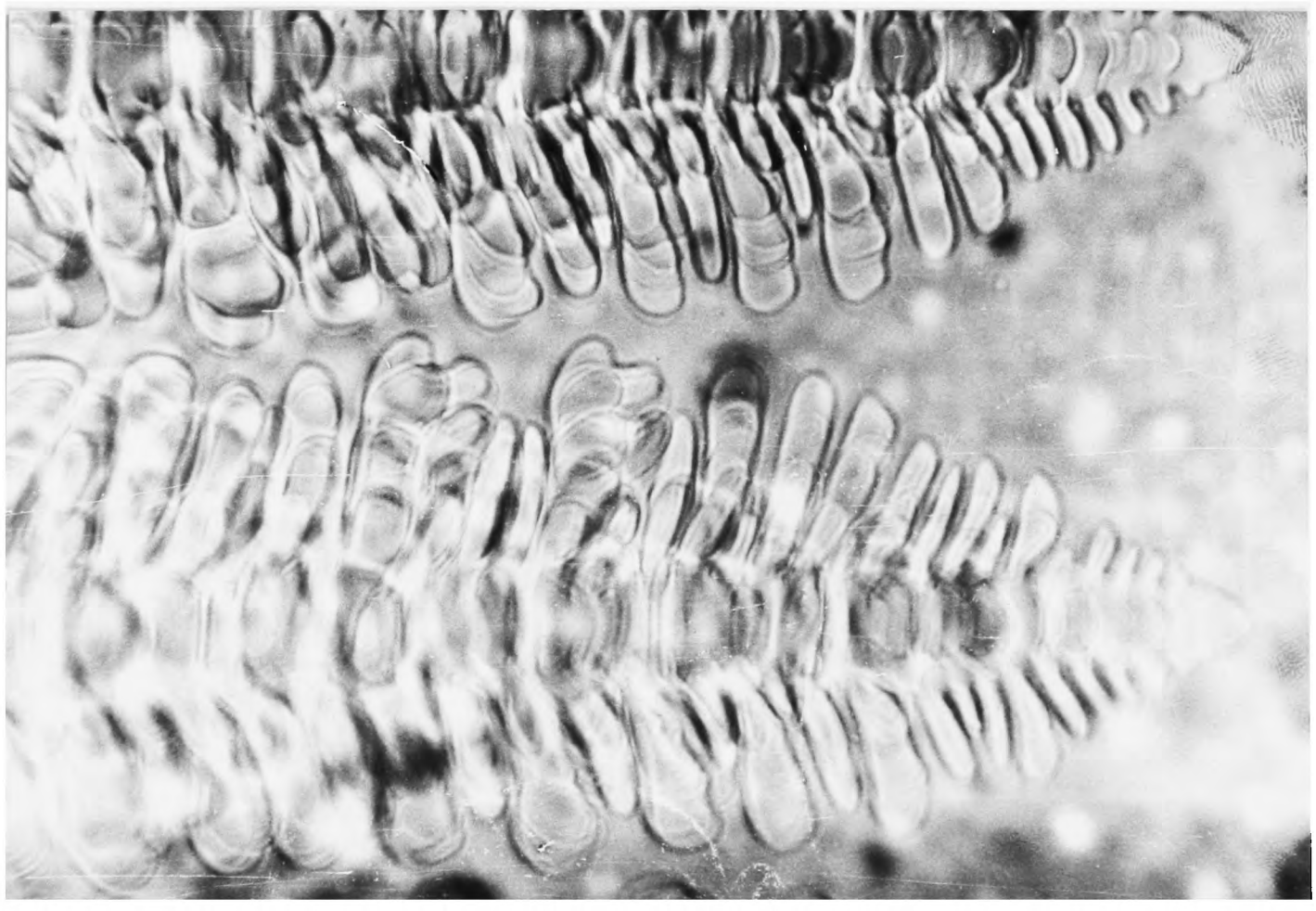


PLATE 17. As above but growth at base of cell, type 1

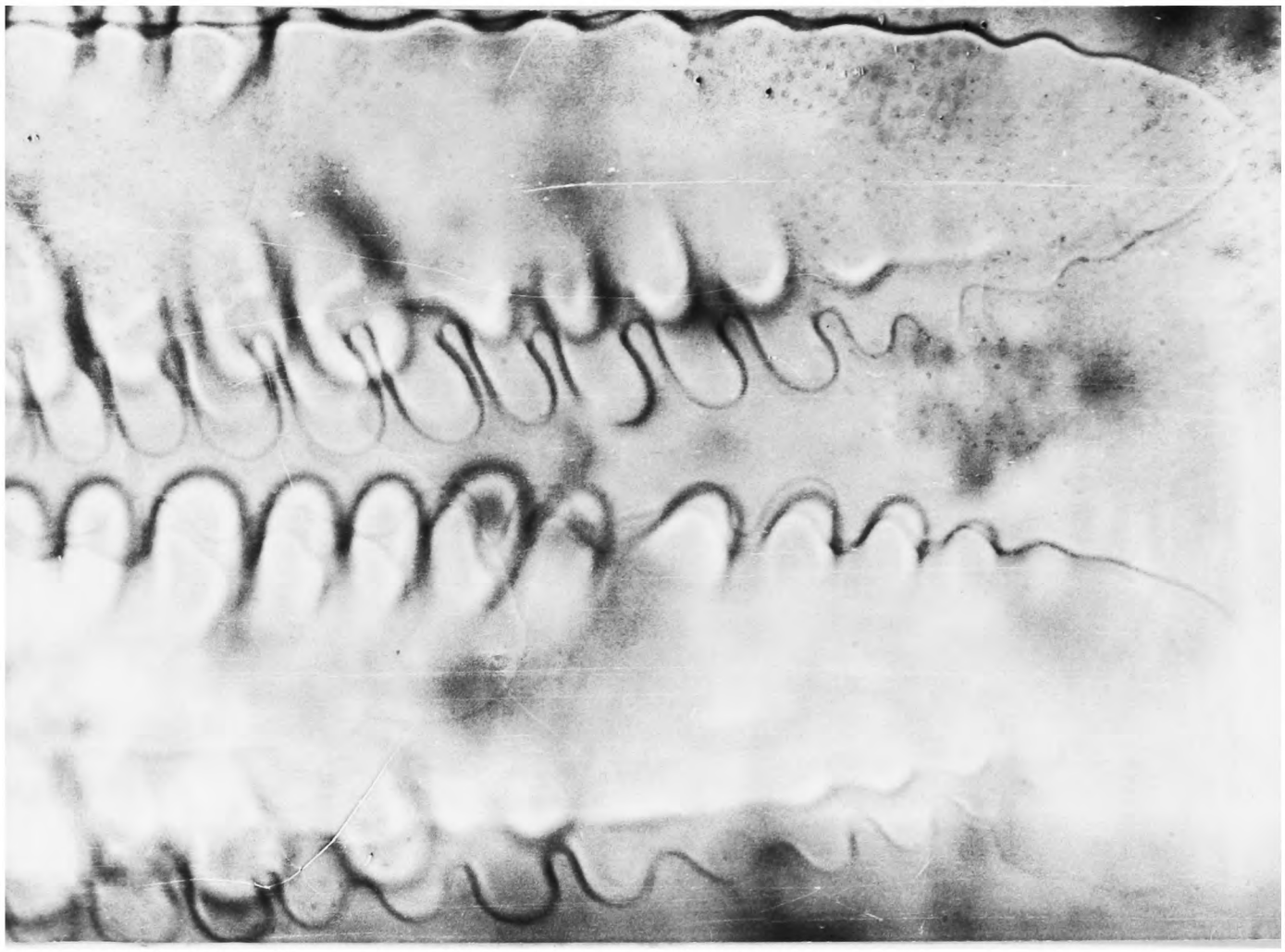


PLATE 18. As 16 but R = 5.92 μms.

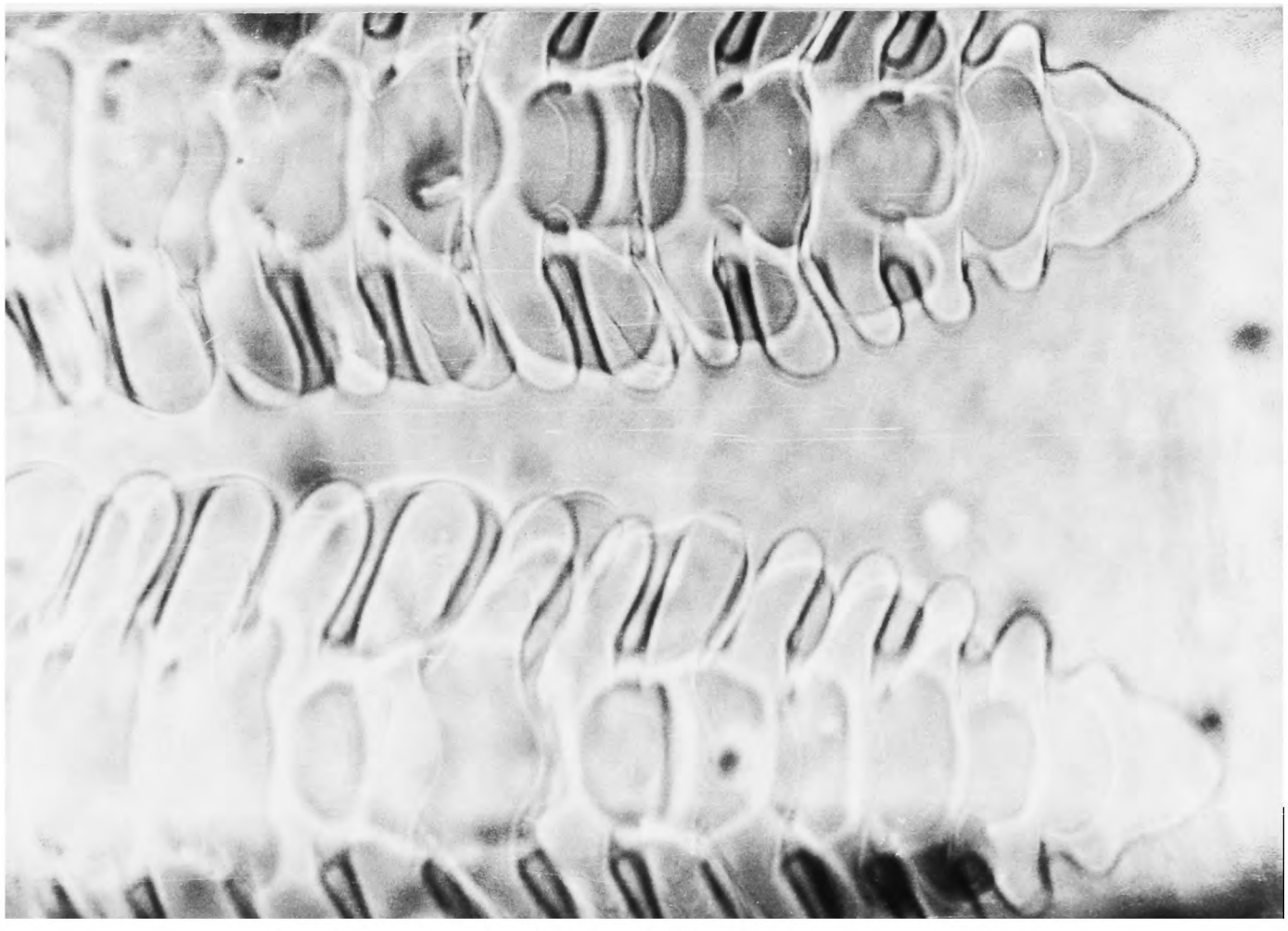
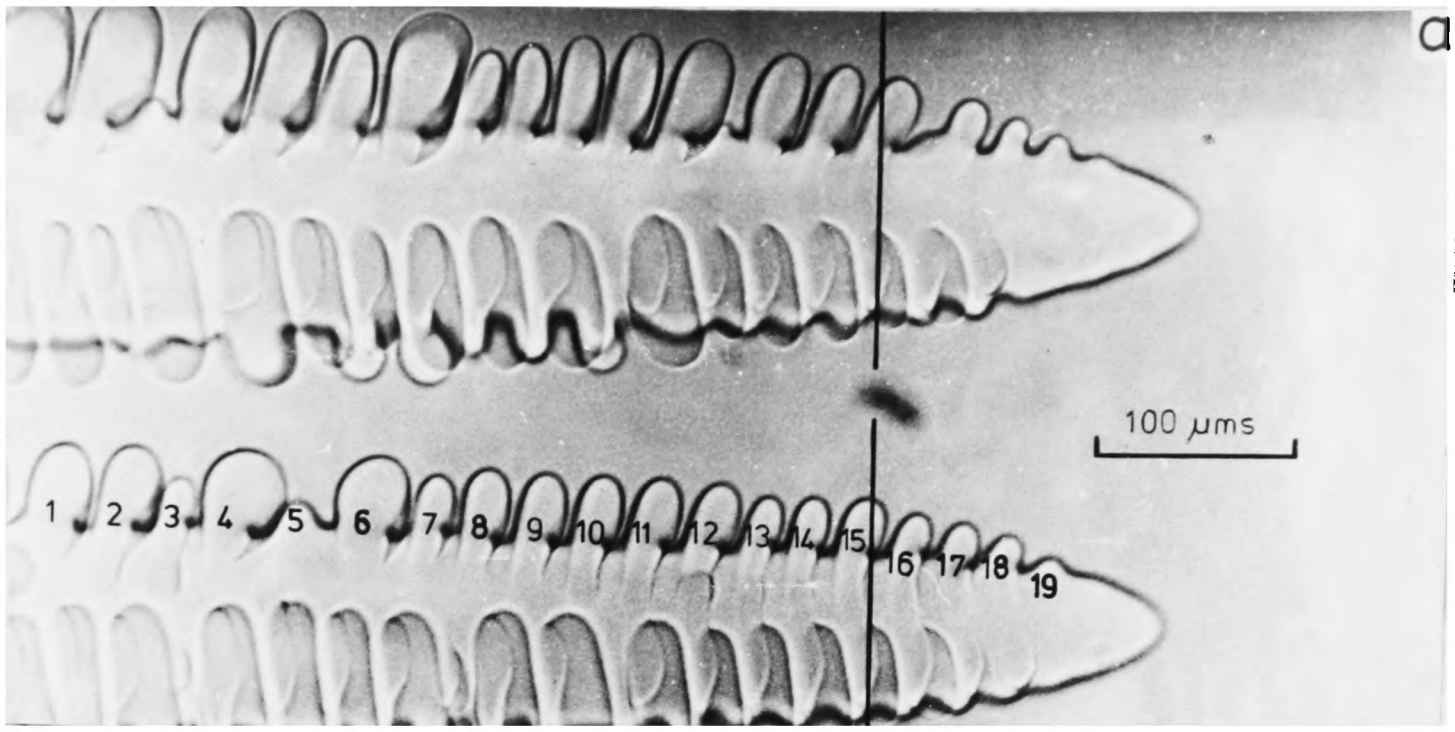
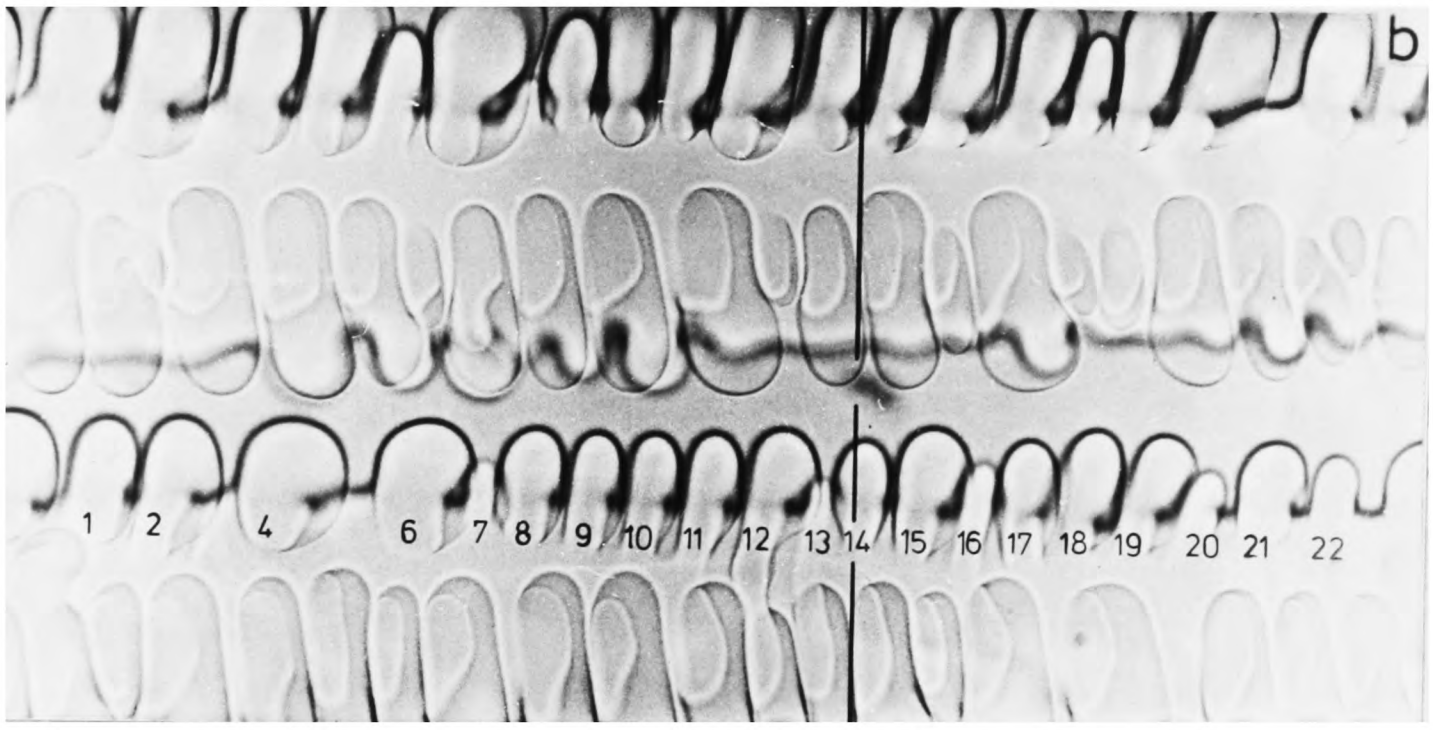


PLATE 19. As 17 but R = 5.92μms.





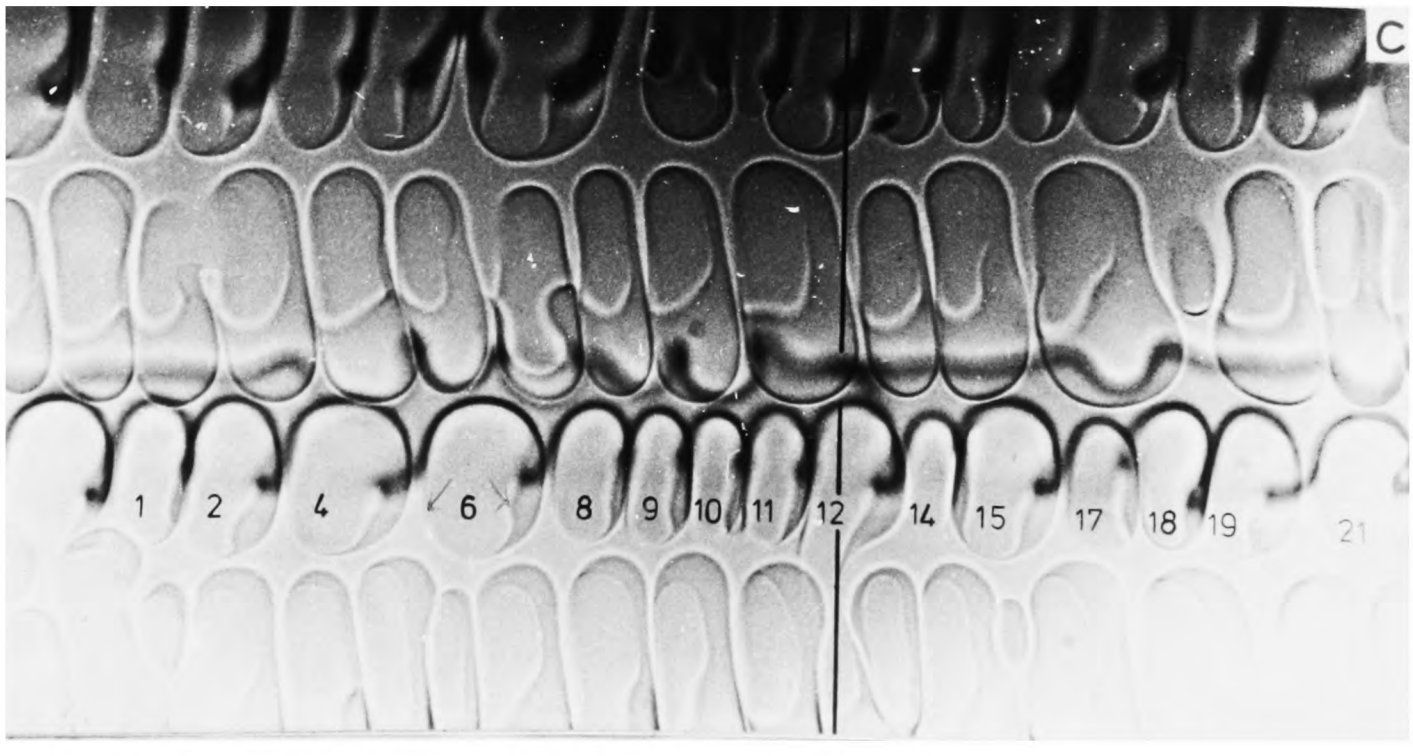
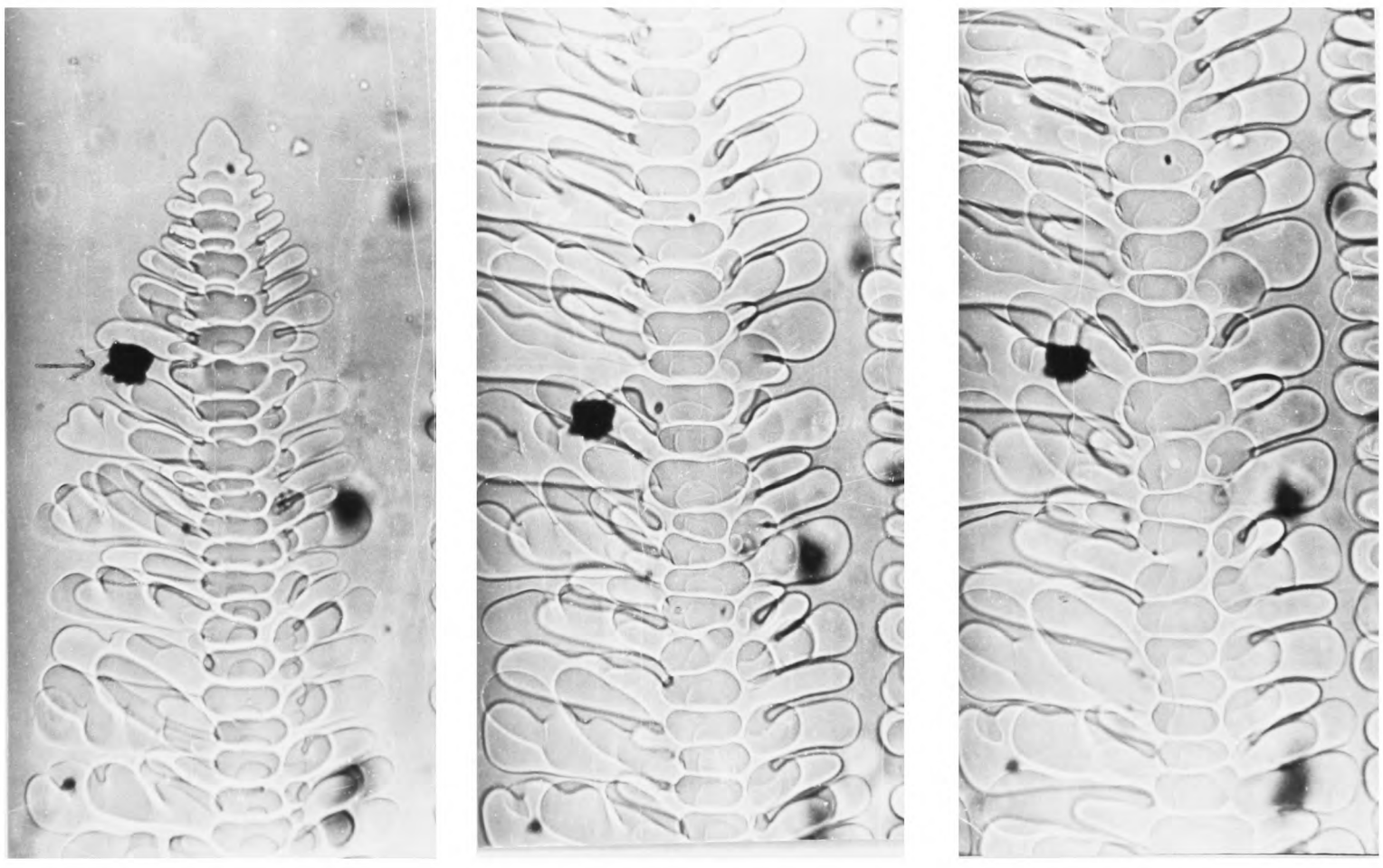


PLATE 21. TGZM during solidification, chap. VII.(d).
(a.) 0 sec., (b.) 180 sec., (c.) 480 sec.



PLATE 20. Liquid layer instability. (x 459)
(See chap. 7)



PLATES 22 - 24. Sequence showing TGZM past dust particle (arrowed) during solidification. (x 146)

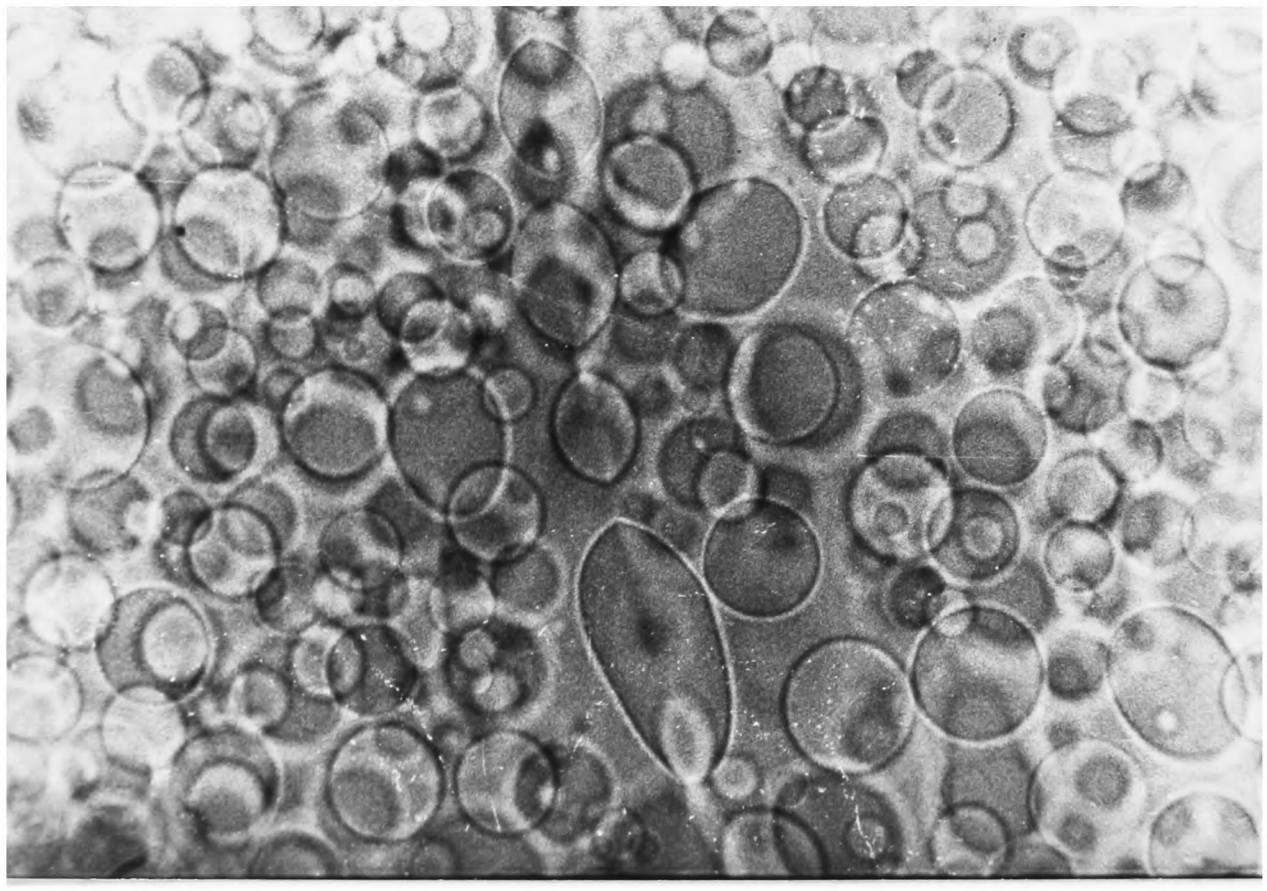


PLATE 25. Droplet TGZM (high - temperature run of Chap. VII. (e).) Migration to the right. (x 439)

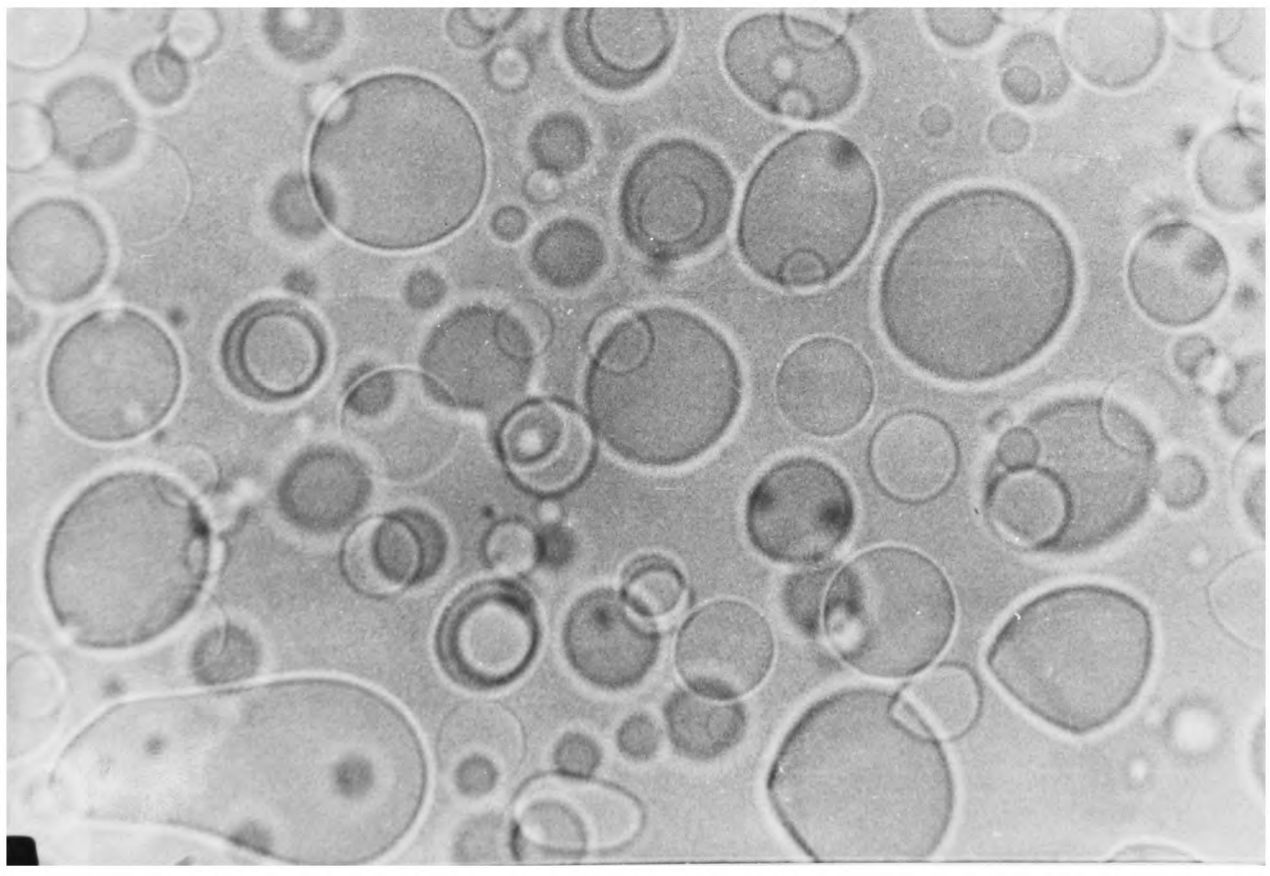


PLATE 26. As above but lower - temperature run.

Appendix A

To solve:

$$\frac{dx^*}{dt} = \frac{-(x^* - \frac{1}{2}\lambda)}{(1 - k)(t + \theta_d)} - \frac{kD_S}{(x^* - \frac{1}{2}\lambda)} \qquad (V.35)$$

This may be written in the form:

$$\frac{dx^*}{dt} = \frac{f}{g} = 0 \qquad (A.1)$$

when an integrating factor may be found from the formula:

$$w = w(t) = \exp \int \frac{(\partial f/\partial x) - (\partial g/\partial t)}{g}\, dt \qquad (A.2)$$

(A.1) is then made exact by multiplying through by w, and the solution method is then as described by Stephenson(256) p. 363. The result is:

$$(t + \theta_d)^{[2/(1-k)]} \left[(x^* - \tfrac{1}{2}\lambda)^2 + kD_S \frac{2(1 - k)}{3 - k} (t + \theta_d)\right] = K \qquad (A.3)$$

where K is constant. The initial conditions:

$$x^* = x_0 \quad \text{and} \quad f_g = f_{s0} \quad \text{at } t = 0 \qquad (A.4)$$

may be used to eliminate K, obtaining:

$$\left(\frac{t + \theta_d}{\theta_d}\right)^{[2/(1-k)]} \left[\frac{(x^* - \frac{1}{2}\lambda)^2 + kD_S(2 - 2k)(t + \theta_d)/(3 - k)}{(x_o - \frac{1}{2}\lambda)^2 + kD_S(2 - 2k)\theta_d/(3 - k)}\right] = 1 \qquad (A.5)$$

With the substitutions $(t + \theta_d)/\theta_d = c_L^*/(c_L^*)_{t=0}$,

$f_s = (2x^*/\lambda)$ and (V.36), (A.5) yields (V.37). The solution (A.3) has been tested by re-differentiation: after implicit differentiation of (A.3), (V.35) is obtained by substituting an expression for $K(t + \theta_d)^{-2/(1-k)}$ from (A.3) back into the differential form of (A.3).

Appendix B

(a) To solve:

$$(D_{LO} + az_i)\frac{d^2f}{dz_i^2} + (v + a)\frac{df}{dz_i} = 0 \qquad (VI.28)$$

Substituting $p = (df/dz_i)$ and separating the variables:

$$\int\frac{dp}{p} = \frac{-(v + a)}{a}\int\frac{dz_i}{(z_i + D_{LO}/a)} \qquad (1)$$

$$\therefore\ p = \left[K_1(z_i + D_{LO}/a)\right]^{-(\frac{v+a}{a})} \qquad (2)$$

where K terms all represent constants. Integrating again:

$$f = \left(\frac{-a}{v}\right)\left(K_1^{-\left(\frac{v+a}{a}\right)}\right)(z_i + D_{LO}/a)^{-v/a} + K_2 \qquad (3)$$

provided $v \neq 0$. Since, from (VI.21), g is zero:

$$c_L = \left(\frac{-a}{v}\right)\left(K_1^{-\left(\frac{v+a}{a}\right)}\right)(z_i + D_{LO}/a)^{-v/a} + K_2 \qquad (4)$$

However, if $v = 0$, integrating (B.2) yields:

$$c_L = K_1^{-1} \ln(z_i + D_{LO}/a) + K_3 \qquad (5)$$

The boundary conditions are:

$$c_L = c_{Lf}^* \text{ at the freezing interface, } z_i = 0 \qquad (6)$$

$$c_L = c_{Lm}^* \text{ at the melting interface, } z_i = l \ (= z_m^* - z_f^*) \qquad (7)$$

where l is zone length. Hence (B.4) becomes:

$$c_L = c_{Lf}^* + (c_{Lm}^* - c_{Lf}^*)\left(\frac{1 - (1 + az_i/D_{LO})^{-v/a}}{1 - (1 + al/D_{LO})^{-v/a}}\right) \qquad (8)$$

while (B.5) becomes:

$$c_L = c_{Lf}^* + (c_{Lm}^* - c_{Lf}^*)\left[\frac{\ln(1 + az_i/D_{LO})}{\ln(1 + al/D_{LO})}\right] \qquad (9)$$

It follows from (B.9) that:

$$D_L \frac{dc_L}{dz_i} \quad \frac{a(c_{Lm}^* - c_{Lf}^*)}{\ln(1 + al/D_{LO})} \qquad (10)$$

for any z_i, when $v = 0$.

A common representation for D_L is:

$$D_L = D_O \exp(-Q/RT). \qquad (11)$$

In this case,

$$a = G\frac{dD_L}{dT} = \frac{GD_OQ}{RT^2} \exp\left(\frac{-Q}{RT}\right) \qquad (12)$$

Provided that $(al/D_{LO}) \ll 1$, (B.12) may be combined with (B.9) to give a good approximate treatment of the temperature-dependence of D_L.

(b) <u>To solve</u>:

$$D_L \frac{d^2f}{dz_i^2} + v\frac{df}{dz_i} = \frac{G(v - R)}{m} \qquad (VI.29)$$

we use the method of particular integrals (e.g. Stephenson[256] p. 369 ff.) The reduced equation

$$D_L \frac{d^2f}{dz_i^2} + v\frac{df}{dz_i} = 0 \qquad (13)$$

has the well-known solution (c.f. (I.15)):

$$f = K_1 \exp(-vz_i/D_L) + K_2 \qquad (14)$$

For the particular integral, we use the trial function:

$$f = A + Bz_i + Cz_i^2 \quad (A,B,C \text{ constants}) \qquad (15)$$

Hence, by substituting (B.15) into (B.12) and comparing coefficients, we find:

$$f = \frac{G(v - R)z_i}{mv} \tag{16}$$

Conbining complementary function (B.14) with particular integral (B.16):

$$f = \frac{G(v - R)z_i}{mv} + K_1 \exp\left(\frac{-vz_i}{D_L}\right) + K_2 \tag{17}$$

is the general solution.

Using the boundary conditions:

$$f = f_f^* \text{ at the freezing interface, } z_i = 0 \tag{18}$$

$$f = f_m^* \text{ at the melting interface } \quad z_i = l \tag{19}$$

(B.17) becomes:

$$f = f_f^* + \frac{G(v - R)z_i}{mv}$$
$$+\left[(f_m^* - f_f^*) - \frac{G(v - R)l}{mv}\right]\left[\frac{(\exp(-vz_i/D_L)) - 1}{(\exp(-vl/D_L)) - 1}\right] \tag{20}$$

If f_f^* and f_m^* are specified by (VI.30), (B.20) is:

$$f = c + \frac{\Delta T_{kf}}{m} + \frac{G(v - R)z_i}{mv}$$
$$+\left[\frac{\Delta T_{km} - \Delta T_{kf}}{m} + \frac{GRl}{mv}\right]\left[\frac{(\exp(-vz_i/D_L)) - 1}{(\exp(-vl/D_L)) - 1}\right] \tag{21}$$

For the special case v = 0, (VI.29) becomes:

$$D_L \frac{d^2 f}{dz_i^2} = - \frac{GR}{m} \qquad (22)$$

This may be solved by simple integration. Using boundary conditions as above and combining the result with (VI.21), equation (VI.45) is obtained as an exact solution.

(c)

We now assume R = 0, v ≠ 0, and assert that D_L is a function of z_i alone, in contradiction to the assumption (VI.25) used in B.(a). Then, assuming (VI.18), (VI.8) gives (see (VI.20)):

$$\frac{dg}{dt} = \frac{Gv}{m} \quad \therefore \quad g = \frac{Gvt}{m} + K \qquad (23)$$

and, from (VI.24) and (VI.27):

$$(D_{LO} + az_i)\frac{d^2 f}{dz_i^2} + (v + a)\frac{df}{dz_i} = \frac{Gv}{m} \qquad (24)$$

This may be solved by the same method as B.(b), where (VI.28) is the reduced equation and so (B.3) is the complementary function in this case. Using a trial function of form (B.15), the particular integral is:

$$f = \frac{Gv}{m(v + a)} \qquad (25)$$

Combining (B.3) and (B.25), and putting in boundary

conditions (B.18) and (B.19):

$$f = f_f^* + \frac{Gvz_i}{m(v+a)} + (f_m^* - f_f^*)\left(\frac{a}{v+a}\right)\left(\frac{1-(1+az_i/D_{LO})^{-v/a}}{1-(1+al/D_{LO})^{-v/a}}\right) \qquad (26)$$

Putting in (VI.30) with ΔT_k terms equal to zero,

$$c_L = c + \frac{Gvz_i}{m(v+a)} + \left(\frac{Gl}{m}\right)\left(\frac{a}{v+a}\right)\left(\frac{1-(1+az_i/D_{LO})^{-v/a}}{1-(1+al/D_{LO})^{-v/a}}\right) \qquad (27)$$

Now, if $(al/D_{LO}) \ll 1$, the terms in the final bracket may be expanded binomially. This produces an expression in terms of successive powers of (vz_i/D_{LO}) and (vl/D_{LO}). If only the first terms are taken, this reduces to $(\partial c_L/\partial z) = G/m)$ throughout as in McLean's treatment, so that the diffusion fluxes at opposite ends of the zone are $(D_{LO}G/m)$ and $(D_{LO} + al)G/m$, and therefore differ by a multiplying facotr $(1 + al/D_{LO})$. If the second $((vl/D_{LO})^2)$ terms are also taken, it emerges that the diffusion flux equals $(D_{LO} + \frac{1}{2}al)G/m$ throughout the zone. So when higher terms are also included, the diffusion fluxes at opposite ends of the zone differ by a multiplying factor of the form $(1 + K_1(al/D_{LO})^3 + K_2(al/D_{LO})^4\ldots)$. Provided that (al/D_{LO}) and $vl/D_{LO})$ are $\ll 1$, this binomial expansion procedure is valid and the difference in diffusion fluxes between opposite ends of the zone is very much smaller that the factor $(1 + al/D_{LO})$ found from the McLean-type analysis.

Appendix C. The Curvature Effect in Binary Alloys.

The following treatment is similar to that of Appendix I, ref. 1, but removes unnecessary complications: it is based on an analysis by Lesoult and Turpin.[275]

For chemical equilibrium at the solid-liquid interface

$$\mu_{iS}\,(p_S,\ T,\ x_{BS}) = \mu_{iL}\,(p_L,\ T,\ x_{BL}) \qquad (1)$$

where μ_i is chemical potential of the i th component, x_B the mole fraction of the B component. Expanding (C.1) in differential form:

$$\bar{V}_i^{\,S} dp_S - \bar{V}_i^{\,L} dp_L + (\bar{S}_i^{\,L} - \bar{S}_i^{\,S})dT + \left(\frac{\partial \mu_{is}}{\partial x_{BS}}\right) d_{xBS}$$

$$- \left(\frac{\partial \mu_{iL}}{x_{BL}}\right) dx_{BL} = 0 \qquad (2)$$

where $\bar{V}_i$, $\bar{S}_i$ are partial molar volume and entropy respectively and the superscripts S,L refer to solid and liquid. In binary alloys there are two equations of the form (C.2). These may be simplified by the use of the Gibbs-Duhem equation:[3b]

$$d\mu_B = \frac{-(1 - x_B)}{x_B}\, d\mu_A \qquad (3)$$

to eliminate one composition variable. Then equations (C.2) may be written:

$$\bar{V}_A^S dp_S - \bar{V}_A^L dp_L + (\bar{S}_A^L - \bar{S}_A^S)dT + \left(\frac{\partial \mu_{AS}}{\partial x_{BS}}\right) dx_{BS}$$

$$- \left(\frac{\partial \mu_{AL}}{\partial x_{BL}}\right) dx_{BL} = 0 \qquad (4)$$

$$\bar{V}_B^S dp_S - \bar{V}_B^L dp_L + (\bar{S}_B^L - \bar{S}_B^S)dT$$

$$- \frac{1 - x_{BS}}{x_{BS}} \left(\frac{\partial \mu_{AS}}{\partial x_{BS}}\right) dx_{BS} + \left(\frac{1 - x_{BL}}{x_{BL}}\right) \left(\frac{\partial \mu_{AL}}{\partial x_{BL}}\right) dx_{BL} = 0$$

(5)

Now, any one variable can be eliminated between (C.4) and (C.5). Multiplying (C.4) by $(1 - x_{BS})$, multiplying (C.5) by x_{BS}, and adding the equations together, we may eliminate dx_{BS}:

$$\left[x_{BS}\bar{V}_B^S + (1 - x_{BS})\bar{V}_A^S\right] dp_S$$

$$- \left[x_{BS}\bar{V}_B^L + (1 - x_{BS})\bar{V}_A^L\right] dp_L$$

$$+ \left[x_{BS}(\bar{S}_B^L - \bar{S}_B^S) + (1 - x_{BS})(\bar{S}_A^L - \bar{S}_A^S)\right] dT$$

$$+ \left(\frac{x_{BS} - x_{BL}}{x_{BS}}\right) \left(\frac{\partial \mu_{AL}}{\partial x_{BL}}\right) dx_{BL} = 0 \qquad (6)$$

We may simplify the notation of (C.6) by rewriting it as:

$$V^S dp_s - V^L dp_L + \Delta S^S dT + \left(\frac{x_{BS} - x_{BL}}{x_{BS}}\right)\left(\frac{\partial \mu_{AL}}{\partial x_{BL}}\right) dx_{BL} = 0 \qquad (7)$$

where the terms V^S, V^L, ΔS^S are defined by comparison with (C.6).

Rearranging (C.7):

$$dT = \frac{-V^S}{\Delta S^S} dp_S + \frac{V^L}{\Delta S^S} dp_L + \left(\frac{x_{BS} - x_{BL}}{\Delta S^S x_{BS}}\right)\left(\frac{\partial \mu_{AL}}{\partial x_{BL}}\right) dx_{BL} \qquad (8)$$

Now, as all the variables in (C.8) are independent, this is of the form:

$$dT = \left(\frac{\partial T}{\partial p_S}\right)_{x_{BL},p_L} dp_s + \left(\frac{\partial T}{\partial p_L}\right)_{x_{BL},p_S} dp_L + \left(\frac{\partial T}{\partial x_{BL}}\right)_{p_L,p_S} dx_{BL}$$

(9)

Therefore, we may equate coefficients in (C.8) and (C.9) and integrate from the actual temperature $T(p_S, p_L, x_{BL})$ to whatever arbitrary reference temperature $T_O(p_{SO}, p_{LO}, x_{BLO})$ is chosen. The integrations may be performed in any order but our convention (chapter I.(a)) will be to integrate first with respect to p_S, then p_L, and finally x_{BL}:

$$\Delta T = \int_{p_S}^{p_{SO}} \left(\frac{\partial T}{\partial p_S}\right)_{p_L,x_{BL}} dp_S + \int_{p_L}^{p_{LO}} \left(\frac{\partial T}{\partial p_L}\right)_{p_{SO},x_{BL}} dp_L$$

$$+ \int_{x_{BL}}^{x_{BLO}} \left(\frac{\partial T}{\partial x_{BL}}\right)_{p_{SO},p_{LO}} dx_{BL} \qquad (10)$$

Taking $p_{SO} = p_L$, the first term of (C.10) is the curvature undercooling as conventionally defined (I.2). Taking p_{LO} = 1 atmosphere, the second term might be termed "pressure undercooling" and the third term refers to integration along the conventional phase diagram liquidus line. Taking $x_{BLO} = 0$, this is the solute undercooling as defined in chapter I.(a). From (C.8 - 10), the curvature undercooling is:

$$\Delta T_c = \frac{-V^S(p_{SO} - p_S)}{\Delta S^S} = \frac{-V^S(p_L - p_S)}{\Delta S^S} \qquad (11)$$

For mechanical equilibrium at the solid-liquid interface:[4]

$$p_S = p_L + \left(\frac{\sigma + \partial^2\sigma/\partial\theta_1^2}{r_1}\right) + \left(\frac{\sigma + \partial^2\sigma/\partial\theta_2^2}{r_2}\right) \qquad (12)$$

where θ_i is the angle between the surface-normal and an arbitrary direction, such that this direction and the surface-normal define the plane corresponding to the radius of curvature r_i.

Neglecting the $\partial^2\sigma/\partial\theta_i^2$ terms:

$$\Delta T_c = \frac{\sigma V^S}{\Delta S^S}\left(\frac{1}{r_1} + \frac{1}{r_2}\right) \qquad (13)$$

with V^S, ΔS^S as defined by (C.6 - 7). This may be compared to (I.2) for the one-component case.

The particular rearrangement of (C.7) used in (C.8) was chosen in order to calculate an undercooling. Strictly speaking,

$$\left(\frac{\partial T}{\partial p_S}\right)_{p_L,x_{BL}} = \left(\frac{\partial T}{\partial c_L}\right)_{p_L,x_{BL}} \left(\frac{\partial c_L}{\partial p_S}\right)_{p_L,x_{BL}} \tag{14}$$

in (C.10) so that,

$$(\Delta c_L)_c = \Delta T_c / \left(\frac{\partial T}{\partial c_L}\right)_{p_L,x_{BL}} \tag{15}$$

describes the effect of curvature on c_L at constant T, where $(\partial T/\partial c_L)_{p_L,x_{BL}}$ is not exactly equal to m from the phase diagram. The error is small and may generally be ignored. The quantity $(\Delta c_L)_c$ could have been more directly obtained from a different rearrangement of (C.7): the quantity $(\Delta c_S)_c$ could have been obtained by eliminating a different variable between (C.4) and (C.5). Hunt[276] has shown that a simpler, less general treatment suffices to calculate any one of these quantities. Lesoult and Turpin[275] showed that k is nearly, but not exactly, held constant as surface curvature changes.

Tiller[274] suggested that the curvature equations required modifications for moving interfaces. However, his predicted modifications were independent of velocity so that markedly different predictions were made for infinitesimally small velocity and for zero velocity. This is in contradiction with the general thermodynamic principle of reversible changes.